Design and Characterization of Functional Structures for Electromagnetic Waves

Ericsson, Andreas

2017

Document Version:
Publisher's PDF, also known as Version of record

Design and Characterization of Functional Structures for Electromagnetic Waves

Andreas Ericsson

Doctoral Dissertation
Electromagnetic Theory

Lund University
Lund, Sweden
2017

Doctoral dissertation which, by due permission of the Faculty of Engineering, Lund University, will be publicly defended on October 27, 2017, at 10:15 a.m. in lecture hall E:1406, John Ericssons väg 4, Lund, for the degree of Doctor of Philosophy in Engineering in Electromagnetic Theory.

Department of Electrical and Information Technology
Electromagnetic Theory Group
Lund University
P.O. Box 118, S-221 00 Lund, Sweden

Series of licentiate and doctoral theses
ISSN 1654-790X; No. 103
ISBN 978-91-7753-323-8 (print)
ISBN 978-91-7753-324-5 (digital)

Typeset in Computer Modern 10 pt using LaTeX and BibTeX.
Printed in Sweden by *Tryckeriet i E-huset*, Lund University, Lund.
October, 2017

The illustration on p. iii is a comic from "Piled Higher and Deeper", www.phdcomics.com,

To my wife Malin,
Thank you for your love, endless patience, and unfaltering belief in me.

&

To my family,
Mom and Dad, thank you for your wisdom, encouragement and support.
Anna and Alexander, thank you for our special bond and true friendship.

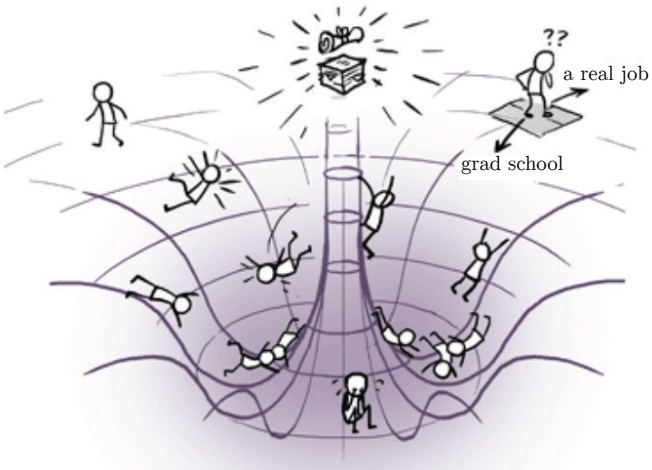

"The thesis repulsory field is a generalized model of the forces experienced by an individual in the final stages of graduate space-time. It is characterized by an attractor vector field directed towards completion of the thesis but with an intense repulsive singularity at its origin."

The Thesis Repulsory Field

"Piled Higher and Deeper" by Jorge Cham
www.phdcomics.com

Abstract

This dissertation deals with design and characterization of functional structures for scattering of electromagnetic waves. An abundance of these structures can be found in nature, such as the structural coloration in the feathers of a peacock, the scales of butterflies and the shell of scarab beetles. Human design of structures providing specific interactions with electromagnetic waves have a long history. Today, these structures can be found in everyday products and applications like the filter of a microwave oven, shaded windows, polarizing glasses and 3D movies. A high demand of functional structures is also found in more advanced applications such as antenna design, electromagnetic scattering reduction for stealth applications, and in satellite communication systems.

The dissertation consists of a general introduction and nine scientific papers, of which the majority have been published in peer-reviewed international journals. The general introduction sets the stage for the technical details contained in the included papers. Fundamental relations and scattering concepts in electromagnetic theory are presented, alongside with the approaches for design, optimization and experimental characterization of functional structures. The included papers can be divided into two main tracks: Papers I–VI concern satellite communications and Papers VII–IX are related to electromagnetic scattering characterization and reduction.

In Papers I–V circular polarization selective structures for satellite communication applications are designed and characterized numerically and experimentally. A novel concept design is presented providing more than double the frequency bandwidth of previous designs. Furthermore, an experimental procedure and a data post processing scheme are presented for accurate characterization of circular polarization selective structures. In Paper VI a multiphysics study of a triaxial weave functioning as a reflector antenna surface is presented. The electromagnetic scattering properties of the structure are evaluated using numerical simulations and approximation models. These results are combined with an acoustic study and design guidelines for such space antennas are specified.

In Papers VII–VIII electromagnetic radiation-absorbing materials for scattering reduction applications are evaluated. By using an analytic framework in canonical scattering problems, and numerical methods in more application oriented scenarios, two fast computation methods are developed. These methods are used to evaluate a number of different radiation-absorbing materials in different scenarios, and provide information of the physical interaction between electromagnetic waves and scatterers coated with said materials.

Finally, in Paper IX different methods are utilized to locate defects in composite materials. Compressive sensing techniques are implemented to achieve sub-wavelength resolution of data extracted from experimentally acquired scattered fields. A key point is identifying that the scattering from hidden defects can be formulated as a sparse inverse scattering problem in some basis.

Populärvetenskaplig sammanfattning (in Swedish)

Elektromagnetiska vågor finns överallt runt omkring oss och är en förutsättning för livet som vi känner det. Det är dessa vågor som ger oss värme från solen, vår syn och som transporterar information genom våra hjärnor. Konsten att förstå och kontrollera elektromagnetiska vågor har intresserat många av vår tids största vetenskapsmän som Isaac Newton, James Clerk Maxwell och Albert Einstein. På samma sätt som vattenvågor skapas och utbreder sig när en sten släpps i vatten genereras elektromagnetiska vågor av laddade partiklars acceleration och utbreder sig genom rummet och tiden med ljusets hastighet. Avståndet mellan två vågtoppar kallas signalens våglängd och är en viktig parameter som styr hur vi upplever dessa signaler. Vågor med en kort våglängd på 390–700 nm svarar mot synligt ljus medan vågor med en våglängd på 5–30 mm, som är i fokus i denna avhandling, är osynliga för våra ögon och kallas för mikro- och millimetervågor.

Det är elektromagnetiska vågor som ligger till grund för det trådlösa kommunikationsnätverk som idag sammankopplar i stort sett hela vår planet. Teknikutvecklingen i samhället går framåt med rasande fart och framtiden kommer med största sannolikhet innebära högre ställda krav på kapaciteten hos trådlösa kommunikationssystem. För att möta dessa krav krävs ingående kunskap om underliggande fysik såväl som teknik i form av hårdvara och mjukvara. I denna doktorsavhandling har dessa kunskaper använts för att dra slutsatser vid design och karaktärisering av funktionella strukturer för spridning av elektromagnetiska vågor. Med hjälp av matematik beräknas här hur mikro- och millimetervågor interagerar med sin omgivning. Fysikalisk intuition, matematiska modeller och kommersiella simuleringsprogram utnyttjas för att designa strukturer som kontrollerar hur mikrovågor utbreder sig, där vissa signaler släpps igenom och andra blockeras eller absorberas.

Nedan följer tre exempel på olika tillämpningsområden där funktionella strukturer har designats och karaktäriserats i denna avhandling. Cirkulärpolarisationsselektiva strukturer har designats för tillämpningar i system för satellitkommunikation. Dessa strukturer möjliggör högre kapacitet i kommunikationslänken mellan en satellit och jorden, vilket kan resultera i snabbare internet i våra mobiltelefoner. Nästa tillämpning innefattar undersökningar av olika typer av elektromagnetiska absorbenter för smygteknik inom radarsignaturminimering, där till exempel flygplan och fordon kan anpassas för att inte upptäckas av radarsystem. Nya matematiska modeller och en numerisk approximationsmetod har i denna avhandling utvecklats som ger insikt i hur dessa absorbenter fungerar. Ett tredje användningsområde som undersökts är elektromagnetisk karaktärisering av kompositа strukturer, bestående av en sammansättning av olika material. Denna typ av karaktärisering har använts till icke-förstörande defektdetektering inuti material, samt utvärdering av elektromagnetiska spridningsegenskaper.

Preface

This thesis summarizes the research I have carried out over the past four years at the Department of Electrical and Information Technology, Lund University, Sweden. The thesis starts with a research overview followed by the scientific papers as listed below.

List of included papers

I. A. Ericsson and D. Sjöberg, "A resonant circular polarization selective structure of closely spaced wire helices." *Radio Science*, Vol. 50, No. 8, pp. 804–812, 2015.[1]

Contributions of the author: The author of this thesis is the main contributor to this paper. I co-designed the structure, performed a numerical optimization and a parametric study, and wrote the paper.

II. A. Ericsson and D. Sjöberg, "A Performance Study of Circular Polarization Selective Structures." *9th European Conference on Antennas and Propagation (EuCAP)*, pp. 1–5, IEEE, 2015.

Contributions of the author: The author of this thesis is the main contributor to this paper. I implemented the simulation models, generated the presented data and wrote the paper.

III. A. Ericsson and D. Sjöberg, "Design and Analysis of a Multilayer Meander Line Circular Polarization Selective Structure." *IEEE Transactions on Antennas and Propagation*, Vol. 65, No. 8, pp. 4089–4101. 2017.

Contributions of the author: The author of this thesis is the main contributor to this paper. I optimized the structure in a numerical software, fabricated a prototype, carried out experimental characterizations of the structure, and wrote the paper.

IV. A. Ericsson, J. Lundgren and D. Sjöberg, "Experimental Characterization of Circular Polarization Selective Structures using Linearly Single-Polarized Antennas." *IEEE Transactions on Antennas and Propagation*, Vol. 65, No. 8, pp. 4239–4249. 2017.

Contributions of the author: The author of this thesis is the main contributor to this paper. I designed and fabricated the measurement setup, performed the measurements, wrote post-processing algorithms for the experimental data, and wrote the majority of the paper.

[1] Honored with a student paper award at URSI-GASS XXXI in Beijing, 2014.

V. J. Lundgren, A. Ericsson and D. Sjöberg, "Design and Optimization of Dual Band Circular Polarization Selective Structures." Intended for submission to: *IEEE Transactions on Antennas and Propagation*, 2017. Preprint published as: Technical report LUTEDX/(TEAT-7257), pp. 1–21, 2017, Department of Electrical and Information Technology, Lund University, Sweden.

Contributions of the author: The author of this thesis was the supervisor of the main author. We co-designed a measurement setup, fabricated a prototype and performed the measurements. I wrote parts of the paper.

VI. A. Ericsson, R. Rumpler, D. Sjöberg, P. Göransson, J. Johansson and N. Wellander, "A combined electromagnetic and acoustic analysis of a triaxial carbon fiber weave for reflector antenna applications." *Aerospace Science and Technology*, Vol. 58, pp. 401–417, 2016.

Contributions of the author: The author of this thesis is the main contributor to this paper. I implemented electromagnetic approximation models and full wave simulation models, generated simulation data of the electromagnetic analysis, and wrote all sections of the paper except the acoustic analysis.

VII. A. Ericsson, D. Sjöberg, C. Larsson and T. Martin, "Scattering from a multilayered sphere - Applications to electromagnetic absorbers on double curved surfaces." *Progress In Electromagnetics Research B*, pp. 1–23, 2017, under review. Preprint published as: Technical report LUTEDX/(TEAT-7249), pp. 1–32, 2017, Department of Electrical and Information Technology, Lund University, Sweden.

Contributions of the author: The author of this thesis is the main contributor to this paper. I derived the analytic expressions presented in this work, wrote a numerical implementation of these expressions, generated simulation results and wrote the paper.

VIII. A. Ericsson, D. Sjöberg, C. Larsson and T. Martin, "Approximative computation methods for monostatic scattering from axially symmetric objects." *Progress In Electromagnetics Research B*, pp. 1–24, 2017, under review. Preprint published as: Technical report LUTEDX/(TEAT-7256), pp. 1–36, 2017, Department of Electrical and Information Technology, Lund University, Sweden.

Contributions of the author: The author of this thesis is the main contributor to this paper. I implemented numerical models and a data post processing scheme, generated all simulation results and wrote the paper.

IX. J. Helander, A. Ericsson, M. Gustafsson, T. Martin, D. Sjöberg and C. Larsson, "Compressive Sensing Techniques for mm-Wave Non-Destructive Testing of Composite Panels." *IEEE Transactions on Antennas and Propagation*, Vol. PP, No. 99, pp. 1–9, 2017, accepted for publication.

Contributions of the author: I co-designed the experimental setup, carried out the measurements and wrote parts of the paper. The compressive sensing algorithms in this work were implemented by Jakob Helander.

Other publications by the author

The author of this dissertation is also the author or co-author of the following publications which are related to but not considered part of the dissertation:

X. D. Sjöberg and A. Ericsson, "Computation of monostatic scattering using the physical optics approximation." Technical report LUTEDX/(TEAT-7255), pp. 1–16, 2017, Department of Electrical and Information Technology, Lund University, Sweden.

XI. A. Ericsson, D. Sjöberg, C. Larsson and T. Martin, "Scattering for doubly curved functional surfaces and corresponding planar designs." *10th European Conference on Antennas and Propagation (EuCAP)*, pp. 1–2, Davos, Switzerland, 2016.

XII. J. Helander, A. Ericsson, M. Gustafsson, T. Martin, D. Sjöberg and C. Larsson, "60 GHz imaging of panels for defect detection using planar scanning," *International Symposium on Antennas and Propagation (APS URSI)*, pp. 1025–1026, Fajardo, Puerto Rico, 2016.

XIII. B. Xu, J. Helander, A. Ericsson, Z. Ying, S. He, M. Gustafsson, and D. Sjöberg, "Investigation of planar near-field measurement of millimeter-wave antenna for 5G application." *International Symposium on Antennas and Propagation (ISAP)*, pp. 600–601, Okinawa, Japan, 2016.

XIV. E. Sedhed, A. Ericsson, N. Wellander, D. Sjöberg, "Quasi periodicity in moiré patterns and a numerical approximation method of dual weaves." *International Symposium on Antennas and Propagation and USNC-URSI Radio Science Meeting*, pp. 1620–1621, Vancouver, Canada, 2015.

XV. D. Sjöberg and A. Ericsson, "A multi layer meander line circular polarization selective structure (MLML-CPSS)." *8th European Conference on Antennas and Propagation (EuCAP)*, pp. 464–468, The Hague, Netherlands, 2014.[2]

[2]Honored as runner up for best conference paper award at EuCAP 2014.

XVI. A. Ericsson and D. Sjöberg, "A Resonant Circular Polarization Selective Structure of Closely Spaced Morin Helices." *XXXIth URSI General Assembly and Scientific Symposium (URSI GASS)*, pp. 1–4, Beijing, China, 2014.

XVII. D. Sjöberg, N. Wellander and A. Ericsson, "A homogenization procedure for microstructured resistive sheets." *XXXIth URSI General Assembly and Scientific Symposium (URSI GASS)*, pp. 1–4, Beijing, China, 2014.

Other scientific work by the author

The author of this dissertation is also the author or co-author of the following scientific work presented at conferences which are related to but not considered part of the dissertation:

XVIII. A. Ericsson, D. Sjöberg, C. Larsson and T. Martin, "Approximative Computation Methods for Electromagnetic Scattering Reduction." *IEEE AP-S Symposium on Antennas and Propagation and USNC-URSI Radio Science Meeting*, San Diego, USA, 2017.

XIX. A. Ericsson, J. Lundgren and D. Sjöberg, "A Portable Measurement Setup for Characterizing Circular Polarization Selective Structures." *11th European Conference on Antennas and Propagation (EuCAP)*, Paris, France, 2017.

XX. J. Lundgren, A. Ericsson and D. Sjöberg, "An Optimization Strategy for Dual Band Circular Polarization Selective Structures." *International Conference on Electromagnetics in Advanced Applications (ICEAA)*, Verona, Italy, 2017.

XXI. A. Ericsson, D. Sjöberg, C. Larsson and T. Martin, "Functional Structures Applied to Doubly Curved Surfaces." *International Conference on Electromagnetics in Advanced Applications (ICEAA)*, Cairns, Australia, 2016.

XXII. A. Ericsson, D. Sjöberg, C. Larsson and T. Martin, "Scattering for doubly curved functional surfaces and corresponding planar designs." *GigaHertz/Antenn EMB*, Linköping, Sweden, 2016.

XXIII. A. Ericsson and D. Sjöberg, "Sum Rules and Physical Bounds on Frequency Selective Structures." *Progress In Electromagnetics Research Symposium (PIERS)*, p. 87, Prague, Czech Republic, 2015.

XXIV. A. Ericsson and D. Sjöberg, "Design and Optimization of a Wideband Circular Polarization Selective Structure." *Progress In Electromagnetics Research Symposium (PIERS)*, p. 1231, Guangzhou, China, 2014.

Acknowledgments

First and foremost, I would like to express my deepest gratitude to my main supervisor Prof. Daniel Sjöberg. Your patience, knowledge and passion for science has motivated me to work harder and become a better researcher. Our adventures together during these last four years have taken me around the world and back multiple times and given me invaluable experiences in life.

Secondly, I thank my co-supervisors Prof. Christer Larsson, Dr. Torleif Martin and Prof. Mats Gustafsson. Christer and Torleif, you have given me guidance and an industrial perspective on research that I highly value. Mats, you have shown me what it takes to be successful in research, and that the best results are achieved in collaboration with others.

Many thanks to Prof. Gerhard Kristensson and Prof. Anders Karlsson for the encouragement and for introducing me to the beautiful theory of electrodynamics. I gratefully acknowledge Prof. Buon Kiong Lau for our time together teaching electromagnetics to undergraduate students. I like to believe we really made a difference to some of them. A group of people that have meant a lot to me during my PhD studies are my colleagues. Thank you all for providing me with energy, and for the fact that we have managed to achieve inspiring results while having a great time together.

I am very thankful for the research grants I have been awarded from the Royal Physiographic Society of Lund and Stiftelsen Lars Hierta's minne. Without this financial support, none of the experimental results in this thesis would have been realized. I would like to thank Ron van Hoorn and Oliver Krause at Evonik for providing free samples of Rohacell for the manufacturing of circular polarization selective structures, and Christian Nelson for lending a helping hand in the assembly of a test panel. The travel grants I have been awarded from LM Ericsson Research Foundation and the Royal Physiographic Society of Lund are also acknowledged.

I want to thank my parents Carin and Johan for always believing in me, and providing a safe space for me to return to whenever I need it. To my siblings Anna and Alexander, I am very thankful for our special bond and friendship, and how you always make me laugh. To my second family, thank you Åsa for the support and for teaching me the ways of academia, and thank you Johan for opening my eyes to the beauty of the world we live in.

Last but not least, I would like to thank my wife Malin for her endless love, support and encouragement. Without you this thesis would most likely have consumed me, and my life would be missing many wonderful memories. I am now looking forward to starting a new chapter in life with you.

Lund, October 2017

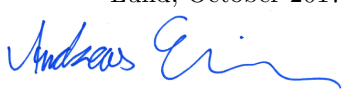

Andreas Ericsson

Acronyms and abbreviations

2D	two-dimensional
3D	three-dimensional
3D-FSS	three-dimensional frequency selective structure
5G	fifth generation mobile networks
BPDN	basis pursuit denoising
AR	axial ratio
CBFM	characteristic basis function method
CEM	computational electromagnetics
CP	circular polarization
CPSS	circular polarization selective structure
CS	compressive sensing
CST MWS	Computer Simulation Technology Microwave Studio
DBF	digital beam forming
DUT	device under test
EBM	electromagnetic bandgap metamaterial
FDTD	finite difference time domain
FEKO	Feldberechnung für Körper mit beliebiger Oberfläche
FEM	finite element method
FIT	finite integration technique
FFT	fast Fourier transform
FSS	frequency selective structure
HP	horizontal polarization
IF	intermediate frequency
IL	insertion loss
LHCP	left hand circular polarization
LHCPSS	left hand circular polarization selective structure
LP	linear polarization

LPSS	linear polarization selective structure
MATLAB®	matrix laboratory
MLFMM	multilevel fast multipole method
mm-wave	millimeter wave
MoM	method of moments
NDT	non-destructive testing
PDE	partial differential equation
PEC	perfect electric conductor
PO	physical optics
PTD	physical theory of diffraction
radar	radio detection and ranging
radome	radar dome
rasorber	radar dome absorber
RAM	radiation-absorbing material
RCS	radar cross section
RHCP	right hand circular polarization
RHCPSS	right hand circular polarization selective structure
RL	return loss
RX	receiver
SATCOM	satellite communications
SNR	signal to noise ratio
T-matrix	transition matrix
TE	transverse electric
TM	transverse magnetic
TX	transmitter
VNA	vector network analyzer
VP	vertical polarization
XPD	cross polarization discrimination

Contents

Part I: Introduction and Research Overview

Andreas Ericsson

1 Background and motivation

Electromagnetic waves are present everywhere in our world and are a prerequisite for life as we know it. These waves provide us with heat from the sun, vision and transport information through our brains. Understanding and controlling electromagnetic waves is a topic with a long history. It has intrigued some of the greatest physicists in history, like Isaac Newton, James Clerk Maxwell and Albert Einstein [44, 115–117, 128]. Today, these waves are the source of the wireless communication network that encompasses the whole world.

A functional structure for electromagnetic waves is an object that interacts with said waves in a purposeful way. An abundance of these structures can be found in nature, such as the structural coloration in the feathers of a peacock, the scales of butterflies and the shell of scarab beetles [86]. A multitude of man made functional structures are utilized in everyday applications, such as the filter of a microwave oven, tinted windows, polarized camera filters, and glasses for three-dimensional (3D) movies.

The long history of our ingenuity in designing functional structures for electromagnetic waves has its roots in the field of optics, dating back to a few centuries B.C.E. From these times, early use of lenses for magnification and focusing of light have been found in Egypt, Babylon and Greece [36]. The succeeding development of geometrical optics, treating visible light as rays, in ancient Greece laid the foundation for scientific studies of reflection and refraction of light [36, 182]. Since then, functional structures have played a key role in optical systems in the form of prisms, beam splitters, polarization filters, quarter wave plates and other optical components. In the 1950s, the invention of the laser started an avalanche of advancements in the field of photonics [17]. To this day, a continuous stream of novel functional structures for photonics applications have been presented, for example metamaterials displaying extraordinary optical properties [159].

In the micro- and millimeter wave regime, which is the main frequency region of interest in this work, rapid development of new concepts and ideas took place in the late 19th century. After the introduction of Maxwell's equations [115–117], the invention of the wireless communication system by Heinrich Hertz [67], the waveguide by Lord Rayleigh [142], and the radio detection and ranging (radar) by Christian Hülsmeyer [71] were all presented during a time period of 20 years. In the wake of the second world war, intense research was carried out in applications of electromagnetic theory, and functional structures were introduced in a number of applications. Some examples are: the radar dome (radome) for shielding of antennas [90] and radiation-absorbing materials (RAMs) [88] for electromagnetic scattering reduction, see Figure 1. One potential building block for designing these structures is the frequency selective surface (FSS), also commonly referred to as frequency selective structure, which was introduced and studied intensively at that time [127]. Other functional structures put forward were a number of waveguide microwave components such as filters and directional couplers [136]. In 1962, the world's first active communications satellite, Telstar 1, was launched

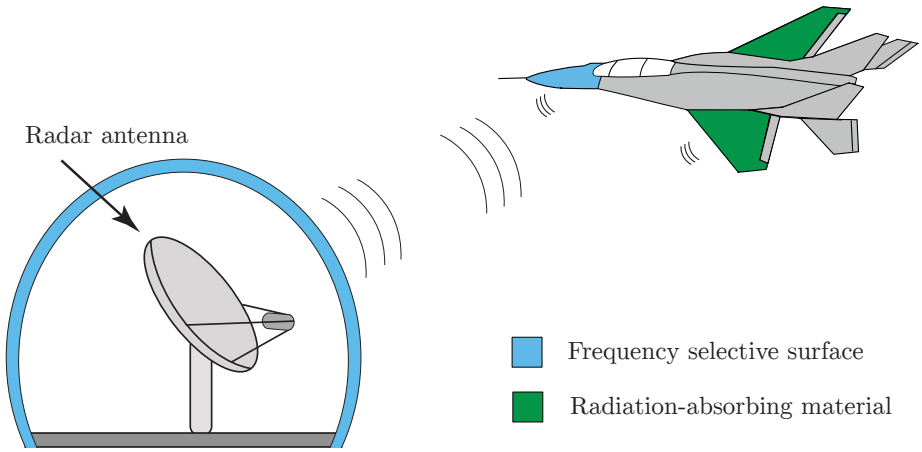

Figure 1: Functional structures for electromagnetic waves in applications related to radar technology. To the left and center, functional structures are used as radomes, and to the right radiation-absorbing materials are used to reduced the radar cross section of an aircraft.

[72]. During the 1960s and 1970s, advances in satellite performance came quickly and a new application area for functional structures was established.

Today, these structures are widely used in all previously mentioned applications. In satellite communication applications polarization diplexers and frequency selective surfaces are used to direct signals and increase the data capacity of communication systems [9]. In electromagnetic scattering reduction applications FSSs and RAMs are used to direct and suppress electromagnetic waves [88]. Furthermore, functional structures are used in antenna design in the form of FSSs, as well as metamaterials and metasurfaces, to acquire desired current distributions and radiation patterns [40].

As technology advances at an ever increasing pace higher requirements are specified for communication systems in general. Moreover, the current development of the fifth generation mobile networks (5G) is a strong driving force in the development of new antenna designs and communication systems [145]. The importance of functional structures in this area is evident, as they constitute useful tools to the antenna and communications system designers. These structures can be used in designing antennas and communication systems at different levels of the communication chain, such as at the base stations, hand-held terminals, or the satellite payload. This is illustrated in Figure 2.

As a result of this constant communication expansion, future satellite communication (SATCOM) systems require even higher data throughput. One way to achieve this is by utilizing multiple spot beam systems and frequency/polarization reuse schemes [9, 94], as in Figure 3. In these systems, a circular polarization selective structure (CPSS) can play a key roles as a diplexer, and a polarizer as a polarization converter.

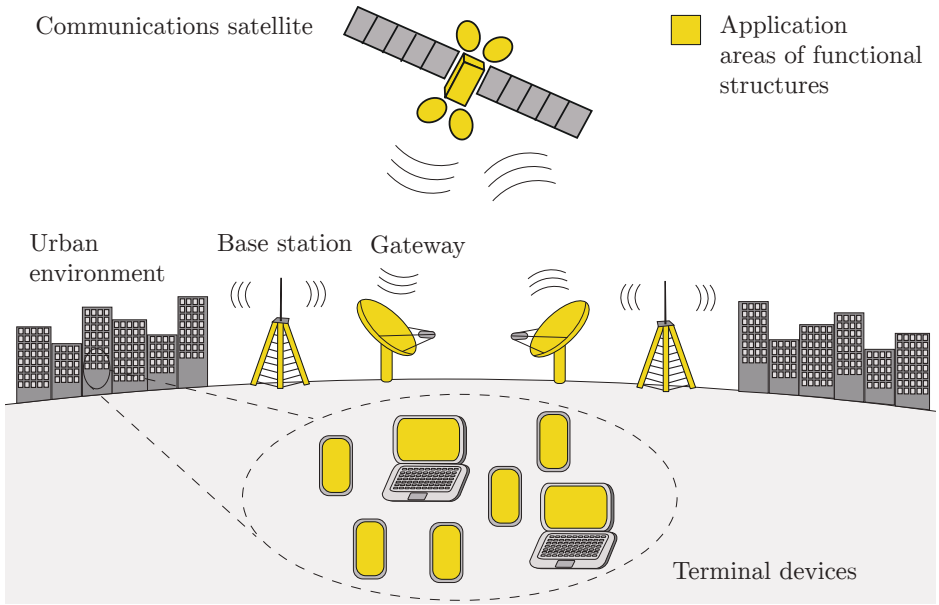

Figure 2: Applications of functional structures in different communication systems. In each transmitting/receiving component in the communication link functional structures can be used to achieve specific radiation properties and increase the data throughput.

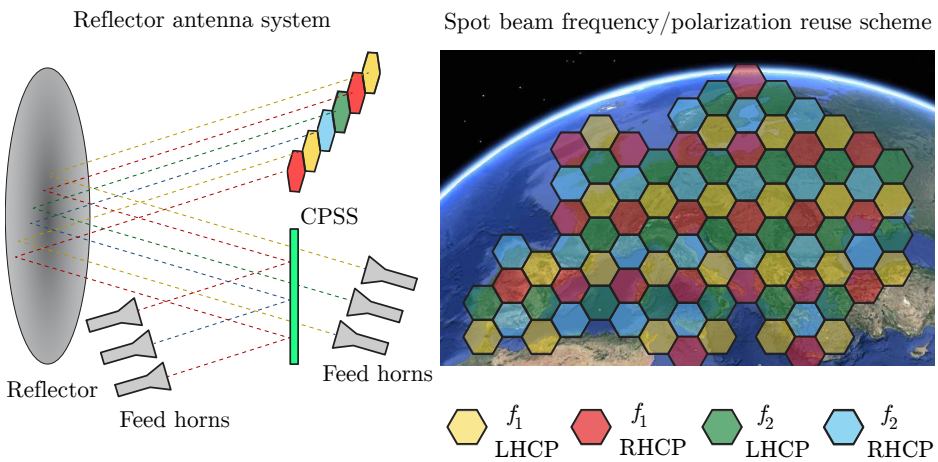

Figure 3: Example of a CPSS implemented as a diplexer in a satellite communication system utilizing a four color frequency and polarization reuse scheme. Here f_1, f_2 correspond to two separate frequency bands and RHCP, LHCP correspond to right/left hand circular polarization, respectively.

In stealth applications, improvements in the sensitivity of radar systems have resulted in a demand for more effective radar cross section (RCS) reduction solutions [144]. These radar system improvements are driven by novel processing techniques such as compressive sensing (CS), machine learning and deep learning, together with improvements in available computational power from better processors and random access memory [12, 189]. By designing and optimizing functional structures using novel approaches, improved filtering and absorption properties can be achieved. This provides a useful addition to the stealth aspects of the detection race between the target and the radar sensing system.

In relation to the high demand of novel functional structures, it should be pointed out that significant amounts of work have already been done in this field during the last century. However, new possibilities in design and synthesis of functional structures for electromagnetic waves are materializing since the computational power available for scientific computations keeps growing. By combining theoretical insights from previous work in the field with new modeling and optimization tools, a wide-open playing field of possibilities unfolds. This marks the starting point of the work presented in this thesis.

2 Electromagnetic theory and scattering concepts

2.1 Fundamental theory and equations

All classical electromagnetic phenomena are governed by Maxwell's equations. When combined with the equation of the Lorentz force and Newton's second law of motion, these equations provide a complete description of the classical dynamics of interacting charged particles and electromagnetic fields [74]. In the time domain, these equations read

$$\nabla \times \boldsymbol{\mathcal{E}}(\boldsymbol{r}, t) = -\frac{\partial \boldsymbol{\mathcal{B}}(\boldsymbol{r}, t)}{\partial t}, \tag{2.1}$$

$$\nabla \times \boldsymbol{\mathcal{H}}(\boldsymbol{r}, t) = \frac{\partial \boldsymbol{\mathcal{D}}(\boldsymbol{r}, t)}{\partial t} + \boldsymbol{\mathcal{J}}(\boldsymbol{r}, t), \tag{2.2}$$

$$\nabla \cdot \boldsymbol{\mathcal{D}}(\boldsymbol{r}, t) = \rho(\boldsymbol{r}, t), \tag{2.3}$$

$$\nabla \cdot \boldsymbol{\mathcal{B}}(\boldsymbol{r}, t) = 0, \tag{2.4}$$

where $\boldsymbol{\mathcal{E}}, \boldsymbol{\mathcal{B}}, \boldsymbol{\mathcal{H}}, \boldsymbol{\mathcal{D}}, \boldsymbol{\mathcal{J}}$ are real valued vector fields and ρ is a real valued scalar

field, defined as

$\boldsymbol{\mathcal{E}}(\boldsymbol{r},t)$	Electric field intensity, [V/m],
$\boldsymbol{\mathcal{B}}(\boldsymbol{r},t)$	Magnetic flux density, [Vs/m^2],
$\boldsymbol{\mathcal{H}}(\boldsymbol{r},t)$	Magnetic field intensity, [A/m],
$\boldsymbol{\mathcal{D}}(\boldsymbol{r},t)$	Electric flux density, [As/m^2],
$\boldsymbol{\mathcal{J}}(\boldsymbol{r},t)$	Current density, [A/m^2],
$\rho(\boldsymbol{r},t)$	Charge density, [C/m^3].

Charge density ρ and current density $\boldsymbol{\mathcal{J}}$ are the sources in Maxwell's equations. It can be seen that (2.1)–(2.4) contain four unknown vector fields, each with three spatial components, resulting in a total of 12 unknowns. But the fact that (2.3)–(2.4) can be derived from (2.1)–(2.2), using the equation of continuity of charge, implies that (2.1)–(2.4) consist of six independent equations. In order to achieve a fully determined system of equations constitutive relations can be utilized [92]. These relations couple the electric and magnetic flux densities to the electric and magnetic fields by an operator $\boldsymbol{\mathcal{F}}(\cdot)$ acting on the fields

$$\{\boldsymbol{\mathcal{D}},\boldsymbol{\mathcal{B}}\} = \boldsymbol{\mathcal{F}}\{\boldsymbol{\mathcal{E}},\boldsymbol{\mathcal{H}}\}. \tag{2.5}$$

The mapping (2.5) has to satisfy certain requirements or physical assumptions to correspond to a realistic model, such as causality [187]. Generally, this relation consists of a temporal convolution relating the coupled fields. By the addition of the constitutive relations, which contain six equations, Maxwell's equations are no longer underdetermined and a single solution can be found.

In many cases the sources of an electromagnetic problem display time harmonic behaviour, for example time harmonic currents feeding an antenna or time harmonic acceleration of charge. Provided that linear media are considered, Maxwell's equations can be simplified by applying a Fourier transform and thus expressing (2.1)–(2.4) in the frequency domain, where the unknown fields are represented by complex valued vectors [181]. Using the time convention $\mathrm{e}^{\mathrm{j}\omega t}$ the (physical) time domain fields are acquired from the frequency domain fields through the relation

$$\boldsymbol{\mathcal{E}}(\boldsymbol{r},t) = \mathrm{Re}\{\boldsymbol{E}(\boldsymbol{r},\omega)\mathrm{e}^{\mathrm{j}\omega t}\}. \tag{2.6}$$

The transition to the frequency domain implies that time derivatives take the form $\frac{\partial}{\partial t} \to \mathrm{j}\omega$, and Maxwell's equations can then be written as

$$\nabla \times \boldsymbol{E}(\boldsymbol{r},\omega) = -\mathrm{j}\omega\boldsymbol{B}(\boldsymbol{r},\omega), \tag{2.7}$$

$$\nabla \times \boldsymbol{H}(\boldsymbol{r},\omega) = \mathrm{j}\omega\boldsymbol{D}(\boldsymbol{r},\omega) + \boldsymbol{J}(\boldsymbol{r},\omega), \tag{2.8}$$

$$\nabla \cdot \boldsymbol{D}(\boldsymbol{r},\omega) = \rho(\boldsymbol{r},\omega), \tag{2.9}$$

$$\nabla \cdot \boldsymbol{B}(\boldsymbol{r},\omega) = 0, \tag{2.10}$$

where $\boldsymbol{E},\boldsymbol{B},\boldsymbol{H},\boldsymbol{D},\boldsymbol{J}$ are the frequency domain fields related to $\boldsymbol{\mathcal{E}},\boldsymbol{\mathcal{B}},\boldsymbol{\mathcal{H}},\boldsymbol{\mathcal{D}},\boldsymbol{\mathcal{J}}$ through (2.6). One significant simplification implied from solving Maxwell's equations, for time harmonic fields, in the frequency domain is that the constitutive

relations take the form of a dyadic multiplication. In anisotropic media, where no coupling between $(\boldsymbol{E}, \boldsymbol{D})$ and $(\boldsymbol{H}, \boldsymbol{B})$ exists, the constitutive relations take the form

$$\boldsymbol{D}(\boldsymbol{r},\omega) = \epsilon_0 \boldsymbol{\epsilon}_{\mathrm{r}}(\omega) \cdot \boldsymbol{E}(\boldsymbol{r},\omega), \qquad \boldsymbol{B}(\boldsymbol{r},\omega) = \mu_0 \boldsymbol{\mu}_{\mathrm{r}}(\omega) \cdot \boldsymbol{H}(\boldsymbol{r},\omega), \tag{2.11}$$

where $\epsilon_0 \approx 8.854 \cdot 10^{-12}\,\mathrm{F/m}$ is the free space permittivity, $\mu_0 = 4\pi \cdot 10^{-7}\,\mathrm{H/m}$ is the free space permeability, $\boldsymbol{\epsilon}_{\mathrm{r}}(\omega)$ is a 3×3 relative permittivity dyadic and $\boldsymbol{\mu}_{\mathrm{r}}(\omega)$ is a 3×3 relative permeability dyadic. In homogeneous, isotropic media the constitutive relations simplify further and the material dyadics are given by $\boldsymbol{\epsilon}_{\mathrm{r}}(\omega) = \epsilon_{\mathrm{r}}(\omega)\mathbf{I}$, $\boldsymbol{\mu}_{\mathrm{r}}(\omega) = \mu_{\mathrm{r}}(\omega)\mathbf{I}$, where $\mathbf{I}$ is the identity dyadic. The constitutive relations in (2.11) then take the form

$$\boldsymbol{D}(\boldsymbol{r},\omega) = \epsilon_0 \epsilon_{\mathrm{r}}(\omega) \boldsymbol{E}(\boldsymbol{r},\omega), \qquad \boldsymbol{B}(\boldsymbol{r},\omega) = \mu_0 \mu_{\mathrm{r}}(\omega) \boldsymbol{H}(\boldsymbol{r},\omega). \tag{2.12}$$

In a source free region, containing a homogeneous isotropic material characterized by the permittivity $\epsilon(\omega) = \epsilon_0 \epsilon_{\mathrm{r}}(\omega)$ and the permeability $\mu(\omega) = \mu_0 \mu_{\mathrm{r}}(\omega)$, (2.7)–(2.10) can be reformulated as the Helmholtz vector wave equation

$$\nabla^2 \boldsymbol{E}(\boldsymbol{r},\omega) + \left(\frac{\omega}{c_0}\right)^2 \boldsymbol{E}(\boldsymbol{r},\omega) = \mathbf{0}, \tag{2.13}$$

$$\nabla^2 \boldsymbol{H}(\boldsymbol{r},\omega) + \left(\frac{\omega}{c_0}\right)^2 \boldsymbol{H}(\boldsymbol{r},\omega) = \mathbf{0}. \tag{2.14}$$

The solution of (2.13)–(2.14) is a propagating wave that travels with the speed of light $c = 1/\sqrt{\epsilon_0 \epsilon_{\mathrm{r}} \mu_0 \mu_{\mathrm{r}}}$. In vacuum this corresponds to $c_0 = 299\,792\,458\,\mathrm{m/s}$. At each point in space the electric and magnetic fields oscillate in directions orthogonal to the direction of propagation. There are two types of very simple solutions of Maxwell's equations in a source-free region: the plane and the spherical waves. The plane wave solution is given by

$$\boldsymbol{E}(\boldsymbol{r},\omega) = \boldsymbol{E}_0(\omega) \mathrm{e}^{-\mathrm{j}k\hat{\boldsymbol{k}}\cdot\boldsymbol{r}}, \qquad \boldsymbol{H}(\boldsymbol{r},\omega) = \eta \hat{\boldsymbol{k}} \times \boldsymbol{E}_0(\omega) \mathrm{e}^{-\mathrm{j}k\hat{\boldsymbol{k}}\cdot\boldsymbol{r}}, \tag{2.15}$$

where $\hat{\boldsymbol{k}}$ is an arbitrary real-valued unit vector, and $\boldsymbol{E}_0(\omega)$ is an arbitrary complex-valued vector, satisfying $\boldsymbol{E}_0(\omega) \cdot \hat{\boldsymbol{k}} = 0$. Here $k = k_0 \sqrt{\epsilon_{\mathrm{r}}(\omega)\mu_{\mathrm{r}}(\omega)}$ is the wave number of the material, $k_0 = \sqrt{\epsilon_0 \mu_0}$ is the vacuum wave number, $\eta = \eta_0 \sqrt{\mu_{\mathrm{r}}(\omega)/\epsilon_{\mathrm{r}}(\omega)}$ is the wave impedance of the material, and $\eta_0 = \sqrt{\mu_0/\epsilon_0} \approx 376.7\,\Omega$ is the vacuum wave impedance. The spherical wave solution is defined in a similar manner

$$\boldsymbol{E}(\boldsymbol{r},\omega) = \boldsymbol{V}(\hat{\boldsymbol{r}},\omega) \frac{\mathrm{e}^{-\mathrm{j}kr}}{r}, \qquad \boldsymbol{H}(\boldsymbol{r},\omega) = \eta \hat{\boldsymbol{k}} \times \boldsymbol{V}(\hat{\boldsymbol{r}},\omega) \frac{\mathrm{e}^{-\mathrm{j}kr}}{r}, \tag{2.16}$$

where $\hat{\boldsymbol{r}}$ is the unit vector in the radial direction and $\boldsymbol{V}(\hat{\boldsymbol{r}},\omega)$ is an arbitrary complex-valued vector, satisfying $\boldsymbol{V}(\hat{\boldsymbol{r}},\omega) \cdot \hat{\boldsymbol{r}} = 0$ [92]. Illustrations of these waves are presented in Figure 4. In Paper VII, a more elaborate solution of Maxwell's equations is utilized to characterize scattering from spherical objects using spherical vector waves [53, 56].

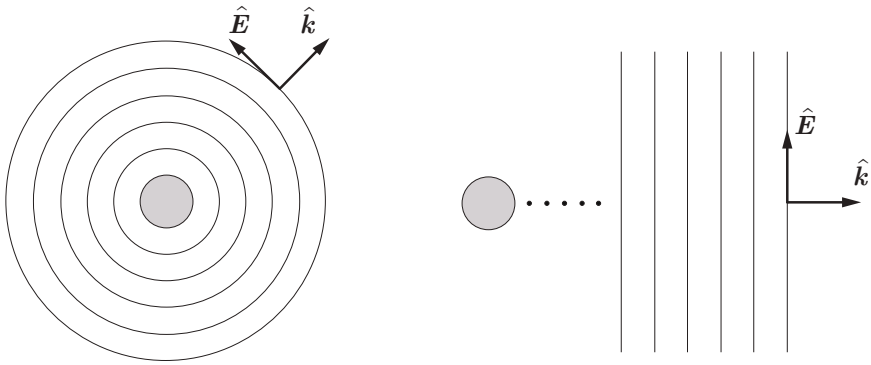

Figure 4: Spherical electromagnetic waves radiating from a point source can be seen in the illustration to the left. Far away from the source radiated waves propagate as plane electromagnetic waves, as depicted to the right.

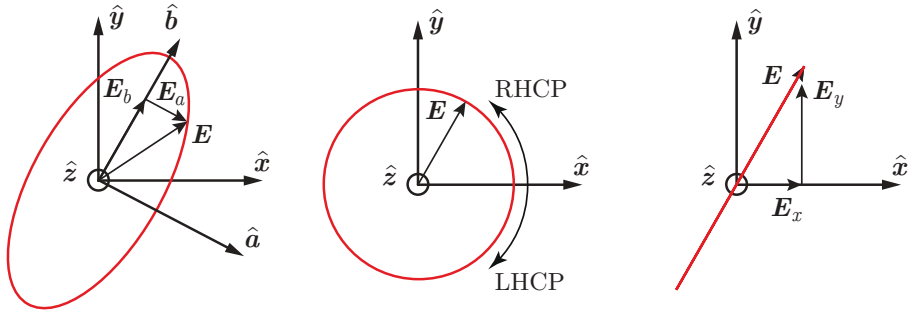

Figure 5: Polarization of a plane wave propagating in the $\hat{\boldsymbol{z}}$-direction. To the left an elliptically polarized wave is illustrated, in the middle a circularly polarized wave is shown and to the right a linearly polarized wave is illustrated.

As an electromagnetic wave propagates in space in the $\hat{\boldsymbol{z}}$-direction the electric field will oscillate in a plane orthogonal to $\hat{\boldsymbol{k}} = \hat{\boldsymbol{z}}$ at a given location z. This oscillation traces a pattern in the plane, referred to as the plane of polarization. The most general polarization state is elliptical, and two specific polarization states commonly identified are linear polarization (LP) and circular polarization (CP), illustrated in Figure 5. Linear polarization can be described as $\boldsymbol{E}_0 = E_x\hat{\boldsymbol{x}} + E_y\hat{\boldsymbol{y}}$, where $E_x\hat{\boldsymbol{x}}$ correspond to horizontal polarization (HP) and $E_y\hat{\boldsymbol{y}}$ to vertical polarization (VP). Circular polarization is described as $\boldsymbol{E}_0 = E_0\hat{\boldsymbol{x}} \pm \mathrm{j}E_0\hat{\boldsymbol{y}}$, where right hand circular polarization (RHCP) is given by $\boldsymbol{E}_0 = E_0(\hat{\boldsymbol{x}} - \mathrm{j}\hat{\boldsymbol{y}})$, and left hand circular polarization (LHCP) is given by $\boldsymbol{E}_0 = E_0(\hat{\boldsymbol{x}} + \mathrm{j}\hat{\boldsymbol{y}})$. In Figure 6 LP and CP waves propagating in the $\hat{\boldsymbol{z}}$-direction are presented as a function of space at a fixed time $t = 0$.

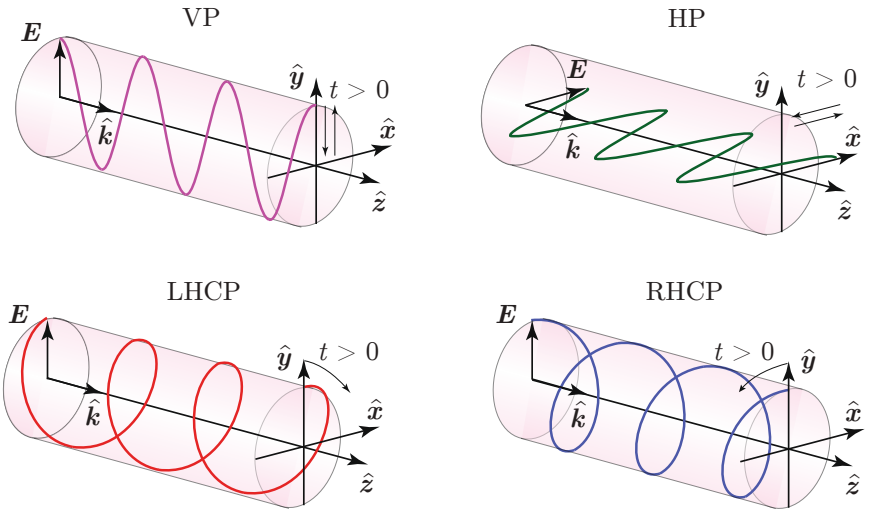

Figure 6: Plane waves propagating in the $\hat{\boldsymbol{z}}$-direction plotted as a function of the distance z at a given time $t = 0$. A VP wave is presented to the upper left, a HP wave is presented to the upper right, an LHCP wave is presented to the lower left and an RHCP wave is presented to the lower right.

2.2 Electromagnetic scattering concepts

Electromagnetic scattering theory is the framework of how electromagnetic fields interact with objects. When defining a scattering problem it is common to separate the total fields $\boldsymbol{E}(\boldsymbol{r})$, $\boldsymbol{H}(\boldsymbol{r})$ into incident fields $\boldsymbol{E}_{\mathrm{i}}(\boldsymbol{r})$, $\boldsymbol{H}_{\mathrm{i}}(\boldsymbol{r})$ and scattered fields $\boldsymbol{E}_{\mathrm{s}}(\boldsymbol{r})$, $\boldsymbol{H}_{\mathrm{s}}(\boldsymbol{r})$ according to

$$\boldsymbol{E}(\boldsymbol{r}) = \boldsymbol{E}_{\mathrm{i}}(\boldsymbol{r}) + \boldsymbol{E}_{\mathrm{s}}(\boldsymbol{r}), \qquad \boldsymbol{H}(\boldsymbol{r}) = \boldsymbol{H}_{\mathrm{i}}(\boldsymbol{r}) + \boldsymbol{H}_{\mathrm{s}}(\boldsymbol{r}). \tag{2.17}$$

If the incident fields are known and the scattered fields are unknown the problem of calculating the unknown fields is referred to as a direct scattering problem [92]. Conversely, if the scattered fields are known but the sources of the scattered fields are unknown, the problem is referred to as an inverse scattering problem [33].

Far away from the scattering source, in the far field region, the scattered fields constitute of transverse field components and no radial part. The definition of this region is given in [92] and here the far field amplitude of the scattered electric field is defined as

$$\boldsymbol{F}(\hat{\boldsymbol{r}}) = \lim_{r\to\infty} r\mathrm{e}^{\mathrm{j}kr}\boldsymbol{E}_{\mathrm{s}}(\boldsymbol{r}). \tag{2.18}$$

Similarly, the scattered electric field can be determined from the far field amplitude $\boldsymbol{F}(\hat{\boldsymbol{r}})$ by the relation

$$\boldsymbol{E}_{\mathrm{s}}(\boldsymbol{r}) = \frac{\mathrm{e}^{-\mathrm{j}kr}}{r}\boldsymbol{F}(\hat{\boldsymbol{r}}). \tag{2.19}$$

We define the incident field as a plane wave $\boldsymbol{E}_\mathrm{i}(\boldsymbol{r}) = \boldsymbol{E}_0 \mathrm{e}^{\mathrm{j}k\hat{\boldsymbol{k}}_\mathrm{i}\cdot\boldsymbol{r}}$, propagating in the $\hat{\boldsymbol{k}}_\mathrm{i}$-direction with the observation direction $\boldsymbol{r}$ fixed and non-parallel to the direction of propagation. A mapping from the incident field $\boldsymbol{E}_0(\boldsymbol{r})$ to the scattered far field amplitude $\boldsymbol{F}(\hat{\boldsymbol{r}})$ is given by

$$\boldsymbol{F}(\hat{\boldsymbol{r}}) = \mathbf{S}(\hat{\boldsymbol{r}}, \hat{\boldsymbol{k}}_\mathrm{i})\boldsymbol{E}_0(\boldsymbol{r}), \tag{2.20}$$

where $\mathbf{S}(\hat{\boldsymbol{r}}, \hat{\boldsymbol{k}}_\mathrm{i})$ is the scattering dyadic. Another useful scattering property is the differential scattering cross section $\partial\sigma/\partial\Omega(\hat{\boldsymbol{r}}, \hat{\boldsymbol{k}}_\mathrm{i})$, which can be expressed in the scattering dyadic as

$$\frac{\partial\sigma}{\partial\Omega}(\hat{\boldsymbol{r}}, \hat{\boldsymbol{k}}_\mathrm{i}) = 4\pi\frac{|\boldsymbol{F}(\hat{\boldsymbol{r}})|^2}{|\boldsymbol{E}_0|^2} = 4\pi|\mathbf{S}(\hat{\boldsymbol{r}}, \hat{\boldsymbol{k}}_\mathrm{i})\cdot\hat{\boldsymbol{p}}_\mathrm{i}|^2, \tag{2.21}$$

where the unit vector $\hat{\boldsymbol{p}}_\mathrm{i}$ is defined as

$$\hat{\boldsymbol{p}}_\mathrm{i} = \frac{\boldsymbol{E}_0}{|\boldsymbol{E}_0|}. \tag{2.22}$$

In this work, the scattering cross section in the backscattering direction, referred to as the monostatic radar cross section (or RCS), is of main interest. It takes the form

$$\sigma_\mathrm{RCS} = \frac{\partial\sigma}{\partial\Omega}(-\hat{\boldsymbol{k}}_\mathrm{i}, \hat{\boldsymbol{k}}_\mathrm{i}) = 4\pi\frac{|\boldsymbol{F}(-\hat{\boldsymbol{k}}_\mathrm{i})|^2}{|\boldsymbol{E}_0|^2} = 4\pi|\mathbf{S}(-\hat{\boldsymbol{k}}_\mathrm{i}, \hat{\boldsymbol{k}}_\mathrm{i})\cdot\hat{\boldsymbol{p}}_\mathrm{i}|^2. \tag{2.23}$$

2.3 Network theory and the scattering matrix

When solving Maxwell's equations the electric and magnetic fields are given at all points in space. This commonly results in large quantities of information and gives a complete description of the scattering scenario under study. However, in many cases we are only interested in the voltage or current at a set of terminals, the power flow through a structure, or some other type of terminal quantity. In these cases, the concept of network theory is a useful tool for simplifying a scattering problem and to place focus only on relevant quantities of interest [136]. This topic has its roots in low frequency applications where circuit theory is applicable. Here, the voltage and current are identified with respect to a terminal pair, and objects are modeled as lumped impedance elements displaying reactive and resistive properties. In a microwave system, the concept of voltages and currents can be applied individually for each propagating mode in a guided wave system, such as a waveguide, or a free space propagation system [113].

The scattering dyadic introduced in (2.20), relating the incident electric field $\boldsymbol{E}_0(\boldsymbol{r})$ to the far field $\boldsymbol{F}(\hat{\boldsymbol{r}})$, is a useful tool for analytic investigations of scattering problems concerning scatterers of arbitrary shape enclosed by free space or some other homogeneous, isotropic medium. A representation that is more in accord with direct measurements, and with the ideas of incident, reflected and

transmitted waves, is given by the scattering matrix [136]. The scattering matrix relates the voltage waves incident on the ports to those reflected from the ports. For some components and circuits, the scattering parameters can be calculated using network analysis techniques. Otherwise, the scattering parameters can be measured directly with a vector network analyzer (VNA), described further in Section 6. The scattering matrix of an N-port network is

$$\begin{pmatrix} V_1^- \\ V_2^- \\ \vdots \\ V_N^- \end{pmatrix} = \begin{pmatrix} S_{11} & S_{12} & \cdots & S_{1N} \\ S_{21} & \ddots & & \vdots \\ \vdots & & \ddots & \vdots \\ S_{N1} & \cdots & \cdots & S_{NN} \end{pmatrix} \begin{pmatrix} V_1^+ \\ V_2^+ \\ \vdots \\ V_N^+ \end{pmatrix}, \tag{2.24}$$

where V_i^-, $i = 1, 2, ..., N$ is the amplitude of the scattered wave voltage at port i and V_j^+ is the amplitude of the incident wave voltage at port j. The scattering matrix elements are defined as

$$S_{ij} = \left. \frac{V_i^-}{V_j^+} \right|_{V_k^+ = 0 \text{ for } k \neq j}. \tag{2.25}$$

This means that S_{ij} is given by the ratio between the scattered wave voltage V_i^- at port i and the incident wave voltage V_j^+ at port j, when all other ports are terminated with matched loads [136].

3 Analytic and numerical modeling of scattering problems

The complexity associated with solving Maxwell's equations for scattering from an object implies that analytic closed form solutions can only be obtained in a number of canonical scenarios [180]. Two approaches that are heavily utilized to solve complex electromagnetic problems that can not be treated analytically are:

- discretize the problem and use full wave simulations,
- utilize approximations to simplify the formulation of the problem.

These two methods are described in this section, alongside an approach to solve certain scattering problems analytically.

3.1 Analytic solutions to scattering problems

3.1.1 Scattering from layered planar structures

One of the most simple wave propagation problems is scattering from a planar stratified structure with layers of homogeneous, isotropic materials. The following material is classical and can to a large extent be found in [131]. However, the

combination of multilayer structures with thin admittance layers is used extensively in Papers VII–VIII included in the thesis, which motivates the inclusion of a more detailed description here. This type of problem is solved by matching the tangential electric and magnetic fields on both sides of each interface of the structure. By iterating through all interfaces of the structure the total reflection coefficient Γ and transmission coefficient $\mathcal{T}$ can be determined.

Consider an incident linearly polarized plane wave propagating along the $\hat{\boldsymbol{z}}$-direction in a homogeneous, isotropic medium. The electric and magnetic fields of the wave are given by $\boldsymbol{E}(z) = \hat{\boldsymbol{x}}E(z)$, $\boldsymbol{H}(z) = \hat{\boldsymbol{y}}H(z)$. The wave impinges at normal incidence to the boundary of a second medium, as in Figure 7. The tangential fields at each side of the interface can be represented as forward and backwards traveling waves as

$$\begin{aligned} E &= E_+ \mathrm{e}^{-\mathrm{j}kz} + E_- \mathrm{e}^{\mathrm{j}kz}, & E' &= E'_+ \mathrm{e}^{-\mathrm{j}kz} + E'_- \mathrm{e}^{\mathrm{j}kz}, \\ H &= \frac{1}{\eta} E_+ \mathrm{e}^{-\mathrm{j}kz} - \frac{1}{\eta} E_- \mathrm{e}^{\mathrm{j}kz}, & H' &= \frac{1}{\eta} E'_+ \mathrm{e}^{-\mathrm{j}kz} - \frac{1}{\eta} E'_- \mathrm{e}^{\mathrm{j}kz}. \end{aligned} \tag{3.1}$$

If an admittance sheet is located at the interface, this implies the boundary conditions

$$\hat{\boldsymbol{n}} \times (\boldsymbol{E}' - \boldsymbol{E}) = \boldsymbol{0}, \qquad \hat{\boldsymbol{n}} \times (\boldsymbol{H}' - \boldsymbol{H}) = \boldsymbol{J}_\mathrm{S} = Y_\mathrm{S} \hat{\boldsymbol{n}} \times (\boldsymbol{E}' \times \hat{\boldsymbol{n}}), \tag{3.2}$$

where $\boldsymbol{J}_\mathrm{S} = Y_\mathrm{S} \hat{\boldsymbol{n}} \times (\boldsymbol{E}' \times \hat{\boldsymbol{n}})$ is the surface current density at the interface, which can also be represented as the product of a surface admittance and the tangential electric field. These relations can be written in matrix form

$$\begin{pmatrix} E \\ H \end{pmatrix} = \begin{pmatrix} E' \\ H' + Y_\mathrm{S} E' \end{pmatrix} = \begin{pmatrix} 1 & 0 \\ Y_\mathrm{S} & 1 \end{pmatrix} \begin{pmatrix} E' \\ H' \end{pmatrix}, \tag{3.3}$$

which can be expressed in the forward and backward propagating fields as

$$\begin{pmatrix} E_+ \\ E_- \end{pmatrix} = \left(\frac{1}{\tau} \begin{pmatrix} 1 & \rho \\ \rho & 1 \end{pmatrix} + \frac{Y_\mathrm{S} \eta_1}{2} \begin{pmatrix} 1 & 1 \\ -1 & -1 \end{pmatrix} \right) \begin{pmatrix} E'_+ \\ E'_- \end{pmatrix}. \tag{3.4}$$

The first matrix of the final expression in (3.4) is recognized as the ordinary matching matrix at an interface in [131], where the reflection coefficient ρ and the transmission coefficient τ at an interface, illuminated from the left, are identified as

$$\rho = \frac{\eta' - \eta}{\eta' + \eta}, \qquad \tau = \frac{2\eta'}{\eta' + \eta}, \tag{3.5}$$

and where the wave impedance in the two regions are $\eta = \eta_0 \sqrt{\mu_\mathrm{r}/\epsilon_\mathrm{r}}$, $\eta' = \eta_0 \sqrt{\mu'_\mathrm{r}/\epsilon'_\mathrm{r}}$. If the interface is illuminated from the other side, the reflection coefficient ρ' and the transmission coefficient τ' are defined in the same way. In conclusion, an admittance layer at a planar interface between two media is treated by adding the second matrix in (3.4). Propagation of the fields through a slab

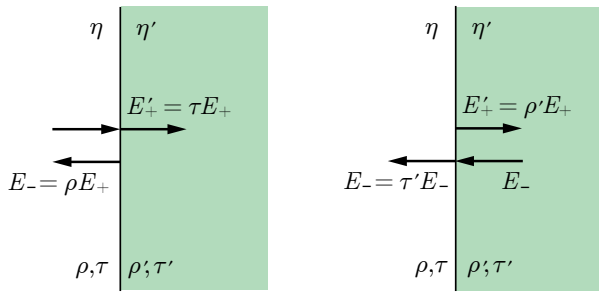

Figure 7: The forward and backward traveling electric fields at an interface.

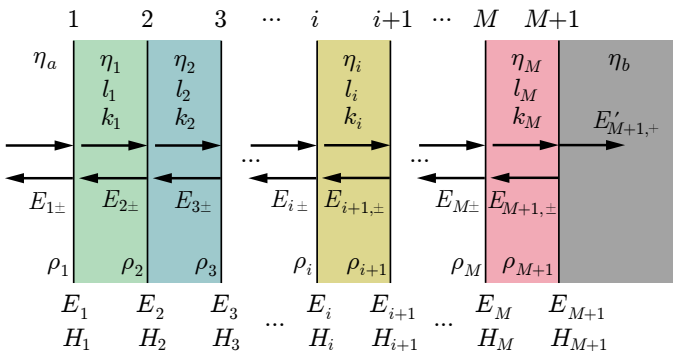

Figure 8: The forward and backward travelling electric fields inside a multilayer structure.

up to the next interface is modeled by the matrix relation

$$\begin{pmatrix} E'_{1+} \\ E'_{1-} \end{pmatrix} = \begin{pmatrix} \mathrm{e}^{\mathrm{j}k_1 l_1} & 0 \\ 0 & \mathrm{e}^{-\mathrm{j}k_1 l_1} \end{pmatrix} \begin{pmatrix} E_{2+} \\ E_{2-} \end{pmatrix}, \tag{3.6}$$

where $k_i = 2\pi/\lambda_i$ is the wave number in the material, and l_i is the physical thickness of the slab. If a layered structure is backed by a perfect electric conductor (PEC) the impedance of that region is $\eta_{\mathrm{PEC}} = 0$, resulting in that the reflection coefficient at the interface is $\rho = -1$ and the transmission is $\tau = 0$.

Now we are ready to treat the case of any given number of slabs cascaded after each other, as in Figure 8. The field matching condition for a setup consisting of M layers, is given by

$$\boldsymbol{E}_{1,\pm} = \mathbf{M}_1\mathbf{P}_1\mathbf{M}_2\mathbf{P}_2 \cdots \mathbf{P}_{M-1}\mathbf{M}_M\mathbf{P}_M\mathbf{M}_{M+1}\boldsymbol{E}'_{M+1,\pm} = \mathbf{A}\boldsymbol{E}'_{M+1,\pm} \tag{3.7}$$

where $\mathbf{M}_i$ are matching matrices at each interface i on the form (3.4) and $\mathbf{P}_i$ are propagation matrices on the form (3.6). The total transmission coefficient and reflection coefficient of the stratified structure are

$$\Gamma_1 = A_{21}/A_{11}, \qquad \mathcal{T} = 1/A_{11}, \tag{3.8}$$

where A_{11}, A_{12}, A_{21} and A_{22} are the matrix elements of the 2×2 matrix $\mathbf{A}$ in (3.7).

The framework just described can be extended to treat oblique incidence. The main difference in comparison to the case of normal incidence is that the fields have to be divided into TM and TE components, parallel and orthogonal to the scattering plane of each interface, defined in Figure 9. When a wave impinges on each interface i in Figure 8 at an oblique angle θ_{i-1} the transmitted wave is refracted according to Snell's law [131], which can be rearranged to determine the refraction angle θ_i as

$$\theta_i = \sin^{-1}\left(\frac{n_{i-1}\sin\theta_{i-1}}{n_i}\right). \tag{3.9}$$

The refractive index in region i is given by $n_i = \sqrt{\epsilon_{\mathrm{r},i}\mu_{\mathrm{r},i}}$, and the refraction angle θ_i is determined in each region $i = 1, 2, ..., M+1$ given an initial incidence angle θ_0. The wave impedances and the propagation factors in (3.1)–(3.6) are modified with consideration to the TM and TE components according to

$$\eta_i \rightarrow \begin{cases} \eta_{\mathrm{TM},i} = \eta_i \dfrac{k_{z,i}}{k_i} \\ \eta_{\mathrm{TE},i} = \eta_i \dfrac{k_i}{k_{z,i}}, \end{cases} \qquad \mathrm{e}^{\pm \mathrm{j} k_i z} \rightarrow \mathrm{e}^{\pm \mathrm{j} k_{z,i} z} = \mathrm{e}^{\pm \mathrm{j} k_i z \cos\theta_i}, \tag{3.10}$$

where the z-component of the wave vector $\boldsymbol{k}_i$ is given by $k_{z,i} = \sqrt{k_i^2 - k_{t,i}^2}$, and the transverse component of the wave vector is given by $k_{t,i} = k_i \sin\theta_i$. A numerical implementation of this oblique scattering scheme is utilized in Paper VIII for extracting the reflection coefficient of different RAMs at a number of oblique angles of incidence. This data is imported as a reflection dyadic into a physical optics (PO) solver for RCS simulations of axially symmetric scatterers [52, 165].

3.1.2 Scattering from layered non-planar structures

For electromagnetic scattering from more general layered, non-planar objects it is uncertain if an analytic solution can be found. If an analytic formulation of a scattering problem can be formulated (or not) depends strongly on the geometry of the scatterer. If the geometry can be described in a set of coordinates where separation of variables of the partial differential equation (PDE) is possible, this type of solution can be found [149]. Some geometries where analytic solutions can be found are spheres, cylinders and ellipsoids [22, 149, 171].

The approach used in this type of scattering problems is based on expanding the known incident field and the unknown scattered field in a set of orthogonal vector waves suitable to the specific geometry. These vector waves are typically constructed from special functions. The tangential fields are then matched at each interface in the same way as in the previous section for planar stratified structures. The incident field is described by the known expansion coefficients a_n, and the expansion coefficients describing the scattered fields f_n are unknown.

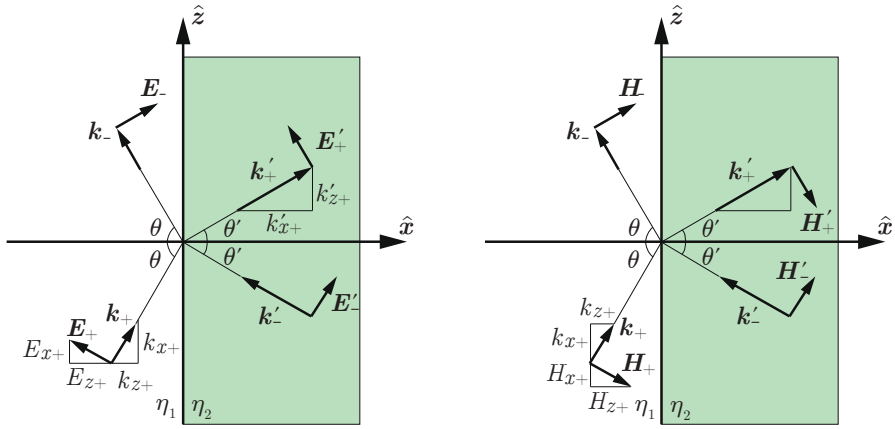

TM, parallel polarization TE, perpendicular polarization

Figure 9: TM and TE waves in the scattering plane of an interface between two media.

Provided that the scatterer consists of linear materials, there is a linear relation between the two sets of expansion coefficients

$$f_n = \sum_{n'} T_{nn'} a_{n'}, \tag{3.11}$$

where the infinite dimensional matrix $T_{nn'}$ is called the transition matrix (or the T-matrix) of the scatterer. In Paper VII in this work, the problem of scattering from a PEC sphere coated by different kinds of RAMs is solved using this kind of analytic expressions.

3.2 Full wave simulation methods

Full wave simulations of an electromagnetic problem consist of modeling the interaction of electromagnetic fields with physical objects and the environment. In order to determine the fields in this interaction, computationally efficient approximations to Maxwell's equations are used to discretize the analytic problem into a finite number of points where the fields or currents are evaluated [37]. Different numerical approximations and types of discretization (also referred to as meshing) are utilized depending on which type of computational method that is used. In each mesh element, the fields or currents are evaluated using a simple functional dependence of the spatial variation. For instance, a linear or higher order approximation is commonly utilized.

One of the predominant methods in computational electromagnetics (CEM) is the method of moments (MoM). It is heavily used in open-region electromagnetic problems such as wave scattering and antenna radiation [32, 75]. In this method, radiating and scattering structures are replaced by surface currents and

the surfaces of objects are divided into wire segments and surface patches. The unknown scattered fields are computed using the Green's function and Sommerfeld's radiation condition. The method is very effective for simulating PEC or homogeneous penetrable objects. The fact that only the surfaces of objects are meshed imply reduced simulation requirements in many problems when compared to alternative methods.

An alternative approach is given by the finite difference method (FDM), which is a numerical method for converting PDEs of a boundary-value problem into a set of algebraic equations that can be used to compute an approximate solution to the problem [75]. This method was used to develop the finite difference time domain method (FDTD), which is heavily used in CEM problems of penetrable scatterers, inhomogeneous media and wideband simulations. The formulation of this method uses cuboidal mesh elements, which implies that a fine mesh has to be used in order to accurately model the geometry of curved scatters. In FDTD a volume enclosing the scattering objects and its surroundings needs to be meshed.

A third CEM method, based on approximating the solution of a partial differential equation instead of the differential operators, is given by the finite element method (FEM). The unknown fields are discretized using a finite element mesh, and the mesh elements typically consist of triangular elements for surfaces and tetrahedrons for volume meshes, although other types of elements such as cuboids are available [37]. This method is very well suited for simulating bounded electromagnetic problems such as waveguides and cavities, but also plane wave propagation through inhomogeneous media such as scattering from functional structures.

Different numerical methods have been used in the papers presented in the thesis depending on the applications. The choice of which software and solver to use in each project was made with respect to the properties of the solvers, as well as the functionality and flexibility of each software. In Papers I–V CPSS were simulated using the frequency domain finite integration technique (FIT) solver in Computer Simulation Technology Microwave Studio (CST MWS) [48–50, 55]. This metod is similar to the FEM in terms of meshing and the numerical formulation [38, 183]. In Paper VI a triaxial carbon fiber weave was simulated using the 2D low frequency and 3D full wave FEM solvers in Comsol Multiphysics [54]. The 2D axially symmetric FEM solver in Comsol Multiphysics was utilized in Paper VIII for simulating RCS of different objects [51]. Finally, in Papers VII and IX the MoM solver in Feldberechnung für Körper mit beliebiger Oberfläche (FEKO) was used for benchmarking experimental results and in-house simulation results of the scattering from small scatterers [53, 66].

3.2.1 Simulations of scattering from planar structures

When simulating the scattering of planar functional structures consisting of periodic elements, illuminated by a plane wave, commercial numerical software commonly utilize Floquet's theorem to model the geometry with a unit cell enclosed by periodic boundary conditions in the plane of the structure, see Figure 10.

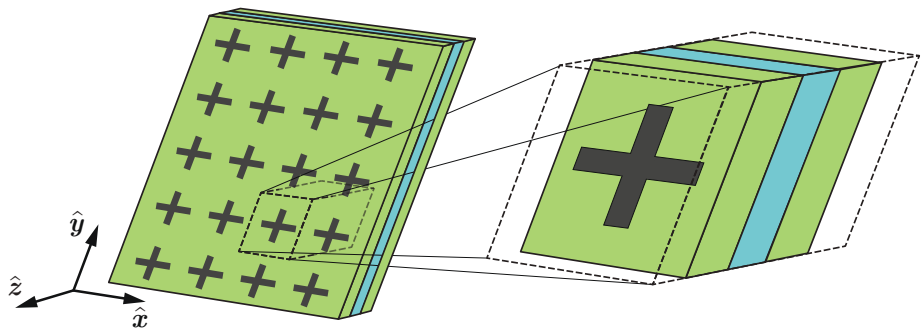

Figure 10: Functional structure consisting of periodic layers (left) modeled numerically by a unit cell (right).

The theorem states that the solution of a partial differential equation with periodic coefficients will have a periodic solution with the same periodicity as the coefficients [58]. In our case this implies that the induced currents on each element, given by a row index q and a column index m, of a periodic lattice can be represented as

$$I_{qm} = I_{00}\mathrm{e}^{-\mathrm{j}\beta q D_x s_x}\mathrm{e}^{-\mathrm{j}\beta m D_y s_y}, \tag{3.12}$$

where I_{00} is the current on the center element, β is the wave number of the incident wave, D_x and D_y is the inter-element spacing in the $\hat{\boldsymbol{x}}$ and $\hat{\boldsymbol{y}}$-directions of the lattice, and s_x, s_y are components of the excitation incidence direction $\hat{\boldsymbol{s}} = s_x\hat{\boldsymbol{x}}+s_y\hat{\boldsymbol{y}}+s_z\hat{\boldsymbol{z}}$. This type of formulation implies that the simulated structure will have infinite extent in the xy-plane and is illuminated by a plane wave. In most cases this approximation accurately models the scattering from a structure of finite size illuminated by an antenna, even though the illuminating signal may not be a plane wave. This is shown in Section 6, where a single layer FSS is experimentally characterized and the results are compared to simulations.

The structure is excited by Floquet ports on each side of the device under test (DUT) generating an incident plane wave with a desired polarization state and incidence direction, typically user defined by the polar angle θ and the azimuth angle ϕ. When analyzing the reflection and transmission properties of such a system it is common to represent the scattering problem as a four port network, introduced in Section 2.3. Each port corresponds to one out of two polarization states, preferably orthogonal to each other. For example, a scattering scenario using horizontal and vertical linearly polarized excitations can be modeled using

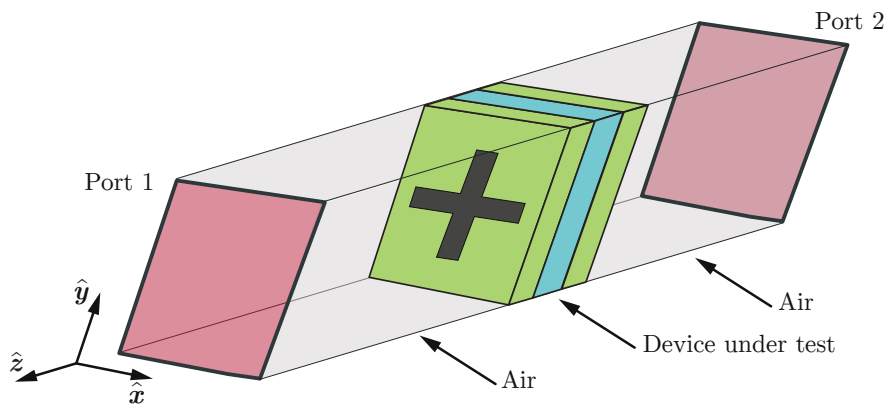

Figure 11: Typical simulation setup of a planar functional structure.

a scattering matrix of the form

$$\begin{pmatrix} V_1^{\mathrm{X}-} \\ V_1^{\mathrm{Y}-} \\ V_2^{\mathrm{X}-} \\ V_2^{\mathrm{Y}-} \end{pmatrix} = \begin{pmatrix} S_{11}^{\mathrm{XX}} & S_{11}^{\mathrm{XY}} & S_{12}^{\mathrm{XX}} & S_{12}^{\mathrm{XY}} \\ S_{11}^{\mathrm{YX}} & S_{11}^{\mathrm{YY}} & S_{12}^{\mathrm{YX}} & S_{12}^{\mathrm{YY}} \\ S_{21}^{\mathrm{XX}} & S_{21}^{\mathrm{XY}} & S_{22}^{\mathrm{XX}} & S_{22}^{\mathrm{XY}} \\ S_{21}^{\mathrm{YX}} & S_{21}^{\mathrm{YY}} & S_{22}^{\mathrm{YX}} & S_{22}^{\mathrm{YY}} \end{pmatrix} \begin{pmatrix} V_1^{\mathrm{X}+} \\ V_1^{\mathrm{Y}+} \\ V_2^{\mathrm{X}+} \\ V_2^{\mathrm{Y}+} \end{pmatrix} \tag{3.13}$$

where port 1 and 2 are located on each side of the scatterer and are excited by X or Y polarized waves, defined in Figure 11. The superscript + indicates waves entering the port, and − indicates waves leaving the port. Different notation is used in the literature depending on if the ports on one side of the DUT are referred to as one single port containing two separate polarization states (as in Figure 11) or if these ports are labeled with individual port numbers (as in Paper VI in this work).

3.2.2 Simulations of scattering from non-planar structures

When simulating scattering from non-planar functional structures a unit cell can not be defined in the same way as in the planar case and a different approach is taken. For periodic non-planar structures, the whole geometry of the scatterer is often implemented in a numerical solver and brute force simulations are carried out, typically by a cluster of workstations. If the geometry under study contains symmetries, this can be utilized to significantly reduce the computational complexity of the problem. However, the fact that the geometry itself contains symmetries does not directly imply that the electromagnetic scattering problem will have the same symmetry. Since this type of scattering problems are vector valued the symmetry must hold with respect to both the geometry and the excitation. In Paper VIII RAMs are applied to axially symmetric scatterers to reduce the monostatic RCS, and the symmetry of the problems is utilized as simulations

are carried out using axially symmetric simulation models. An alternative way to reduce the complexity and computation time of a problem is to use approximation methods suitable for the specific scenario. The approximation methods used in this thesis are presented in Section 3.3.

3.3 Approximation methods

Full wave simulations can yield high accuracy if carried out correctly, but a disadvantage with these methods is that the scaling of required random access memory and simulation time with respect to frequency becomes problematic for electrically large structures [37]. In [19] it is shown that, in a simulation at the wave frequency f of a 3D system of fixed spatial extent, the number of floating point operations and the memory requirements scales as $\mathcal{O}(f^4)$ in all of the methods mentioned in Section 3.2 (MoM, FEM and FDTD). If a two-dimensional (2D) simulation system is considered, the MoM scales as $\mathcal{O}(f^2)$ and the FEM and FDTD scales as $\mathcal{O}(f^3)$ [19, p. 224].

Also, if an electrically small structure is to be optimized through hundreds or thousands of design iterations, it is of significant interest to reduce the required simulation time for each iteration as much as possible. An alternative simulation approach which can achieve this goal is to use approximations to simplify the problem. Different approximations are of interest depending on if the low- or high-frequency response of a scatterer is required, and the specific problem dictates if an approximation can be accurately utilized or not.

3.3.1 Circuit models

Network theory can be used to simulate plane wave scattering from planar structures by describing the system as a transmission line, where each layer and interface of the structure is modeled using equivalent circuit parameters [136]. This approximation is valid if the transverse structure of each layer is small with respect to the wavelength, which is equivalent to referring to the method as a low frequency approximation. Although, this method is also often utilized in FSS design where larger resonant elements on the order of a wavelength in size are used. The details of this method lies in relating physical geometries to effective circuit parameters through full wave simulations or variational expressions. In [113] the equivalent circuit parameters have been derived for a number of conducting obstacles. Circuit models result in fast optimizations, where thousands of evaluations are carried out in a number of seconds. The described approximation method was used in Paper III in this work to optimize a wideband CPSS [50,166].

3.3.2 Homogenization

A different low frequency approximation method can be derived from homogenization theory, which studies the effect of rapid oscillations in the coefficients PDEs [119]. In [57] it is shown that by introducing separate microscopic and

a macroscopic length scales, and letting the microscopic length scale tend to zero, the microscopic oscillations will average out resulting in a simpler macroscopic PDE that is solved. In electromagnetic problems, homogenization can be utilized to calculate effective material parameters of objects with microscopic structure [91, 162, 163].

This method is utilized in Paper VI, where the effective conductivity dyadic of a triaxial weave is studied. By implementing a low frequency simulation model of the periodic geometry under study the transverse and longitudinal conductivity homogenization parameters ($\sigma_{\text{eff},xy}$ and $\sigma_{\text{eff},z}$) are determined from the expression

$$\langle \boldsymbol{J}(\boldsymbol{r}) \rangle = \frac{1}{A} \iint\limits_{\Omega} \left[\sigma(\boldsymbol{r}) (\boldsymbol{E}_0 - \nabla V(\boldsymbol{r})) \right] \, \mathrm{d}x \, \mathrm{d}y = \boldsymbol{\sigma}_{\text{eff}} \cdot \langle \boldsymbol{E}(\boldsymbol{r}) \rangle \,, \tag{3.14}$$

where $\boldsymbol{E}_0$ is a static applied electric field, $-\nabla V(\boldsymbol{r})$ is the induced field in the structure, A is the area of the 2D unit cell, Ω is denoting the conductive part of the unit cell, and the effective conductivity tensor can be written as

$$\boldsymbol{\sigma}_{\text{eff}} = \begin{pmatrix} \sigma_{\text{eff},xy} & 0 & 0 \\ 0 & \sigma_{\text{eff},xy} & 0 \\ 0 & 0 & \sigma_{\text{eff},z} \end{pmatrix}. \tag{3.15}$$

The advantage of this method is that the effective material parameters determined from the microscopic homogenization formulation can be used as input parameters for macroscopic simulations, thus potentially reducing the complexity of the problem [54]. A number of problems where homogenization techniques are of interest are described in detail in [119]. Some examples are: electric conductivity problems, magnetotransport, elasticity, thermoelectric and thermoelastic problems.

3.3.3 Physical optics (PO)

As previously mentioned, when the scatterer under study is many wavelengths in size in relation to the incident wave the computational requirements of numerical calculations increase rapidly in comparison to that of smaller scatterers [37]. To this end, high frequency approximations can be introduced to reduce the computational complexity of the problem of interest. If the radius of curvature of the scatterer is larger than a few wavelengths in size the tangent plane approximation can be utilized locally at the surface of the scatterer. This implies that at each point of the surface the tangential fields are treated as if the surface is flat and of infinite extent, simplifying the evaluation of the surface integral of the tangential fields. These results are then used to determine the scattered far field. Many applications of this technique exist in optics, electrical engineering and applied physics and the method is referred to as PO [167]. It is an intermediate method between geometrical optics, which treats electromagnetic waves as rays, and full wave electromagnetism [37]. An advantage of this method is that the simulation complexity and computation time does not significantly increase

with frequency as in the previous methods [5]. Drawbacks of PO is that it does not model edge diffraction and the accuracy of the method is reduced for scattering in directions other than the specular direction [5]. Modified versions of PO have been presented throughout the years where these problem have been successfully addressed, utilizing physical theory of diffraction (PTD) or other techniques [122, 178].

In Paper VIII in this work, the PO approximation is used to calculate the monostatic RCS of axially symmetric scatterers coated by RAMs, illuminated by a plane wave incident along the axis of rotation. Here comparisons are made between simulations using the PO approximation and full wave simulations.

4 Functional structures for electromagnetic waves

4.1 Frequency selective structures

An FSS is the archetypical example of an electromagnetic functional structure. All FSSs can be divided into two groups of structures: *band stop* FSSs and *band pass* FSSs [127, 186]. As the names imply, a band stop FSS ideally reflects or absorbs waves in a given frequency range, whereas a band pass FSS ideally reflects or absorbs waves for all frequencies except in a given frequency range where most waves are transmitted. A conceptual sketch is presented in Figure 12 where the relative power transmitted T is shown as a function of frequency for a band pass and a band stop FSS, respectively. Most FSSs consist of single or multiple layers of periodic lattices of conductive elements or apertures and dielectric slabs and other design components. In [127] the history and design of frequency selective structures (there referred to as frequency selective surfaces) are described in detail.

Due to the wave nature of electromagnetic fields, a simple band pass FSS can be constructed from a single dielectric slab as in Figure 13. The structure will transmit most of an incident wave when the electrical thickness is $d\sqrt{\epsilon_\mathrm{r}} = n\lambda_0/2$, $n = 1, 2, ...$ and the wave impinges at normal incidence [131]. This property is utilized in radome design for shielding of antennas from weather as well as wear and tear from the surroundings [90], where composite materials of fiber glass are commonly used. In the last half century radome designs utilizing FSSs have been proposed, such as the work in [134, 135].

Simulated transmission and reflection of a dielectric slab are presented in Figure 14. The relative permittivity of the slab is $\epsilon_\mathrm{r} = 4$ and the slab thickness $d = \lambda_0/4$, where λ_0 is the center wavelength of operation which for $f_0 = 10\,\mathrm{GHz}$ corresponds to 3 cm. It can be seen that at the center frequency the structure is transparent to incident waves in both TE and TM polarization, and when oblique incidence angles are considered the transmission window of the FSS starts to drift in frequency.

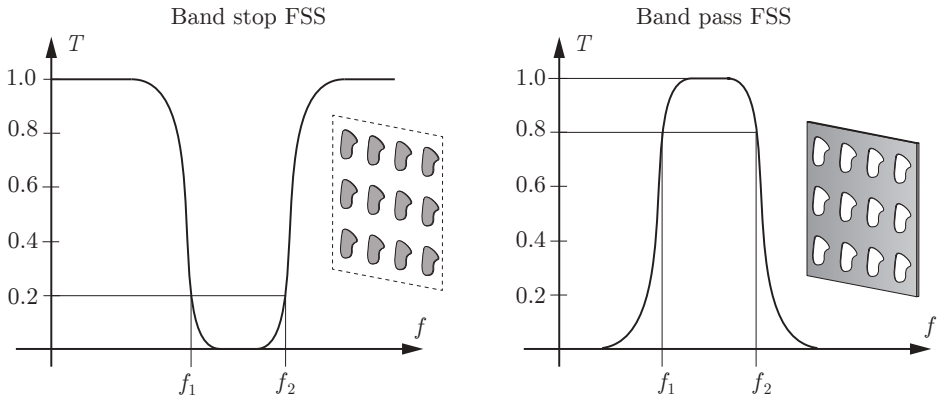

Figure 12: Conceptual sketch of the operation of a band stop FSS (left) and a band pass FSS (right), where the relative transmitted power $T = |\mathcal{T}|^2$ is presented as a function of frequency f.

A fundamental band stop FSS design with improved filtering performance is realized if conducting strips, or other resonant elements, of length $\lambda_0(2n-1)/2$, $n = 1, 2, ...$ are arranged in a periodic lattice as in Figure 15. Adjusting the width of the strips w and the period in the vertical and horizontal directions P_x, P_y tunes the filtering properties of the structure. This type of single layer FSSs typically have relatively narrow bandwidth with respect to some reference level in reflection. Nevertheless, wider bandwidth can be achieved if multiple periodic lattices and dielectric slabs are cascaded after each other [127]. Designing an FSS typically results in a trade-off between desired bandwidth, stability with respect to angle of incidence variations and the physical thickness of the structure with respect to the wavelength of operation. If the elements of the periodic lattice are either rotated or folded up on each other, the period of the structure can be reduced. This typically leads to improved stability with respect to angle of incidence variations [127]. In Figure 16 simulation results are presented of a dipole array FSS designed to operate at about $f_0 = 10\,\mathrm{GHz}$, where the width of the strips is $w = 0.2\,\mathrm{mm}$, the length of the strips is $l_\mathrm{xy} = 15.3\,\mathrm{mm}$, the thickness of the strips is $t = 0.05\,\mathrm{mm}$ and the horizontal and vertical periods of the lattice are $P_\mathrm{x} = 10.4\,\mathrm{cm}$ and $P_\mathrm{y} = 17.3\,\mathrm{cm}$, respectively.

Although the strips only occupy about 2 % of the physical area of the structure, almost all power is reflected at the center frequency of operation for vertically polarized incident waves. This effect can be explained by the fact that the FSS consists of an infinite number of elements that radiate in phase at the center frequency of operation, thus resulting in destructive interference with the incident wave in transmission. It can also be seen that the horizontally polarized waves perceive the structure as transparent over the frequency range of interest. This type of diplexing between waves of different polarization is a feature that has many applications, especially in satellite communication systems [73], and is discussed further in Sections 4.2–4.3.

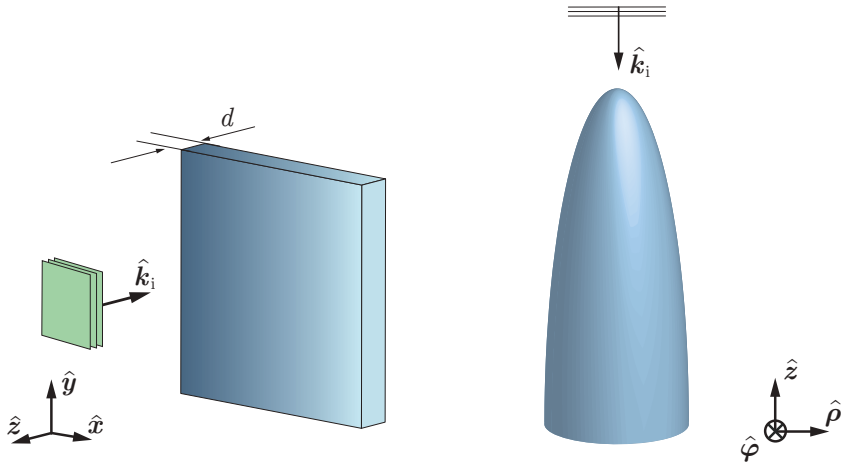

Figure 13: The geometry of a half wavelength dielectric slab FSS is presented to the left and a corresponding aircraft nose radome is presented to the right.

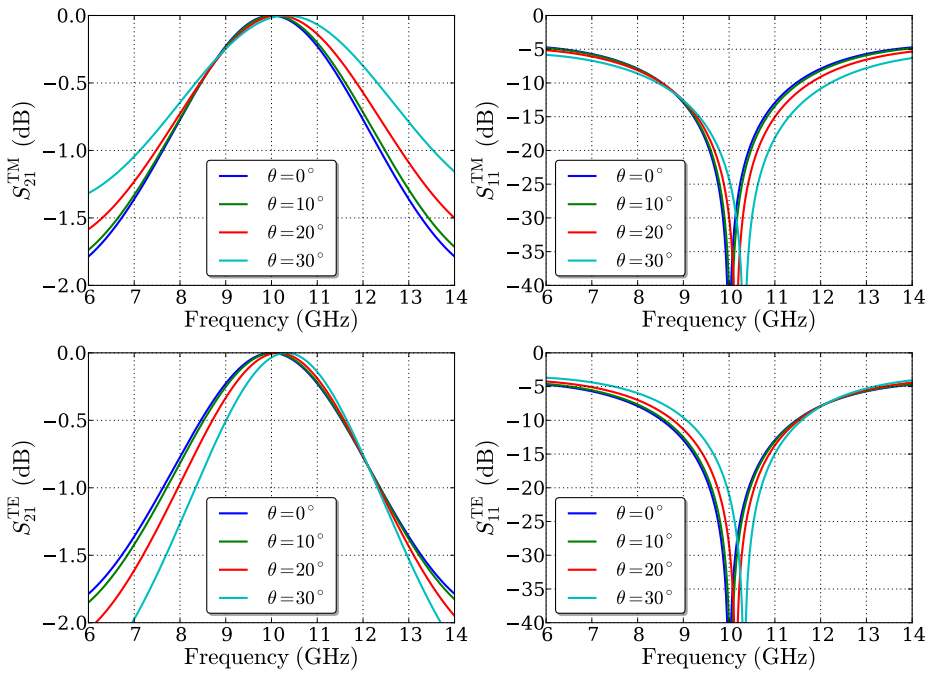

Figure 14: Simulation results of a planar dielectric slab acting as an FSS. The upper plots show the TM transmission and reflection and the lower plots the TE transmission and reflection.

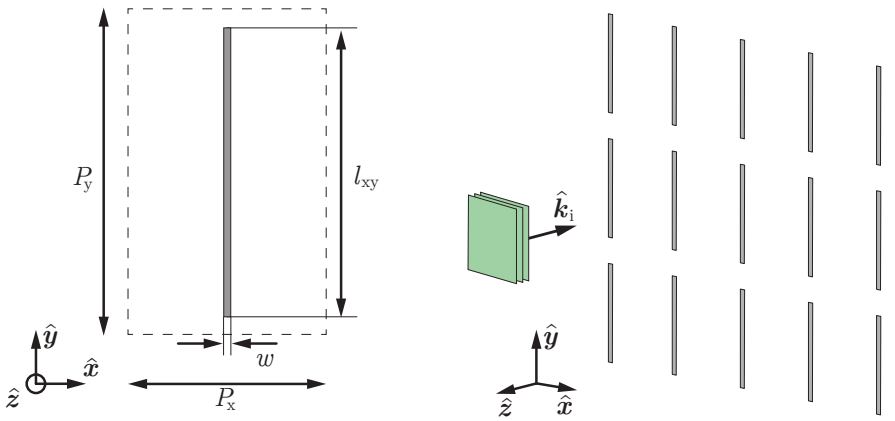

Figure 15: Geometry of a dipole array band stop FSS.

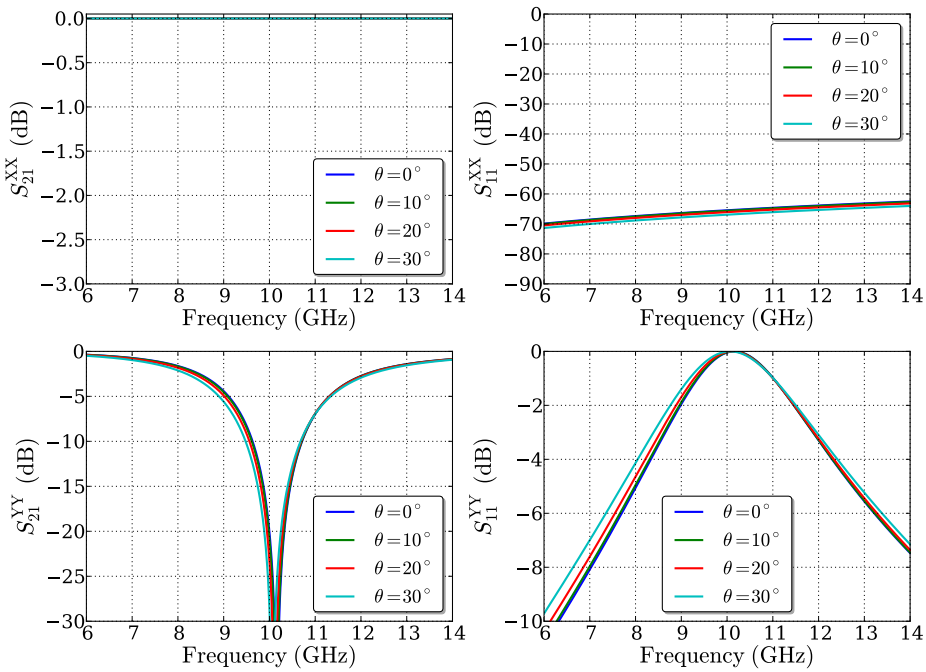

Figure 16: Simulation results of a dipole array band stop FSS, illuminated in the plane of incidence $\phi = 0°$ at different oblique angles θ.

If the strips are PEC and made infinitely thin, Babinet's principle can be used to extract the scattering properties of the complementary structure, which would correspond to an infinitely thin PEC sheet with a periodic lattice of slots as in Figure 17. This principle states that: "*The diffraction pattern from an opaque body is identical to that from a hole of the same size and shape except for the overall forward beam intensity*" [20]. Simulation results of the slotted array are presented in Figure 18, where it can be seen that the transmission of the horizontal polarization in the slotted case is almost identical to the reflection of the vertical polarization in the strip case, and vice versa. This type of structure transmits waves polarized orthogonal to the slots when the length of the slots is $l_{xy} = \lambda_0(2n-1)/2$, $n = 1, 2, ...$ and completely reflects waves polarized parallel to the slots. In the same manner as in the strip FSS scenario it can be seen in Figure 18 that, even though the slots correspond to about 2 % of the physical area of the structure, almost 100 % transmission is achieved at the center frequency of operation for waves polarized orthogonal to the slots. When comparing the results in Figure 14 and Figure 18 it can be seen that the slotted dipole array FSS achieves a much sharper roll off at the edges of its transmission peak, and a better reflection outside the transmission band, in comparison to the dielectric slab.

Novel FSS designs have been presented in the last two decades utilizing different concepts to achieve superior performance in comparison to classical FSS designs. In [1, 4, 6–8, 14–16, 102, 150, 154] different band pass FSS designs based on miniature resonant elements are presented. Higher order filter characteristics are achieved by cascading a single resonant FSS layer with multiple layers of sub wavelength lattices, resulting in wide bandwidth and significant stability with respect to angle of incidence variations. The geometrical parameters of the microscopic structures of these layers can be connected to effective capacitances and inductances based on variational expressions. In [113] effective network parameters are derived for a number of non-resonant structures. This type of circuit modeling can also be applied to a resonant structure, but the main strength of the method lies in simplifying complex designs to be optimized in a fast circuit model.

Another design approach that has been recently investigated is to design FSS elements with an extent in the direction of propagation of incident waves [11, 97–100, 109, 110, 139–141, 192]. These structures are commonly referred to as three-dimensional frequency selective structures (3D-FSS). A 3D-FSS typically comprises a two-dimensional periodic array of multimode cavities, where the mode coupling with the surrounding space can be controlled to obtain a desired frequency response. In [139] an overview of the characteristics of recently published 3D-FSSs was presented. There it is concluded that by utilizing the third dimension when designing an FSS, the stability with respect to angle of incidence variations can be significantly improved in comparison to classical 2D resonant FSSs. A different approach to improve the angle of incidence stability of the FSS performance was investigated in [104], where an FSS is constructed from two complementary resonant structures, arranged closely together.

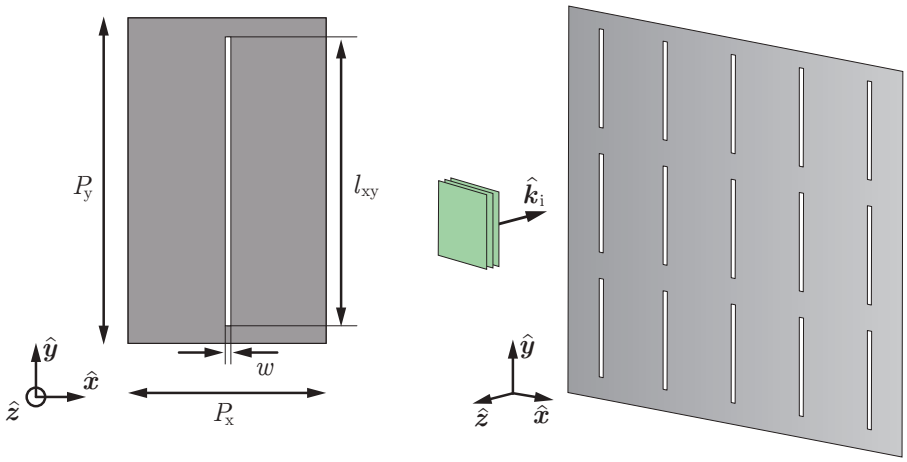

Figure 17: Geometry of a slotted dipole array band pass FSS.

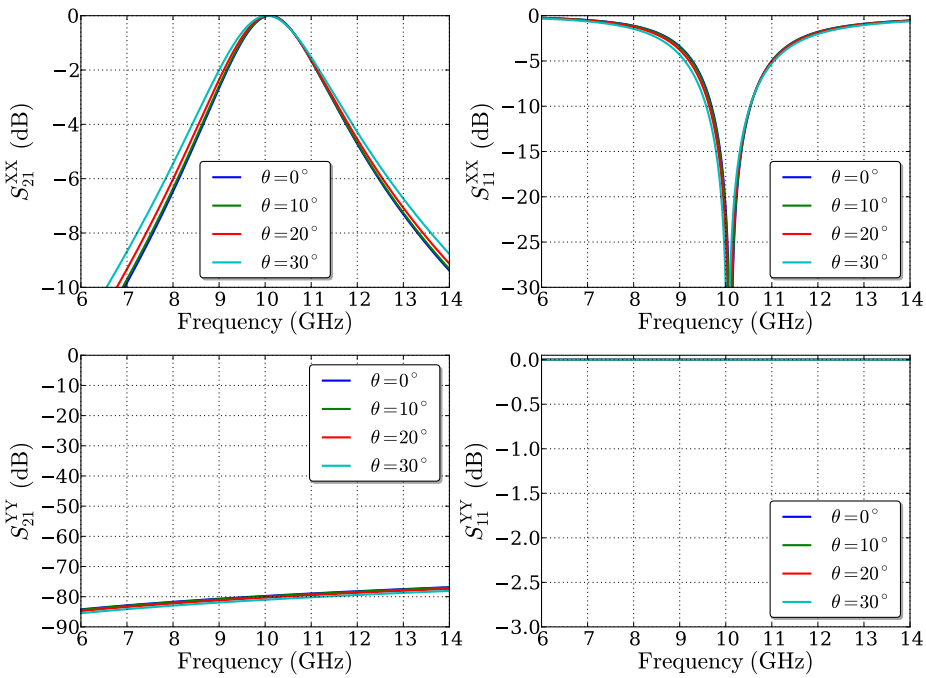

Figure 18: Simulation results of a slotted dipole array band pass FSS, illuminated in the plane of incidence $\phi = 0°$ at different oblique angles θ.

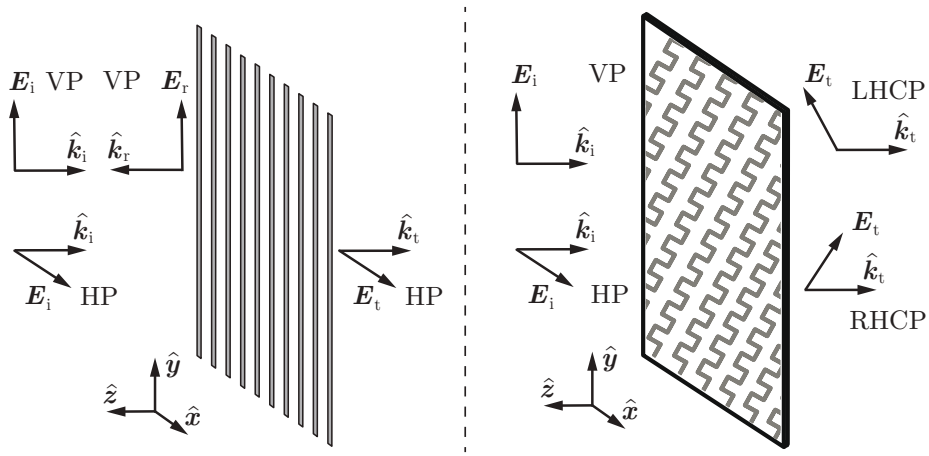

Figure 19: Conceptual sketch of a strip grid structure (left) and an electromagnetic polarizer (right). The strip grid reflects signals polarized parallel to the grids and transmit signals polarized orthogonal to the grids. The polarizer transforms incident LP signals to CP and vice versa, where the handedness of the CP signals depend on the polarization of the incident LP signal.

4.2 Polarization selective structures

As was shown in the previous section, an FSS typically interacts differently with electromagnetic waves depending on the polarization state of the incident signal. If the same response is desired for different polarizations, the FSS is composed of isotropic materials and/or symmetrical conductive layers. In Paper VI in this work, a porous triaxial weave is designed to have the same electromagnetic behavior as a solid reflector, *i.e.* reflect all signals with minimum return loss (RL), but improved mechanical properties. In some applications, for instance when different polarizations are used for different communication channels, it is desirable to separate signals of orthogonal polarization from each other and direct the separated signals in different directions. This can be achieved with a polarization selective structure. In linear polarization, selectivity between vertically and horizontally polarized signals is achieved by a single layer strip grid of metal wires as in the left illustration in Figure 19. Incident signals polarized parallel to the wires induce strong currents in the grid and the signal is reflected. Meanwhile, signals polarized orthogonal to the grids induce practically no currents in the grid and the signal is transmitted. In order to achieve said properties the grid should consist of thin wires with a spacing smaller than $\lambda/2$. This type of structure is utilized in a dual grid reflector for satellite communication (SATCOM) applications [13, 132, 146], typically operating in the $\mathrm{K_u}$ or $\mathrm{K_a}$ bands.

As stated in Section 1, it is common in SATCOM applications to utilize CP instead of LP. One way to transmit CP signals from a feed horn in a SATCOM

reflector system is to excite an LP signal and in the feed chain utilize an electromagnetic polarizer to convert the LP signal to a CP signal with either LHCP or RHCP depending on the polarization state of the LP signal [73]. This is achieved by decomposing the incident wave into two orthogonal LP components and then imparting different phase shifts to these two components to achieve the desired sign of phase quadrature. Some different polarizer designs commonly introduced in the feed chain include septum polarizers, pin polarizers, ridged-waveguide polarizers and corrugated polarizers, all of which work along the principles of transforming guided waves (propagating waveguide modes) between LP and CP or vice versa [73, 179].

The same type of polarization conversion can be achieved for waves propagating in free space with a structure similar to an FSS. By cascading multiple layers of anisotropic sheets oriented such that a different insertion phase is introduced to each LP component, an LP wave is converted to CP, and vice versa [47, 63, 87, 93, 95, 127] as in the right illustration in Figure 19.

The performance of a polarizer is typically evaluated based on the insertion loss (IL) of incident signals and the polarization state of the converted signal, quantified as axial ratio (AR), these performance measures are defined in detail in Section 4.3. In recent years, a multitude of novel polarizer designs have been put forward operating both in transmission [3, 43, 76, 77, 79, 80] and in reflection [41, 42, 59, 60]. In most of these cases the desired electromagnetic properties of the polarizer is to achieve a wide bandwidth with low IL and AR, and stability with respect to angle of incidence variations. At the same time, the structure should be as thin as possible with respect to the wavelength of the incident signal, and be composed of space compliant materials.

4.3 Circular polarization selective structures

In the same manner as for a linear polarization selective structure (LPSS), a CPSS reflects one handedness of CP and transmits the orthogonal polarization. Designing polarization selective structures for CP is a current key challenge in satellite communication applications [73, p. 710]. The design and characterization of this type of structures constitutes a large part of the novel work presented in this thesis, and thus a description of previous works and design choices related to CPSSs are outlined in detail in this section.

In [125, 147] theoretical characteristics of CPSSs were defined, and it was concluded that all CPSSs can be divided into four classes depending on its transmission and reflection properties. These classes are described in detail in Figure 20, and can be summarized as: if the handedness of the transmitted signal is unchanged, the CPSS is symmetric. If the reflection and transmission properties of the CPSS are maintained when the transmitter and receiver are interchanged, the CPSS is reciprocal. In order to achieve a structure with nonreciprocal scattering properties, nonreciprocal materials must be used such as magnetized ferrite crystals. Due to their weight, radiation sensitivity and outgassing [27], this type

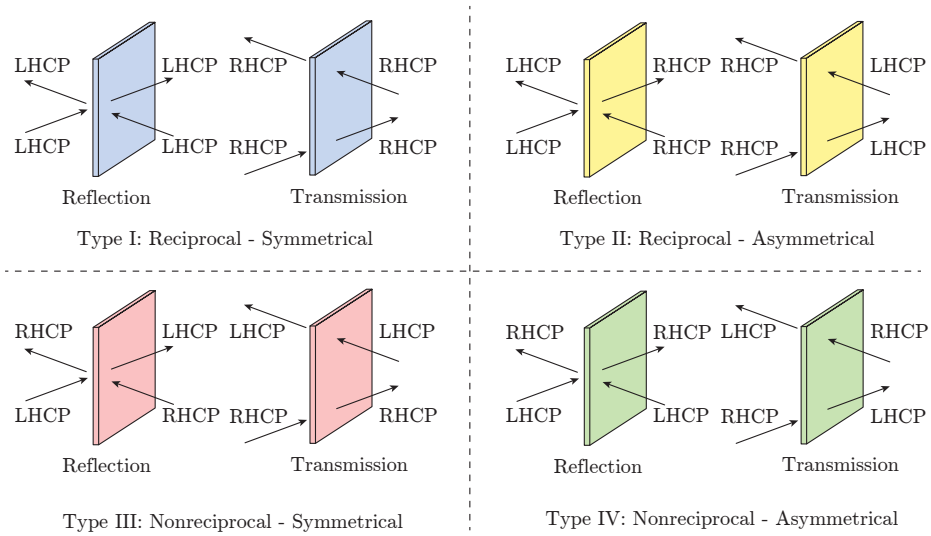

Figure 20: The four possible types of a LCPSS, characterized with respect to the polarization state of the transmitted and reflected signals in relation to the polarization state of the incident signal.

of materials are not well suited for space applications. The most common type of CPSS is reciprocal and symmetric, and it is shown in [125, 147] that these structures have the following properties:

1. The CP wave reflected by a CPSS will be of the same polarization as the incoming wave.
2. The CP wave transmitted by a CPSS will be of the same polarization as the incoming wave.
3. CP selectivity cannot be achieved by an infinitely thin surface.

This puts constraints on the polarization state of the reflected and transmitted signals; it also implies that a CPSS must have a finite thickness.

The scattering properties of main interest when characterizing the performance of a CPSS are: the RL of the co-polarized reflected signal, the IL of the co-polarized transmitted signal, and AR of the transmitted and reflected signals. For a left hand circular polarization selective structure (LHCPSS), these quantities are defined in dB as

$$\mathrm{RL} = -20\log_{10}(|S_{11}^{\mathrm{LL}}|), \qquad \mathrm{AR_r} = 10\log_{10}\left(\left|\frac{|S_{11}^{\mathrm{LL}}| + |S_{11}^{\mathrm{RL}}|}{|S_{11}^{\mathrm{LL}}| - |S_{11}^{\mathrm{RL}}|}\right|\right), \tag{4.1}$$

$$\mathrm{IL} = -20\log_{10}(|S_{21}^{\mathrm{RR}}|), \qquad \mathrm{AR_t} = 10\log_{10}\left(\left|\frac{|S_{21}^{\mathrm{RR}}| + |S_{21}^{\mathrm{LR}}|}{|S_{21}^{\mathrm{RR}}| - |S_{21}^{\mathrm{LR}}|}\right|\right), \tag{4.2}$$

where the subscripts r and t represent reflection and transmission, respectively. The AR is a measure of the polarization state of a signal, where 0 dB corresponds to a perfectly circular polarization state and as AR grows this corresponds to an increasing ellipticity of the polarization. A result of this definition is that a linearly polarized wave will have an infinite AR in dB. An alternative definition to the AR also commonly used is the cross polarization discrimination (XPD) in CP, defined for an LHCPSS as

$$\mathrm{XPD_r} = 20\log_{10}\left(\frac{|S_{11}^{\mathrm{LL}}|}{|S_{11}^{\mathrm{RL}}|}\right), \qquad \mathrm{XPD_t} = 20\log_{10}\left(\frac{|S_{21}^{\mathrm{RR}}|}{|S_{21}^{\mathrm{LR}}|}\right). \tag{4.3}$$

The fractional bandwidth of a CPSS is commonly determined with respect to some requirements on the RL, IL, $\mathrm{AR_r}$ and $\mathrm{AR_t}$. In [9] requirements based on integration of a CPSS in a satellite communication system were put forward

$$\mathrm{RL} < 0.5\,\mathrm{dB}, \qquad \mathrm{AR_r} < 0.78\,\mathrm{dB}, \tag{4.4}$$

$$\mathrm{IL} < 0.5\,\mathrm{dB}, \qquad \mathrm{AR_t} < 0.78\,\mathrm{dB}. \tag{4.5}$$

In the literature [2, 3, 76–78] relaxed requirements of

$$\mathrm{RL} < 1.0\,\mathrm{dB}, \qquad \mathrm{AR_r} < 3.0\,\mathrm{dB}, \tag{4.6}$$

$$\mathrm{IL} < 1.0\,\mathrm{dB}, \qquad \mathrm{AR_t} < 3.0\,\mathrm{dB}, \tag{4.7}$$

are also used when designing and characterizing CPSSs. These requirements are, to the knowledge of the author of this work, not based on a specific application scenario.

Throughout the last 60 years, a multitude of CPSSs have been presented. The first design was presented in 1966 by Pierrot [133] and is based on a periodic lattice of thin wires bent in the shape of a crank, as in Figure 21. This type of structures based on resonant wires are in this work referred to as classical CPSSs. When the total length of the wires is an integer of a half wavelength $l = 2l_{\mathrm{xy}} + l_{\mathrm{z}} = n\lambda/2$, $n = 1, 2, ...$, and the length of the wire component in the direction of propagation is $l_{\mathrm{z}} = \lambda/4$, CP signals will rotate either along or against the structure and strong currents will be induced in the vertical and horizontal wires. For example, if the structure in Figure 21 has a total element length of $l = \lambda$ and is illuminated with an LHCP wave the currents in the vertical and horizontal wire components will be in phase and the signal will be reflected. If the structure is illuminated by an RHCP wave the currents will be out of phase and cancel out, resulting in the signal being transmitted, as can be seen in Figure 22.

Simulation results of the Pierrot CPSS are presented as a function of frequency in Figure 23, for different angles of incidence θ in a fixed incidence plane $\phi = 90°$. The design parameters of the structure, originally found in [103], are presented in Table 1. In order to reduce the unit cell size, the wire elements were rotated 45° with respect to the unit cell boundaries. It can be seen that the bandwidth of the CPSS with respect to the requirements in (4.4)–(4.5) is about 10 % and the filtering performance quickly deteriorates at oblique angles of incidence. In [49] it was demonstrated that the performance of the Pierrot CPSS is

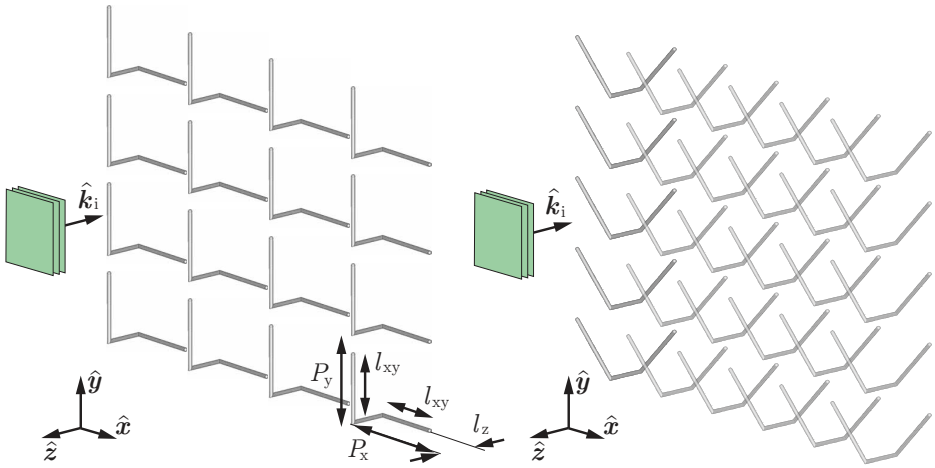

Figure 21: Two different arrangements of a Pierrot LHCPSS consisting of a periodic lattice of crank wires. To the left the elements are arranged in a horizontal and vertical manner, and to the right the individual elements are rotated 45° in order to fit the elements closer together.

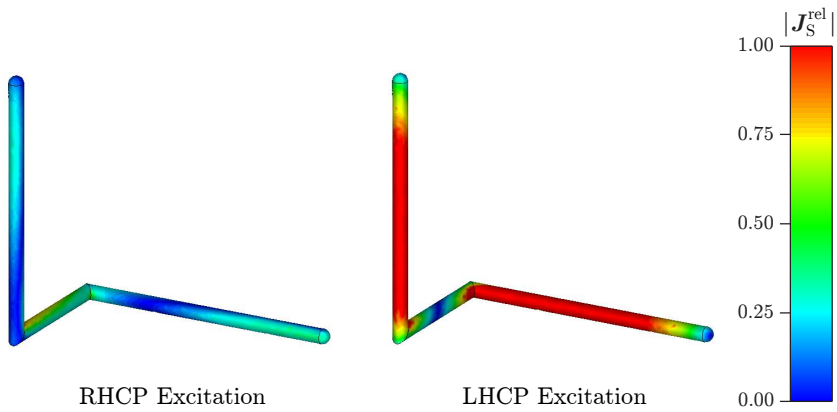

Figure 22: Induced currents on an element of a Pierrot LHCPSS illuminated by an RHCP and LHCP plane wave at the center frequency of operation.

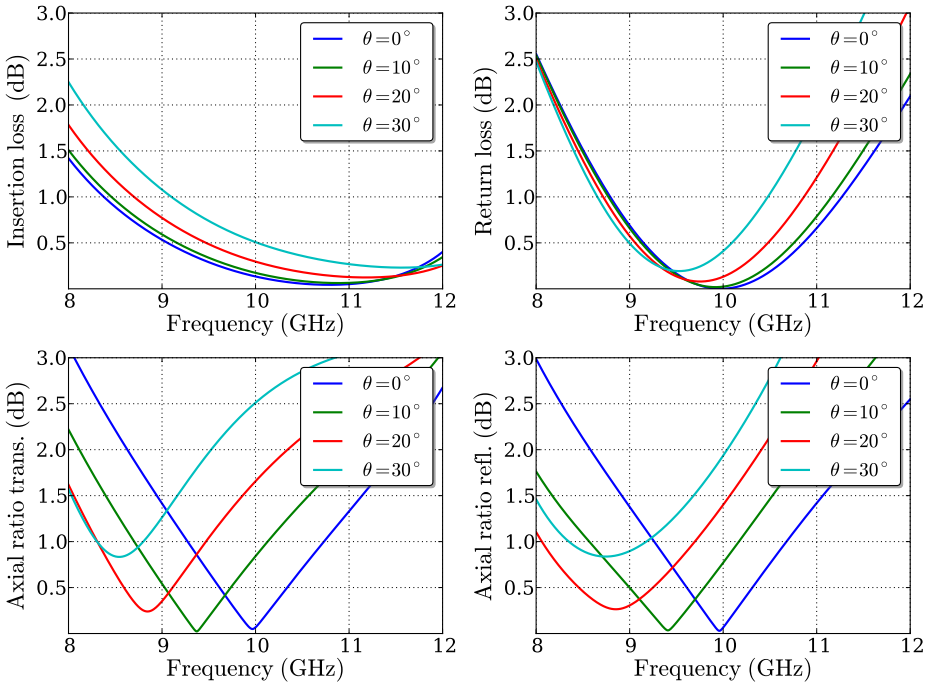

Figure 23: Simulation results of the Pierrot CPSS. The RHCP IL is presented in the upper left plot, and the corresponding AR_t is presented in the lower left plot. The LHCP RL is presented in the upper right plot, and the corresponding AR_r is presented in the lower right plot.

also strongly affected by the choice of incidence plane that is considered. By evaluating the scattering characteristics of a CPSS for all angles of incidence (θ, ϕ) at discrete frequencies, an alternative way of evaluating a CPSS is achieved [49], see Paper II in this work. The plane of incidence sensitivity of the Pierrot CPSS is demonstrated in Figure 24, where the angle of incidence $\theta = 30°$ is fixed and the plane of incidence is varied.

Different realizations and variations of the Pierrot CPSS have been presented the last eleven years [61, 105, 106, 152, 153]. The first experimental verification of a Pierrot CPSS was presented in 2006 [61]. The CPSS consisted of a periodic lattice of metal wires threaded through a slab of Rohacell, and in this work IL and AR_t were characterized. Recently, a different realization of the Pierrot CPSS consisting of two printed circuit boards interspaced by a Rohacell core and connected by copper vias was manufactured and characterized experimentally both in reflection and transmission [152], and good agreement between simulated and measured results were observed. In [105, 106] different versions of the Pierrot CPSS were realized by printing patterns on a flexible substrate that was folded into a corrugated shape.

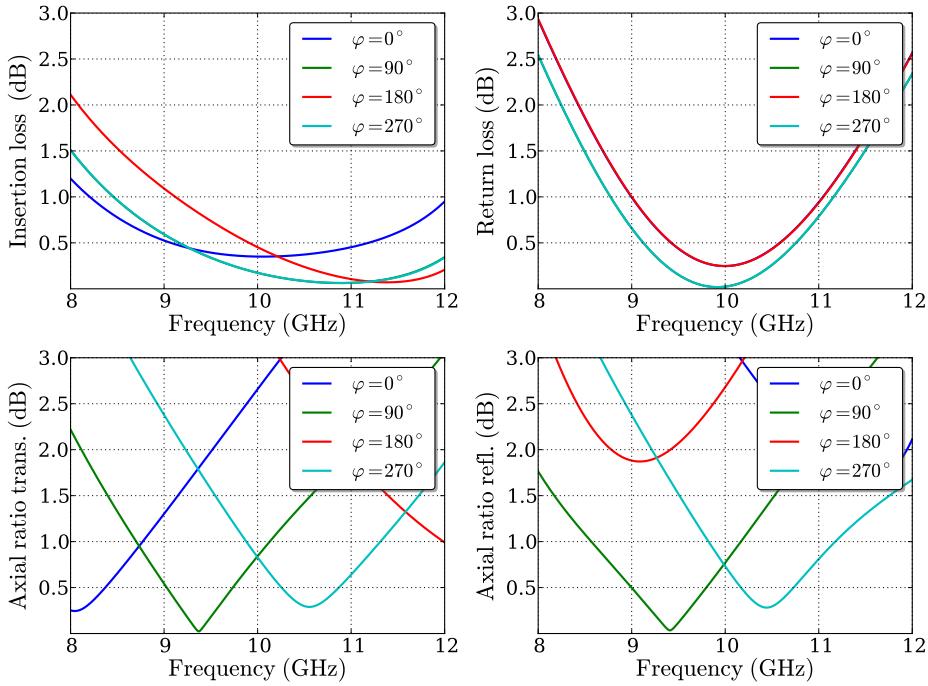

Figure 24: Simulation results of the Pierrot CPSS. The RHCP IL is presented in the upper left plot, and the corresponding AR_t is presented in the lower left plot. The LHCP RL is presented in the upper right plot, and the corresponding AR_r is presented in the lower right plot. The RL curves for $\phi = 0°, 90°$ are on top of each other, and the same is true for the RL curves for $\phi = 180°, 270°$.

Another classical CPSS presented in 1988 by Tilston [174,175] consists of two Pierrot-like elements arranged closely together, making the parallel wires in the propagation direction act as a twin wire transmission line. In order to achieve a strong resonance in the structure, the transmission line part of the structure should have an electrical length of $\lambda_0/2$, in combination with a physical length of $l_z = \lambda_0/4$. This can be achieved either by embedding the wires in a dielectric cylinder as in Figure 25, or by shaping the twin wires as helices [103]. The total physical length of each bent wire in the Tilston CPSS is $3\lambda_0/4$ and the corresponding electrical length is λ_0. Simulation results of a Tilston CPSS are presented in Figure 26, where it can be seen that the structure has a similar bandwidth as the Pierrot design, but the angle of incidence stability is slightly improved. In Paper II the angle of incidence sensitivity of the CPSS performance is studied in detail for these two designs alongside with other CPSSs.

The third classical CPSS presented by Morin in 1990 [123–125] is another modification of the Pierrot CPSS. In this design, the resonant elements are interconnected and form wire helices at a 45° angle with respect to the horizontal

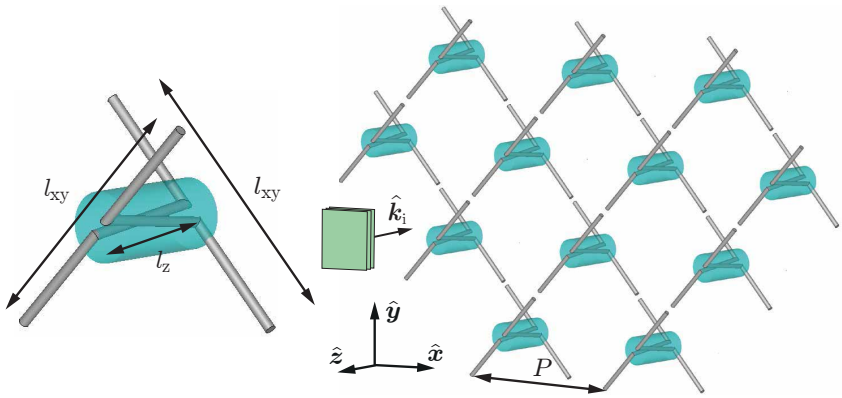

Figure 25: Geometry of the Tilston CPSS.

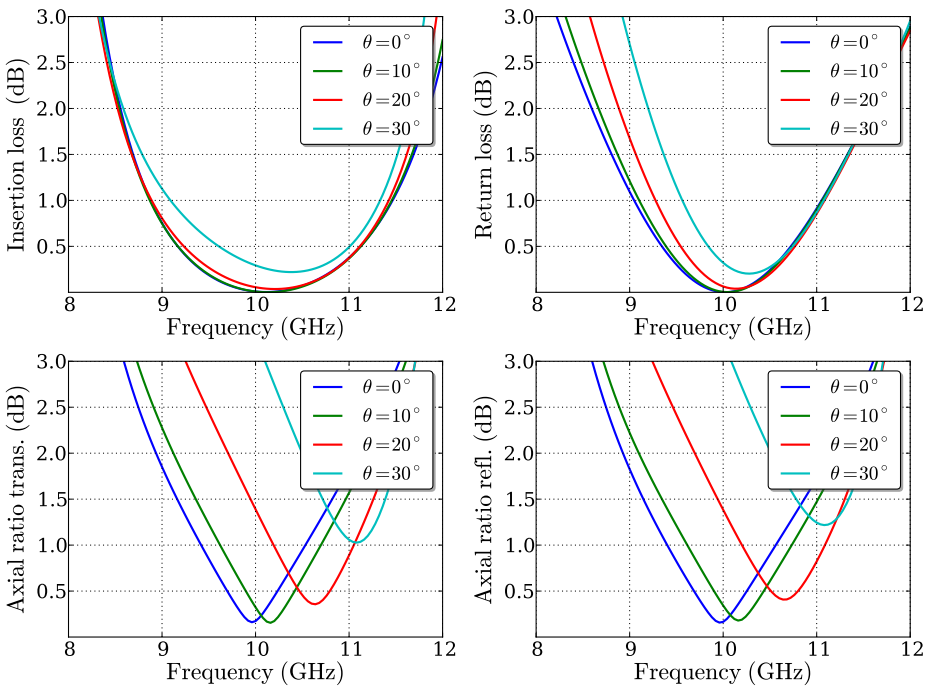

Figure 26: Simulation results of the Tilston CPSS. The RHCP IL is presented in the upper left plot, and the corresponding AR_t is presented in the lower left plot. The LHCP RL is presented in the upper right plot, and the corresponding AR_r is presented in the lower right plot.

direction, as in Figure 27. The length of the horizontal and vertical wire components is $l_{xy} \approx \lambda_0/4$ and the wire component in the direction of propagation is $l_z = \lambda_0/4$. Simulation results of the Morin CPSS are presented in Figure 28, where it can be seen that the structure has a similar bandwidth as the Pierrot design, but the angle of incidence stability is improved in the Morin CPSS.

In the last decade, a number of novel CPSS designs have been presented based on the concept of cascading a polarizer, see Section 4.2, a strip grid and a second polarizer [2,76,78]. The principle of operation of this structure is the following: an incident CP wave is transformed to an LP wave and depending on if the incident wave was RHCP or LHCP the LP wave is either reflected or transmitted of the strip grid at the center. The transmitted LP wave is then transformed back to CP. In [78] CP selectivity is achieved over a wider bandwidth of approximately 27 % at 3 dB AR.

A more thorough overview of most CPSS designs presented up to date is presented in Paper III in this work. The current key challenges in CPSS design is to achieve: wider bandwidth with respect to the requirements in (4.4)–(4.7), and improved stability with respect to angle of incidence variations compared to previous designs. Ideally, these performance properties should be achieved by a relatively simple structure with a small thickness with respect to the wavelength of the incident signals. The most wideband CPSS presented up to date is presented in Paper III in this work and is based on cascaded anisotropic sheets of meander lines, where each consecutive layer is rotated with respect to the incident signal. This type of structure achieves a bandwidth of approximately 45 % and shows significant improvements in stability with respect to angle of incidence variations compared to previous designs [50, 166]. An alternative design utilizing the same concept of operation is presented in Paper V, where operation in dual frequency bands is achieved [107, 108].

Table 1: Design parameters of classical CPSSs simulated in this work.

CPSS	l_{xy}	l_z	l_{tot}	a	P_x	P_y	ϵ_r	w
Pierrot	13.6	7.5	34.7	0.2	13.3	11.9	-	-
Tilston	16.4	7.1	23.5	0.1	12.5	12.5	4.3	0.7
Morin	10.9	7.5	29.3	0.1	4.2	$\sqrt{2}l_{xy}$	-	-

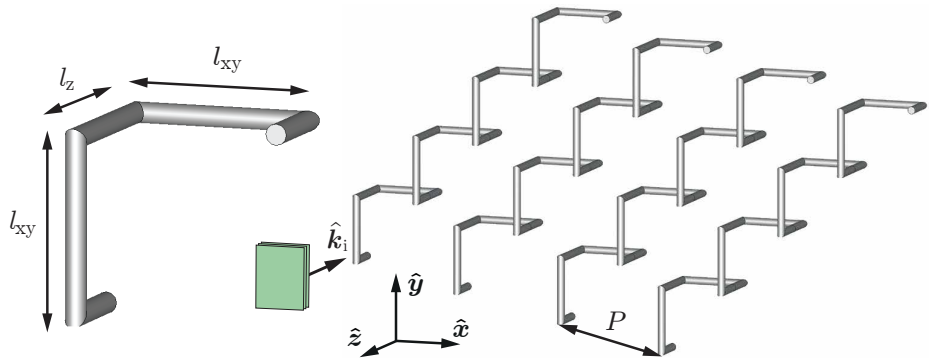

Figure 27: Geometry of the Morin CPSS.

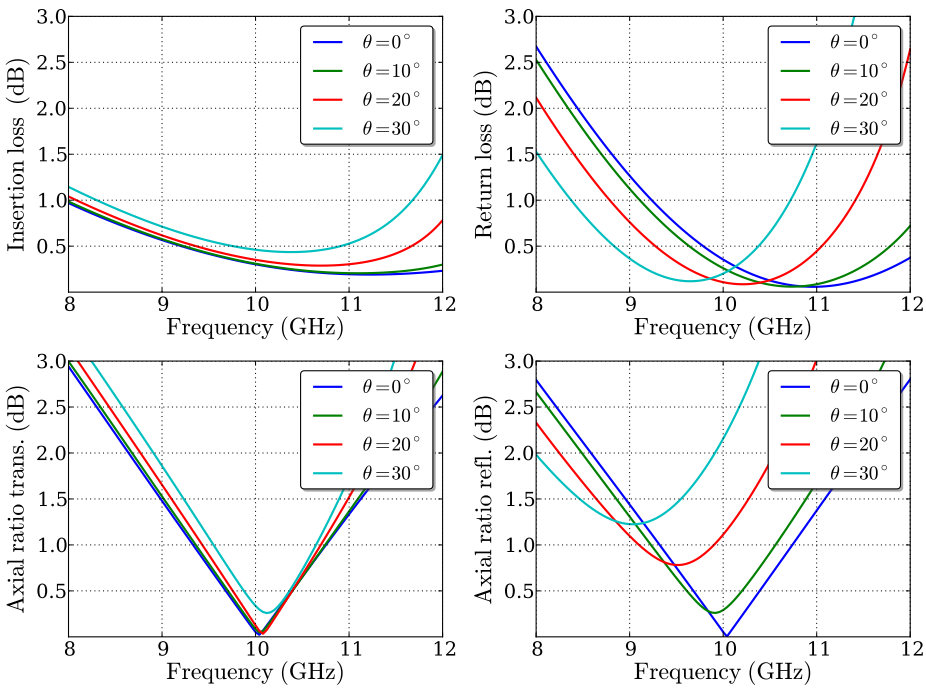

Figure 28: Simulation results of the Morin CPSS. The LHCP IL is presented in the upper left plot, and the corresponding AR_t is presented in the lower left plot. The RHCP RL is presented in the upper right plot, and the corresponding AR_r is presented in the lower right plot.

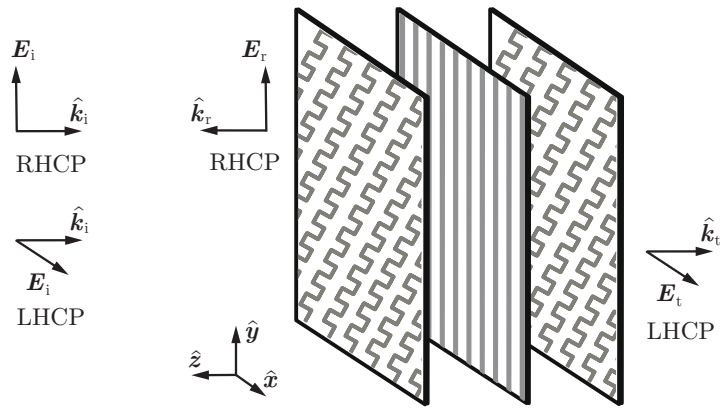

Figure 29: CPSS based on cascading a polarizer, a strip grid and a second polarizer. An incident LHCP wave is transformed to a HP wave that is transmitted by the strip grid, and an LHCP wave is transformed to a VP wave that is reflected by the strip grid.

4.4 Radiation-absorbing materials

Radiation-absorbing materials (also commonly referred to as electromagnetic absorbers or RAMs) are, as mentioned in Section 1, structures that minimize the reflection and transmission of electromagnetic waves at certain frequencies [149]. These structures have a wide range of applications, such as to create a "quiet zone" for experimental characterization of antennas and electromagnetic scattering characterization of a device under test [68], or to minimize the electromagnetic scattering from the scatterer itself [88, 149]. The physical process behind the functionality of electromagnetic absorbers is that radiated power associated with a propagating electromagnetic wave is transformed into heat inside the absorber. This is typically achieved by using materials with significant dielectric losses or magnetic losses. Depending on the application, different requirements are imposed on the properties of the absorber. Just as in the case of FSSs a thicker absorber, with respect to the wavelength of incident waves, can in general achieve a wider bandwidth and better absorption properties [127]. This was proven by Rozanov in [148], where a physical bound was derived relating the absorber thickness to the maximum achievable bandwidth of the structure with respect to a predefined reference level. This physical limitation is formulated through the relation

$$\Delta\lambda\, \Gamma_0 \leq 172d(1 + \gamma_\mathrm{m}/(Ad)), \tag{4.8}$$

where $\Delta\lambda$ is the absolute wavelength bandwidth of the absorber with respect to Γ_0, the minimum allowed RL in dB, γ_m/A is the magnetic polarizability per unit area, and d is the absorber thickness.

In applications where absorbers are used to create a quiet zone, the thickness

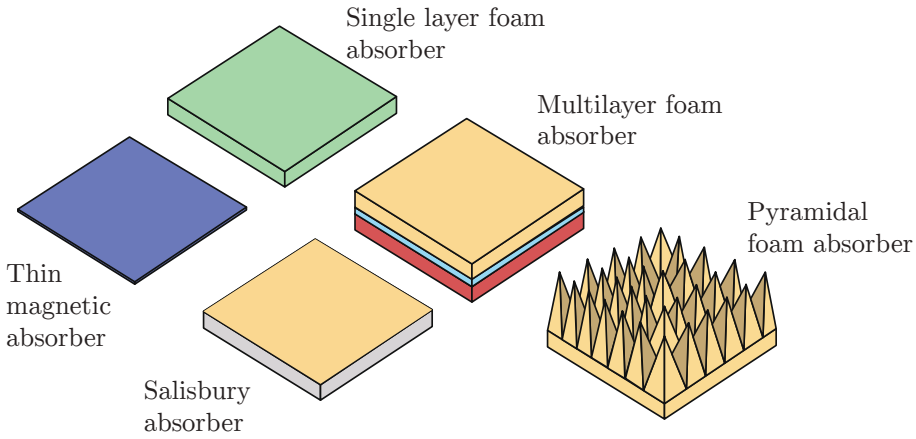

Figure 30: Examples of electromagnetic absorbers.

of the absorber does not neccesarily need to be small and it is then common to use pyramidal foam absorbers doped with carbon, such as in the rightmost structure in Figure 30 [185]. These absorbers typically provide a relatively wide bandwidth and high attenuation for waves impinging at oblique angles of incidence. In other applications, such as RCS reduction, it is common that the thickness and weight of the absorber shold be kept at a minimium [88, 149]. In those cases it is more common to utilize a planar absorber backed by a PEC. Some examples of simple absorbers commonly used are: thin magnetic absorbers designed from ferrite and carbonyl iron [88], foam material absorbers loaded with carbon resulting in conductivity losses [149], a Salisbury screen consisting of a resistive sheet located quarter of a wavelength from a PEC [151], and graded index absorbers of multiple layers of carbon doped foam with gradually increasing conductivity [88], see Figure 30.

Typical design and performance characteristics are presented for a Salisbury absorber and a single layer foam absorber (referred to as a Dällenbach absorber) in Figures 31–32. The Salisbury absorber consists of a thin resistive sheet, with surface admittance matched to the free space wave impedance $Y_S = 1/\eta_0$, located a distance $\lambda_0/4$ from a PEC ground plane, where λ_0 is the center wavelength of operation of the absorber. The foam absorber consists of a conductivity loaded low permittivity material with thickness $\lambda_0/4$ and relative permittivity $\epsilon_r = \epsilon_r' - j\epsilon_r''(f) = 1.1 - j1.12 f_0/f$, where ϵ_r'' was determined through a simple optimization where the bandwidth of the absorber was maximized with respect to the reference level RL < -10 dB for $\epsilon_r' = 1.1$ and $d = \lambda_0/4$. In Figure 32 it can be seen that the Salisbury absorber has a relatively narrow bandwidth and the center frequency of operation is shifted at oblique angles of incidence. The Dällenbach absorber has a much wider bandwidth with respect to the reference level RL < -10 dB, but also displays a shift in the RL at oblique angles of incidence.

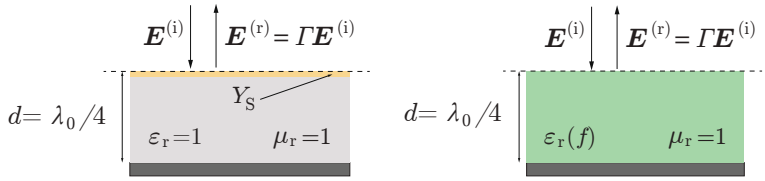

Figure 31: Electromagnetic absorbers used in this work. To the left a Salisbury screen is presented and to the right is a Dällenbach absorber based on conductivity loss.

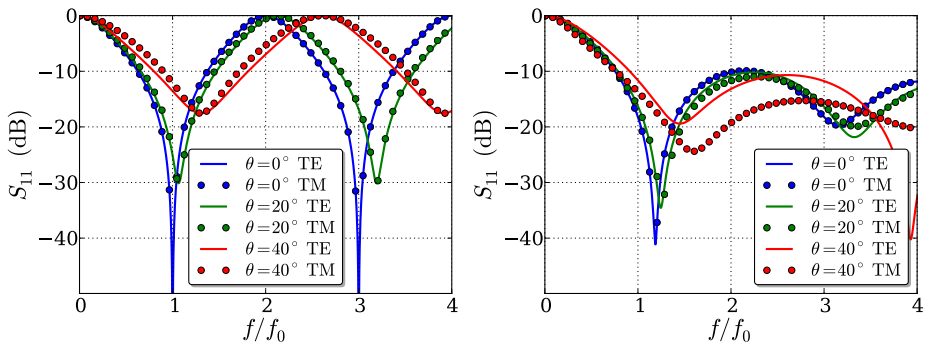

Figure 32: Simulation results of a Salisbury absorber (left) and a Dällenbach absorber (right) for TE and TM illumination. Both absorbers have the thickness $d = \lambda_0/4$.

Many novel absorber designs have been presented in the last decades targeting different performance requirements, see for example [34,39,45,62,81–84,101,111, 143,164,173]. Minimizing the thickness to bandwidth ratio of the absorber and at the same time achieve stable performance for oblique angles of incidence, both in TE and in TM, are common desirable performance features in absorbers [127]. These properties can for example be approached by utilizing resonant structures [62], non-resonant layers of resistive sub-wavelength patches [81–84], metamaterials [39, 101], or by implementing a high impedance surface in the absorber to reduce the thickness to bandwidth ratio of the structure [34,45,111, 164]. If the ground plane of the absorber is replaced by an FSS, a combination of an absorber and a frequency selective structure is achieved. These pass band, or radome absorbers (rasorbers), operate as an ordinary absorber except in a given frequency band where the structure is transparent to incident signals [126]. A rasorber can also be designed by utilizing the concept of 3D-FSSs as was introduced in Section 4.1 [96,160].

4.5 Additional types of functional structures

4.5.1 Metamaterials

The functional structures designed and characterized in this work are all evaluated and categorized with respect to their transmission and reflection properties. A different way of categorizing these structures is to determine their effective electric and magnetic material parameters ϵ and μ. This can for example be done using the homogenization technique presented in Section 3.3.2, where the macroscopic properties of a material are extracted. Some exotic materials have been designed in the last two decades that display peculiar properties, which can be modeled by negative permittivity and/or permeability [161,168]. These materials are referred to as metamaterials and typically consist of a periodic arrangement of resonant elements on a length scale smaller than the wavelength [28, 190, 191]. Some interesting effects and applications of this type of materials are:

- Near zero refractive index, causing electromagnetic waves to travel with nearly zero phase velocity [24].
- Negative refraction, causing electromagnetic waves to refract in a direction opposite to that of ordinary materials [168].
- Chiral metamaterials, displaying negative refraction for one circular polarization. Given the chirality of a material is strong enough, negative refraction may occur for one circularly polarized wave, while for the other circular polarization the refractive index remains positive [177, 188].
- Electromagnetic bandgap metamaterials (EBM) that inhibit wave propagation at certain frequencies. This type of metamaterials are based on periodic structures with a periodicity on the order of the wavelength. In theory, these structures are based on the same concept of operation as band stop FSSs, but can also be periodic in three dimensions.
- Metamaterial lenses, also refered to as perfect lenses, being able to reproduce not only the traveling waves associated with the object but all the evanescent waves as well [28].
- Metamaterial antennas, where metamaterials are used to achieve unusual wave propagation and radiation fetaures [46].

One drawback with metamaterials is that the relative bandwidth over which negative material parameters are achieved is limited to a few percent as a consequence of the Kramers-Kronig relations [65]. Furthermore, losses in metamaterials are common and can cause problems for specific applications [46]. The development of metamaterial functional structures is outside of the scope of this thesis. Still, the design and optimization techniques used in this work could also be applied to this kind of design problem. For more information on metamaterials and their applications, see for example [24, 26, 28, 46, 168, 184].

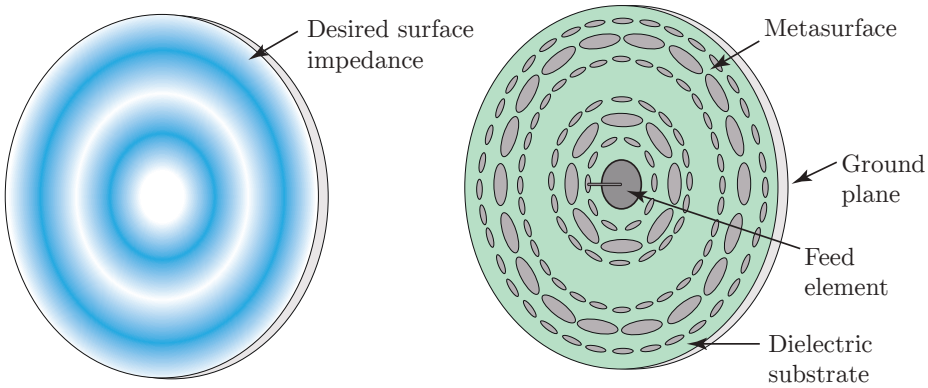

Figure 33: Desired surface impedance (left) and a sketch of a corresponding metasurface antenna (right).

4.5.2 Metasurfaces

A potential problem with metamaterials is the losses of electromagnetic waves propagating through these structures. An alternative approach to achieve the exotic scattering properties associated with metamaterials with reduced loss is to utilize thin surfaces of metamaterials, also referred to as metasurfaces [137]. In the same way as FSSs, metasurfaces consist of a periodic array of resonant elements. The classification of what is referred to as a metasurface or an FSS varies depending on the field of research, but one distinction typically made is that a structure is referred to as a metasurface if the periodicity of the structure is much smaller than the wavelength [69]. From this perspective, the miniature element FSSs in Section 4.1 and the non-resonant CPSS in Papers III–V could all be referred to as cascaded metasurfaces. A different classification of metasurfaces is presented in [137]. There it is stated that the main difference between FSSs and metasurfaces is that metasurfaces require both electric and magnetic responses in the structure, which can be modeled as electric and magnetic surface susceptibilities.

Metasurfaces can be used in a number of applications, such as in miniaturized cavity resonators, waveguiding structures, controllable surfaces, RAMs, antennas and biomedical devices [25,69]. By using the surface equivalence principle, desired field distributions can be achieved by utilizing electric and magnetic polarizable elements in the design of such surfaces [137].

Metasurfaces may under certain conditions support surface wave propagation [112]. This is a useful feature which is currently being utilized in antenna design. Here the properties of the metasurfaces are modeled by its surface impedance, which can be tailored to vary globally across the surface. Some examples of antennas, based on this concept, with interesting features are: CP broadside antennas with anisotropic modulated metasurface [120], isoflux CP antennas [121]

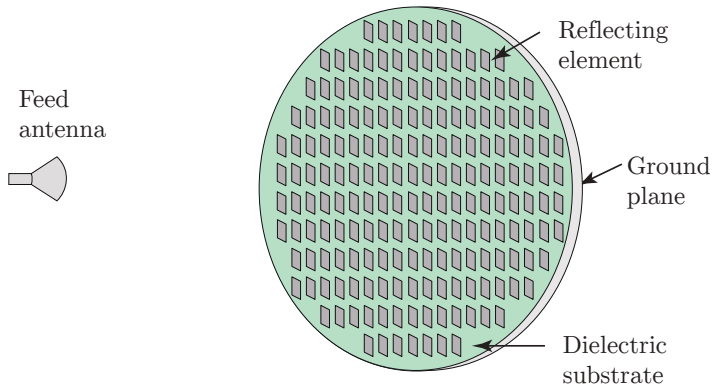

Figure 34: Reflectarray consisting of printed elements on a dielectric substrate backed by a ground plane.

and Luneburg lens antennas [21]. In these designs, the global periodicity of the metasurfaces is broken and the local elements are rotated and modified to achieve desired surface impedance variations, as in the antenna sketch in Figure 33. For further information regarding the principles and current research of this type of structures, see for example [21, 25, 69, 112, 120, 121, 137].

4.5.3 Reflectarrays

A category of antennas similar to metasurfaces is reflectarray antennas. The designation reflectarray antennas refers to the class of radiating structures that are comprised of an array of elements reradiating impinging energy from one or more radiating feeds that are located in free space [158], as in Figure 34. This type of antennas combine advantages of phased arrays and reflector antennas. They consist of a flat or slightly curved reflecting surface covered by reflecting elements of varying size, shape and orientation. In the same way as in some metasurfaces, this kind of local variation of the reflecting elements is utilized to achieve the desired global radiation properties of the whole reflectarray surface.

Some advantages of reflectarrays in comparison to traditional parabolic reflectors are the simplicity of using a planar structure in favor of a doubly curved structure for deployment purposes, and the possibility of designing the main beam to tilt at a large angle ($> 50°$) from its broadside direction [70]. Additionally, low-loss electronic phase shifters can be incorporated into the elements for wide angle electronic beam scanning [176]. These properties make reflectarrays suitable for contour beam applications, for example to provide a specified coverage area of Earth.

The main disadvantage of reflectarray antennas is the inherent narrow bandwidth associated with the reflecting elements, as well as the differential spatial phase delay. The bandwidth generally cannot exceed much beyond ten percent

depending on the element design, aperture size, focal length and other design factors. Extensive overviews and future challenges related to reflectarrays and its applications can be found in [35, 70, 158].

5 Design and optimization of functional structures

5.1 Design of functional structures

The design process of a functional structure can be described in a number of steps. The procedure used throughout this thesis to develop functional structures is outlined in Figure 35. First, the desired transmission and reflection properties of the structure are specified. A common secondary goal when designing a functional structure is to keep the thickness of the structure as small as possible with respect to the design wavelength. Thicker structures tend to display deteriorating performance at oblique incidence angles. Also, the period of the structure should be kept smaller than $\lambda_0/2$ in order to avoid grating lobes at oblique angles of incidence [127].

Next, relevant previous works are evaluated and from this information the concept of operation of the functional structure is chosen. In most cases, some similar technology exists that can be used as a starting point when designing a novel functional structure. If for example narrow band filtering characteristics of first order are required, a single layer resonant structure is a possible candidate due to its simple design and small thickness with respect to the wavelength of incident waves. If higher order filtering characteristics are to be achieved, the spacing between subsequent resonant layers should be at least $\lambda_0/4$ to avoid higher order mode coupling between adjacent layers [127]. This will most likely result in a relatively thick structure and thus it is common to consider other solutions for structures with higher order filtering performance. An alternative design strategy to achieve higher order filtering performance without significantly increasing the thickness of the structure was introduced in Sections 4.1 and 4.3. This method is based on cascading multiple non-resonant layers with sub-wavelength patterns with resonant layers of sub-wavelength periodicity [1,4,6–8,14–16,102,150,154]. Another alternative design approach introduced in Section 4.1 is to design FSS elements extending in the direction of propagation of incident waves [11, 97–100, 109, 110, 139–141, 192]. These structures are commonly referred to as 3D-FSSs.

After the physical concept of operation of the structure has been specified, a choice is made whether the functional structure should be optimized as a simple concept design, using only freely hanging conductive elements in free space, or as a realistic design based on materials suited for the application. One advantage with initially evaluating the performance of a functional structure using a concept design is that the optimal performance of the structure can be investigated. As

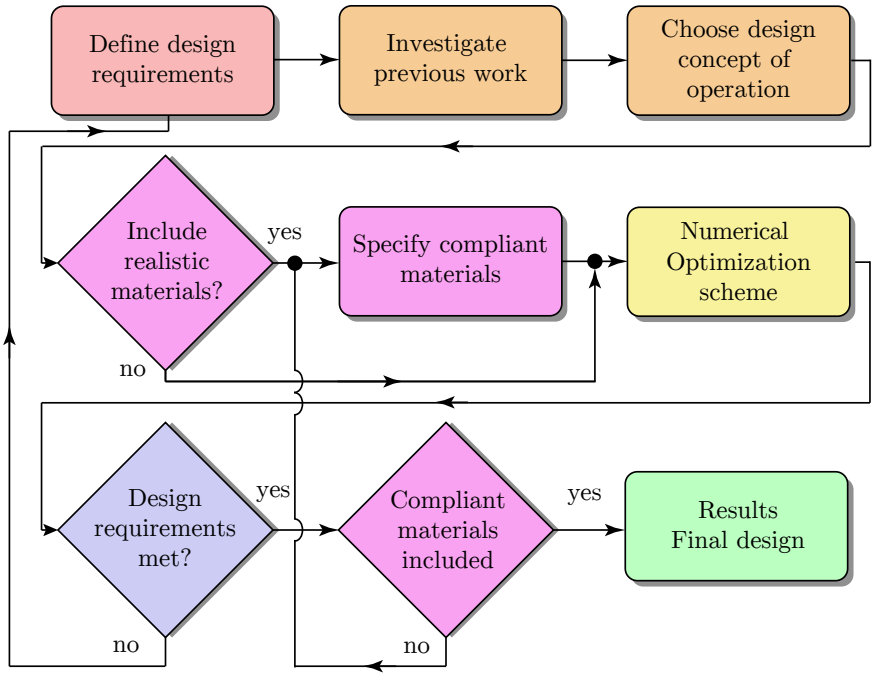

Figure 35: Flow chart for designing functional structures.

a consequence, this extra step in the design process implies that a re-design of the structure needs to be carried out when the compliant materials are added to the structure. Specifications from the application of the functional structure commonly affect the choice of materials at this point of the design process [73].

Next, the structure is optimized in numerical software. The organization of this particular step is described in detail in Section 5.2. After thorough optimizations, typically involving hundreds or thousands of design iterations, the functional structure is evaluated with respect to the initial desired performance properties. If the structure is not able to fulfill these requirements, the whole process is repeated. Either the design requirements are redefined, or a different design concept is utilized.

5.2 Optimization of functional structures

When a design candidate has been identified, according to the procedure in the previous section, it is optimized in a number of steps. A penalty function F is introduced and minimized to achieve desired performance properties of the functional structure. This function is designed to take all relevant performance properties into account by some kind of product or summation over the scatter-

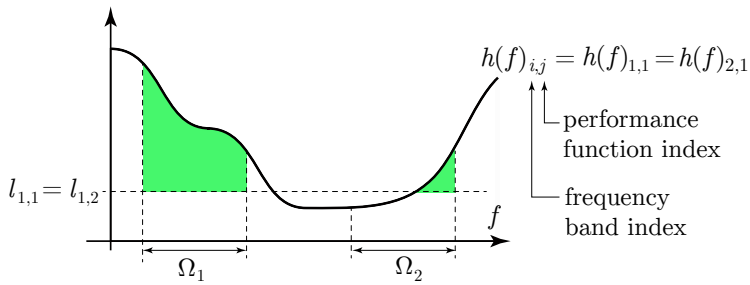

Figure 36: A visual example of the penalty function F in (5.1) here corresponding to the green area in the illustration. The performance function $h_{i,j} = h_{1,1} = h_{2,1}$ is integrated over two separate frequency bands with respect to $p = 1$ and a reference level defined by $l_{i,j} = l_{1,1} = l_{2,1}$.

ing measures of interest, represented by a number of performance functions $h_{i,j}$ defined for $j = 1, 2, ..., N$ scattering measures in $i = 1, ..., M$ separate frequency bands. The performance functions are positive, real valued, and can be represented in either linear scale or in dB. They can be formulated either in linear or circular polarizations, and are compared to specified performance threshold levels $l_{i,j}$. The general form of the total penalty function is

$$F = \sum_{i=1}^{M} \sum_{j=1}^{N} \frac{a_{i,j}}{\Delta\Omega_i} \int_{\Omega_i} |g_{i,j}|^p \cdot \mathrm{H}(g_{i,j}) \, \mathrm{d}f, \tag{5.1}$$

with

$$g_{i,j} = h_{i,j}(f) - l_{i,j}, \tag{5.2}$$

where $h_{i,j}$ are the performance functions of interest, $l_{i,j}$ are the thresholds under which the integrands are zero, Ω_i are the regions of integration specified by the frequency bands $i = 1, 2, ..., M$, $a_{i,j}$ are the weights of the performance functions and H is the Heaviside (or unit step) function. The functions $g_{i,j}$ are raised to the power of p, where p is a positive number affecting the penalization of the performance functions. A visual example of a penalty function F is presented in Figure 36.

If the optimization problem of interest is convex a single optimum solution can be found [23]. Unfortunately, most optimization problems related to functional structures are non-convex, with multiple local minima in the parameter space. To this end other non-covex optimization algorithms are utilized in a number of steps [18]. In Figure 37 a common optimization procedure for functional structures is presented. If the functional structure consists of many design parameters it can be useful to utilize a circuit model for fast optimization, where thousands of evaluations are carried out in a number of seconds or minutes. When the optimization requirements are met, the structure is implemented in a full wave

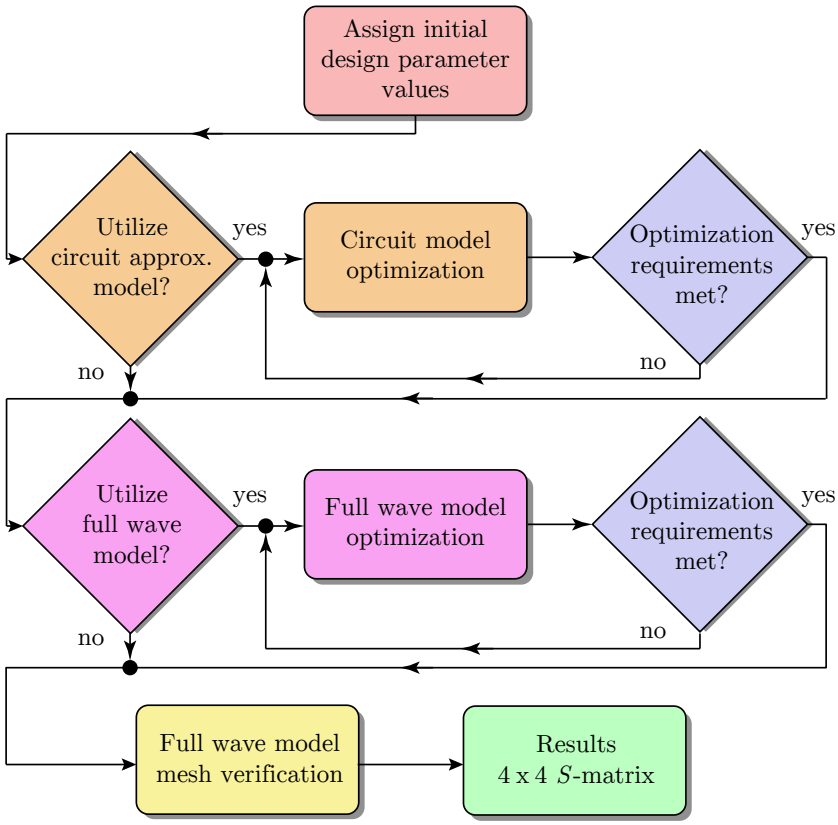

Figure 37: Optimization flow chart for functional structures.

simulation model for further optimization. Often a discrepancy is observed between the scattering properties of the approximate circuit model and full wave simulations. This discrepancy can be caused by higher order mode excitation not accounted for in the circuit model, approximations in the variational expressions used to derive the circuit parameters, or other factors. Nevertheless, the circuit model optimization often results in an adequate starting point for full wave optimization.

When designing complex structures, which can prove difficult to optimize using a circuit model, the full wave optimization procedure is broken down into several steps. For example, in Computer System Technology Microwave Studio (CST MWS) a number of built-in optimization algorithms such as particle swarm, genetic algorithms, Nelder-Mead simplex algorithm and trust region framework algorithm can be used [172]. An efficient approach is to start with an algorithm with a very wide search area in the multidimensional parameter space under study. When a parameter region has been identified that yields promising

results, which can take hundreds to thousands of iterations, a more narrow optimization algorithm such as the Nelder-Mead simplex or trust region framework can be utilized. Relatively coarse mesh settings are utilized to reduce the time required for each design evaluation. If the built-in optimization algorithms of the commercial software are not sufficient, external optimization schemes can be arranged. In this setting, only the simulations are carried out in the computational software. Meanwhile, the evaluation of the design performance with respect to a penalty function and the generation of updated design parameters are carried out externally, for example in matrix laboratory (MATLAB®).

Finally, when the optimization requirements of the full wave model are met, the structure is simulated once more using a much refined mesh to verify that mesh convergence is achieved by the optimized design. As was mentioned in Section 5.1, many functional structures consist of single or multiple sheets of conducting elements, and use dielectric materials mainly for low permittivity spacers and thin substrates to give physical stability to the design. In these cases, it can be fruitful to initially exclude any dielectric and magnetic materials and make a simplified concept design, see Figure 35. Later, at the end of the design process, when the desired performance properties have been achieved the dielectric materials are added and the structure is re-optimized and fine tuned.

6 Experimental characterization of functional structures

6.1 Characterization of electromagnetic material properties

The responses of a material to electromagnetic fields are determined in essence by three constitutive parameters: permittivity ϵ, permeability μ and conductivity σ. The methods used to determine these parameters generally fall into the categories of resonant methods and non-resonant methods [31]. Resonant methods are based on placing a sample inside a cavity and observing the change in resonance frequency. The sample could also constitute a key part of the resonator itself. These methods are primarily used to characterize the electromagnetic properties of materials at a single frequency or a number of discrete frequencies [31]. For this reason, resonant methods have not been used in this work. Non-resonant methods on the other hand are used to acquire electromagnetic properties over a frequency range from the impedance and wave velocities in a material. These parameters can be evaluated by investigating the reflection and transmission properties of a material.

Two methods based on reflection only are open-circuited reflection and short-circuited reflection. In these methods, a sample is placed next to the aperture of an open- or short-circuited waveguide probe arrangement and the reflection of

Figure 38: Experimental setups for characterizing a planar DUT. To the left is a rectangular waveguide setup and to the right is a free space setup.

incident signals from the sample is evaluated. The information acquired can be used to evaluate one, but not all of the material parameters. Reflection methods are well suited for characterizing conductive materials [31]. In methods based on both reflection and transmission, the material is placed in between two ports of a waveguide, and the reflected and transmitted signals are acquired. The waveguide of these methods could consist of for example a coaxial waveguide, rectangular waveguide or circular waveguide. This type of method is well suited for penetrable materials where some transmission of incident signals through the sample occurs.

Experimental characterization using non-resonant methods is typically carried out using a VNA. This instrument treats the experimental setup as an electrical network. It generates an excitation which is incident at the sample and collects the transmitted and reflected signals in the form of network parameters [136]. A VNA typically operates in the frequency domain, transmitting signals of one frequency at a time using a small carrier bandwidth. By stepping through the desired frequency range one point at a time, the scattering parameters as functions of frequency are evaluated. For our purposes, this instrument is used for measuring the transmission and reflection coefficients of a device under test (DUT).

6.2 Characterization of functional structures

When characterizing functional structures, the main parameters of interest are in most cases not the material parameters ϵ, μ, σ but rather the reflection, transmission and absorption properties of the structure. Since the material parameters are typically extracted from the reflection and transmission properties of a material, the same type of measurement methods can be utilized for functional structures as for electromagnetic material characterization. The two most commonly used

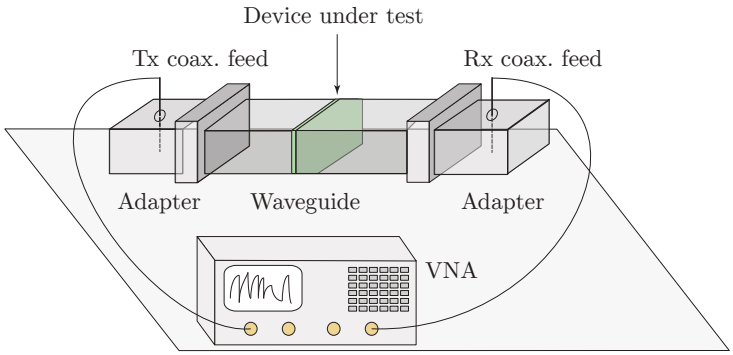

Figure 39: Waveguide setup for experimental characterization of a planar device under test.

methods for characterizing functional structures are presented in Figure 38, where to the left a rectangular waveguide setup is presented and to the right a free space setup is presented. The two methods both have their strengths and weaknesses, discussed further below.

A concept sketch of a waveguide measurement setup is presented in Figure 39. The device under test is inserted between two waveguide sections connected to a VNA through coaxial to waveguide adapters. Some advantages associated with using a waveguide setup are that a controlled environment with high signal strength is achieved, and that the location of the DUT can be determined to very high accuracy. This information is of importance to achieve an accurate calibration when extracting material parameters of a DUT through for example the Nicolson-Ross-Weir algorithm [129]. Another advantage associated with a waveguide setup is that the size of the sample is relatively small in comparison to a free space setup. Due to the PEC boundary conditions present at the sides of a waveguide, the periodicity of the DUT should match the size of the waveguide. The elements of the sample should be symmetric order for the corresponding free space periodic structure to be reconstructed correctly by the imaging of the sample with respect to the PEC boundary conditions. If the sample does not match the waveguide, an adapter section of different cross section can be used. A potential problem with characterizing functional structures in a waveguide system is that small irregularities in the sample or the waveguide will, due to the PEC boundary conditions inside the structure, be present in each element of the reconstructed periodic structure. This can cause amplification of the errors associated with these irregularities.

A sketch of a free space measurement setup is presented in Figure 40. Here the DUT is placed in between a transmitting (Tx) and a receiving antenna (Rx). If single polarized antennas are used the relative orientation of the antennas determine if the co- or cross polarization scattering coefficients are evaluated. If

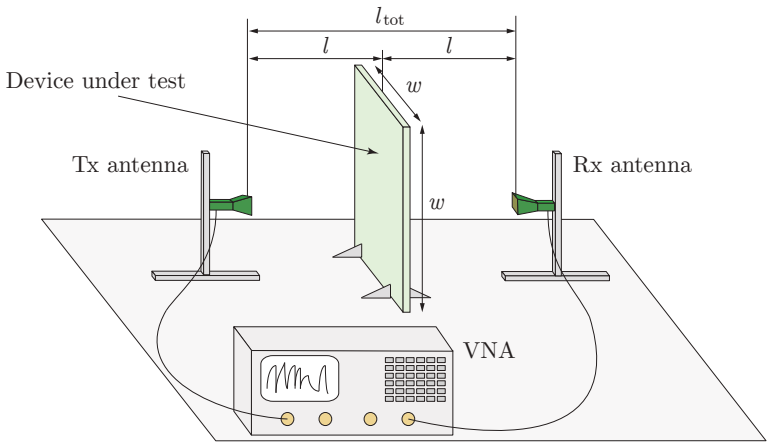

Figure 40: Free space setup for experimental characterization of a planar device under test.

the co-polarized reflection is to be evaluated the reflected signal is received by the transmitting antenna. But if the cross polarized reflection is to be evaluated both antennas are placed on one side of the DUT and the reflected signal is received by the second antenna. If dual polarized antennas are utilized, cross polarized signals can be received by the transmitting antenna and no rearrangement of the system is needed. This flexibility of dual polarized antennas comes at a price of reduced XPD with respect to single polarized antennas. The distance between the antennas is chosen such that the DUT is outside of the reactive near field of the antennas, but not so far away such that the edges of the DUT are illuminated by the main beam of the antennas. One way to avoid edge illumination is to use dielectric lenses to focus the signals at the center of the DUT and achieve plane wave propagation [155]. These lenses are typically many wavelengths in size and can become large at X-band and lower frequencies.

Some advantages associated with free space measurements are: measurements are non-destructive and contactless, samples do not have to be machined to fit a specific aperture, and problems arising from higher order mode excitation from uneven samples are not as severe as in waveguide measurements [31]. The last property is a consequence of the fact that in a free space setup, an area of the DUT is illuminated which means that local defects and variation can, to some extent, average out in the total scattering from the DUT. On the other hand, unwanted curvature of the sample can be a source of error in a free space setup since relatively large samples are used. Also, the sample has to be aligned with respect to incident signals. This is typically done using some kind of sample holder or fixture.

In this work, free space setups similar to that in Figure 38 have been used for characterization of CPSSs, see Papers III–V. Reasons for using this type of setup

are: the flexibility of being able to rotate the orientation of the transmitting and receiving antennas with respect to the DUT, and to have the possibility of evaluating the transmission and reflection at oblique angles of incidence by simply turning the sample or moving the antennas.

6.3 Post processing of experimental data

A common problem with microwave measurements is that the received signals contain not only the desired boresight scattering information, but also multipath scattering components from the surroundings, resulting in a noisy signal. By applying electromagnetic absorbers as in the free space setup in Figure 38 the undesired scattering can be reduced. An additional way to mitigate this problem is to apply an inverse fast Fourier transform (FFT) to the measured data and observe the results in the time domain. The time domain resolution δt of a set of measurement data is related to the measured frequency bandwidth as

$$\delta t = \frac{1}{\Delta f}, \tag{6.1}$$

where Δf is the frequency bandwidth of the measurements. Provided that the spatial separation between the DUT and the sources of the undesired scattering is large enough these separate signals can be resolved and separated in the time domain. A window function can then be applied to filter the signals [30]. This method is commonly referred to as time gating [138]. A consequence of (6.1) is that time gating can not be applied to single frequency measurement data. A flexible and useful window function used heavily in Papers III–V and IX is the cosine-tapered Tukey window, defined as

$$w(x) = \begin{cases} \frac{1}{2}\left(1 + \cos\left(\frac{2\pi}{r}(x - r/2)\right)\right), & 0 \le x < r/2 \\ 1, & r/2 \le x < 1 - r/2 \\ \frac{1}{2}\left(1 + \cos\left(\frac{2\pi}{r}(x - 1 + r/2)\right)\right), & 1 - r/2 \le x \le 1 \end{cases} \tag{6.2}$$

where x is a normalized vector and the parameter r is the ratio of the cosine-tapered section length to the entire window length with $0 \le r \le 1$. For $r = 0$ a rectangular window is achieved and for $r = 1$ a Hann window is returned, which is simply a vertically shifted cosine window

$$w(x) = \frac{1}{2}\Big(1 - \cos\left(2\pi x\right)\Big). \tag{6.3}$$

In Figure 41 the vertically co-polarized transmission coefficient S_{21}^{YY} of an empty free space setup at $\mathrm{K_u}$-band, as in Figure 38, is presented. To the left the signal is presented in the time domain with a Tukey window function. Here the normalized

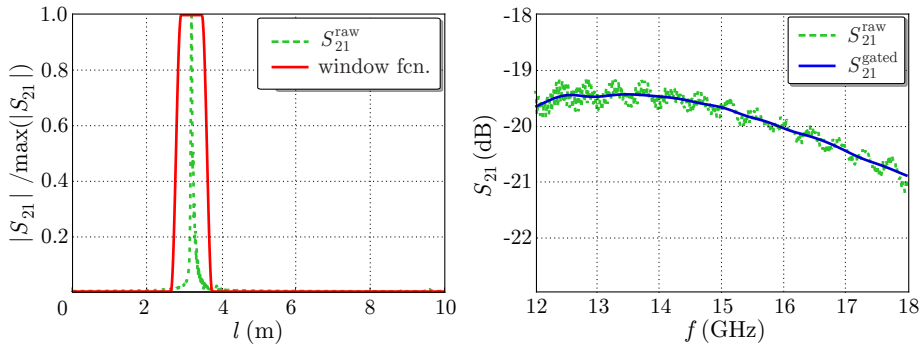

Figure 41: Experimental results of the co-polarized transmission coefficient S_{21}^{YY} of an empty free space setup. To the left the signal is presented in the time domain with a Tukey window function, where the normalized magnitude of the signal is plotted as a function of distance. To the right the frequency domain signals are presented before and after applying time gating.

magnitude of the signal is plotted as a function of distance. To the right the frequency domain signals are presented before and after applying time gating with a Tukey window with $r = 0.5$. In these results a significant improvement in signal quality can be seen after the time gating has been applied.

In order to acquire the relative power transmitted and reflected of a DUT, measured S-parameters are normalized with a reference measurement according to

$$S_{ij}^{kl,\text{rel}} = \frac{S_{ij}^{kl,\text{DUT}}}{S_{ij}^{kl,\text{ref}}}, \tag{6.4}$$

where $k, l = \text{X}, \text{Y}$ are the polarization state of the received and transmitted signals and $i, j = 1, 2$ describe which antenna is receiving and transmitting the signals. In transmission, a suitable reference corresponds to measuring the transmission coefficient of the empty setup. In reflection, a relevant reference scenario is the reflection coefficient of a conducting test panel of the same size and shape as the DUT. The co-polarized transmission coefficient of a split ring band stop FSS is presented in Figure 42. The period between the elements is 3.3 mm, the thickness of the split rings and the width of the gap 0.3 mm, and the structure is printed on an FR4 substrate with thickness 0.36 mm. The structure was optimized to have maximum reflection for vertically polarized signals at $f = 15$ GHz. In Figure 42 it can be seen that after applying the time gating and normalization with a reference measurement the experimental curve is almost exactly on top of the simulated curve from CST MWS.

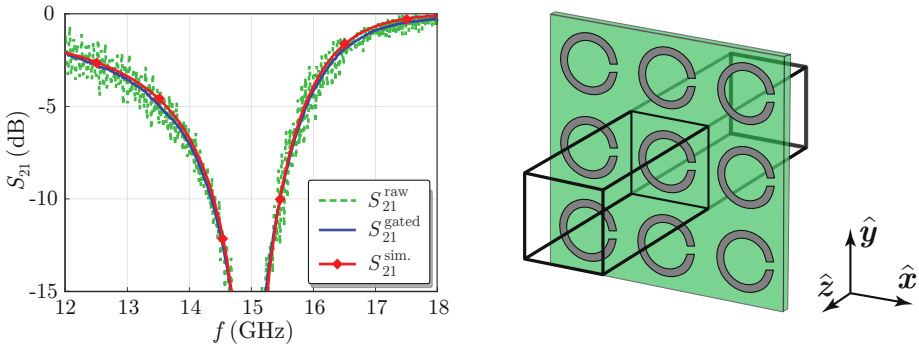

Figure 42: Simulated and measured transmission coefficient of a split ring band stop FSS, where the green curve is measured raw data, the blue curve represents measured, time gated data and the red curve is simulated data.

7 Inverse scattering problems and compressive sensing

In most problems discussed up to this point, focus has been on calculating the scattered fields from different structures given that the geometry and material parameters of the scatterer, as well as the incident fields, are known. This is referred to as a direct scattering problem. The opposite problem is also of great interest, where the scattered fields are known and the sources of these fields are to be found or characterized. This type of problem is referred to as an inverse scattering problem [92]. Applications of inverse scattering problems can be found in a number of areas of technology. Some examples are: in tomography to image and diagnose human organs without surgery [10], in geophysics for oil- and ore prospecting [85], and in non-destructive testing of materials [89]. In electromagnetic theory, inverse problems can be divided into two groups: search of spatial and time-dependent distributions of field sources, and search of shapes and structures of bodies affecting electromagnetic field distribution [89]. The first group include antenna synthesis, where a desired radiation pattern is known and the currents needed to generate such pattern are found. The second group include material characterization and security scanning, where material characteristics of observable objects, or information of hidden objects, are extracted from the scattered fields.

In general, inverse scattering problems have a tendency to be more complex than direct scattering problems. This is a consequence of the fact that in most inverse scattering problems the mapping between the scattered and incident fields is non-linear, while a direct scattering problem, including linear materials, can be modeled using a linear mapping. Depending on the formulation of the specific inverse problem, a number of techniques and approximations can be used to

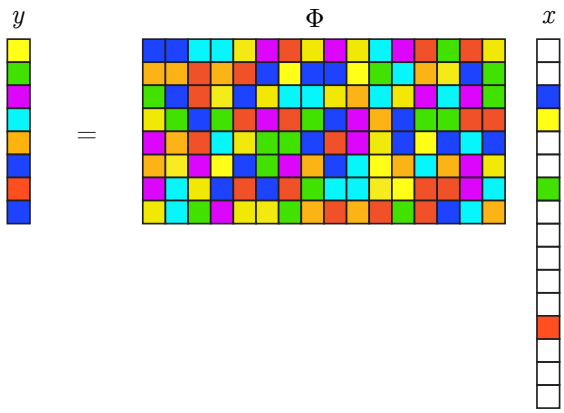

Figure 43: Matrix relation where an unknown sparse source signal x is determined from a known sampled signal y using the linear mapping Φ.

simplify the problem and find a solution. For example, in Paper IX hidden defects are located in planar composite panels by using field reconstruction in the Fourier domain, commonly referred to in literature as time reversal, digital beam forming (DBF), aperture synthesis, back propagation, back projection or migration technique [169, 170].

An alternative reconstruction method is to formulate the relation between the measured field and unknown source currents as a linear mapping, and utilize a minimization with respect to some norm. A technique based on this theory that is used in Paper IX is compressive sensing (also referred to as CS) [66]. In this method, the strategy is to model the mapping between the data and unknowns by a rectangular matrix, and where the unknown vector has only a few non-zero entries, as in Figure 43. Consequently, the detection of small-scale defects and inhomogeneities, which in practice should result in few non-zero entries, are applications suitable for CS techniques. Furthermore, the theory behind CS states that, if adapted to a sparse problem, the sought after solution can be recovered using far fewer samples than what is classically required by the Nyquist theorem [114], allowing for a potentially reduced measurement time as the number of required data samples decreases. The potential of CS has resulted in fast development in a variety of applications related to electromagnetics [114] such as: array synthesis [130], antenna diagnostics [118], direction-of-arrival estimation [29] and ground penetrating radar [64].

8 Conclusions

In this thesis, functional structures for electromagnetic waves have been designed, characterized and evaluated. A physical understanding of the interaction between

electromagnetic waves and different structures has been achieved by the use of electromagnetic scattering theory. This knowledge was used to design and optimize structures with respect to predefined performance requirements, to experimentally and numerically evaluate the scattering properties of said structures, and to find unwanted defects in composite materials. The relatively wide scope of this thesis is a consequence of the power of the underlying theory of electromagnetic scattering. Novel solutions to problems in different applications have been found by understanding the physical interactions of the fields and objects, as well as which approximations that could be utilized depending on the specific problem.

Circular polarization selective structures for satellite communication applications have been designed and characterized numerically and experimentally in Papers I–V. Three novel designs have been presented, all of which provide unique performance properties with respect to previous designs. The first structure displays improved stability with respect to incidence variations, the second structure provides more than double the frequency bandwidth of previous designs, and the third structure operates in dual frequency bands. An accurate method to experimentally characterize said structures has been presented, together with a data post processing scheme. In Paper VI, the electromagnetic scattering properties of a triaxial weave functioning as a reflector antenna surface have been evaluated using numerical simulations and approximation models. This information was used in collaboration with a parallel acoustics study to define design guidelines from a multiphysics perspective.

Radiation-absorbing materials for scattering reduction applications have been evaluated and utilized for RCS minimization. The impact of curvature on the performance of these structures has been evaluated in Paper VII using an analytical framework for canonical scatterers. In Paper VIII, two fast computation methods for axially symmetric scatterers have been presented. These methods were used to evaluate a number of different radiation-absorbing materials in different scenarios, and the type of problems suitable for using these methods have been identified.

Finally, different techniques have been utilized for defect detection in composite materials in Paper IX. Information in experimentally acquired scattered fields is used to find these defects, and by implementing compressive sensing techniques sub-wavelength resolution is achieved in the processed data. The key point of the method is identifying that the scattering from the defects can be formulated as a sparse inverse scattering problem in some basis.

9 Research outlook and future work

The mathematical framework modeling the interaction of electromagnetic waves with obstacles is a powerful tool for designing new functional structures. In fact, a significant amount of novel functional structures and antennas presented today are generated using mathematical calculations or theoretical intuition stemming

from the underlying equations. As technology advances at an ever increasing pace, the demand for functional structures in communications and scattering reduction applications is growing rapidly. Furthermore, advances in computational resources imply new possibilities in design and synthesis of functional structures for electromagnetic waves, as well as antennas.

A number of possibilities and ideas for continuing the work presented in this thesis have materialized during the four years I have spent on this work. The combination of circuit models for fast optimization and full wave optimization models with carefully assigned penalty functions can be used to create novel interesting structures with desired scattering properties. This is especially useful in the development of novel FSS and CPSS designs. Another point well worth investigating is whether similar performance levels of those presented in Papers III and V can be achieved using lower numbers of layers in the designs. To reduce the design complexity is a key factor in the design of functional structures for specific application purposes. Furthermore, the experimental procedure presented in Paper IV can be used for accurate characterization of future designs.

Regarding the multiphysics analysis of the triaxial weave presented in Paper VI, a continuation suggested by the contractor RUAG Space is to evaluate the electromagnetic and acoustic implications of utilizing two stacked triaxial weaves with a relative rotation. This was investigated from an electromagnetic perspective in [156, 157] where it was concluded that this type of arrangement would result in a global quasi-periodicity for certain relative orientations. Complemented by a similar acoustics study, this work could be used for further multiphysics investigations.

The work presented in Papers VII–VIII have resulted in a wide range of simulation tools for designing and characterizing RAMs. The main strength of these tools is that application oriented geometries, such as axially symmetric scatterers, can be simulated with RAM coatings for RCS minimization. Also, the speed of the PO solver implies that a great number of scenarios can be evaluated in short periods of time. An additional way to further verify the accuracy of the presented methods is to manufacture prototypes of some scatterers and perform experimental characterizations. A continuation of this work includes designing novel RAMs using the presented methods, as well as characterizing and simulating the scattering from different objects coated with absorbers.

Finally, the experimental setup and data post processing for defect detection in composite panels, presented in Paper IX could be further improved. The CS technique that is utilized to improve the dynamics range of the setup is currently operating on single frequency data. However, experimental data have been acquired over a wide bandwidth in order to be able to utilize time gating in the post processing. If all this information from different frequencies could be evaluated simultaneously in the CS algorithm the performance of the setup could be further improved in terms of both speed and dynamic range.

References

[1] S. M. A. M. H. Abadi and N. Behdad. Inductively-coupled miniaturized-element frequency selective surfaces with narrowband, high-order bandpass responses. *IEEE Trans. Antennas Propag.*, **63**(11), pp. 4766–4774, 2015.

[2] S. M. A. M. H. Abadi and N. Behdad. A broadband, circular-polarization selective surface. *Journal of Applied Physics*, **119**(24), pp. 244901, 2016.

[3] S. M. A. M. H. Abadi and N. Behdad. Wideband linear-to-circular polarization converters based on miniaturized-element frequency selective surfaces. *IEEE Trans. Antennas Propag.*, **64**(2), pp. 525–534, 2016.

[4] S. M. A. M. H. Abadi, M. Li, and N. Behdad. Harmonic-suppressed miniaturized-element frequency selective surfaces with higher order bandpass responses. *IEEE Trans. Antennas Propag.*, **62**(5), pp. 2562–2571, 2014.

[5] S. A. Akhmanov and S. Y. Nikitin. *Physical Optics*. Clarendon Press, 1997.

[6] M. Al-Joumayly and N. Behdad. A new technique for design of low-profile, second-order, bandpass frequency selective surfaces. *IEEE Trans. Antennas Propag.*, **57**(2), pp. 452–459, 2009.

[7] M. A. Al-Joumayly and N. Behdad. A generalized method for synthesizing low-profile, band-pass frequency selective surfaces with non-resonant constituting elements. *IEEE Trans. Antennas Propag.*, **58**(12), pp. 4033–4041, 2010.

[8] M. A. Al-Joumayly and N. Behdad. Low-profile, highly-selective, dual-band frequency selective surfaces with closely spaced bands of operation. *IEEE Trans. Antennas Propag.*, **58**(12), pp. 4042–4050, 2010.

[9] M. Albani, P. Balling, L. Datashvili, G. Gerini, P. Ingvarson, K. Pontoppidan, M. Sabbadini, D. Sjöberg, S. Skokic, and G. Vecchi. Concepts for polarising sheets & "dual-gridded" reflectors for circular polarisation. In *ICECom Proceedings*, pp. 1–4, 2010.

[10] R. Aster, B. Borchers, and C. Thurber. *Parameter Estimation and Inverse Problems*. Academic Press, New York, NY, 2005.

[11] S. N. Azemi, K. Ghorbani, and W. S. Rowe. 3D frequency selective surfaces. *Progress in Electromagnetics Research C*, **29**, pp. 191–203, 2012.

[12] R. Baraniuk and P. Steeghs. Compressive radar imaging. In *2007 IEEE Radar Conference*, pp. 128–133, April 2007.

[13] M. Baunge, H. Ekström, P. Ingvarson, and M. Petersson. A new concept for dual gridded reflectors. In *Proceedings of the fourth European Conference on Antennas and Propagation (EuCAP)*, pp. 1–5. IEEE, 2010.

[14] N. Behdad. A second-order band-pass frequency selective surface using nonresonant subwavelength periodic structures. *Microwave and Optical Technology Letters*, **50**(6), pp. 1639–1643, 2008.

[15] N. Behdad, M. Al-Joumayly, and M. Salehi. A low-profile third-order band-pass frequency selective surface. *IEEE Trans. Antennas Propag.*, **57**(2), pp. 460–466, 2009.

[16] N. Behdad and M. A. Al-Joumayly. A generalized synthesis procedure for low-profile, frequency selective surfaces with odd-order bandpass responses. *IEEE Trans. Antennas Propag.*, **58**(7), pp. 2460–2464, 2010.

[17] M. Bertolotti. *The History of the Laser*. CRC press, 2004.

[18] D. Bertsimas and J. N. Tsitsiklis. *Introduction to Linear Optimization*, volume 6. Athena Scientific Belmont, MA, 1997.

[19] A. Bondeson, T. Rylander, and P. Ingelström. *Computational Electromagnetics*. Springer-Verlag, Berlin, 2005.

[20] M. Born and E. Wolf. *Principles of Optics*. Cambridge University Press, Cambridge, seventh edition, 1999.

[21] M. Bosiljevac, M. Casaletti, F. Caminita, Z. Sipus, and S. Maci. Non-uniform metasurface Luneburg lens antenna design. *IEEE Trans. Antennas Propag.*, **60**(9), pp. 4065–4073, 2012.

[22] J. J. Bowman, T. B. Senior, and P. L. Uslenghi. Electromagnetic and acoustic scattering by simple shapes. Technical report, Michigan Univ Ann Arbor Radiation Lab, 1970.

[23] S. P. Boyd and L. Vandenberghe. *Convex Optimization*. Cambridge Univ. Pr., 2004.

[24] W. Cai and V. Shalaev. *Optical Metamaterials: Fundamentals and Applications*. Springer Science & Business Media, 2009.

[25] M. Caiazzo, S. Maci, and N. Engheta. A metamaterial surface for compact cavity resonators. *IEEE Antennas and Wireless Propagation Letters*, **3**(1), pp. 261–264, 2004.

[26] C. Caloz and T. Itoh. *Electromagnetic Metamaterials: Transmission Line Theory and Microwave Applications*. John Wiley & Sons, 2005.

[27] W. A. Campbell Jr, R. S. Marriott, and J. J. Park. Outgassing data for selecting spacecraft materials. Technical Report NASA-RP-1124, NASA, Washington DC 20546-0001, 1984.

[28] F. Capolino, editor. *Theory and Phenomena of Metamaterials.* CRC Press, 2009.

[29] M. Carlin, P. Rocca, G. Oliveri, F. Viani, and A. Massa. Directions-of-arrival estimation through bayesian compressive sensing strategies. *IEEE Trans. Antennas Propag.*, **61**(7), pp. 3828–3838, July 2013.

[30] C. Cattani. *Wavelet and Wave Analysis as applied to Materials with Micro or Nanostructure*, volume 74. World Scientific, 2007.

[31] L. F. Chen, C. K. Ong, C. P. Neo, V. V. Varadan, and V. K. Varadan. *Microwave electronics: Measurement and materials characterisation.* John Wiley & Sons, New York, NY, 2004.

[32] W. C. Chew, M. S. Tong, and B. Hu. *Integral equation methods for electromagnetic and elastic waves*, volume 12. Morgan & Claypool, 2008.

[33] D. Colton and R. Kress. *Inverse Acoustic and Electromagnetic Scattering Theory.* Springer-Verlag, Berlin, 1992.

[34] F. Costa, A. Monorchio, and G. Manara. Analysis and design of ultra thin electromagnetic absorbers comprising resistively loaded high impedance surfaces. *IEEE Trans. Antennas Propag.*, **58**(5), pp. 1551–1558, May 2010.

[35] S. Costanzo. Reflectarray antennas: analysis and synthesis techniques. *International Journal of Antennas and Propagation*, 2012.

[36] O. Darrigol. *A history of optics from Greek antiquity to the nineteenth century.* OUP Oxford, 2012.

[37] D. B. Davidson. *Computational Electromagnetics for RF and Microwave Engineering.* Cambridge University Press, 2005.

[38] A. Demenko, J. K. Sykulski, and R. Wojciechowski. On the equivalence of finite element and finite integration formulations. *IEEE Transactions on Magnetics*, **46**(8), pp. 3169–3172, 2010.

[39] F. Dincer, M. Karaaslan, E. Unal, K. Delihacioglu, and C. Sabah. Design of polarization and incident angle insensitive dual-band metamaterial absorber based on isotropic resonators. *Progress In Electromagnetics Research*, **144**, pp. 123–132, 2014.

[40] Y. Dong and T. Itoh. Metamaterial-based antennas. *Proceedings of the IEEE*, **100**(7), pp. 2271–2285, July 2012.

[41] E. Doumanis, G. Goussetis, R. Cahill, V. Fusco, and H. Legay. Dual frequency polarizing surfaces: For Ka-band applications. In *Antennas and Propagation (EUCAP), 2012 6th European Conference on*, pp. 2206–2208. IEEE, 2012.

[42] E. Doumanis, G. Goussetis, J.-L. Gómez-Tornero, R. Cahill, and V. Fusco. Single layer anisotropic impedance surface for linear to circular polarization conversion in reflect mode. In *Antennas and Propagation (EUCAP), Proceedings of the 5th European Conference on*, pp. 1666–1670. IEEE, 2011.

[43] E. Doumanis, G. Goussetis, J. L. Gomez-Tornero, R. Cahill, and V. Fusco. Anisotropic impedance surfaces for linear to circular polarization conversion. *IEEE Trans. Antennas Propag.*, **60**(1), pp. 212–219, 2012.

[44] A. Einstein. Über einen die Erzeugung und Verwandlung des Lichtes betreffenden heuristischen Gesichtspunkt. *Annalen der Physik*, **322**(6), pp. 132–148, 1905.

[45] N. Engheta. Thin absorbing screens using metamaterial surfaces. In *Antennas and Propagation Society International Symposium, 2002*, volume 2, pp. 392–395. IEEE, 2002.

[46] N. Engheta and R. W. Ziolkowski. *Metamaterials: Physics and Engineering Explorations*. John Wiley & Sons, 2006.

[47] J. Epis. Broadband antenna polarizer, August 21 1973. US Patent 3,754,271.

[48] A. Ericsson, J. Lundgren, and D. Sjöberg. Experimental characterization of circular polarization selective structures using linearly single-polarized antennas. *IEEE Trans. Antennas Propag.*, **65**(8), pp. 4239–4249, 2017.

[49] A. Ericsson and D. Sjöberg. A performance study of circular polarization selective structures. In *Proceedings of the 9th European Conference on Antennas and Propagation (EuCAP)*. IEEE, 2015.

[50] A. Ericsson and D. Sjöberg. Design and analysis of a multilayer meander line circular polarization selective structure. *IEEE Trans. Antennas Propag.*, **65**(8), pp. 4089–4101, 2017.

[51] A. Ericsson and D. Sjöberg. Design and analysis of a multilayer meander line circular polarization selective structure. Technical Report LUTEDX/(TEAT-7250)/1–26/(2017), Lund University, Department of Electrical and Information Technology, P.O. Box 118, S-221 00 Lund, Sweden, 2017.

[52] A. Ericsson, D. Sjöberg, C. Larsson, and T. Martin. Approximative computation methods for monostatic scattering from axially symmetric objects. Technical Report LUTEDX/(TEAT-7256)/1–36/(2017), Lund University, Department of Electrical and Information Technology, P.O. Box 118, S-221 00 Lund, Sweden, 2017.

[53] A. Ericsson, D. Sjöberg, C. Larsson, and T. Martin. Scattering from a multilayered sphere - applications to electromagnetic absorbers on double curved surfaces. Technical Report LUTEDX/(TEAT-7249)/1–32/(2017), Lund University, Department of Electrical and Information Technology, P.O. Box 118, S-221 00 Lund, Sweden, 2017.

[54] A. Ericsson, R. Rumpler, D. Sjöberg, P. Göransson, N. Wellander, and J. Johansson. A combined electromagnetic and acoustic analysis of a triaxial carbon fiber weave for reflector antenna applications. *Aerospace Science and Technology*, **58**, pp. 401–417, 2016.

[55] A. Ericsson and D. Sjöberg. A resonant circular polarization selective structure of closely spaced wire helices. *Radio Science*, **50**(8), pp. 804–812, 2015. 2014RS005641.

[56] A. Ericsson, D. Sjöberg, C. Larsson, and T. Martin. Scattering for doubly curved functional surfaces and corresponding planar designs. In *Antennas and Propagation (EuCAP), 2016 10th European Conference on*, pp. 1–2. IEEE, 2016.

[57] L. C. Evans. *Partial Differential Equations*. American Mathematical Society, Providence, RI, 1998.

[58] G. Floquet. Sur les équations différentielles linéaries à coefficients périodique. *Ann. École Norm. Sup.*, **12**, pp. 47–88, 1883.

[59] N. J. Fonseca and C. Mangenot. Low-profile polarizing surface with dual-band operation in orthogonal polarizations for broadband satellite applications. In *Antennas and Propagation (EuCAP), 2014 8th European Conference on*, pp. 471–475. IEEE, 2014.

[60] N. J. Fonseca and C. Mangenot. High-performance electrically thin dual-band polarizing reflective surface for broadband satellite applications. *IEEE Trans. Antennas Propag.*, **64**(2), pp. 640–649, 2016.

[61] V. Fusco and B. Nair. Circular polarisation selective surface characterisation and advanced applications. *IEE Proceedings Microwaves Antennas and Propagation*, **153**(3), pp. 247–252, 2006.

[62] S. Ghosh and K. V. Srivastava. An equivalent circuit model of FSS-based metamaterial absorber using coupled line theory. *IEEE Antennas and Wireless Propagation Letters*, **14**, pp. 511–514, 2015.

[63] L. Goldstone. Mm wave transmission polarizer. In *Antennas and Propagation Society International Symposium, 1979*, volume 17, pp. 606–609. IEEE, 1979.

[64] A. C. Gurbuz, J. H. McClellan, and W. R. Scott. A compressive sensing data acquisition and imaging method for stepped frequency GPRS. *IEEE Trans. Signal Process.*, **57**(7), pp. 2640–2650, 2009.

[65] M. Gustafsson and D. Sjöberg. Sum rules and physical bounds on passive metamaterials. *New Journal of Physics*, **12**, pp. 043046, 2010.

[66] J. Helander, A. Ericsson, M. Gustafsson, T. Martin, D. Sjöberg, and C. Larsson. Imaging using compressive sensing techniques for planar non-destructive testing at 60 GHz. Technical Report LUTEDX/(TEAT-7246)/1–17/(2017), Lund University, Department of Electrical and Information Technology, P.O. Box 118, S-221 00 Lund, Sweden, 2017.

[67] H. Hertz. On electromagnetic waves in air and their reflection. *Heinrich Rudolph Hertz. Electrical waves*, pp. 124–136, 1888.

[68] C. L. Holloway, R. R. DeLyser, R. F. German, P. McKenna, and M. Kanda. Comparison of electromagnetic absorber used in anechoic and semi-anechoic chambers for emissions and immunity testing of digital devices. *IEEE Transactions on Electromagnetic Compatibility*, **39**(1), pp. 33–47, Feb 1997.

[69] C. L. Holloway, E. F. Kuester, J. A. Gordon, J. O'Hara, J. Booth, and D. R. Smith. An overview of the theory and applications of metasurfaces: The two-dimensional equivalents of metamaterials. *IEEE Antennas and Propagation Magazine*, **54**(2), pp. 10–35, 2012.

[70] J. Huang. *Reflectarray Antenna*. Wiley Online Library, 2007.

[71] C. Hülsmeyer. Verfahren, um metallische Gegenstände mittels elektrischer Wellen einem Beobachter zu melden, 30. April 1904. German patent: Reichspatent Nr. 165546.

[72] P. T. Hutchison and R. A. Swift. Results of the Telstar satellite space experiments. *The Bell System Technical Journal*, **42**(4), pp. 1475–1504, July 1963.

[73] W. A. Imbriale, S. S. Gao, and L. Boccia, editors. *Space Antenna Handbook*. Wiley, 2012.

[74] J. D. Jackson. *Classical Electrodynamics*. John Wiley & Sons, New York, NY, third edition, 1999.

[75] J. M. Jin. *Theory and Computation of Electromagnetic Fields*. Wiley Online Library, 2010.

[76] M. Joyal and J. Laurin. A cascaded circular-polarization-selective surface at K band. In *Antennas and Propagation (APSURSI), 2011 IEEE International Symposium on*, pp. 2657–2660. IEEE, 2011.

[77] M. Joyal and J. Laurin. Analysis and design of thin circular polarizers based on meander lines. *IEEE Trans. Antennas Propag.*, **60**(6), pp. 3007–3011, 2012.

[78] M. Joyal and J. Laurin. Design and analysis of a cascade circular-polarization-selective surface at K band. *IEEE Trans. Antennas Propag.*, **62**(6), pp. 3043–3052, 2014.

[79] M.-A. Joyal, J.-J. Laurin, M. Riel, and Y. Demers. A circularly polarized dual-gridded reflector prototype with a meander-line circular polarizer. In *Antennas and Propagation Society International Symposium (APSURSI), 2012 IEEE*, pp. 1–2. IEEE, 2012.

[80] M.-A. Joyal, M. Riel, Y. Demers, and J.-J. Laurin. A meander-line circular polarizer optimized for oblique incidence. *IEEE Trans. Antennas Propag.*, **63**(12), pp. 5391–5398, 2015.

[81] A. Kazemzadeh. Nonmagnetic ultra wideband absorber with optimal thickness. *IEEE Trans. Antennas Propag.*, **59**(1), pp. 135–140, 2011.

[82] A. Kazemzadeh and A. Karlsson. Capacitive circuit method for fast and efficient design of wideband radar absorber. *IEEE Trans. Antennas Propag.*, **57**(8), pp. 2307–2314, 2009.

[83] A. Kazemzadeh and A. Karlsson. Multilayered wideband absorbers for oblique angle of incidence. *IEEE Trans. Antennas Propag.*, **58**(11), pp. 3637–3646, 2010.

[84] A. Kazemzadeh and A. Karlsson. On the absorption mechanism of ultra thin absorbers. *IEEE Trans. Antennas Propag.*, **58**(10), pp. 3310–3315, 2010.

[85] A. Kiamanesh. In-situ tuned microwave oil extraction process, January 21 1992. US Patent 5,082,054.

[86] S. Kinoshita. *Structural Colors in the Realm of Nature*. World Scientific, 2008.

[87] H. Kirschbaum and S. Chen. A method of producing broad-band circular polarization employing an anisotropic dielectric. *IRE Transactions on Microwave Theory and Techniques*, **5**(3), pp. 199–203, 1957.

[88] E. F. Knott, J. F. Shaeffer, and M. T. Tuley. *Radar Cross Section*. SciTech Publishing Inc., 5601 N. Hawthorne Way, Raleigh, NC 27613, 2004.

[89] N. V. Korovkin, V. L. Chechurin, and M. Hayakawa. *Inverse Problems in Electric Circuits and Electromagnetics*. Springer Science & Business Media, 2007.

[90] D. J. Kozakoff. *Analysis of radome-enclosed antennas*. Artech House, 2010.

[91] G. Kristensson, S. Rikte, and A. Sihvola. Mixing formulas in the time domain. *J. Opt. Soc. Am. A*, **15**(5), pp. 1411–1422, May 1998.

[92] G. Kristensson. *Scattering of Electromagnetic Waves by Obstacles*. SciTech Publishing, an imprint of the IET, Edison, NJ, 2016.

[93] A. Lait. Broadband circular polarisers. *Marconi Review*, **32**(173), pp. 159, 1969.

[94] C. A. Leal-Sevillano, J. A. Ruiz-Cruz, J. R. Montejo-Garai, and J. M. Rebollar. Novel dual-band single circular polarization antenna feeding network for satellite communications. In *The 8th European Conference on Antennas and Propagation (EuCAP 2014)*, pp. 3265–3269, April 2014.

[95] D. Lerner. A wave polarization converter for circular polarization. *IEEE Trans. Antennas Propag.*, **13**(1), pp. 3–7, 1965.

[96] B. Li and Z. Shen. Wideband 3D frequency selective rasorber. *IEEE Trans. Antennas Propag.*, **62**(12), pp. 6536–6541, Dec 2014.

[97] B. Li and Z. Shen. Angular-stable and polarization-independent frequency selective structure with high selectivity. *Applied Physics Letters*, **103**(17), pp. 171607, 2013.

[98] B. Li and Z. Shen. Synthesis of quasi-elliptic bandpass frequency-selective surface using cascaded loop arrays. *IEEE Trans. Antennas Propag.*, **61**(6), pp. 3053–3059, 2013.

[99] B. Li and Z. Shen. Three-dimensional bandpass frequency-selective structures with multiple transmission zeros. *IEEE Trans. Microwave Theory Tech.*, **61**(10), pp. 3578–3589, 2013.

[100] B. Li and Z. Shen. Dual-band bandpass frequency-selective structures with arbitrary band ratios. *IEEE Trans. Antennas Propag.*, **62**(11), pp. 5504–5512, 2014.

[101] L. Li, Y. Yang, and C. Liang. A wide-angle polarization-insensitive ultrathin metamaterial absorber with three resonant modes. *Journal of Applied Physics*, **110**(6), pp. 063702, 2011.

[102] M. Li and N. Behdad. A third-order bandpass frequency selective surface with a tunable transmission null. *IEEE Trans. Antennas Propag.*, **60**(4), pp. 2109–2113, 2012.

[103] V. Liljegren. Evaluation of circular polarization selective surfaces for space applications. Master's thesis, Lund University, Department of Electrical and Information Technology, P.O. Box 118, SE-221 00 Lund, Sweden, 2013.

[104] D. Lockyer, J. Vardaxoglou, and R. Simpkin. Complementary frequency selective surfaces. *IEE Proceedings-Microwaves, Antennas and Propagation*, **147**(6), pp. 501–507, 2000.

[105] I. Lopez and J. Laurin. A circular polarization selective surface implemented on a flexible substrate. *IEEE Trans. Antennas Propag.*, **62**(7), pp. 3847–3852, 2014.

[106] I. Lopez and J.-J. Laurin. Alternative topologies of circular polarization selective surfaces based on modifications of the Pierrot cell. *IEEE Trans. Antennas Propag.*, **63**(4), pp. 1465–1472, 2015.

[107] J. Lundgren, A. Ericsson, and D. Sjöberg. Design and optimization of dual band circular polarization selective structures. Technical Report LUTEDX/(TEAT-7257)/1–21/(2017), Lund University, Department of Electrical and Information Technology, P.O. Box 118, S-221 00 Lund, Sweden, 2017.

[108] J. Lundgren. Dual band circular polarization selective structures for space applications. Master's thesis, Lund University, Department of Electrical and Information Technology, P.O. Box 118, SE-221 00 Lund, Sweden, 2016. Rep. No. LU/LTH-EIT 2016-540.

[109] G. Q. Luo, W. Hong, Z.-C. Hao, B. Liu, W. D. Li, J. X. Chen, H. X. Zhou, and K. Wu. Theory and experiment of novel frequency selective surface based on substrate integrated waveguide technology. *IEEE Trans. Antennas Propag.*, **53**(12), pp. 4035–4043, 2005.

[110] G. Q. Luo, W. Hong, Q. H. Lai, K. Wu, and L. L. Sun. Design and experimental verification of compact frequency-selective surface with quasi-elliptic bandpass response. *IEEE Trans. Microwave Theory Tech.*, **55**(12), pp. 2481–2487, 2007.

[111] O. Luukkonen, F. Costa, C. R. Simovski, A. Monorchio, and S. A. Tretyakov. A thin electromagnetic absorber for wide incidence angles and both polarizations. *IEEE Trans. Antennas Propag.*, **57**(10), pp. 3119–3125, Oct 2009.

[112] S. Maci, G. Minatti, M. Casaletti, and M. Bosiljevac. Metasurfing: Addressing waves on impenetrable metasurfaces. *IEEE Antennas and Wireless Propagation Letters*, **10**, pp. 1499–1502, 2011.

[113] N. Marcuvitz. *Waveguide Handbook*. McGraw-Hill, New York, NY, 1951.

[114] A. Massa, P. Rocca, and G. Oliveri. Compressive sensing in electromagnetics-a review. *IEEE Antennas Propag. Mag.*, **57**(1), pp. 224–238, 2015.

[115] J. C. Maxwell. A dynamical theory of the electromagnetic field. *Philos. Trans. R. Soc. London*, **155**, pp. pp. 459–512, 1865.

[116] J. C. Maxwell. *A Treatise on Electricity and Magnetism*, volume 1. Dover Publications, New York, NY, 1954.

[117] J. C. Maxwell. *A Treatise on Electricity and Magnetism*, volume 2. Dover Publications, New York, NY, 1954.

[118] M. D. Migliore. A compressed sensing approach for array diagnosis from a small set of near-field measurements. *IEEE Trans. Antennas Propag.*, **59**(6), pp. 2127–2133, June 2011.

[119] G. W. Milton. *The Theory of Composites*. Cambridge University Press, Cambridge, 2002.

[120] G. Minatti, M. Faenzi, E. Martini, F. Caminita, P. D. Vita, D. G. lez Ovejero, M. Sabbadini, and S. Maci. Modulated metasurface antennas for space: Synthesis, analysis and realizations. *IEEE Trans. Antennas Propag.*, **63**(4), pp. 1288–1300, April 2015.

[121] G. Minatti, S. Maci, P. D. Vita, A. Freni, and M. Sabbadini. A circularly-polarized isoflux antenna based on anisotropic metasurface. *IEEE Trans. Antennas Propag.*, **60**(11), pp. 4998–5009, Nov 2012.

[122] K. Mitzner. Incremental length diffraction coefficients. Technical report, DTIC Document, 1974.

[123] G. A. Morin. A simple circular polarization selective surface (CPSS). In *Antennas and Propagation Society International Symposium, 1990. AP-S. Merging Technologies for the 90's. Digest.*, pp. 100–103. IEEE, 1990.

[124] G. Morin. Circular polarization selective surface made of resonant spirals, 1994. US Patent 5,280,298.

[125] G. A. Morin. A circular polarization selective surface made of resonant helices. Technical report, DTIC Document, 1995.

[126] A. Motevasselian and B. L. G. Jonsson. Design of a wideband rasorber with a polarisation-sensitive transparent window. *IET Microwaves, Antennas Propagation*, **6**(7), pp. 747–755, May 2012.

[127] B. Munk. *Frequency Selective Surfaces: Theory and Design*. John Wiley & Sons, New York, NY, 2000.

[128] S. I. Newton. *Opticks; Or, a Treatise of the Reflections, Refractions, Inflections and Colours of Light*. William and John Innys, 1721.

[129] A. M. Nicolson and G. F. Ross. Measurement of the intrinsic properties of materials by time-domain techniques. *IEEE Trans. Instrum. Meas.*, **19**, pp. 377–382, 1970.

[130] G. Oliveri and A. Massa. Bayesian compressive sampling for pattern synthesis with maximally sparse non-uniform linear arrays. *IEEE Trans. Antennas Propag.*, **59**(2), pp. 467–481, Feb 2011.

[131] S. J. Orfanidis. Electromagnetic Waves and Antennas, 2010. Available at: http://www.ece.rutgers.edu/~orfanidi/ewa/, accessed 2017-09-24.

[132] S. V. Parekh. Dual gridded reflector structure, November 25 1986. US Patent 4,625,214.

[133] R. Pierrot. Reflector for circularly polarized waves, 1970. US Patent 3,500,420.

[134] S. Poulsen. Artificial puck plate radomes. In *Proc. International Conference on Electromagnetics in Advanced Applications (ICEAA'05)*, Torino, Italy, 2005.

[135] S. Poulsen. *Stealth radomes*. PhD thesis, Lund University, Department of Electroscience, Lund University, P.O. Box 118, S-221 00 Lund, Sweden, 2006.

[136] D. M. Pozar. *Microwave Engineering*. John Wiley & Sons, New York, NY, third edition, 2005.

[137] Y. Ra'di. *Functional Metasurfaces*. PhD thesis, Aalto University, 2015.

[138] S. M. Rao. *Time Domain Electromagnetics*. Academic Press, 1999.

[139] A. K. Rashid, B. Li, and Z. Shen. An overview of three-dimensional frequency-selective structures. *IEEE Antennas and Propagation Magazine*, **56**(3), pp. 43–67, 2014.

[140] A. K. Rashid and Z. Shen. A novel band-reject frequency selective surface with pseudo-elliptic response. *IEEE Trans. Antennas Propag.*, **58**(4), pp. 1220–1226, 2010.

[141] A. K. Rashid and Z. Shen. Scattering by a two-dimensional periodic array of vertically placed microstrip lines. *IEEE Trans. Antennas Propag.*, **59**(7), pp. 2599–2606, 2011.

[142] L. Rayleigh. XVIII. on the passage of electric waves through tubes, or the vibrations of dielectric cylinders. *The London, Edinburgh, and Dublin Philosophical Magazine and Journal of Science*, **43**(261), pp. 125–132, 1897.

[143] J. Reinert, J. Psilopoulos, J. Grubert, and A. F. Jacob. On the potential of graded-chiral Dällenbach absorbers. *Microwave and Optical Technology Letters*, **30**(4), pp. 254–257, 2001.

[144] M. A. Richards, J. Scheer, W. A. Holm, and W. L. Melvin. *Principles of Modern Radar*. Citeseer, 2010.

[145] J. Rodriguez. *Fundamentals of 5G Mobile Networks*. John Wiley & Sons, 2015.

[146] A. G. Roederer and G. A. Crone. Double grid reflector antenna, March 3 1987. US Patent 4,647,938.

[147] J. E. Roy and L. Shafai. Reciprocal circular-polarization-selective surface. *Antennas and Propagation Magazine, IEEE*, **38**(6), pp. 18–33, 1996.

[148] K. N. Rozanov. Ultimate thickness to bandwidth ratio of radar absorbers. *IEEE Trans. Antennas Propag.*, **48**(8), pp. 1230–1234, August 2000.

[149] G. T. Ruck, D. E. Barrick, W. D. Stuart, and C. K. Krichbaum. *Radar Cross-Section Handbook*, volume 1 and 2. Plenum Press, New York, 1970.

[150] M. Salehi and N. Behdad. A second-order dual X-/Ka-band frequency selective surface. *IEEE Microwave and Wireless Components Letters*, **18**(12), pp. 785–787, 2008.

[151] W. Salisbury. Absorbent body for electromagnetic waves, 1952. Patent number 2,599,944.

[152] J. Sanz-Fernandez, E. Saenz, and P. de Maagt. A circular polarization selective surface for space applications. *IEEE Trans. Antennas Propag.*, **63**(6), pp. 2460–2470, 2015.

[153] J. Sanz-Fernandez, E. Saenz, P. de Maagt, and C. Mangenot. Circular polarization selective surface for dual-optics CP offset reflector antennas in Ku-band. In *Proceedings of the 6th European Conference on Antennas and Propagation (EuCAP)*, pp. 2683–2687. IEEE, 2012.

[154] K. Sarabandi and N. Behdad. A frequency selective surface with miniaturized elements. *IEEE Trans. Antennas Propag.*, **55**(5), pp. 1239–1245, 2007.

[155] J. W. Schultz. *Focused Beam Methods: Measuring Microwave Materials in Free Space*. John Schultz, 2012.

[156] E. Sedhed. Electromagnetic analysis of reflector antenna surfaces. Master's thesis, Lund University, Department of Electrical and Information Technology, P.O. Box 118, SE-221 00 Lund, Sweden, 2015. Rep. No. LU/LTH-EIT 2015-428.

[157] E. Sedhed, A. Ericsson, N. Wellander, and D. Sjöberg. Quasi periodicity in moiré patterns and a numerical approximation method of dual weaves. In *Antennas and Propagation & USNC/URSI National Radio Science Meeting, 2015 IEEE International Symposium on*, pp. 1620–1621. IEEE, 2015.

[158] J. Shaker, M. R. Chaharmir, and J. Ethier. *Reflectarray Antennas: Analysis, Design, Fabrication, and Measurement*. Artech House, 2013.

[159] V. M. Shalaev. Optical negative-index metamaterials. *Nature photonics*, **1**(1), pp. 41–48, 2007.

[160] Y. Shang, Z. Shen, and S. Xiao. Frequency-selective rasorber based on square-loop and cross-dipole arrays. *IEEE Trans. Antennas Propag.*, **62**(11), pp. 5581–5589, 2014.

[161] A. Sihvola. Metamaterials in electromagnetics. *Metamaterials*, **1**(1), pp. 2–11, 2007.

[162] A. H. Sihvola. *Electromagnetic Mixing Formulas and Applications*. Number 47 in IET electromagnetic wave series. IET, 1999.

[163] A. H. Sihvola and J. A. Kong. Effective permittivity of dielectric mixtures. *IEEE Trans. Geoscience and Remote Sensing*, **26**(4), pp. 420–429, 1988.

[164] S. Simms and V. Fusco. Thin radar absorber using artificial magnetic ground plane. *Electronics Letters*, **41**(24), pp. 1311–1313, Nov 2005.

[165] D. Sjöberg and A. Ericsson. Computation of radar cross section using the physical optics approximation. Technical Report LUTEDX/(TEAT-7255)/1–16/(2017), Lund University, Department of Electrical and Information Technology, P.O. Box 118, S-221 00 Lund, Sweden, 2017.

[166] D. Sjöberg and A. Ericsson. A multi layer meander line circular polarization selective structure (MLML-CPSS). In *Proceedings of the 8th European Conference on Antennas and Propagation (EuCAP)*, pp. 464–468. IEEE, 2014.

[167] D. G. Smith. *Field Guide to Physical Optics*. SPIE Press, 2013.

[168] L. Solymar and E. Shamonina. *Waves in Metamaterials*. Oxford University Press, 2009.

[169] M. Soumekh. *Fourier Array Imaging*. Prentice-Hall, Inc., 1994.

[170] R. H. Stolt. Migration by fourier transform. *Geophysics*, **43**(1), pp. 23–48, 1978.

[171] J. A. Stratton. *Electromagnetic Theory*. McGraw-Hill, New York, NY, 1941.

[172] C. S. T. Studio Suite. Optimization, 2017. Available at https://www.cst.com/products/csts2/optimization, accessed 2017-07-03.

[173] F. Terracher and G. Berginc. A broadband dielectric microwave absorber with periodic metallizations. *Journal of Electromagnetic Waves and Applications*, **13**(12), pp. 1725–1741, 1999.

[174] D. Tilston, M. Tilston, S. Tilston, W. V. Tilston, and T. Tralman. Polarization selective surface for circular polarization, 1991. US Patent 5,053,785.

[175] W. V. Tilston, T. Tralman, and S. M. Khanna. A polarization selective surface for circular polarization. In *Antennas and Propagation Society International Symposium, 1988. AP-S. Digest*, pp. 762–765. IEEE, 1988.

[176] A. Tolkachev, V. Denisenko, A. Shishlov, and A. Shubov. High gain antenna systems for millimeter wave radars with combined electronical and mechanical beam steering. In *Phased Array Systems and Technology, 1996., IEEE International Symposium on*, pp. 266–271. IEEE, 1996.

[177] S. Tretyakov, I. Nefedov, A. Sihvola, S. Maslovski, and C. Simovski. Waves and energy in chiral nihility. *Journal of electromagnetic waves and applications*, **17**(5), pp. 695–706, 2003.

[178] P. Y. Ufimtsev. Method of edge waves in the physical theory of diffraction. Technical report, DTIC Document, 1971.

[179] J. Uher, J. Bornemann, and U. Rosenberg. *Waveguide components for antenna feed systems: Theory and CAD*. Artech House Publishers, 1993.

[180] P. L. E. Uslenghi, editor. *Electromagnetic Scattering*. Academic Press, New York San Fransisco London, 1978.

[181] J. G. van Bladel. *Electromagnetic Fields*. IEEE Press, Piscataway, NJ, second edition edition, 2007.

[182] D. F. Vanderwerf. *The Story of Light Science*. Springer International Publishing, 2017.

[183] M. Weiland and C. T. Discrete electromagnetism with the finite integration technique. *Progress In Electromagnetics Research*, **32**, pp. 65–87, 2001.

[184] D. H. Werner and D.-H. Kwon. *Transformation Electromagnetics and Metamaterials*. Springer, 2015.

[185] H. E. William. Electromagnetic wave absorbers and anechoic chambers through the years. *IEEE Trans. Antennas Propag.*, **21**(4), 1973.

[186] T. K. Wu. *Frequency Selective Surface and Grid Array*. New York, John Wiley & Sons Inc., 1995.

[187] A. H. Zemanian. *Distribution theory and transform analysis: an introduction to generalized functions, with applications*. Dover Publications, New York, NY, 1987.

[188] S. Zhang, Y.-S. Park, J. Li, X. Lu, W. Zhang, and X. Zhang. Negative refractive index in chiral metamaterials. *Phys. Rev. Lett.*, **102**, pp. 023901, Jan 2009.

[189] Q. Zhao and J. C. Principe. Support vector machines for sar automatic target recognition. *IEEE Transactions on Aerospace and Electronic Systems*, **37**(2), pp. 643–654, Apr 2001.

[190] S. Zouhdi, A. Sihvola, and M. Arsalane. *Advances in electromagnetics of complex media and metamaterials*, volume 89. Springer Science & Business Media, 2012.

[191] S. Zouhdi, A. Sihvola, and A. P. Vinogradov. *Metamaterials and plasmonics: fundamentals, modelling, applications*. Springer Science & Business Media, 2008.

[192] Y. Zuo, A. K. Rashid, Z. Shen, and Y. Feng. Design of dual-polarized frequency selective structure with quasi-elliptic bandpass response. *IEEE Antennas and Wireless Propagation Letters*, **11**, pp. 297–300, 2012.

Part II: Included Papers

A Resonant Circular Polarization Selective Structure of Closely Spaced Wire Helices

Paper I

Andreas Ericsson and Daniel Sjöberg

Published as: A. Ericsson and D. Sjöberg, "A resonant circular polarization selective structure of closely spaced wire helices," *Radio Science*, Vol. 50, No. 8, pp. 804–8012, 2015.

Abstract

A circular polarization selective structure (CPSS) reflects one handedness of circular polarization and transmits the other. We present a resonant CPSS consisting of closely spaced wire helices. Simulation results demonstrate that the design can operate over $\pm 20^\circ$ angle of incidence variation and has a bandwidth of about 10 % at normal incidence. A suggested design case is presented, where the CPSS is implemented in a shared aperture circular polarization offset reflector antenna for satellite communication in the K_u-band uplink of Australia at $17.3\,\mathrm{GHz} < f < 18.1\,\mathrm{GHz}$.

1 Introduction

The satellite communication situation of today consists of crowded geostationary orbits, where the aperture of each satellite is very limited. The antennas used in this type of applications are in general large, bulky reflector antennas, thus to optimize the aperture use of satellites is an important task. A space antenna aperture can be shared by using separate frequency bands for up- and downlink communication. To improve the aperture sharing further it is a desirable feature to separate signals of different polarization in separate channels [5, p.282]. Polarization selectivity is easily achieved for linear polarizations by utilizing a grid surface of parallel metal vanes arranged closely together, referred to as a linear polarization selective surface (LPSS) [2]. Incident signals polarized parallel to the vanes are reflected and signals polarized orthogonal to the vanes are transmitted. This type of surface can be implemented in a satellite communication system, either as a shared aperture reflector antenna by backing a curved LPSS with a solid reflector, where the front surface reflects one polarization and the back surface reflects the orthogonal polarization [2], or as a flat polarization diplexing surface.

To design polarization selective structures for circular polarization (CP) is a current key challenge in satellite communication applications [5, p.710]. In [7, 9] theoretical characteristics of CPSSs are defined, where it is concluded that there are four possible types of circular polarization selective structures, which are described in detail in Figure 1. In order to manufacture a structure with nonreciprocal scattering properties, nonreciprocal materials must be used (such as magnetized ferrite crystals). Due to their lack of practicality, this type of materials are not well suited for space applications. The most common type of CPSS is reciprocal and symmetric, it can be shown from theory [7, 9] that this type of design have the following properties:

1. The CP wave reflected by a CPSS will be of the same polarization as the incoming wave.

2. The CP wave transmitted by a CPSS will be of the same polarization as the incoming wave.

3. An infinite CPSS can not be made of an infinitely thin surface.

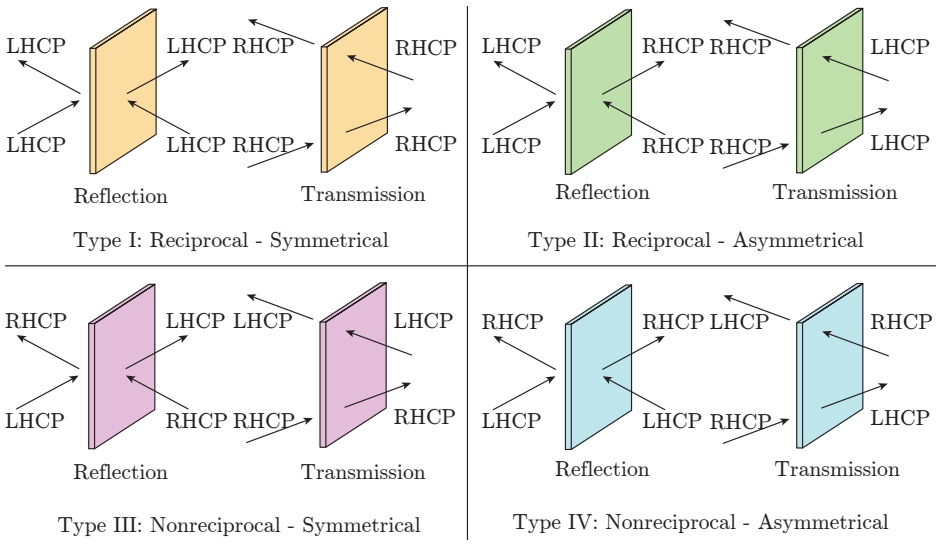

Figure 1: The four possible types of an LHCPSS, characterized with respect to the polarization state of the transmitted and reflected signals in relation to the polarization state of the incident signal.

This puts constraints on the polarization state of the reflected and transmitted signals, it also implies that a CPSS must have a finite thickness. Different CPSS concept designs have been presented through the last 40 years in [6, 8, 11] and based on resonant structures. Different implementations of CPSSs are discussed in [10] where a structure based on the concept in [8] was manufactured. A weakness the designs in [6, 8, 10, 11] all have in common is instability of the circular polarization purity with respect to the angle of incidence.

An ideal, reciprocal, symmetric left hand circular polarization selective structure (LHCPSS) can be represented by a 4×4 scattering matrix in circular polarization

$$\boldsymbol{S}^{\mathrm{CP}} = \begin{pmatrix} S_{11}^{\mathrm{RR}} & S_{12}^{\mathrm{RL}} & S_{13}^{\mathrm{RR}} & S_{14}^{\mathrm{RL}} \\ S_{21}^{\mathrm{LR}} & S_{22}^{\mathrm{LL}} & S_{23}^{\mathrm{LR}} & S_{24}^{\mathrm{LL}} \\ S_{31}^{\mathrm{RR}} & S_{32}^{\mathrm{RL}} & S_{33}^{\mathrm{RR}} & S_{34}^{\mathrm{RL}} \\ S_{41}^{\mathrm{LR}} & S_{42}^{\mathrm{LL}} & S_{43}^{\mathrm{LR}} & S_{44}^{\mathrm{LL}} \end{pmatrix} = \begin{pmatrix} 0 & 0 & \mathrm{e}^{-\mathrm{j}\phi_{\mathrm{t}}} & 0 \\ 0 & \mathrm{e}^{-\mathrm{j}\phi_{\mathrm{r}}} & 0 & 0 \\ \mathrm{e}^{-\mathrm{j}\phi_{\mathrm{t}}} & 0 & 0 & 0 \\ 0 & 0 & 0 & \mathrm{e}^{-\mathrm{j}\phi_{\mathrm{r}}} \end{pmatrix}, \quad (1.1)$$

where $\phi_{\mathrm{r}}, \phi_{\mathrm{t}} \in \mathbb{R}$ are the phase terms of the reflected and transmitted signals, S_{22}^{LL} is the co-polarized reflection of an incident left hand circular polarization (LHCP) wave and the other S-parameters are defined in the same way.

In this paper, we present a CPSS design with improved stability with respect to the angle of incidence compared to previous results. This type of robustness is of major importance when implementing a CPSS in a satellite communication system, either as a curved surface in a circularly polarized shared aperture reflector antenna, or as a flat circular polarization diplexer [10]. Our design is based

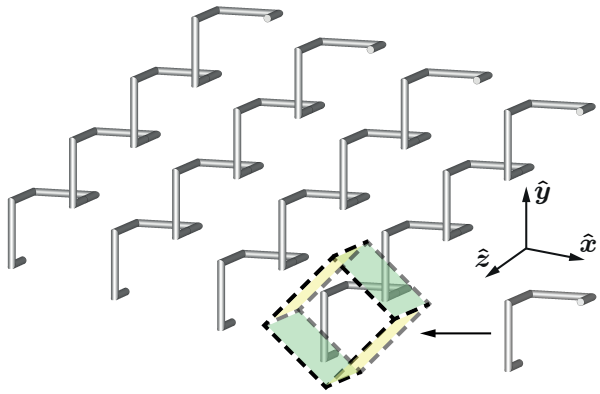

Figure 2: CPSS concept design in [6]. The unit cell structure is presented to the right and the corresponding periodic structure to the left. The green and yellow sides of the unit cell represent periodic boundary conditions.

on the concept in [6] with crossed bent wires of infinite extent in two dimensions, kept in place by a foam material. A concept design case of our structure is demonstrated in a shared aperture circular polarization reflector antenna operating in the K_u-band uplink of Australia at $17.3\,\text{GHz} < f < 18.1\,\text{GHz}$.

2 Design

The CPSS presented in [6] consists of bent wires in the shape of helices arranged in a periodic array as in Figure 2. By arranging two of these helices close to each other in one unit cell, our novel CPSS design presented in Figure 3 is achieved. The side length of the unit cell in Figure 3 is approximately $\lambda_0/4$ and the length of the wire components in the direction of propagation, the z-direction, is about $\lambda_0/4$, resulting in a total length of each wire inside the unit cell of $\lambda_0/2$. The fact that the side length of the unit cell is smaller than $\lambda_0/2$ minimizes the risk of grating lobes from the CPSS. The wires have a diameter of about 0.1 mm and are made of a metallic material such as copper or aluminum. A low permittivity, low loss, foam material, $\epsilon_r = 1.17$, $\tan(\delta) = 0.0017$, suitable for space applications is added as support to the structure. A full wave, frequency domain, simulation model implemented in Computer Simulation Technology Microwave Studio (CST MWS) for optimization is presented in Figure 4, where the optimization parameters of the model (a, d, l_{xy} and l_z) are depicted. The simulated CPSS is of infinite extent in the xy-plane and is modeled using a unit cell with periodic boundaries.

When an electromagnetic wave impinges on the structure currents are first induced in the horizontal components of the wires in Figure 3 (the part of the structure closest to the incoming wave). When the wave is propagating through

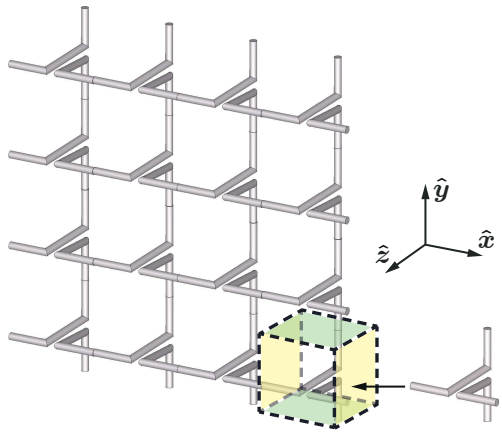

Figure 3: Our novel CPSS concept design. The unit cell structure is presented to the right and the corresponding periodic structure to the left. The green and yellow sides of the unit cell represent periodic boundary conditions.

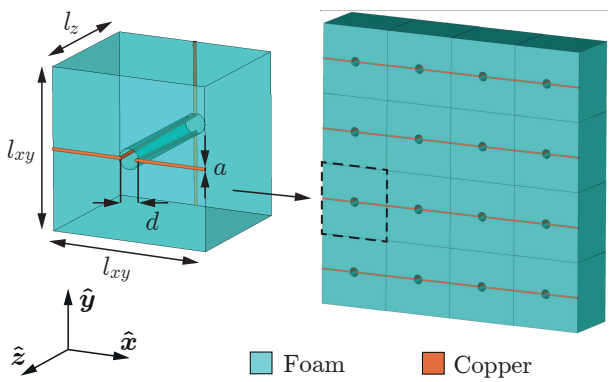

Figure 4: CPSS design implemented in a commercial software. The direction of normal incidence of the structure is in the $\hat{z}$-direction. The length of the wire components in the xy-direction is $l_{xy}^{\text{wire}} = l_{xy} - d$ and the length of the wire components in the z-direction is $l_z^{\text{wire}} = l_z$, resulting in a total length of each of the two wires in the unit cell of about $\lambda_0/2$. The background material consists of a low permittivity foam, the wires are made of copper, and the wire diameter is approximately 0.1 mm.

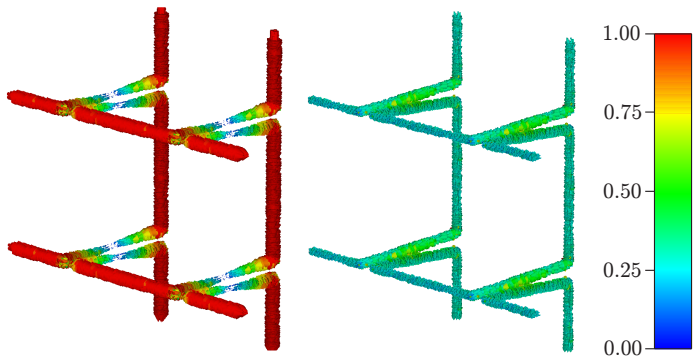

Figure 5: The absolute value of the normalized currents induced on the wires of the CPSS when illuminated at normal incidence ($\theta = 0°$). If the structure is illuminated by an LHCP wave strong currents are induced in the horizontal and vertical wire components and the signal is reflected. If the structure is illuminated by an RHCP wave weak, uniformly distributed currents are induced in the wires and the signal is transmitted.

the structure currents are induced in the vertical components of the wires in Figure 3 (at the back of the structure). If the polarization of the propagating wave is LHCP the polarization is rotating in a direction along the structure, which implies that the induced currents in the structure add up and the wave is reflected, as in the left illustration in Figure 5. If the the polarization state of the wave is right hand circular polarization (RHCP) the polarization is rotating in a direction opposite to the structure, this implies that the induced currents cancel each other and the wave is transmitted, as in the right illustration in Figure 5.

The physical explanation of why the CPSS concepts in [6, 8, 10, 11] are relatively unstable with respect to variations in the angle of incidence is as follows. An incident signal induces currents in the wire components in the direction normal to the CPSS, and the radiation from this part of the structure carries a strong cross polarization component. This results in a degeneration of the polarization purity of the circularly polarized signals, which is commonly measured as cross polarization discrimination (XPD) or axial ratio (AR). Our concept design in Figures 3–4 utilizes the fact that the two wires at the center of the unit cell run parallel to each other in the direction of propagation. If these wires are close enough to each other they act as a twin wire transmission line and their radiation contributions cancel each other out [3, Ch.4], as in Figure 6. This implies that even if the incident wave is propagating at a slightly oblique angle of incidence towards the CPSS the circular polarization XPD is still high.

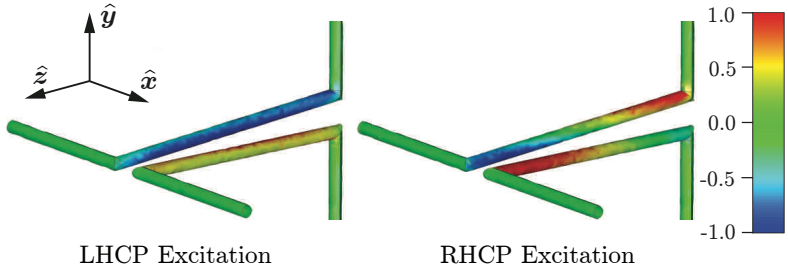

Figure 6: The maximum amplitude of the normalized currents induced in the z-direction on the wires of the CPSS when illuminated at an oblique angle of incidence ($\theta = 30°$). The paired blue and red colors of the wires corresponds to currents flowing in opposite directions along the parallel wires. By placing these wire components close to each other they act as a twin wire transmission line and the radiation from this part of the structure is minimized.

3 Results

The design was implemented in a K_u-band uplink scenario, $17.3\,\text{GHz} < f < 18.1\,\text{GHz}$, with the performance requirements defined in [1] and used in [10]:

1. Insertion loss and return loss better than 0.5 dB.
2. Axial ratio of the reflected and transmitted signals better than 0.78 dB.

In the optimization of the structure the parameters presented in Figure 4 were varied using the built-in optimization tools in CST MWS to minimize the optimization integral

$$\frac{1}{f_2 - f_1} \int_{f_1}^{f_2} (\text{AR}_{\text{refl}} + \text{AR}_{\text{trans}} + \text{RL} + \text{IL})\ \text{d}f, \tag{3.1}$$

here f is the frequency, AR_{refl} is the axial ratio of the reflected signal for incident LHCP, AR_{trans} is the axial ratio of the transmitted signal for incident RHCP, RL is the return loss for LHCP and IL is the insertion loss for RHCP. Simulation results of the optimized design are presented in Figure 7 where the requirements in [1] are fulfilled up to 20° angle of incidence. If the axial ratio requirement is relaxed to XPD $> 20\,\text{dB}$ (axial ratio $< 1.7\,\text{dB}$) the structure can operate at up to 30° angle of incidence. The diameter of the wires (a) is 0.06 mm, the side length of the unit cell (l_{xy}) is 4.54 mm, the length of the wires in the direction of propagation (l_z) is 3.86 mm and the drilled hole in the foam (d) is 0.60 mm in diameter. The design is scalable with respect to the center frequency of operation in the same manner as previous resonant designs in [6, 8, 10, 11].

If the relative permittivity of the foam is introduced as a variable in the optimization process ($\epsilon_{\text{r}}^{\text{foam}} \in [1.04, 1.25]$) the performance of the structure can be

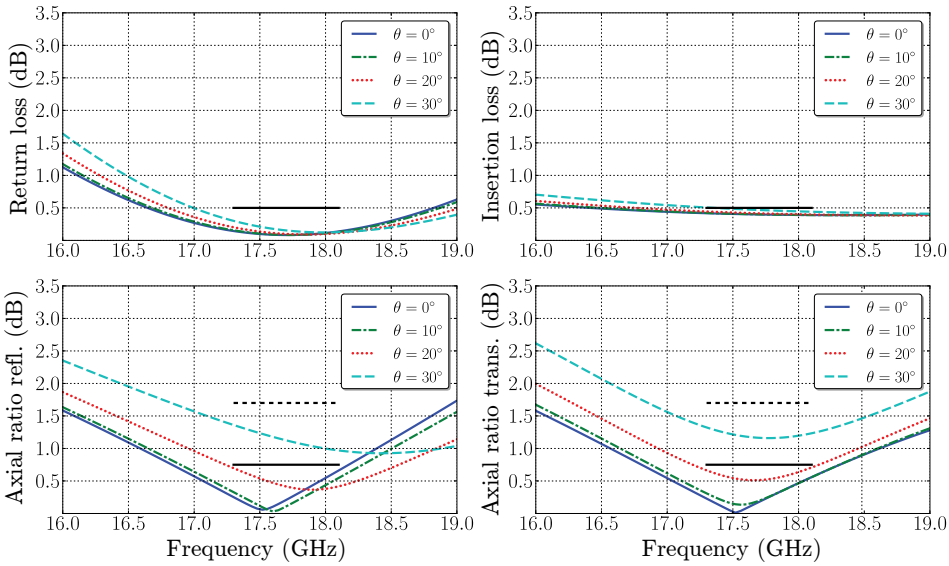

Figure 7: Simulation results of the CPSS design at different angles of incidence, in the plane $\phi = 135°$. Upper left is the LHCP return loss, and lower left is the corresponding axial ratio. Upper right is the RHCP insertion loss, and lower right is the corresponding axial ratio. The black solid lines represent the design requirements defined in [1], and the black dashed lines represent the relaxed requirements of XPD $> 20\,\text{dB}$, corresponding to AR $< 1.7\,\text{dB}$.

maximized at an oblique angle of incidence. When the support material permittivity is increased in the optimization process the AR curves for oblique angles of incidence such as $\theta = 20°, 30°$ are shifted down, compared to the results in Figure 7. This is an interesting feature, although materials with ϵ_r corresponding to the optimized concept design might be inappropriate for space applications.

A parametric study was performed to analyze the electromagnetic stability of the CPSS and to characterize the dependency between the geometrical parameters of the structure and the circular polarization XPD. The side length of the unit cell l_{xy} was varied and the results in Figure 8 show that this parameter is mainly affecting the return loss of the structure. The insertion loss and the axial ratio of the transmitted and reflected signal are shifted slightly when l_{xy} is varied.

The length of the wire components in the direction of propagation (l_z) was varied, the results in Figure 9 show that when l_z is increased the resonance frequency is shifted down. This follows from the fact that the center frequency of operation of the structure is given by $l_z \simeq \lambda_0/4$. When the wire diameter (a) is increased the IL of the CPSS is slightly increased and the RL and AR are almost unaffected. From an electromagnetic perspective infinitely thin wires

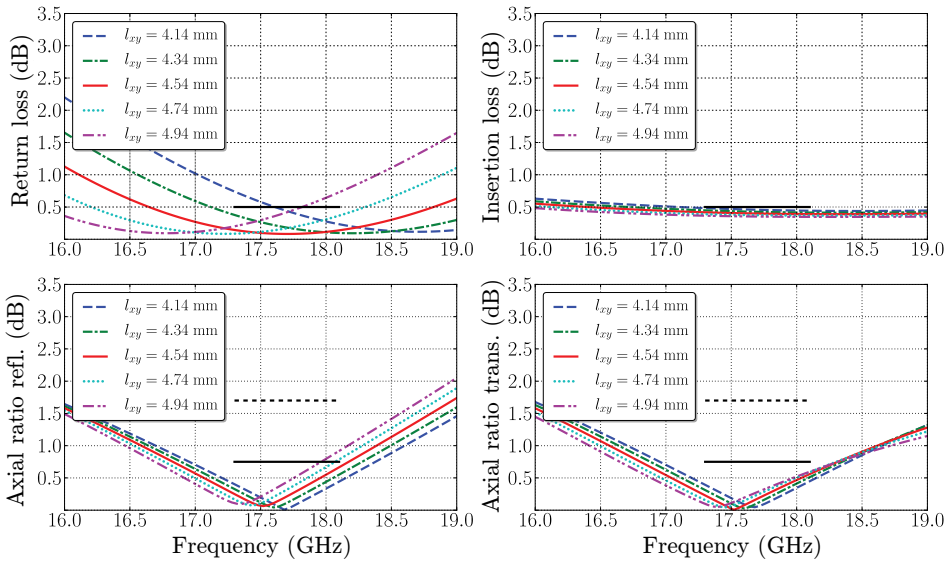

Figure 8: Simulation results of the CPSS design at normal incidence, where the side length of the unit cell (l_{xy}) is varied. Upper left is the LHCP return loss, and lower left is the corresponding axial ratio. Upper right is the RHCP insertion loss, and lower right is the corresponding axial ratio. The black solid lines represent the design requirements defined in [1], and the black dashed lines represent the relaxed requirements of XPD $>$ 20 dB, corresponding to AR $<$ 1.7 dB.

of the CPSS are desirable to minimize the insertion loss. However, to achieve structural and thermal stability of the design, a lower limit of the wire diameter is taken into consideration, the value of which is a subject of further analysis.

If the diameter of the holes in the support material (d) is varied the results are slightly affected in the sense that the $\mathrm{AR}_{\mathrm{trans}}$ and $\mathrm{AR}_{\mathrm{refl}}$ curves are shifted apart. If the normal components of the wires are seen as a twin wire transmission line, an increase in d results in an increase of the characteristic impedance of this part of the structure, which implies a mismatch of the CPSS impedance to the surrounding vacuum.

A coarse mesh, with about 12 000 tetrahedral elements, was used for the optimization of the model. With this mesh setting, 6 GB of memory is used and one simulation of the structure at the polar incidence angles $\theta = \{0°, 10°, 20°, 30°\}$ finishes in around 30 minutes. The optimized simulation model was then checked for convergence by greatly decreasing the mesh element size. The fine mesh setting was using smaller tetrahedral elements and an improved element size transition ratio, resulting in a mesh of around 110 000 elements, using 12 GB of memory and finishing in about 2.5 hours. Almost no discrepancy was found

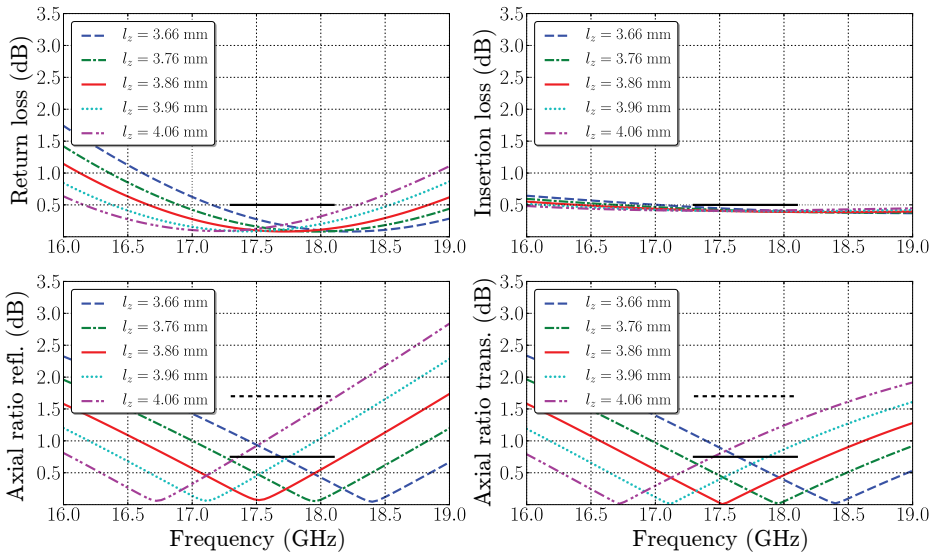

Figure 9: Simulation results of the CPSS design at normal incidence where the wire length in the propagation path (l_z) is varied. Upper left is the LHCP return loss, and lower left is the corresponding axial ratio. Upper right is the RHCP insertion loss, and lower right is the corresponding axial ratio. The black solid lines represent the design requirements defined in [1], and the black dashed lines represent the relaxed requirements of XPD $> 20\,\mathrm{dB}$, corresponding to AR $< 1.7\,\mathrm{dB}$.

when comparing the results with the different mesh settings.

To evaluate the performance of the CPSS for all possible incidence angles (θ, ϕ), defined in Figure 10, at the center frequency of operation f_0 the structure was illuminated with a plane wave of LHCP/RHCP at the front side of the structure for each combination of $\theta = 0°, 5°, ..., 85°$ and $\phi = 0°, 5°, ..., 355°$. The performance of the structure with respect to RL, IL, $\mathrm{AR_{refl}}$, or $\mathrm{AR_{trans}}$ was plotted on a half sphere, where the performance at each incidence direction is represented by the color of a pixel. Blue colors correspond to low values in the dB scale, which indicates good performance, while red colors correspond to high values in the dB scale, indicating poor performance. If we observe this half sphere from above the circular polarization selectivity of the CPSS is plotted as polar contour plots for all incidence angles when the structure is illuminated from the front side. The radius of the polar plot corresponds to $\sin\theta$ so that the cartesian coordinates are $x = \sin\theta\cos\phi$, and $y = \sin\theta\sin\phi$, with the z-axis pointing towards the reader.

The mentioned method of evaluating the performance of a CPSS for all incidence angles is described in detail in [4], where it is shown that the polarization

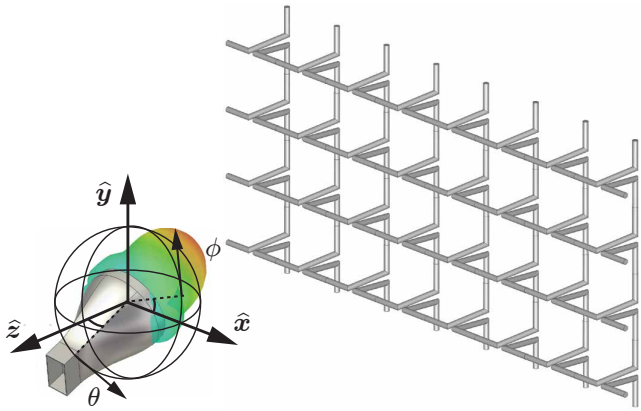

Figure 10: Definition of the spherical angles of incidence (θ, ϕ) of a device under test. The RL, IL and XPD of all CPSS designs presented to date depend strongly on both the polar angle of incidence θ and the plane of incidence ϕ.

selectivity of all resonant CPSS designs is strongly dependent on the incidence direction (θ, ϕ) of the incoming signal. The results in Figure 11 indicate that, for a constant polar angle θ, the performance of the structure varies noticeably with ϕ. Some planes of incidence (constant ϕ) are better than others in the sense that the deterioration of the $\mathrm{AR}_{\mathrm{trans}}$ and $\mathrm{AR}_{\mathrm{refl}}$ for an increased polar angle (θ) has different magnitude. This particular design shows the best performance at the incidence plane where $\phi = 135°$. The high degree of symmetry of the unit cell structure implies that the response of the structure at oblique angles of incidence is independent of the sign of θ, as can be seen in Figure 11. If the structure is designed to operate at normal incidence this implies an angular stability of 40° at the incidence plane of $\phi = 135°$ with respect to the predefined requirements in [1].

When the performance of the novel CPSS in Figure 11 is compared to that of the designs by Pierrot, Morin and Tilston [6,8,11] in [4] it can be concluded that the stability of the performance with respect to variations in (θ, ϕ) is significantly improved in the novel CPSS. The fact that the parallel wires act as a transmission line improves the performance at oblique angles of incidence θ, and the high level of symmetry of the structure implies that the performance variation with respect to ϕ is suppressed.

4 Manufacturing and application

When designing for space applications the materials used have to be able to withstand vibrations at take-off, impacts of micrometeoroids and debris, vacuum,

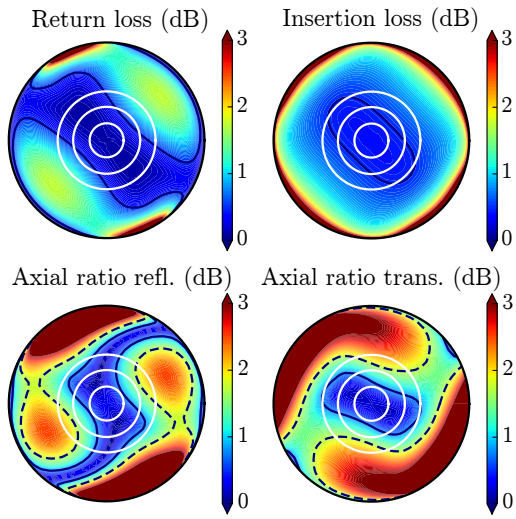

Figure 11: Simulation results of the CPSS for front side illumination at the center frequency of operation $f = 17.7\,\mathrm{GHz}$. The left plots show the return loss and the polarization purity of the reflected signal and the right plots correspond to the insertion loss and the polarization purity of the transmitted signal. The black solid lines represent the design requirements defined in [1], the black dashed lines represent the relaxed requirements of axial ratio XPD $> 20\,\mathrm{dB}$, corresponding to AR $< 1.7\,\mathrm{dB}$, and the white circles correspond to $\theta = 10°, 20°, 30°$.

thermal cycling and radiation [5]. This puts heavy constraints on the materials of having a low thermal expansion coefficient, a high Young's modulus and low weight. From an electromagnetic perspective the most important material properties are the dielectric loss, typically a loss tangent around 0.001 is desirable, and the conductive loss in the metal components of the structure which should be minimized. Our simulated CPSS design in Figure 4 could be manufactured by using a low permittivity foam, such as Rohacell, as a stabilizing background material. By drilling holes in the foam with a diameter given by the simulation parameter d thin copper or aluminum wires could be threaded through the holes to create the full periodic structure.

Our CPSS could be implemented in a shared aperture CP offset reflector antenna as in Figure 12 (a), where the front reflector is a left hand circular polarization selective structure (LHCPSS) and the back reflector is a right hand circular polarization selective structure (RHCPSS) [10]. This system could operate in the K_u-band, either in the downlink frequency range ($11.7\,\mathrm{GHz} < f < 12.5\,\mathrm{GHz}$) as a transmitting system or in the uplink frequency range ($17.3\,\mathrm{GHz} < f < 18.1\,\mathrm{GHz}$) as a receiving system. To realize this type of CPSS, a curved reflector could be manufactured from a low permittivity core and two dielectric panels. Copper wires could then be threaded through drilled holes in the structure to create a

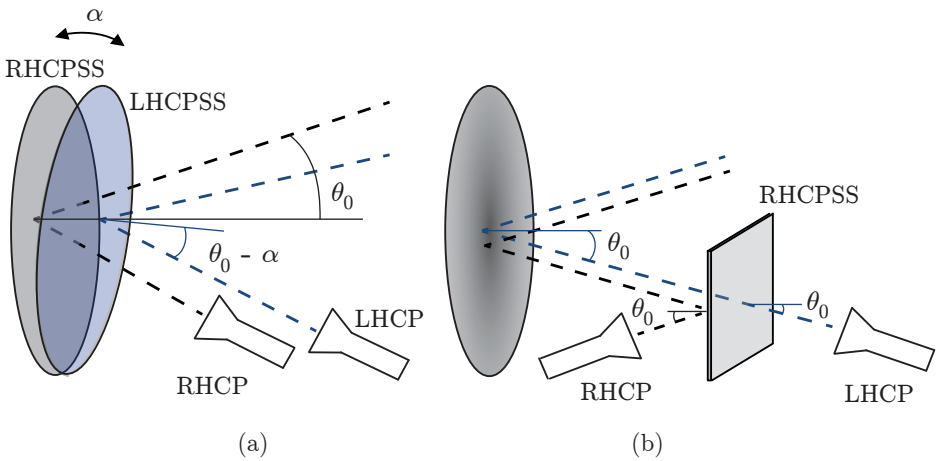

Figure 12: Concepts of satellite communication applications of CPSSs in the K_u- and K_a-bands. To the left the CPSS is implemented as curved surfaces in a shared aperture reflector antenna and to the right as a flat polarization diplexer.

curved CPSS. The offset angle of the front reflector α and the illumination angle from the feed θ_0 in Figure 12 (a) imply that the CPSS will operate at oblique angles of incidence in this application.

Another possible CPSS application is presented in Figure 12 (b), where the CPSS is used as a flat circular polarization diplexer with a solid reflector antenna [10] operating in the K_a-band, either in a downlink scenario ($19.2\,\text{GHz} < f < 20.2\,\text{GHz}$) as a transmitting system or in an uplink scenario ($29\,\text{GHz} < f < 30\,\text{GHz}$) as a receiving system. In this implementation the full CPSS does not need to be illuminated, as was the case in the previous implementation in Figure 12 (a). The fact that the diplexing surface is flat implies that the CPSS does not need to be curved in this application, which greatly improves the electromagnetic stability of the structure compared to a curved implementation. The magnitude of the design angle of incidence θ_0 and the incidence angle variations in the illumination of the CPSS depend on the antenna system design.

Both applications in Figure 12 (a)–(b) indicate that a CPSS that is implemented in a satellite communication system is required to operate at oblique angles of incidence. Stability with respect to the incidence angle θ and the incidence plane ϕ are crucial properties of a CPSS to be implemented in a realistic communication scenario.

5 Conclusions

A CPSS concept design based on closely spaced wire helices has been presented. The design was optimized using full wave simulations in a commercial software.

Simulation results demonstrate an improved stability with respect to variations of the incidence angle and a comparable bandwidth to previous resonant CPSS designs in [6, 8, 10, 11]. The design is scalable with respect to the frequency of operation and can be tuned to have maximum performance at an oblique angle of incidence. A parameter study was performed to analyze the key parameters of the CPSS, the design is relatively robust with respect to variations in the wire length or the wire position of the unit cell.

Two possible applications of our design have been suggested, where the CPSS could be implemented either in a shared aperture reflector antenna system in the K_u-band, or as a polarization diplexing surface in the K_a-band. A general conclusion is that to implement a CPSS in a space antenna system implies high demands on the CPSS to be robust with respect to its design parameters and the angle of incidence.

The choice of manufacturing procedures and materials will be studied further, along with experimental verification of the presented structure. The physical limitations of the design parameters will be examined from a space qualification perspective. Our concept design is a good candidate in the development of circular polarization diplexers and shared aperture CP reflectors for narrow band applications in future satellite communication systems.

Acknowledgments

The work reported in this paper was performed under ESA Contract No. 400010-8854/13/NL/MH. The data used to produce the results of this paper are available from the authors upon request (andreas.ericsson@eit.lth.se).

References

[1] M. Albani, P. Balling, L. Datashvili, G. Gerini, P. Ingvarson, K. Pontoppidan, M. Sabbadini, D. Sjöberg, S. Skokic, and G. Vecchi. Concepts for polarising sheets & "dual-gridded" reflectors for circular polarisation. In *ICECom Proceedings*, pp. 1–4, 2010.

[2] M. Baunge, H. Ekström, P. Ingvarson, and M. Petersson. A new concept for dual gridded reflectors. In *Proceedings of the fourth European Conference on Antennas and Propagation (EuCAP)*, pp. 1–5. IEEE, 2010.

[3] R. E. Collin. *Field Theory of Guided Waves*. IEEE Press, New York, NY, second edition, 1991.

[4] A. Ericsson and D. Sjöberg. A performance study of circular polarization selective structures. In *Proceedings of the 9th European Conference on Antennas and Propagation (EuCAP)*. IEEE, 2015.

[5] W. A. Imbriale, S. S. Gao, and L. Boccia, editors. *Space Antenna Handbook*. Wiley, 2012.

[6] G. Morin. Circular polarization selective surface made of resonant spirals, 1994. US Patent 5,280,298.

[7] G. A. Morin. A circular polarization selective surface made of resonant helices. Technical report, DTIC Document, 1995.

[8] R. Pierrot. Reflector for circularly polarized waves, 1970. US Patent 3,500,420.

[9] J. E. Roy and L. Shafai. Reciprocal circular-polarization-selective surface. *Antennas and Propagation Magazine, IEEE*, **38**(6), pp. 18–33, 1996.

[10] J. Sanz-Fernandez, E. Saenz, P. de Maagt, and C. Mangenot. Circular polarization selective surface for dual-optics CP offset reflector antennas in Ku-band. In *Proceedings of the 6th European Conference on Antennas and Propagation (EuCAP)*, pp. 2683–2687. IEEE, 2012.

[11] D. Tilston, M. Tilston, S. Tilston, W. V. Tilston, and T. Tralman. Polarization selective surface for circular polarization, 1991. US Patent 5,053,785.

A Performance Study of Circular Polarization Selective Structures

Paper II

Andreas Ericsson and Daniel Sjöberg

Published as: A. Ericsson, D. Sjöberg, "A Performance Study of Circular Polarization Selective Structures," *9th European Conference on Antennas and Propagation (EuCAP)*, pp. 1–5, 2015.

Abstract

A circular polarization selective structure (CPSS) reflects one handedness of circular polarization and transmits the other. In this paper the performance of a number of classical CPSS designs has been evaluated at the center frequency of operation for all possible spherical incidence angles. The results are presented in a compact way using two dimensional contour plots to represent the return loss, insertion loss and polarization purity of the transmitted and reflected signals. The results indicate that all CPSS designs presented up to date have preferred incidence planes of operation. The existence of geometrical symmetries in the designs affect the performance stability of the structures with respect to oblique angles of incidence. Applications of CPSSs in satellite communication systems, for example as a circular polarization dual aperture antenna or a circular polarization diplexer, require the structures to operate at wide ranges of oblique angles of incidence, making this type of analysis crucial for future development and evaluation of circular polarization selective structures.

1 Introduction

A strong driving force in the current development of satellite communication systems is the constant demand of increased data rates. Different schemes for increasing the communication link capacity of a satellite system have been identified such as utilizing higher frequency bands, enhanced power budgets, frequency and polarization reuse schemes, and polarization diplexing [1,4,10,11]. To achieve polarization selectivity is a simple task for linear polarizations [2], where a conductive strip grid acts as a polarization filter and reflects signals polarized parallel to the strips, while signals polarized perpendicular to the strips are transmitted. To achieve circular polarization selectivity is a more complicated task. Several structures have been proposed, among which three classical designs by Pierrot, Tilston, and Morin [7,8,13] are given extra attention in this paper. These designs are based on resonant structures, typically a quarter wavelength in thickness relative the propagation path, with less than 10% bandwidth and high sensitivity to angle of incidence variations.

A more broad band solution is presented in the cascading concept [5, 6, 9], which combines two circular-to-linear polarizers with a wire grid reflecting only one linear polarization. An even more broadband design is presented in [12] where meander line sheets are stacked close to each other, at a distance of $\lambda/8$, each with a rotation of 45° with respect to the previous layer. In [9] the performance of finite arrays of different classical CPSS designs was analyzed using an in-house method of moments (MoM) code. It is concluded that future development of CPSSs need to improve the performance at oblique angles of incidence, and that one way to achieve this is to design CPSSs with a two fold rotational symmetry. Up to date, the performance of most CPSS designs have been evaluated simply by plotting the return loss (RL), insertion loss (IL), and the transmission and reflection polarization purity, expressed either as axial ratio (AR) or cross polarization

discrimination (XPD), all as functions of frequency. This type of plots give a very limited insight in the performance of the structures as a function of the spherical angles of incidence (θ, ϕ). It has been concluded that the performance of the classical resonant CPSSs deteriorate at oblique angles of incidence, however, no information has previously been presented on the dependence of the performance of the structures with respect to which plane of oblique incidence angles that is considered.

2 CPSS performance analysis

The classical, resonant, CPSS designs by Pierrot, Tilston and Morin are studied at all possible incidence angles at the center frequency of operation ($f_0 = 12.7\,\mathrm{GHz}$). The performance of these designs is compared to that of a realistic design of the resonant two fold symmetrical CPSS presented in [3]. By illuminating the structures with a plane wave of LHCP/RHCP at the front/back side, the full (4×4) scattering matrix in circular polarizations ($\boldsymbol{S}^{\mathrm{CP}}$) of the structures is determined. By repeating the procedure for each combination of $\theta = 0°, 5°, ..., 85°$ and $\phi = 0°, 5°, ..., 355°$, a database of scattering data is generated for the device under test (DUT). When generating the result plots from this scattering database each incidence angle (defined by a θ, ϕ combination) corresponds to a point on a half sphere, as is illustrated in Figure 1. In this point a color coded pixel represent the performance of the DUT as RL, IL, $\mathrm{AR_r}$, or $\mathrm{AR_t}$ in dB, where indices r and t correspond to reflection and transmission, respectively. If we observe this half sphere from above, as in Figure 1 the circular polarization selectivity of the DUT is plotted as polar contour plots for all incidence angles when the structure is illuminated from the front side. The radius of the polar plot corresponds to $\sin\theta$ so that the cartesian coordinates are $x = \sin\theta\cos\phi$, and $y = \sin\theta\sin\phi$, with the z-axis pointing towards the reader, as is shown in Figure 1. If the structure instead is illuminated from the back side the same half sphere can be defined and the performance of the DUT is plotted in the same manner, where the z-axis is pointing out of the paper for both front and back illumination.

The geometry of each of the CPSSs that were studied is presented in Figure 2, and the values of the design parameters are presented in Table 1, where the wires in the first three models are modeled as perfectly conducting wires hanging in free space. The wire radius is denoted a, w is the wire separation, the length of the wire component in the x-direction is denoted l_{x} and the length of the wire component in the z-direction, which is typically about $\lambda/4$ in all designs described in this paper, is denoted l_{z}. In the Pierrot and the double Morin designs the period of the unit cell in the horizontal and vertical direction are denoted P_{x}, P_{y} and in the Tilston and Morin designs the periods P_{x}, P_{y} are defined as the diagonals of the unit cells in Figure 2. In the Tilston design ϵ_{r} is the relative permittivity of the dielectric cylinder and in the double Morin design ϵ_{r} corresponds to the relative permittivity of the background material that the

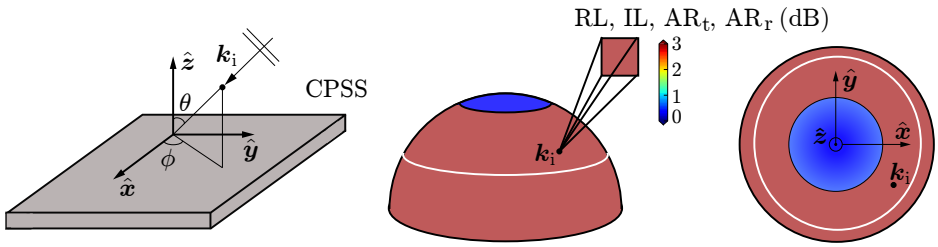

Figure 1: Description of how the result plots are generated. Each direction of incidence corresponds to a combination of the angles θ, ϕ. The performance at each incidence angle of a device under test can be plotted on a half sphere for front side illumination and another half sphere for back side illumination. By viewing the color coded sphere from above a contour plot is realized, where each point on the disc corresponds to the performance of the CPSS at a specific combination of θ, ϕ. The white circle corresponds to the points ($\theta = 50°, \phi \in [0, 2\pi)$).

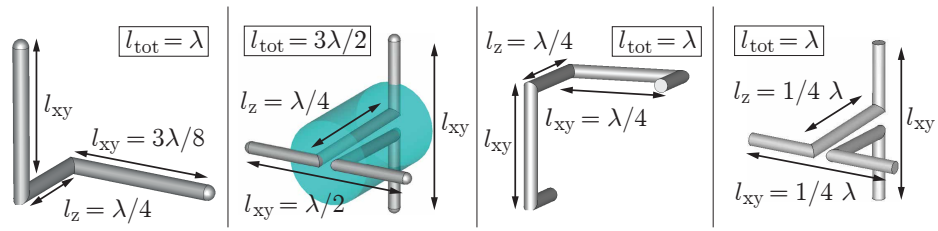

Figure 2: Four resonant CPSSs that have been implemented in a commercial computational software for simulation. To the far left is the Pierrot design, next is the Tilston design, after that is the Morin helix design and finally to the far right is the double Morin design presented in [3].

wires are threaded through. In the double Morin design losses are included to the background material $\tan(\delta) = 0.0017$ and to the metal wires which are modeled as copper wires with $\sigma = 5.8 \cdot 10^7\,\mathrm{S/m}$.

Each design was optimized with respect to the requirements defined in (2.1) to minimize the total penalty function $\mathcal{P}$ for normal incidence:

$$\mathcal{P} = \frac{1}{(f_2 - f_1)} \int_{f_1}^{f_2} (\mathrm{RL} + \mathrm{IL} + \mathrm{AR_r} + \mathrm{AR_t})\ \mathrm{d}f, \tag{2.1}$$

where the frequencies of optimization f_1, f_2 were defined such that the center frequency of operation should be $f_0 = 12.7\,\mathrm{Ghz}$ corresponding to the satellite communication downlink $\mathrm{K_u}$ band. Once the optimum designs were found the scattering data for all incidence angles were generated.

Table 1: Design parameters of the studied CPSSs in millimeters.

CPSS	l_{xy}	l_z	l_{tot}	a	P_x	P_y	ϵ_r	w
Pierrot	9.46	6.00	15.5	0.29	12.4	12.1	-	-
Morin	8.77	5.94	15.7	0.10	12.4	3.11	-	-
Tilston	13.8	5.89	19.7	0.10	11.6	11.2	4.38	0.3
Dbl. Morin	6.05	5.37	14.4	0.04	14.4	14.4	1.17	0.3

3 Results

A full wave frequency domain solver is utilized and the CPSSs are modeled as single unit cells, corresponding to two dimensional periodic structures of infinite extent. A tetrahedral mesh is utilized, where the Pierrot design consists of 44 000 mesh elements, utilizing 6 Gb of RAM and finishing the full set of simulations ($18 \times 72 = 1296$ simulations) in approximately 96 hours, corresponding to 4.5 minutes per simulation. The Morin and double Morin designs consist of approximately the same number of mesh elements as the Pierrot design, they have roughly the same memory requirements and finishes the full set of simulations in approximately the same time. The Tilston design consists of roughly the same number of mesh elements as the other designs. Due to the fact that it has a larger unit cell than the others, with a side length of approximately half a wavelength, it finishes the full set of simulations in approximately 200 hours, which is about twice the computational time of the other designs.

The output data consist of scattering matrices corresponding to all possible combinations of the incidence angle (θ) and incidence plane (ϕ), at a great number of frequency points in a predefined frequency range. The white circles in Figures 3–6 indicate $\theta = 10°, 20°, 30°$, and all values are in dB. The solid black contours in Figures 3–6 are the design requirements defined in [1] (0.5 dB for return loss and insertion loss, 0.78 dB for axial ratio, corresponding to 27 dB XPD), and the dashed black contours are the relaxed requirements for the axial ratio (1.74 dB, or 20 dB XPD).

The results of the Pierrot design in Figure 3 indicate that the performance is very limited to a specific plane of incidence ($\phi \approx 45°$), but it can also be seen that the AR curves for transmission and reflection are not optimal in the same plane of incidence. This indicates that the performance of this design is not sufficient at oblique angles of incidence. When comparing the results for front and back illumination in Figure 3 it is seen that the results are mirror images of each other with respect to the plane at $\phi = 45°$. This is due to the particular rotational symmetry of the geometry. Note that the insertion loss is mirror symmetric for front and back illumination, which is explained by reciprocity (insertion loss is the same regardless of which side is illuminated).

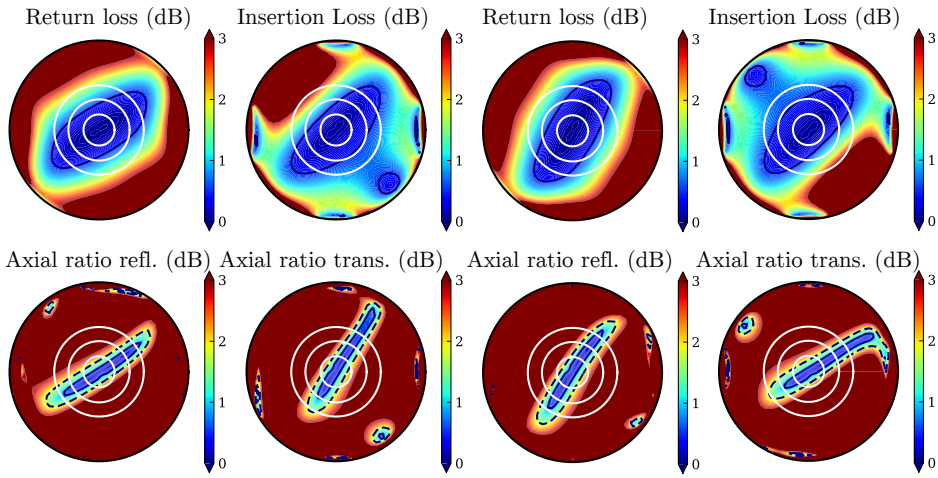

Figure 3: Simulation results of the Pierrot CPSS at the center frequency of operation $f = 12.7$ GHz. The four leftmost plots correspond to front side illumination and the four rightmost plots correspond to back side illumination. For each illumination scenario the left plots show the return loss and axial ratio of the reflected signal, and the right plots correspond to the insertion loss and axial ratio of the transmitted signal.

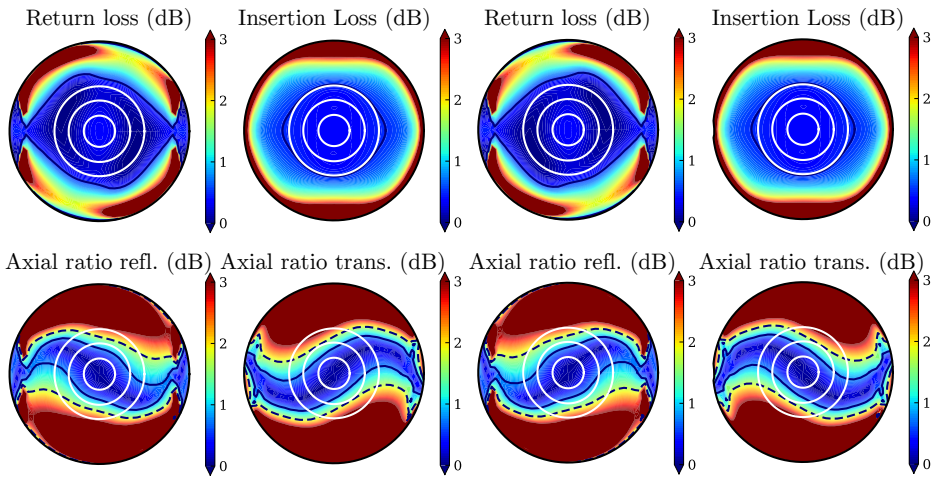

Figure 4: Simulation results of the Morin CPSS at the center frequency of operation $f = 12.7$ GHz. The four leftmost plots correspond to front side illumination and the four rightmost plots correspond to back side illumination. For each illumination scenario the left plots show the return loss and axial ratio of the reflected signal, and the right plots correspond to the insertion loss and axial ratio of the transmitted signal.

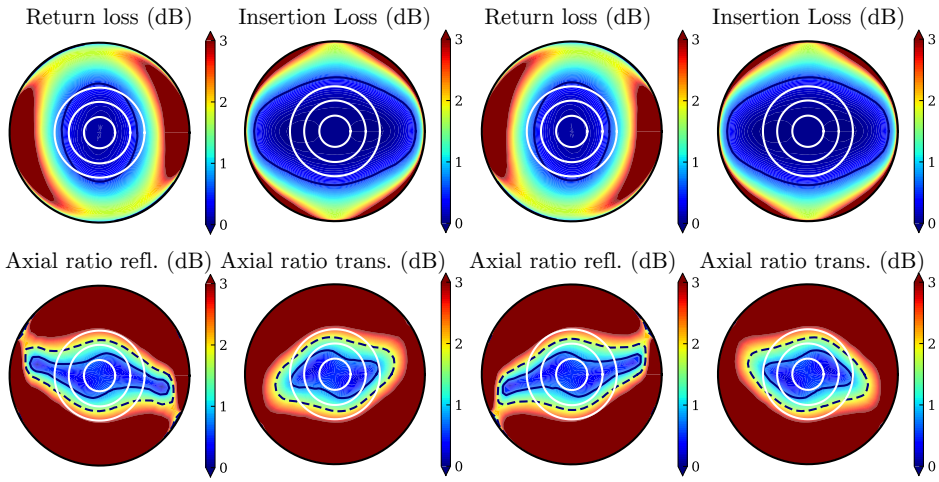

Figure 5: Simulation results of the Tilston CPSS at the center frequency of operation $f = 12.7$ GHz. The four leftmost plots correspond to front side illumination and the four rightmost plots correspond to back side illumination. For each illumination scenario the upper and lower left plots show the return loss and axial ratio of the reflected signal, and the upper and lower right plots correspond to the insertion loss and axial ratio of the transmitted signal.

The results in Figure 4, corresponding to the Morin design, have a much larger blue region than the Pierrot design, which implies that this design provides an improved stability with respect to the angle of incidence. The Morin CPSS also has a preferred plane of incidence ($\phi \approx 0°$) corresponding to the orientation of the wire helices, and it can be seen that also in this design the axial ratio curves for transmission and reflection are not optimal in the same plane of incidence. In [9] it was concluded that the two-fold symmetry of the Tilston design improves the stability with respect tot the angle of incidence. In Figure 5 this is verified by the fact that the axial ratio curves are aligned. The great improvement in the insertion loss of the Tilston design compared to the Pierrot, and Morin comes from the fact that the Tilston unit cell is larger than the others, which implies a more sparse periodic structure.

The three classical CPSS designs discussed above were compared to a realistic design case of the double Morin CPSS presented in [3] and the results of this design are presented in Figure 6. This design possess the two fold rotational symmetry as the Tilston design, but the axial ratio curves are not completely aligned in this design. This might be due to the fact that the axial ratio curves of the Morin design in Figure 4 are mirror symmetric with respect to each other. One can also notice that out of the four designs this structure has the largest region of blue-green color in its axial ratio patterns. This implies an improved stability with respect to oblique angles of incidence, and also to variations with

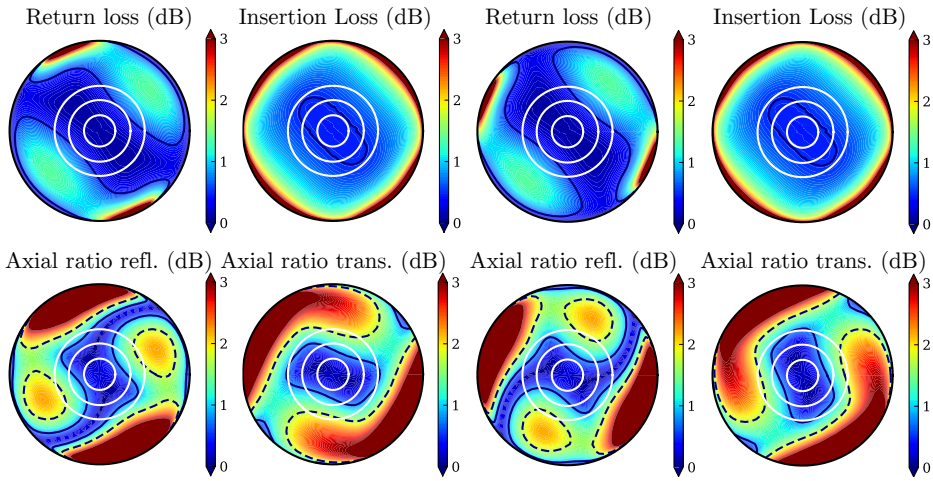

Figure 6: Simulation results of a realistic design case of the CPSS presented in [3] at the center frequency of operation $f = 12.7$ GHz. The four leftmost plots correspond to front side illumination and the four rightmost plots correspond to back side illumination. For each illumination scenario the left plots show the return loss and axial ratio of the reflected signal, and the right plots correspond to the insertion loss and axial ratio of the transmitted signal.

respect to the plane of incidence ϕ. It can be seen that the realistic design has reduced performance with respect to the insertion loss when compared to the ideal, lossless, designs. This is to be expected, both from the fact that losses are added to the model and as a consequence of placing two Morin helices in one unit cell and thus adding more material to the design.

When implementing a CPSS in a satellite communication system, either as a circular polarization dual aperture antenna or as a flat circular polarization diplexer, the structure must be aligned with respect to the offset angle of the feed antennas such that the CPSS is illuminated in its preferred plane of operation. Also, one has to consider that the optimum plane of incidence of the CPSS can be different depending on if the structure is illuminated from the front or the back side.

4 Conclusions

Classical CPSS designs by Pierrot, Tilston and Morin have been analyzed, together with a realistic double Morin design, at all possible angles of incidence. The results of the study are plotted in a compact and illustrative way, using two dimensional polar contour plots, at the center frequency of operation of the structures. The results indicate that all CPSS designs have preferred planes of

incidence, and at oblique angles of incidence the response of a structure can be different depending on from which side the structure is illuminated. The Pierrot design has a very limited angular region of operation in comparison to the other designs. Together with a traditional CPSS analysis, where the performance is plotted as a function of frequency for fixed angles of incidence, this type of study provides a complete performance evaluation of both classical CPSS designs and future concepts. It reveals strengths and weaknesses of the structures that were previously unaccounted for.

Acknowledgment

The work reported in this paper was performed under ESA Contract No. 4000108854/rg/NL/MH.

References

[1] M. Albani, P. Balling, L. Datashvili, G. Gerini, P. Ingvarson, K. Pontoppidan, M. Sabbadini, D. Sjöberg, S. Skokic, and G. Vecchi. Concepts for polarising sheets & "dual-gridded" reflectors for circular polarisation. In *ICECom Proceedings*, pp. 1–4, 2010.

[2] M. Baunge, H. Ekström, P. Ingvarson, and M. Petersson. A new concept for dual gridded reflectors. In *Proceedings of the fourth European Conference on Antennas and Propagation (EuCAP)*, pp. 1–5. IEEE, 2010.

[3] A. Ericsson and D. Sjöberg. A resonant circular polarization selective structure of closely spaced Morin helices. In *International Union for Radio Science (URSI) 2014 Proceedings of the Third Conference on*, pp. 1–5. IEEE, 2014.

[4] W. A. Imbriale, S. S. Gao, and L. Boccia, editors. *Space Antenna Handbook*. Wiley, 2012.

[5] M. Joyal and J. Laurin. A cascaded circular-polarization-selective surface at K band. In *Antennas and Propagation (APSURSI), 2011 IEEE International Symposium on*, pp. 2657–2660. IEEE, 2011.

[6] M. Joyal and J. Laurin. Design and analysis of a cascade circular-polarization-selective surface at K band. *IEEE Trans. Antennas Propag.*, **62**(6), pp. 3043–3052, 2014.

[7] G. Morin. Circular polarization selective surface made of resonant spirals, 1994. US Patent 5,280,298.

[8] R. Pierrot. Reflector for circularly polarized waves, 1970. US Patent 3,500,420.

[9] J. E. Roy and L. Shafai. Reciprocal circular-polarization-selective surface. *Antennas and Propagation Magazine, IEEE*, **38**(6), pp. 18–33, 1996.

[10] J. Sanz-Fernandez, E. Saenz, P. de Maagt, and C. Mangenot. Circular polarization selective surface for dual-optics CP offset reflector antennas in Ku-band. In *Proceedings of the 6th European Conference on Antennas and Propagation (EuCAP)*, pp. 2683–2687. IEEE, 2012.

[11] M. Schneider, C. Hartwanger, and H. Wolf. Antennas for multiple spot beam satellites. *CEAS Space Journal*, **2**(1-4), pp. 59–66, 2011.

[12] D. Sjöberg and A. Ericsson. A multi layer meander line circular polarization selective structure (MLML-CPSS). In *Proceedings of the 8th European Conference on Antennas and Propagation (EuCAP)*, pp. 464–468. IEEE, 2014.

[13] D. Tilston, M. Tilston, S. Tilston, W. V. Tilston, and T. Tralman. Polarization selective surface for circular polarization, 1991. US Patent 5,053,785.

Design and Analysis of a Multilayer Meander Line Circular Polarization Selective Structure

Paper III

Andreas Ericsson and Daniel Sjöberg

Published as: A. Ericsson and D. Sjöberg, "Design and Analysis of a Multilayer Meander Line Circular Polarization Selective Structure," *IEEE Transactions on Antennas and Propagation*, Vol. 65, No. 8, pp. 4089–4101, 2017.

Abstract

We present a non-resonant circular polarization selective structure based on multiple layers of stacked meander line sheets arranged closely after each other. The structure has a total thickness of 13.5 mm (0.68 wavelengths at center frequency 15 GHz) and is realized by cascading printed circuit boards interspaced with a low permittivity foam material, and the different layers are bonded together with thin layers of adhesive spray. A design procedure is presented that can be used to optimize the proposed structure based on its target band of operation. Based on this method, an optimized design has been simulated and the structure shows a return loss and insertion loss better than 0.5 dB, and axial ratio in transmission and reflection better than 0.78 dB, over a fractional bandwidth of 45.8 % at normal incidence, fully covering the K_u-band 12–18 GHz. The functionality of the structure has been verified experimentally through measurements, both in reflection and transmission, with a total bandwidth of 42.0 %, covering 86.7 % of the K_u-band. The simulated performance at oblique angles of incidence shows significant improvements when compared to classical resonant circular polarization selective structures.

1 Introduction

The constant demand for increased data rates in satellite communication systems is a strong driving force in the development of new technology [15, 24]. Meanwhile, the physical aperture of a satellite available for the communication payload, such as communication antennas, receivers and transmitters, is very limited. This implies that a crucial task to achieve maximum performance of a communication satellite is to optimize the use of the available aperture. In recent years, different schemes have been identified to increase the data throughput of a satellite communication system, and it has been shown that the total throughput can be significantly improved by utilizing polarization- and frequency reuse schemes [4, 5, 15, 24, 27].

Polarization reuse can be achieved in linear polarization simply by separating signals using a strip grid of conducting wires, where signals polarized parallel to the wires are reflected and signals polarized perpendicular to the wires are transmitted [5]. In satellite communication systems, it is preferable to utilize circularly polarized signals, which eliminates the problem of aligning receiving antennas with the polarization of the incident signals. This implies that it is crucial to be able to filter signals of different circular polarization (CP). Unfortunately, this is not as easy as filtering signals of linear polarization. It was proven in [26] that in order for a structure to possess circular polarization selectivity, it has to have an extent in the direction of propagation of the incident signal. In this paper, the focus is set on structures that possess circular polarization selectivity both in transmission and reflection.

Many circular polarization selective structures (CPSS) have been presented over the last 50 years. The first design was presented by Pierrot in 1966, and

is based on a periodic array of one wavelength long resonant wires bent in the shape of a crank, and it has a bandwidth of about 10 % at normal incidence [23]. This type of structure has been realized in different shapes, using innovative manufacturing techniques, and measured in transmission in [11, 19, 20] and both in transmission and reflection in [27]. Recently, a similar structure was presented in [25], where the concept behind the Pierrot element is utilized to create a reciprocal CPSS molecule. In 1991, Tilston presented a resonant structure based on two one half wavelength long wires connected with a transmission line with physical length of a quarter wavelength and electrical length of half a wavelength [34]. The bandwidth of this structure is comparable to the Pierrot design, but it shows a slightly improved stability with respect to variations in the angle of incidence. Another resonant design, based on continuous wires bent in the shape of helices, was presented by Morin in 1996 [22].

A common remark on these structures, which we refer to as classical resonant CPSS designs, is that they all have a relatively narrow bandwidth and their performance deteriorate at oblique angles of incidence. In [26], these designs were evaluated and it was concluded that structures that possess a two-fold rotational symmetry possess an improved stability with respect to the angle of incidence. This idea was utilized in [10], where a modified version of the Morin CPSS in [22] consisting of closely spaced helices was presented. The bandwidth of this design is comparable to previous resonant CPSS, about 10 %, but a significant improvement in angular stability is achieved.

As opposed to the classical resonant designs, a non-resonant CPSS concept realized by cascading two polarizers and one linear polarization diplexer is presented by Joyal and Laurin in [16–18]. Each polarizer consists of three layers of printed meander lines, leading to a total of seven layers including the wire grid diplexer. The improvement in bandwidth of this structure is significant compared to the classical designs. The total thickness of this structure is 24 mm, which corresponds to 1.5 wavelengths ($1.5\lambda_0$) at the center frequency of 19 GHz, and it shows a 3 dB axial ratio fractional bandwidth of 26 %. However, for every layer that is introduced the insertion loss of the CPSS increases, and the fact that the structure is relatively thick with respect to the wavelength of the incident signal is undesirable. An alternative design utilizing the same concept (polarizer, grid diplexer, polarizer) was recently presented in [2, 3], where a wider bandwidth and an improved angle of incidence stability are achieved compared to [16–18]. However, this requires a more complex structure composed of ten substrates and fourteen printed layers, which negatively affects the overall insertion loss. Also, the axial ratio of this design is on the order of 4–5 dB, which does not meet the strict requirements of satellite communication systems.

In the last ten years, novel resonant CPSS designs without conducting vias have been presented. In [33] a three layer CPSS utilizing coupling through L-shaped traces is demonstrated, and in [32] a structure consisting of two closely spaced layers of split ring resonators is introduced. Recently, a multilayer CPSS consisting of tensor impedance surfaces was presented in [29]. All these designs provide a very narrow bandwidth, but the structures can be made very thin with

respect to the center wavelength of operation.

Structures possessing circular polarization selectivity have also been developed for optical frequencies. A design for visible light based on rotating dipoles is presented in [36], where it is shown that the performance of the structure improves with the number of layers, but only transmission results are given. In [12], another design for optical frequencies is presented, consisting of metal helices attached to a substrate. This structure has a wide bandwidth but the helices become very large when scaled to microwave frequencies, where each spiral has an electrical length corresponding to multiple wavelengths of the incident signal. Also, the performance of this structure was only investigated in transmission.

It can be concluded that all the circular polarization selective designs satisfying strict demands presented up to date have a relatively narrow frequency band of operation, and are sensitive to variations in the angle of incidence, especially the resonant structures based on bent wire cranks [26]. In [9], it was shown that, at oblique angles of incidence, the performance of a CPSS is also strongly dependent on what incidence plane is considered, and that the classical designs like those by Pierrot, Tilston, and Morin all have a preferred incidence plane of operation. This implies that to meet the high requirements for satellite communication applications, a novel CPSS should have a wide bandwidth and show significant stability with respect to variations in the angle of incidence. Also, a CPSS with multiple incidence planes of operation would improve the design freedom of the feed placement when implementing the structure in a satellite communication system.

In this paper, we present a thorough analysis of a novel non-resonant CPSS that was first presented in [31]. This design possesses a significantly improved bandwidth compared to previous designs and it shows promising stability with respect to variations in the angle of incidence. Simulation data indicate that, due to the high degree of symmetry of the structure, the design has multiple incidence planes of operation. This is a useful feature when implementing a CPSS in a satellite communication system. Our novel design is based on a material concept first presented in [35] for a polarization rotator, and is similar to the structure in [16–18], with an electrical design based on rotating meander lines enabling the use of fewer layers, resulting in a thinner multilayer structure than [18]. The bandwidth of our design is presented in Table 1, where a performance comparison to some of the CPSSs presented up to date is presented, based on the design requirements from [4, 28]. Since not all designs were made with these strict requirements in mind, we also present results for relaxed requirements to give a fair comparison. The bandwidth of most competing designs is mainly limited by high insertion loss, especially with respect to the strict design requirements in Table 1.

The paper is organized as follows: in Section 2, the theory of designing a CPSS from linear elements is presented. By calculating the scattering matrix components of cascaded linear grids with a relative rotation, and transforming the scattering matrix to a circular polarization representation, the functionality of the structure is derived. In Section 3, our novel design is presented and

Table 1: Bandwidth over which each CPSS satisfies all requirements: IL and RL better than 0.5 dB, and AR_t and AR_r better than 0.78 dB, or the relaxed requirements of IL and RL better than 1.0 dB and AR_t and AR_r better than 3.0 dB.

Reference	Simulated/ measured	Bandwidth strict (%)	Bandwidth relaxed (%)	Thickness
Fusco [11]	measured	0.0	2.0	$0.25\lambda_0$
Lopez [19]	measured	0.0	< 5.0	$0.25\lambda_0$
Sanz-Fernandez [27]	measured	7.0	11.0	$0.25\lambda_0$
Ericsson [10]	simulated	8.0	20.0	$0.25\lambda_0$
Joyal [18]	measured	3.0	26.0	$1.50\lambda_0$
Abadi [2]	simulated	0.0	<20.0	$0.23\lambda_0$
Tarn [33]	measured	0.0	<5.0	$0.18\lambda_0$
Present work	simulated	45.9	56.1	$0.68\lambda_0$
	measured	42.0	53.7	

its possible applications in satellite communication systems are discussed. The optimization scheme that was used to generate the end design is described in Section 4, and simulation results of the optimized design are presented in Section 5. An experimental verification of the functionality of the structure is presented in Section6, and some concluding remarks are given in Section 7.

2 Circular polarization selectivity from linear elements

The archetypical linearly polarized element is a strip. The reflection coefficient of a periodic arrangement of strips, illuminated perpendicularly to the surface, is dependent on the polarization of the incident field. This type of scattering problem can be modeled using transmission line theory, where the strip grid is modeled as a lumped capacitance or inductance utilizing approximate expressions in [21, p.227]

$$L \approx \frac{\mu_0 a}{2\pi} \ln\left(\frac{2a}{\pi w}\right), \qquad C \approx 4\frac{\epsilon_0 a}{2\pi} \ln\left(\frac{2a}{\pi d}\right), \tag{2.1}$$

where a is the period of the strips, w is the strip width, and d is the gap between the strips, as can be seen in Figure 1. The permeability and permittivity of vacuum are denoted by μ_0 and ϵ_0, respectively. These expressions are valid when $a \ll \lambda$, and more or less complicated correction terms can be found in [21], but the

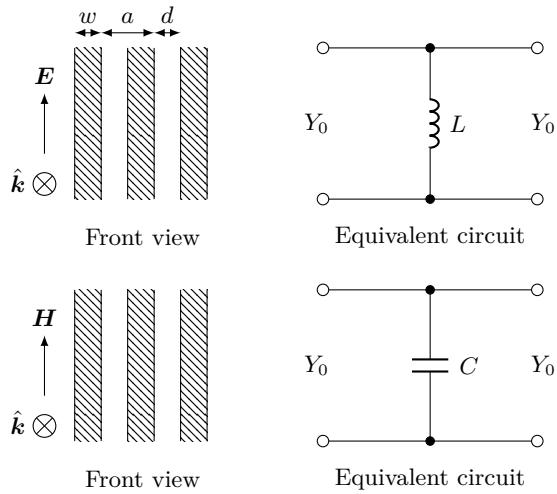

Figure 1: Equivalent circuit models for scattering against infinitely thin metal strips [30], where the direction of propagation is given by $\hat{\boldsymbol{k}}$. In the scenario at the top, where the incident electric field is polarized parallel to the strips, the structure is perceived as a shunt inductance and in the case at the bottom, where the magnetic field is polarized parallel to the strips, the structure is perceived as a shunt capacitance.

range of possible L and C is characterized rather well by these simple formulas. In general, the reflection coefficient for a transmission line with characteristic admittance Y_0 which is shunted with an admittance Y is

$$r = \frac{Y_0 - (Y + Y_0)}{Y_0 + Y + Y_0} = \frac{-Y/(2Y_0)}{1 + Y/(2Y_0)}, \tag{2.2}$$

where $Y = 1/(\mathrm{j}\omega L)$ for an inductive strip and $Y = \mathrm{j}\omega C$ for a capacitive strip. For a plane wave impinging on the strip grid at normal incidence, we have $Y_0 = \sqrt{\epsilon_0/\mu_0} = 2.65\,\mathrm{mS}$.

Assume a linearly polarized element, with zero thickness in the z-direction, with reflection coefficients r_x and r_y in its principal polarizations x and y modeled by an inductance L and a capacitance C

$$r_x = \frac{Y_0 - (Y_0 + 1/(\mathrm{j}\omega L))}{Y_0 + Y_0 + 1/(\mathrm{j}\omega L)} = -\frac{1}{1 + \mathrm{j}\omega L 2Y_0}, \tag{2.3}$$

$$r_y = \frac{Y_0 - (Y_0 + \mathrm{j}\omega C)}{Y_0 + Y_0 + \mathrm{j}\omega C} = -\frac{\mathrm{j}\omega C/(2Y_0)}{1 + \mathrm{j}\omega C/(2Y_0)}. \tag{2.4}$$

Given zero thickness, the transmission coefficients are then $t_{x,y} = 1 + r_{x,y}$. When tilting the element at an angle φ from the x-axis, the scattering matrix in linear

polarization is given by

$$
\begin{aligned}
S_{\text{grid}}^{\text{LP}} &= \begin{pmatrix} S_{11}^{\text{XX}} & S_{11}^{\text{XY}} & S_{12}^{\text{XX}} & S_{12}^{\text{XY}} \\ S_{11}^{\text{YX}} & S_{11}^{\text{YY}} & S_{12}^{\text{YX}} & S_{12}^{\text{YY}} \\ S_{21}^{\text{XX}} & S_{21}^{\text{XY}} & S_{22}^{\text{XX}} & S_{22}^{\text{XY}} \\ S_{21}^{\text{YX}} & S_{21}^{\text{YY}} & S_{22}^{\text{YX}} & S_{22}^{\text{YY}} \end{pmatrix} \\
&= \begin{pmatrix} \cos\varphi & -\sin\varphi & 0 & 0 \\ \sin\varphi & \cos\varphi & 0 & 0 \\ 0 & 0 & \cos\varphi & -\sin\varphi \\ 0 & 0 & \sin\varphi & \cos\varphi \end{pmatrix} \begin{pmatrix} r_x & 0 & t_x & 0 \\ 0 & r_y & 0 & t_y \\ t_x & 0 & r_x & 0 \\ 0 & t_y & 0 & r_y \end{pmatrix} \\
&\qquad \begin{pmatrix} \cos\varphi & \sin\varphi & 0 & 0 \\ -\sin\varphi & \cos\varphi & 0 & 0 \\ 0 & 0 & \cos\varphi & \sin\varphi \\ 0 & 0 & -\sin\varphi & \cos\varphi \end{pmatrix}, \qquad (2.5)
\end{aligned}
$$

where each entry in the matrix is defined as $S_{mn}^{kl} = E_m^k / E_{n0}^l$, E_m^k is the total outgoing field at port m with the polarization k and E_{n0}^l is the incident field from port n with the polarization l, and when all other ports are not excited and terminated with their characteristic impedance. The scattering matrix in circular polarization, using the IEEE standard [14, p.61–77], $\mathrm{e}^{\mathrm{j}\omega t}$ time convention, and defining the z-axis as pointing from port 1 towards port 2, can be identified as

$$
\begin{aligned}
S^{\text{CP}} &= \begin{pmatrix} S_{11}^{\text{RR}} & S_{11}^{\text{RL}} & S_{12}^{\text{RR}} & S_{12}^{\text{RL}} \\ S_{11}^{\text{LR}} & S_{11}^{\text{LL}} & S_{12}^{\text{LR}} & S_{12}^{\text{LL}} \\ S_{21}^{\text{RR}} & S_{21}^{\text{RL}} & S_{22}^{\text{RR}} & S_{22}^{\text{RL}} \\ S_{21}^{\text{LR}} & S_{21}^{\text{LL}} & S_{22}^{\text{LR}} & S_{22}^{\text{LL}} \end{pmatrix} \\
&= \frac{1}{2} \begin{pmatrix} 1 & -\mathrm{j} & 0 & 0 \\ 1 & \mathrm{j} & 0 & 0 \\ 0 & 0 & 1 & \mathrm{j} \\ 0 & 0 & 1 & -\mathrm{j} \end{pmatrix} \begin{pmatrix} S_{11}^{\text{XX}} & S_{11}^{\text{XY}} & S_{12}^{\text{XX}} & S_{12}^{\text{XY}} \\ S_{11}^{\text{YX}} & S_{11}^{\text{YY}} & S_{12}^{\text{YX}} & S_{12}^{\text{YY}} \\ S_{21}^{\text{XX}} & S_{21}^{\text{XY}} & S_{22}^{\text{XX}} & S_{22}^{\text{XY}} \\ S_{21}^{\text{YX}} & S_{21}^{\text{YY}} & S_{22}^{\text{YX}} & S_{22}^{\text{YY}} \end{pmatrix} \begin{pmatrix} 1 & 1 & 0 & 0 \\ -\mathrm{j} & \mathrm{j} & 0 & 0 \\ 0 & 0 & 1 & 1 \\ 0 & 0 & \mathrm{j} & -\mathrm{j} \end{pmatrix}. \qquad (2.6)
\end{aligned}
$$

By combining the expressions (2.5)–(2.6) and collecting the results, we get the following representation of the scattering matrix in circular polarization

$$
\begin{aligned}
S_{\text{grid}}^{\text{CP}} &= \frac{r_x - r_y}{2} \begin{pmatrix} \mathrm{e}^{-2\mathrm{j}\varphi} & 0 & 0 & \mathrm{e}^{-2\mathrm{j}\varphi} \\ 0 & \mathrm{e}^{2\mathrm{j}\varphi} & \mathrm{e}^{2\mathrm{j}\varphi} & 0 \\ 0 & \mathrm{e}^{2\mathrm{j}\varphi} & \mathrm{e}^{2\mathrm{j}\varphi} & 0 \\ \mathrm{e}^{-2\mathrm{j}\varphi} & 0 & 0 & \mathrm{e}^{-2\mathrm{j}\varphi} \end{pmatrix} \\
&\qquad + \frac{r_x + r_y}{2} \begin{pmatrix} 0 & 1 & 1 & 0 \\ 1 & 0 & 0 & 1 \\ 1 & 0 & 0 & 1 \\ 0 & 1 & 1 & 0 \end{pmatrix} + \begin{pmatrix} 0 & 0 & 1 & 0 \\ 0 & 0 & 0 & 1 \\ 1 & 0 & 0 & 0 \\ 0 & 1 & 0 & 0 \end{pmatrix}. \qquad (2.7)
\end{aligned}
$$

The ideal scattering matrix for a symmetric left hand circular polarization selec-

tive structure (LHCPSS) is

$$S^{\mathrm{CP}} = \begin{pmatrix} S_{11}^{\mathrm{RR}} & S_{11}^{\mathrm{RL}} & S_{12}^{\mathrm{RR}} & S_{12}^{\mathrm{RL}} \\ S_{11}^{\mathrm{LR}} & S_{11}^{\mathrm{LL}} & S_{12}^{\mathrm{LR}} & S_{12}^{\mathrm{LL}} \\ S_{21}^{\mathrm{RR}} & S_{21}^{\mathrm{RL}} & S_{22}^{\mathrm{RR}} & S_{22}^{\mathrm{RL}} \\ S_{21}^{\mathrm{LR}} & S_{21}^{\mathrm{LL}} & S_{22}^{\mathrm{LR}} & S_{22}^{\mathrm{LL}} \end{pmatrix} = \begin{pmatrix} 0 & 0 & \mathrm{e}^{-\mathrm{j}\phi_{\mathrm{t}}} & 0 \\ 0 & \mathrm{e}^{-\mathrm{j}\phi_{\mathrm{r}}} & 0 & 0 \\ \mathrm{e}^{-\mathrm{j}\phi_{\mathrm{t}}} & 0 & 0 & 0 \\ 0 & 0 & 0 & \mathrm{e}^{-\mathrm{j}\phi_{\mathrm{r}}} \end{pmatrix}, \tag{2.8}$$

where ϕ_{r} is the phase of the reflection coefficient, and ϕ_{t} is the phase of the transmission coefficient. The expression (2.8) clearly cannot be achieved with a single surface, but we are now ready to motivate our concept design. For simplicity, assume that $r_y = 0$ and $r_x = r$, so that

$$S_{\mathrm{grid}}^{\mathrm{CP}} = \frac{r}{2} \begin{pmatrix} \mathrm{e}^{-2\mathrm{j}\varphi} & 1 & 1 & \mathrm{e}^{-2\mathrm{j}\varphi} \\ 1 & \mathrm{e}^{2\mathrm{j}\varphi} & \mathrm{e}^{2\mathrm{j}\varphi} & 1 \\ 1 & \mathrm{e}^{2\mathrm{j}\varphi} & \mathrm{e}^{2\mathrm{j}\varphi} & 1 \\ \mathrm{e}^{-2\mathrm{j}\varphi} & 1 & 1 & \mathrm{e}^{-2\mathrm{j}\varphi} \end{pmatrix} + \begin{pmatrix} 0 & 0 & 1 & 0 \\ 0 & 0 & 0 & 1 \\ 1 & 0 & 0 & 0 \\ 0 & 1 & 0 & 0 \end{pmatrix}. \tag{2.9}$$

Now, assume we have two sheets separated a distance d with the relative rotation φ, both with the reflection coefficient $|r| \ll 1$. In the single scattering approximation, the total reflection coefficients from the left, with reference plane at the left-most sheet, can then be written

$$S_{11}^{\mathrm{RR}} = \frac{r}{2}\left(1 + \mathrm{e}^{-2\mathrm{j}kd}\mathrm{e}^{-2\mathrm{j}\varphi}\right), \tag{2.10}$$

$$S_{11}^{\mathrm{RL}} = S_{11}^{\mathrm{LR}} = \frac{r}{2}\left(1 + \mathrm{e}^{-2\mathrm{j}kd}\right), \tag{2.11}$$

$$S_{11}^{\mathrm{LL}} = \frac{r}{2}\left(1 + \mathrm{e}^{-2\mathrm{j}kd}\mathrm{e}^{2\mathrm{j}\varphi}\right), \tag{2.12}$$

where the exponential $\mathrm{e}^{-2\mathrm{j}kd}$ corresponds to the two-way delay between the sheets. A bounce diagram for the co-polarized reflection and transmission of the sheets, illuminated by an LHCP wave, is presented in Figure 2. For a symmetric structure, these expressions also apply to the S_{22} elements. By choosing the separation and relative rotation of the sheets according to

$$kd = \varphi = \pi/4 \tag{2.13}$$

we can achieve polarization selectivity in reflection, since then S_{11}^{LL} is maximized and S_{11}^{RR} is minimized. Furthermore, it can be seen that by choosing the positions and rotations according to

$$kd = -\varphi = \pi/4 \tag{2.14}$$

we can achieve polarization selectivity in reflection for the orthogonal polarization, which corresponds to taking the mirror image of the previous CPSS. In addition, we can reduce the cross-polarization terms in reflection if more strip grid sheets are added. The theory of weak interaction can hence predict polarization selectivity in reflection and low cross polarization, but predicts no

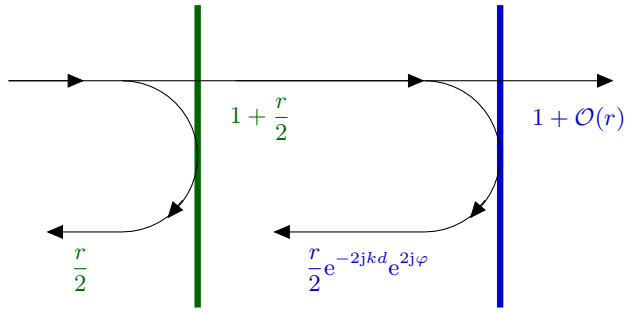

Figure 2: Bounce diagram for the co-polarized reflection and transmission from two linearly polarized layers with a relative rotation of φ, illuminated by an LHCP wave.

selectivity in transmission. This can be seen in (2.9), where the co-polarized transmission coefficients S_{21}^{RR} and S_{21}^{LL} are identical. Furthermore, reducing the cross-polarization terms by adding more layers to the structure, might result in a degradation of the insertion loss. Polarization selectivity in transmission is a higher order effect that can be anticipated by power conservation and extinction: if LHCP is being highly reflected ($|S_{11}^{\mathrm{LL}}|^2 \approx 1$), the maximum transmission is bounded by $|S_{21}^{\mathrm{LL}}|^2 \leq 1 - |S_{11}^{\mathrm{LL}}|^2 - |S_{11}^{\mathrm{RL}}|^2 - |S_{21}^{\mathrm{RL}}|^2 \ll 1$. In the same manner, if the co-polarized reflection of RHCP in (2.10) is minimized ($|S_{11}^{\mathrm{RR}}|^2 \approx 0$) it follows that $|S_{21}^{\mathrm{RR}}|^2$ is maximized, given that the cross-polarized reflection and transmission are both small ($|S_{11}^{\mathrm{LR}}|^2 + |S_{21}^{\mathrm{LR}}|^2 \approx 0$).

The main parameters defining the performance of an LHCPSS, defined in [4], are presented in (2.15)–(2.18): the transmission and reflection parameters insertion loss (IL) and return loss (RL), defined as the ratio of the incident power and the transmitted power in co-polarization (RHCP), and the ratio of the incident power and the reflected power in co-polarization (LHCP), and the axial ratio (AR) of the transmitted and reflected signals, which is a measure of the polarization purity of a circularly polarized wave

$$\mathrm{IL} = -20\log_{10}(|S_{21}^{\mathrm{RR}}|), \tag{2.15}$$

$$\mathrm{RL} = -20\log_{10}(|S_{11}^{\mathrm{LL}}|), \tag{2.16}$$

$$\mathrm{AR_t} = 20\log_{10}\left(\left|\frac{|S_{21}^{\mathrm{LR}}| + |S_{21}^{\mathrm{RR}}|}{|S_{21}^{\mathrm{LR}}| - |S_{21}^{\mathrm{RR}}|}\right|\right), \tag{2.17}$$

$$\mathrm{AR_r} = 20\log_{10}\left(\left|\frac{|S_{11}^{\mathrm{RL}}| + |S_{11}^{\mathrm{LL}}|}{|S_{11}^{\mathrm{RL}}| - |S_{11}^{\mathrm{LL}}|}\right|\right). \tag{2.18}$$

After investigating the circular polarization selective properties of multiple layers of strip grids, a five layer setup seems to yield a good trade-off in the transmission and reflection performance of the structure. The layout of the con-

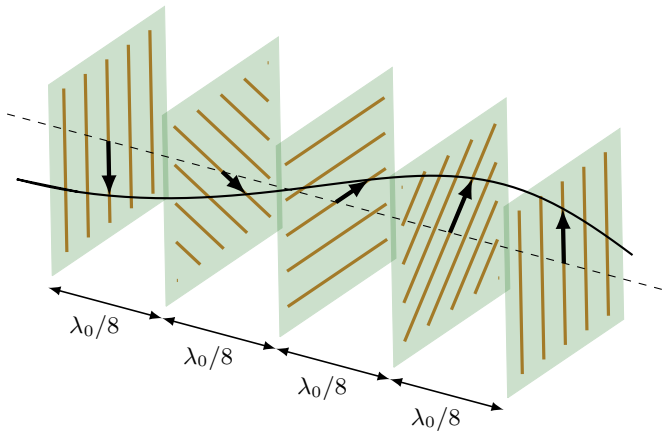

Figure 3: Concept design of a multilayer strip grid CPSS. The layers are cascaded with a separation of $\lambda_0/8$ and each layer is rotated 45° relative to the previous layer. The black line correspond to the polarization direction of an LHCP wave at a fixed time.

cept design is presented in Figure 3, where grids of thin strips are modeled in free space, and the simulated transmission and reflection of the structure is presented in Figure 4, where the strip width is 0.1 mm, the strip separation is 5 mm, the relative rotation is 45° and the separation between the layers is 2.5 mm (corresponding to $\lambda_0/8$ at the center frequency of operation $f = 15\,\text{GHz}$).

More design freedom is obtained by considering meandered strips, as in Figure 5, where each strip is bent in a meandering line and the amplitude of the meandering can be used to obtain effective L and C in a broader range than what is possible with straight strips. Also, by introducing individual design parameters of each layer, and of the separation between the meander line sheets, the bandwidth of the CPSS can be greatly improved.

3 CPSS design and applications

When designing for space applications, the considered device needs to be able to withstand a harsh environment, involving vacuum, thermal cycling, and radiation [1, Ch. 4]. Furthermore, to reach the strict design requirements associated with satellite communication applications, it is imperative to use materials with low thermal expansion coefficients and low electromagnetic loss, typically a loss tangent around 0.001 is desirable. A realistic design of the multilayer meander line CPSS is realized by printing metal wires on thin teflon substrates through a standard etching process. The substrates are separated by low permittivity spacers, consisting of Rohacell HF31, and the substrates and spacers are bonded

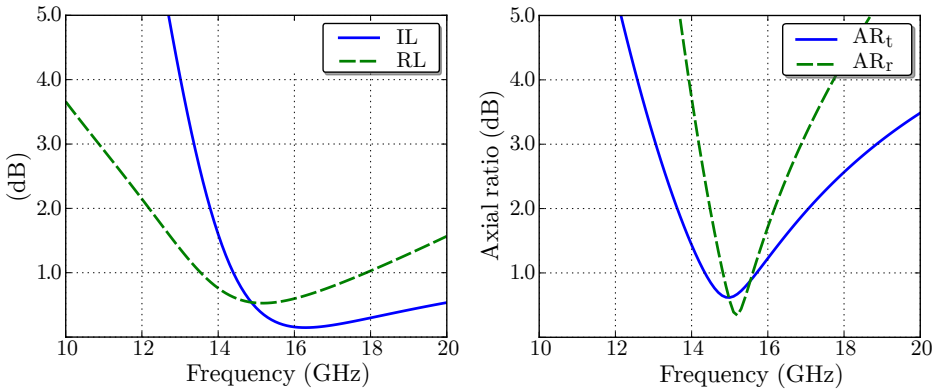

Figure 4: Simulation results for a five layer strip grid CPSS. The RHCP insertion loss and the LHCP return loss are presented in the left graph, and the RHCP axial ratio in transmission and the LHCP axial ratio in reflection are presented in the right graph. The layers are separated a distance of $\lambda_0/8$ and rotated 45° with respect to the previous layer.

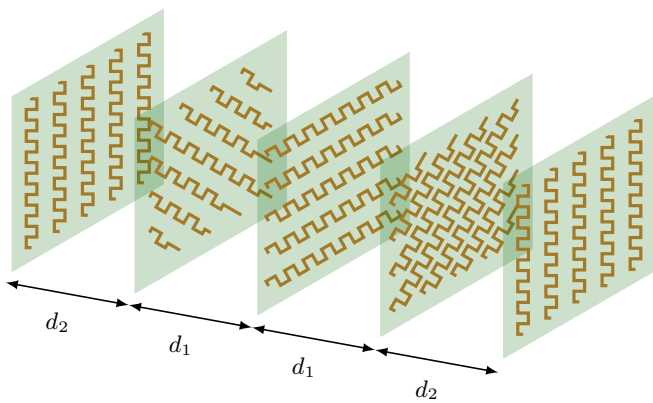

Figure 5: Concept design of a multilayer meander line CPSS. The layers are cascaded symmetrically with the separations d_1, d_2 and each layer is rotated 45° relative to the previous layer.

Table 2: Material parameters of the meander line CPSS.

Material	Permittivity	Loss tangent	Thickness
Rohacell HF31, spacers	1.043	0.0017	d_1 and d_2
Arlon DiClad 880, substrates	2.170	0.0009	0.127 mm
Copper, conducting lines	$\sigma = 58\,\mathrm{MS/m}$		$18\,\mu$m

Table 3: Geometrical parameters of the meander line CPSS.

Parameter	P	d_1	d_2	h_0	h_1	h_2
Value (mm)	5.20	2.61	3.81	2.44	0	2.83
Parameter	w_{0x}	w_{0y}	w_1	w_{2x}	w_{2y}	–
Value (mm)	0.46	0.58	0.21	0.25	0.17	–

together using an adhesive spray 3M Scotch-Weld 76. The main characteristics of the adhesive spray are that it is suitable for the materials to be joined, and that it has a long curing time [1], thus making it possible to readjust the alignment of the materials before they are completely fixed. The material parameters of the mentioned materials are presented in Table 2. Information on the electromagnetic properties and the thickness of the adhesive layers were not available in the design phase of this work.

A unit cell was introduced to simulate the electromagnetic response of a planar test panel of infinite extent in commercial softwares. The design parameters of the CPSS can be seen in Figure 6 and its values are given in Table 3, where P is the side length of the unit cell, the thickness of the innermost spacers is d_1, whereas the outer spacers have thickness d_2. The rest of the parameters describe the meander lines, where index 0 denotes the center layer, index 1 the intermediate layers (diagonal lines), and index 2 the outermost layers. The parameters w_{ij} correspond to the width of the meander line segments of layer i, in the direction j. The height h_1 is zero since there is no meandering in the diagonal lines, which is a result of multiple optimization iterations of the structure. The total thickness of the structure is approximately 13.5 mm, which at the center frequency of operation 15 GHz corresponds to $0.68\lambda_0$. An exploded view of the unit cell geometry is presented in Figure 7, and the optimization scheme that was used to generate the final design, and the numerical implementation of the simulation model, are described in more detail in Sections 4–5.

Two possible satellite communication applications of a CPSS are identified in [28], where a CPSS could be implemented either as curved surfaces in a CP

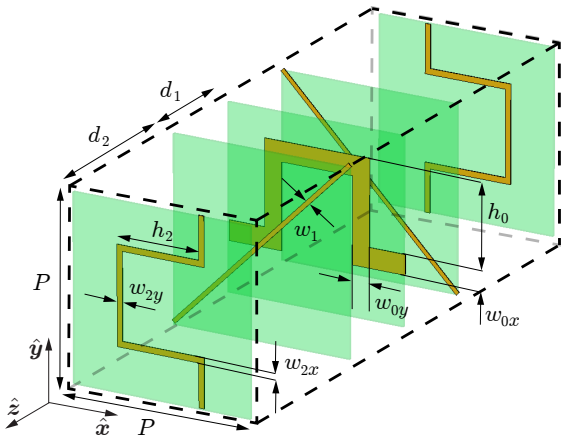

Figure 6: A unit cell of the meander line CPSS design, where the design parameters used in the design optimization process are marked out. The design is symmetric if excluding the center layer which implies that the design parameters of the back layers are the same as those of the first two layers.

version of the DGR presented in [5], or as a flat CP diplexer. The angles of operation of the CPSS depend on the application, and on parameters of the full reflector antenna system such as the ratio of the focal length and the diameter of the reflector (commonly referred to as f/D ratio). Typically, both the DGR and the diplexer applications require the CPSS to be able to operate at oblique angles of incidence up to $20°-40°$ depending on the application. However, relaxed requirements can be considered at high angles of incidence due to the tapering at the edge of the beam illuminating the CPSS. In this type of applications, it is also crucial to consider the orientation of the CPSS with respect to the antennas illuminating the structure, so that the CPSS is illuminated in its preferred plane of oblique incidence.

4 Optimization scheme

The CPSS design was optimized using a three-step process, as can be seen in Figure 8. First, an analytical model implemented in Python was used to find the parameter region of interest for further local optimization (see www.python.org and www.scipy.org). The code uses transmission line theory to model the low permittivity foam and the substrates as propagation matrices, and each interface between the different materials is modeled as a matching matrix [7]. The meander line sheets are modeled as lumped reactances by using explicit formulas for the effective capacitance and inductance of meander lines in [13], which were implemented in [6]. The whole structure is thus described by a cascaded sys-

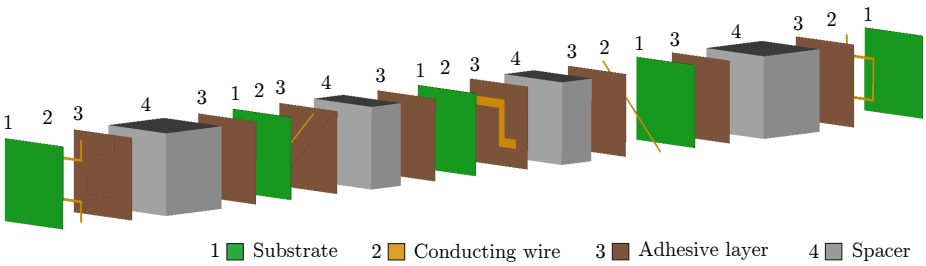

Figure 7: Exploded view of the meander line CPSS implemented for optimization in a commercial software, with realistic, lossy, materials suitable for space applications. The metal wires are printed on substrates that are separated by low permittivity spacers, and the substrates and spacers are bonded together using thin adhesive films.

tem of T-matrices, which can easily be transformed to yield the total scattering matrix S of the CPSS structure. This implementation only considers one mode for each polarization and does not include the effect of higher order modes from coupling between subsequent layers of the CPSS. Depending on the geometry of the structure under study, this might cause a discrepancy between the analytic model and full wave results. The parameters were optimized using the SciPy optimization package routine `fmin`, which is a downhill simplex algorithm, by minimizing a penalty function of the form

$$F = \frac{1}{f_2 - f_1} \int_{f_1}^{f_2} (a_1 \mathrm{AR_r} + a_2 \mathrm{AR_t} + a_3 \mathrm{RL} + a_4 \mathrm{IL}) \, \mathrm{d}f, \tag{4.1}$$

where f is the frequency and a_i are weights assigned in the optimization process. $\mathrm{AR_r}$ and RL are the axial ratio and return loss of the reflected signal for incident LHCP, $\mathrm{AR_t}$ and IL are the axial ratio and insertion loss of the transmitted signal for incident RHCP, and all these quantities are defined in decibels. A few thousand design candidates were generated in a few minutes, and a more detailed discussion of the analytical model is presented in [31].

The found parameter values were then imported from the python model into a full wave simulation software, Computer Simulation Technology Microwave Studio (CST MWS), where further optimization was performed at a reasonable accuracy and speed. The trust region framework optimizer was used to find the best design in a local parameter space, where the parameters were typically varied ±20 % with respect to the initial design. A tetrahedral mesh was utilized consisting of about 35 000 elements, using 2.4 GB of RAM on a dual core Intel Core i7, 3.5 GHz workstation, and finishing one design simulation in 17 minutes. About a hundred designs were generated in one full optimization iteration of 28 hours. In some design cases, a few iterations of this full wave optimization were necessary to reach the goals, using different weights a_i and frequency bands in

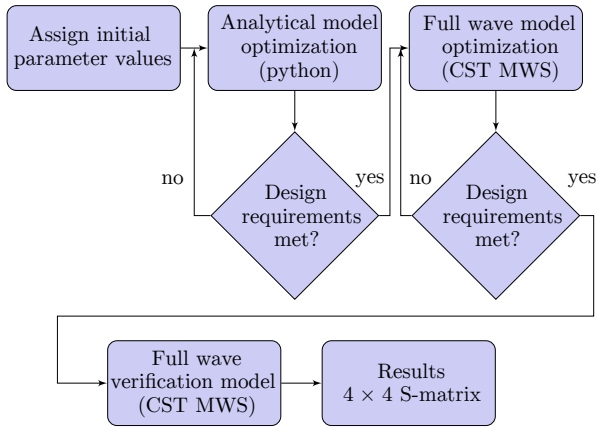

Figure 8: Optimization scheme, utilizing an analytical model implemented in Python and full wave simulation models in CST MWS.

the penalty function F. Finally, the resulting design was verified using a finer simulation mesh, leading to longer simulation times.

5 Simulation results

The meander line CPSS design was simulated in CST MWS, as a unit cell model, in the full wave frequency domain solver that utilizes Floquet mode analysis. At the design stage, the electromagnetic properties and the thickness of the adhesive layers were unknown to the authors, but these layers were expected to be very thin, and thus the adhesive layers were excluded from the simulation model. In Figures 9–10 simulation results after multiple optimization iterations using the analytic model, referred to as design 1, are presented alongside simulation results after multiple optimization iterations in CST MWS, referred to as design 2. Good agreement between the analytic model and full wave simulations of design 1 can be seen in RL, but the IL and AR in reflection and transmission deviate. This difference is mainly due to the previously mentioned higher order mode excitations that are not considered in the analytic model.

The mesh convergence of the final design was investigated, and it was concluded that the results had converged to an accuracy of 0.02 dB with respect to IL, RL, and AR, when using a mesh consisting of 75 000 mesh elements, corresponding to 16 steps per wavelength mesh setting. A simulation with the described settings was using 10 GB of RAM and finishing one simulation in about one hour. When comparing the simulation results using the finer mesh setting to the results generated in the optimization scheme, which used 35 000 mesh elements, corresponding to 12 steps per wavelength mesh setting, a deviation

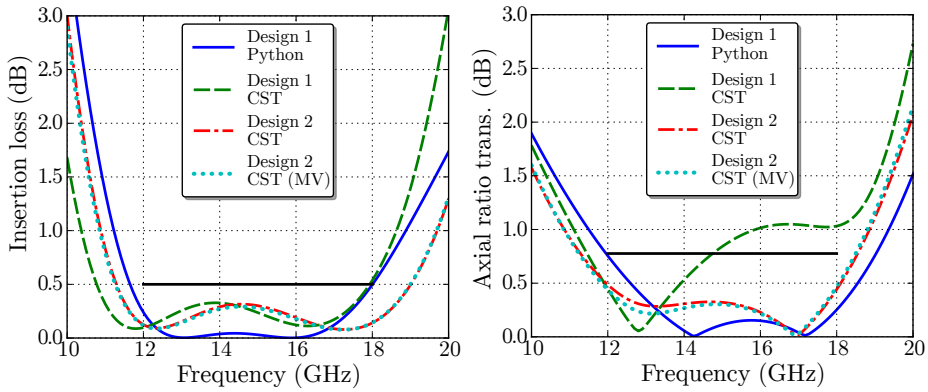

Figure 9: Simulation results of the multilayer CPSS at normal incidence. The solid and dashed curves correspond to simulation results from the analytic model and from CST MWS after optimization in the analytic model. The dash-dotted and the dotted curves correspond to simulation results from CST MWS after full wave optimization using a normal mesh and a finer mesh for verification, respectively. In the left plot is the RHCP IL, and in the right plot is the AR of the corresponding transmitted signal. The solid black lines are the design requirements defined in [4].

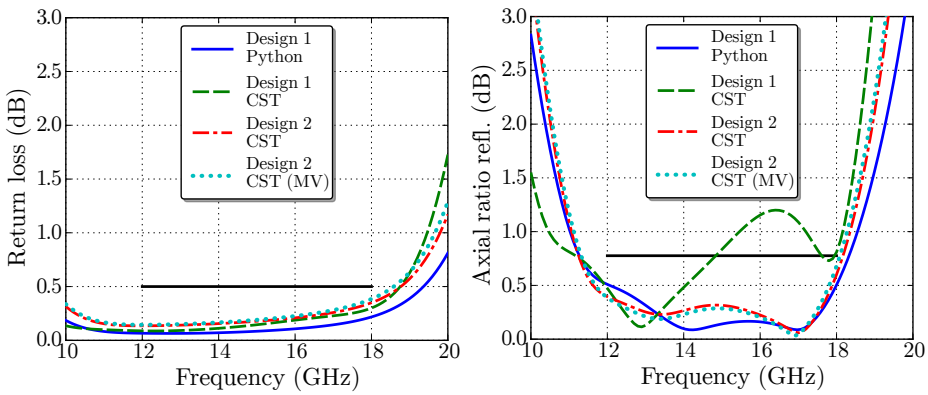

Figure 10: Simulation results of the multilayer CPSS at normal incidence. The solid and dashed curves correspond to simulation results from the analytic model and from CST MWS after optimization in the analytic model. The dash-dotted and the dotted curves correspond to simulation results from CST MWS after full wave optimization using a normal mesh and a finer mesh for verification, respectively. In the left plot is the LHCP RL, and in the right plot is the AR of the corresponding reflected signal. The solid black lines are the design requirements defined in [4].

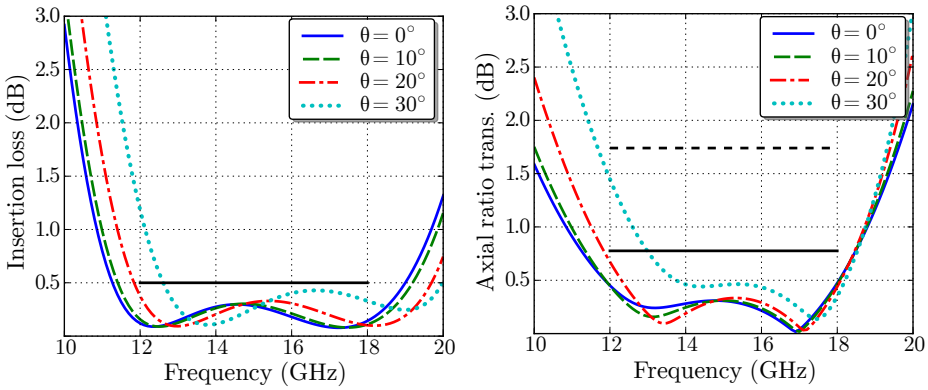

Figure 11: Simulation results of the multilayer CPSS at different angles of incidence, in the plane $\phi = 225°$. In the left plot is the RHCP IL, and in the right plot is the AR of the corresponding transmitted signal. The solid black lines are the design requirements defined in [4], and the dashed black lines are relaxed requirements of AR < 1.74 dB.

smaller than 0.07 dB is observed, see Figures 9–10. In [31], the mesh convergence of the CPSS was studied in detail using finer mesh settings and comparing two separate simulation softwares.

Simulation results of the final design were generated for multiple incidence angles using the fine mesh and are presented in Figures 11–12. The results indicate that the fractional bandwidth of the design is approximately 45 %, which is a significant increase compared to what has previously been presented [2, 3, 10, 11, 16–20, 22, 23, 26, 27, 32–34] as can be seen in the bandwidth comparison in Table 1. Furthermore, the results indicate a significant stability with respect to variations in the angle of incidence, especially in the range $\theta \in (0°, 20°)$. The performance of the CPSS has been compared to the requirements put forward in [4] and used in [28] for a K_u-band scenario:

- Insertion loss and return loss better than 0.5 dB.
- Axial ratio better than 0.78 dB.

The axial ratio requirement corresponds to 27 dB cross polarization discrimination, which can be relaxed to 20 dB (AR better than 1.74 dB) at higher angles of incidence. As can be seen in Figures 11-12, these requirements are satisfied in the incidence plane $\phi = 225°$, up to a 20° angle of incidence in the entire K_u band, or 30° angle of incidence for the relaxed AR requirements, except for a small penalty in IL at lower frequencies.

To evaluate how the performance of the structure varies with respect to the oblique angle of incidence (θ) in all possible incidence planes (ϕ), the scattering matrix of the structure was computed for every combination of $\theta = 0°, 5°, \ldots, 85°$

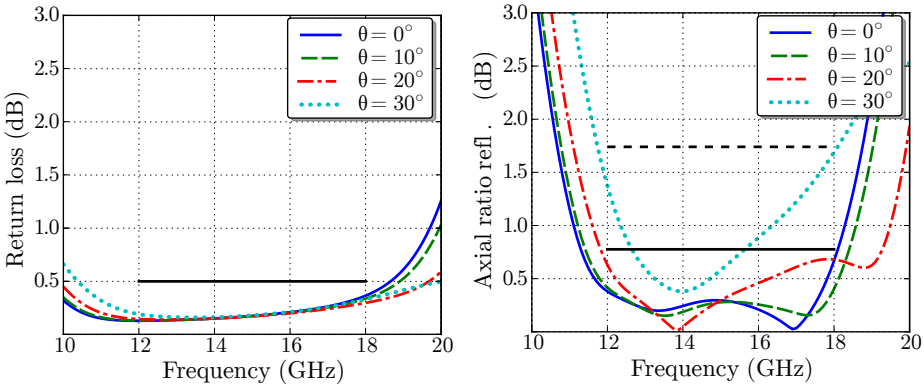

Figure 12: Simulation results of the multilayer CPSS at different angles of incidence, in the plane $\phi = 225°$. In the left plot is the LHCP RL, and in the right plot is the AR of the corresponding reflected signal. The solid black lines are the design requirements defined in [4], and the dashed black lines are relaxed requirements of AR < 1.74 dB.

and $\phi = 0°, 5°, \ldots, 355°$, corresponding to 1296 simulations. In Figures 13–14 simulation results are presented at the fixed frequencies $f = 13, 15, 17$ GHz, utilizing a coarser mesh setting of 10 steps per wavelength, corresponding to about 22 000 mesh elements. To speed up these computations, the simulations were divided between multiple work stations, and multiple simulations were run in parallel on each computer. The full parameter sweep was completed in about 367 hours of CPU time.

Simulating the scattering from the structure in CST MWS at each angle of incidence of interest resulted in scattering data at a great number of frequency points over the full frequency band of interest. This follows from the fact that the program utilizes automatic frequency sampling in a few points and then applies curve fitting to the results in between the sample points. The radius in Figures 13–14 corresponds to $\sin\theta$ so that the Cartesian coordinates are $x = \sin\theta\cos\phi$, and $y = \sin\theta\sin\phi$, with the z-axis pointing towards the reader. It is seen that the performance of the CPSS at oblique angles of incidence is maximized in incidence planes close to $\phi = 45°, 135°$. The reason why the structure has two preferred incidence planes is due to the rotational symmetry of the design. Furthermore, the symmetry of the structure implies that the scattering performance is symmetric with respect to the sign of the incidence angle θ, meaning maximum performance also for $\phi = 225°, 315°$. When comparing the results in Figures 13–14 it can be seen that the stability of the performance of the structure varies with the frequency of the incident signal, and that the performance at more oblique angles of incidence deteriorate for frequencies at the outer parts of the design band of operation. A small discrepancy can be observed between the

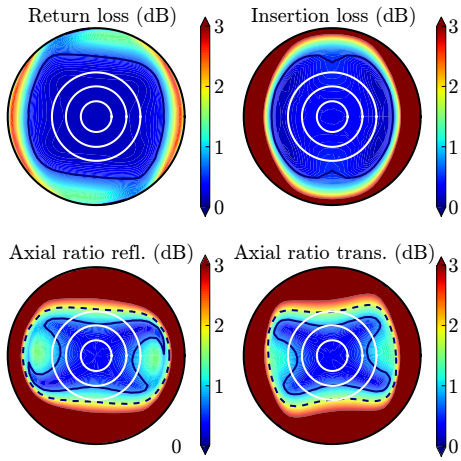

Figure 13: Simulation results for front side illumination of the CPSS at the center frequency of operation $f_0 = 15$. The left plots show the return loss and axial ratio of the reflected LHCP signal, the right plots correspond to the insertion loss and the axial ratio of the transmitted RHCP signal, and all values are in dB. The white circles indicate $\theta = 10°, 20°, 30°$, the solid black contours are the design requirements defined in [4], and the dashed black contours are relaxed requirements of AR < 1.74 dB.

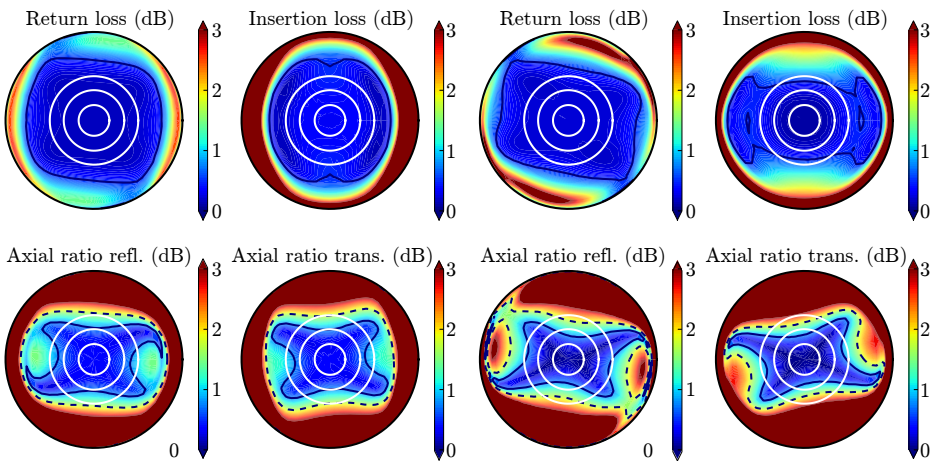

Figure 14: Simulation results for front side illumination of the CPSS at the frequency $f = 13$ GHz to the left, and at the frequency $f = 17$ GHz to the right.

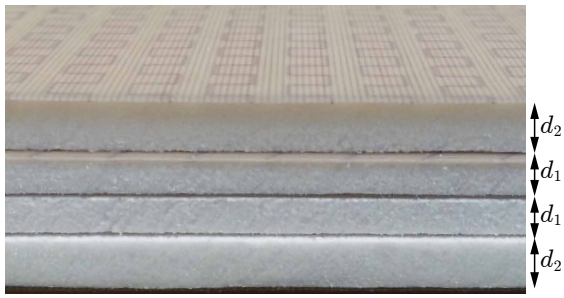

Figure 15: Side view of the manufactured test panel of total size 58x58x1.4 cm

results in Figures 11–12 and in Figures 13–14. This is caused by the fact that a coarser mesh was used when generating the results in Figures 13–14.

The same type of performance evaluation as in Figures 13–14 is found in [9], where the designs by Pierrot [23], Morin [22], and Tilston [34] were studied. There it is shown that all three designs have one preferred incidence plane of operation (identifying directions $\pm\theta$ as being in the same plane). The fact that the novel CPSS presented in this paper possesses multiple incidence planes of operation, results in a significant design freedom for implementations in satellite communication systems.

6 Manufactured test panel and measurements

A prototype of the optimized CPSS design was manufactured as can be seen in Figure 15. The width and height of the test panel is 58 cm, and the total thickness of the structure is 13.7 mm, which should be compared to the total thickness of the simulated structure of 13.5 mm. The thickness of the spacers were controlled to a tolerance of ± 0.2 mm in the manufacturing process, and the effect of the adhesive layers on the total thickness of the structure is unknown. The fact that the thickness of the manufactured test panel only deviates from the desired value by 0.2 mm is a desirable outcome. The full test panel was assembled by joining the thin teflon sheets, see Figure 16, to the Rohacell spacers by applying a thin layer of adhesive spray, and then applying an even pressure over the full surface for an extended amount of time. Since the full prototype consists of five layers of substrates, and four layers of spacers, a total of eight adhesive layers were applied to the structure one layer at a time using the above mentioned technique. When the full prototype was assembled, protective tape was added to the edges to avoid cracks in the spacers and failure in the bonding.

Transmission and reflection measurements of the manufactured prototype were carried out at Lund University, and the measurement setup in transmis-

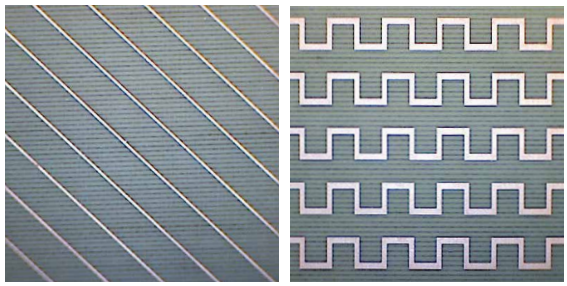

Figure 16: Printed teflon substrates, consisting of Arlon DiClad 880, with a relative permittivity of 2.17, and a thickness of 0.127 mm. The period of the printed pattern is the same in all five layers, where $P = 5.38\,\text{mm}$.

sion is seen in Figure 17. The test panel was illuminated using two rectangular standard gain horn antennas, SATIMO SGH 1240, each with a cross polarization discrimination of about 40 dB. Two free standing antenna fixtures were separated a distance of approximately 3 m, at a height of 1.4 m, and a table with the device under test (DUT) was placed at the center of the setup. The antennas were connected to a vector network analyzer, Agilent E8364b, which in turn was controlled by a laptop through a GPIB connection and a Matlab script. In the reflection case, both antennas were placed at the same side of the DUT, at a small oblique angle $\theta \approx 3^\circ$ due to the size of the antenna apertures.

To reduce the amount of multipath components in the measurement data, portable absorbing panels as can be seen in Figure 17 were placed around the setup during the measurements. That way, the user and the electronics controlling the measurement were shielded from the radiating antennas. Since linearly polarized antennas were used in the measurements, the circular polarization response of the test panel was synthesized from four linearly polarized components. To achieve a similar signal to noise ratio (SNR) in all four linearly polarized components measured, the transmitting and receiving antennas were oriented 45 degrees with respect to each other in each measurement. The advantage of this technique is that when each scattering matrix component of the DUT is normalized with a corresponding reference measurement, all reference measurements have similar and high SNR. This implied that, instead of synthesizing circular polarization through the traditionally used 90 degrees antenna orientations: XX, YY, XY, YX the four 45 degrees components XU, XV, YU, YV were measured, see Figure 18.

The four scattering matrix transmission components $S_{21}^{\text{XU}}, S_{21}^{\text{YU}}, S_{21}^{\text{XV}}, S_{21}^{\text{YV}}$ were measured for the test panel and for a free space through reference setup. These four components of the DUT were each normalized with its reference components and then transformed to the traditional linear co- and cross polarization

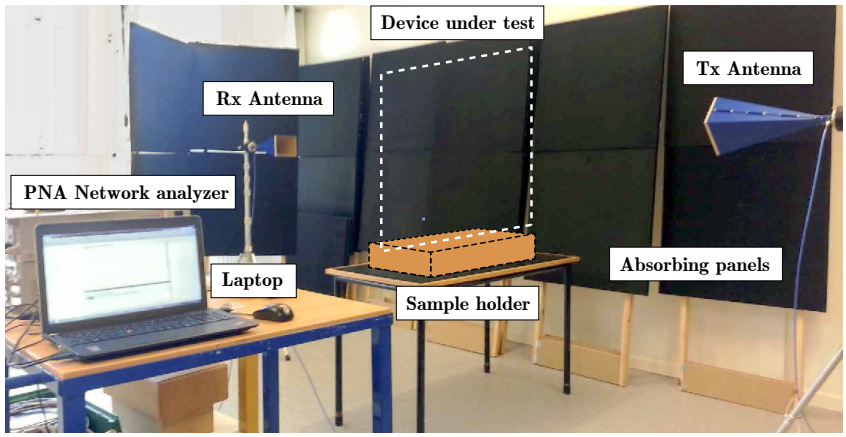

Figure 17: Measurement setup at Lund University, Sweden. The manufactured CPSS test panel was measured using single feed, linearly polarized, standard gain horn antennas in the frequency range $10\,\mathrm{GHz} < f < 20\,\mathrm{GHz}$.

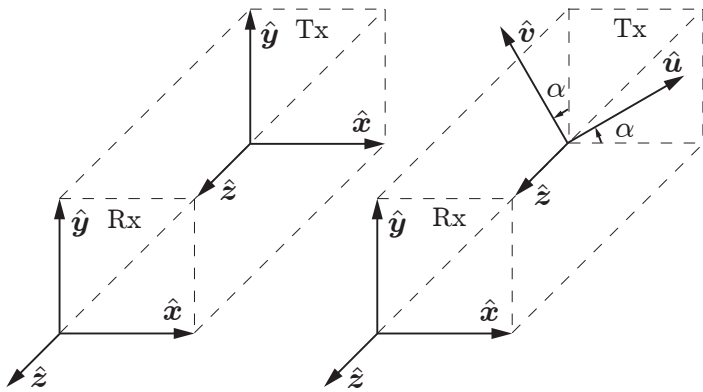

Figure 18: A principal sketch of the antenna orientations for synthesizing circular polarization from linear polarization measurements. To the left, the main directions of the transmitting and receiving antennas are aligned, and the relative rotation between the antennas is either 0° or 90°. To the right, the main directions of the transmitting and receiving antennas are not aligned, and if the antenna orientation angle $\alpha = 45°$, the relative rotation between the antennas is always 45°.

components $S_{21}^{\mathrm{XX}}, S_{21}^{\mathrm{YX}}, S_{21}^{\mathrm{YY}}, S_{21}^{\mathrm{XY}}$ through the matrix rotation relation

$$S_{21}^{\mathrm{LP}} = \begin{pmatrix} S_{21}^{\mathrm{XX}} & S_{21}^{\mathrm{XY}} \\ S_{21}^{\mathrm{YX}} & S_{21}^{\mathrm{YY}} \end{pmatrix} = \begin{pmatrix} S_{21}^{\mathrm{XU}} & S_{21}^{\mathrm{XV}} \\ S_{21}^{\mathrm{YU}} & S_{21}^{\mathrm{YV}} \end{pmatrix} \begin{pmatrix} \cos 45^\circ & \sin 45^\circ \\ -\sin 45^\circ & \cos 45^\circ \end{pmatrix}. \tag{6.1}$$

In the same manner, the four scattering matrix reflection components S_{11}^{XU},S_{11}^{YU}, S_{11}^{XV},S_{11}^{YV} were measured for the test panel and for a reference reflection setup, by adding aluminum foil to the front surface of the test panel. These four components were then normalized and transformed to the traditional linear co- and cross polarization components $S_{11}^{\mathrm{XX}}, S_{11}^{\mathrm{YX}}, S_{11}^{\mathrm{YY}}, S_{11}^{\mathrm{XY}}$ using the same matrix rotation relation as in (6.1). The circular polarization response was then determined applying the relation (2.6) to the linear polarization scattering matrix.

To remove the remaining multipath components from the measured data, time gating was implemented by applying a Gaussian window function to the data in the time domain. The relative measurement error of the setup when rotating the antennas, mainly caused by misalignment of the antennas, was measured in transmission and reflection to approximately $\pm 0.3\,\mathrm{dB}$ in amplitude, and $\pm 3^\circ$ in phase. Part of the effect of antenna misalignments are mitigated by the normalization of each component with a reference measurement, which implies that these values can be seen as a worst case scenario. The AR of a free space measurement in transmission was better than 0.5 dB, and in reflection the AR of a conducting reference panel was better than 0.7 dB, over the full frequency range of interest $10\,\mathrm{GHz} < f < 20\,\mathrm{GHz}$. These results indicate that measured AR values below 0.5 dB in transmission and below 0.7 dB in reflection have to be considered uncertain.

The measurement results presented in Figures 19–20 show a clear selectivity with respect to circular polarizations, both in transmission and reflection. The bandwidths of the simulated and measured CPSS with respect to satisfying all the requirements in IL, RL, $\mathrm{AR_t}$, and $\mathrm{AR_r}$, are summarized in Table 4. The total bandwidth exceeds 40 % in both simulations and measurements. A slight shift down in frequency is observed when comparing the measured data to the simulated results, reducing the coverage of the targeted $\mathrm{K_u}$ band to 86.7 %. The shift in frequency might be caused by the impact of the adhesive spray on the thickness of the structure, the effective conductivity of the spacers, as well as the manufacturing uncertainty of the spacers of $\pm 0.2\,\mathrm{mm}$. Also, a slight increase in level can be noticed in the measured curves in Figures 19–20, which might be caused by air bubbles in the adhesive layers, and additional material losses not accounted for in the simulations. Also, misalignment between the subsequent substrates is a source of error that can affect the AR of the test panel.

In order to account for the impact of the adhesive spray on the performance of the test panel, a simulation model was implemented with adhesive layers added to the structure. Since the thickness of the manufactured test panel was observed to be 0.2 mm thicker than the simulated structure, this difference was distributed evenly over the eight adhesive layers. The material parameters of the adhesive were chosen according to comparable adhesive films commonly used for similar applications, for instance the LTM123 used in [8], having $\epsilon_\mathrm{r} = 2.77$ and $\tan\delta =$

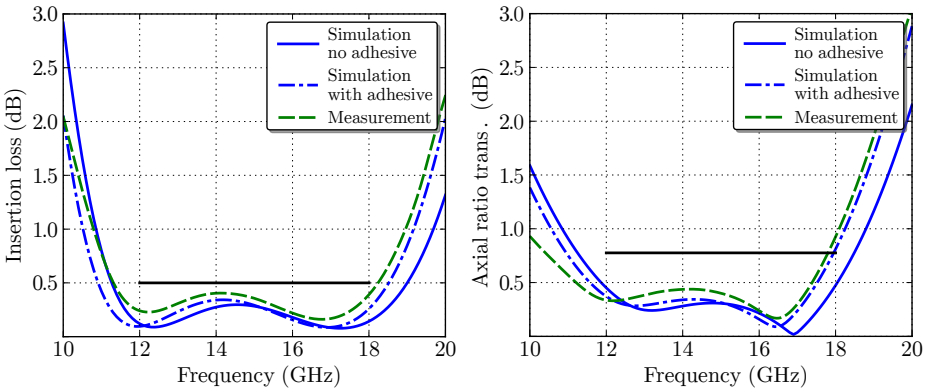

Figure 19: Transmission measurement results of the manufactured test panel, at normal incidence ($\theta = 0°, \phi = 0°$). The left plot shows the RHCP insertion loss from simulated and measured data, and the right plot shows the RHCP AR. The solid black lines are the design requirements defined in [4].

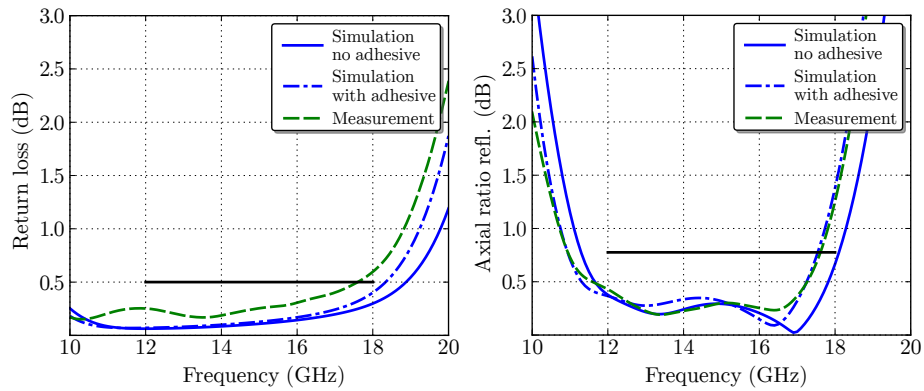

Figure 20: Reflection measurement results of the manufactured test panel, at normal incidence ($\theta = 3°, \phi = 0°$). The left plot shows the LHCP return loss from simulated and measured data, and the lower right shows the LHCP AR. The solid black lines are the design requirements defined in [4].

0.005. The thickness of the adhesive layers was calculated from the deviation in thickness between the simulation model and the manufactured design, resulting in $t = 0.2/8 = 0.025\,\text{mm}$.

The simulated performance of the structure, with adhesive layers, is compared to measurements in Figures 19–20, and the results indicate that adding adhesive layers to the simulations improve the agreement between the simulated

Table 4: Bandwidth over which the CPSS satisfies all requirements IL and RL better than 0.5 dB, and AR_t and AR_r better than 0.78 dB. K_u coverage relates to the target band 12 GHz $< f <$ 18 GHz.

	Min. freq.	Max. freq.	Total BW	K_u coverage
Simulated	11.4 GHz	18.2 GHz	45.9 %	100 %
Measured	11.3 GHz	17.2 GHz	42.0 %	86.7 %

and measured data both in transmission and reflection. However, the IL curves in Figure 19 and the RL curves in Figure 20 still show a small discrepancy. The difference in RL can possibly be caused by a misalignment in the measurement setup, as this was found to be especially sensitive in reflection. A small discrepancy can also still be noticed in the AR curves between simulations and measurements. As previously mentioned, this is most likely caused by measurement errors, misalignment between the meander line substrates, as well as the uncertainty of the Rohacell spacer thickness.

7 Conclusions

This paper presents a novel circular polarization selective structure based on multilayer meander line sheets. Compared to previous CPSS designs, the structure shows significant improvements in bandwidth and stability with respect to variations in the angle of incidence. The performance of the structure was evaluated both as a function of frequency, as well as over all possible angles of incidence at the edges and center of the frequency band, and it is shown to possess two preferred incidence planes of operation. A concept prototype was manufactured and the measurement results are in good agreement with simulation data. The high performance of this design makes it a good candidate for implementations in future satellite communication systems, either as a flat circular polarization diplexer or as a curved shared aperture reflector.

Acknowledgments

The authors of this paper kindly acknowledge Ron van Hoorn and Oliver Krause at Evonik for providing Rohacell samples for the manufacturing of the test panel, Lars Hedenstjerna at Lund University for manufacturing the fixtures for the measurement setup, Christian Nelson at Lund University for assisting in the assembly of the test panel, and Peter Balling, Antenna Systems Consulting ApS (ASC), for the implementation of the analytical free space meander line models. The work reported in this paper was performed under ESA Contract No. 4000108854/13/NL/MH.

References

[1] 3M 76 Scotch Weld spray long open time adhesive, Data sheet, 2016. Available at: http://multimedia.3m.com/mws/media/82819O/spray-76-long-open-time-adhesive.pdf?fn=76.pdf, accessed 2016-08-10.

[2] S. M. A. M. H. Abadi and N. Behdad. A broadband, circular-polarization selective surface. *Journal of Applied Physics*, **119**(24), pp. 244901, 2016.

[3] S. M. A. M. H. Abadi and N. Behdad. Wideband linear-to-circular polarization converters based on miniaturized-element frequency selective surfaces. *IEEE Trans. Antennas Propag.*, **64**(2), pp. 525–534, 2016.

[4] M. Albani, P. Balling, L. Datashvili, G. Gerini, P. Ingvarson, K. Pontoppidan, M. Sabbadini, D. Sjöberg, S. Skokic, and G. Vecchi. Concepts for polarising sheets & "dual-gridded" reflectors for circular polarisation. In *ICECom Proceedings*, pp. 1–4, 2010.

[5] M. Baunge, H. Ekström, P. Ingvarson, and M. Petersson. A new concept for dual gridded reflectors. In *Proceedings of the fourth European Conference on Antennas and Propagation (EuCAP)*, pp. 1–5. IEEE, 2010.

[6] R. S. Chu and K. M. Lee. Radiation impedance of a dipole printed on periodic dielectric slabs protruding over a ground plane in an infinite phased-array. *IEEE Trans. Antennas Propag.*, **35**(1), pp. 13–25, 1987.

[7] R. E. Collin. *Foundations for Microwave Engineering*. McGraw-Hill, New York, NY, second edition, 1992.

[8] J. A. Encinar, L. S. Datashvili, J. A. Zornoza, M. Arrebola, M. Sierra-Castañer, J. L. Besada-Sanmartin, H. Baier, and H. Legay. Dual-polarization dual-coverage reflectarray for space applications. *IEEE Trans. Antennas Propag.*, **54**(10), pp. 2827–2837, 2006.

[9] A. Ericsson and D. Sjöberg. A performance study of circular polarization selective structures. In *Proceedings of the 9th European Conference on Antennas and Propagation (EuCAP)*. IEEE, 2015.

[10] A. Ericsson and D. Sjöberg. A resonant circular polarization selective structure of closely spaced wire helices. *Radio Science*, **50**(8), pp. 804–812, 2015. 2014RS005641.

[11] V. Fusco and B. Nair. Circular polarisation selective surface characterisation and advanced applications. *IEE Proceedings Microwaves Antennas and Propagation*, **153**(3), pp. 247–252, 2006.

[12] J. K. Gansel, M. Thiel, M. S. Rill, M. Decker, K. Bade, V. Saile, G. von Freymann, S. Linden, and M. Wegener. Gold helix photonic metamaterial as broadband circular polarizer. *Science*, **325**(5947), pp. 1513–1515, 2009.

[13] L. Goldstone. A compact broadband CP MM wave horn. In *Antennas and Propagation Society International Symposium, 1982*, volume 20, pp. 640–643. IEEE, 1982.

[14] IEEE standard test procedures for antennas, 2008. IEEE Std 149-1979 (R2008).

[15] W. A. Imbriale, S. S. Gao, and L. Boccia, editors. *Space Antenna Handbook*. Wiley, 2012.

[16] M. Joyal and J. Laurin. A cascaded circular-polarization-selective surface at K band. In *Antennas and Propagation (APSURSI), 2011 IEEE International Symposium on*, pp. 2657–2660. IEEE, 2011.

[17] M. Joyal and J. Laurin. Analysis and design of thin circular polarizers based on meander lines. *IEEE Trans. Antennas Propag.*, **60**(6), pp. 3007–3011, 2012.

[18] M. Joyal and J. Laurin. Design and analysis of a cascade circular-polarization-selective surface at K band. *IEEE Trans. Antennas Propag.*, **62**(6), pp. 3043–3052, 2014.

[19] I. Lopez and J. Laurin. A circular polarization selective surface implemented on a flexible substrate. *IEEE Trans. Antennas Propag.*, **62**(7), pp. 3847–3852, 2014.

[20] I. Lopez and J.-J. Laurin. Alternative topologies of circular polarization selective surfaces based on modifications of the Pierrot cell. *IEEE Trans. Antennas Propag.*, **63**(4), pp. 1465–1472, 2015.

[21] N. Marcuvitz. *Waveguide Handbook*. McGraw-Hill, New York, NY, 1951.

[22] G. Morin. Circular polarization selective surface made of resonant spirals, 1994. US Patent 5,280,298.

[23] R. Pierrot. Reflector for circularly polarized waves, 1970. US Patent 3,500,420.

[24] S. Rao, L. Shafai, and S. K. Sharma. *Handbook of Reflector Antennas and Feed Systems Volume III: Applications of Reflectors*. Artech house, 2013.

[25] J. E. Roy. A reciprocal CPSS molecule. In *Antenna Technology and Applied Electromagnetics (ANTEM), 2016 17th International Symposium on*, pp. 1–2. IEEE, 2016.

[26] J. E. Roy and L. Shafai. Reciprocal circular-polarization-selective surface. *Antennas and Propagation Magazine, IEEE*, **38**(6), pp. 18–33, 1996.

[27] J. Sanz-Fernandez, E. Saenz, and P. de Maagt. A circular polarization selective surface for space applications. *IEEE Trans. Antennas Propag.*, **63**(6), pp. 2460–2470, 2015.

[28] J. Sanz-Fernandez, E. Saenz, P. de Maagt, and C. Mangenot. Circular polarization selective surface for dual-optics CP offset reflector antennas in Ku-band. In *Proceedings of the 6th European Conference on Antennas and Propagation (EuCAP)*, pp. 2683–2687. IEEE, 2012.

[29] M. Selvanayagam and G. V. Eleftheriades. Design and measurement of tensor impedance transmitarrays for chiral polarization control. *IEEE Trans. Microwave Theory Tech.*, **64**(2), pp. 414–428, 2016.

[30] D. Sjöberg. Circuit analogs for wave propagation in stratified structures. In A. Petrin, editor, *Wave Propagation in Materials for Modern Applications*, pp. 489–508. InTech, 2010.

[31] D. Sjöberg and A. Ericsson. A multi layer meander line circular polarization selective structure (MLML-CPSS). In *Proceedings of the 8th European Conference on Antennas and Propagation (EuCAP)*, pp. 464–468. IEEE, 2014.

[32] W. Tang, G. Goussetis, N. J. Fonseca, H. Legay, E. Saenz, and P. de Maagt. Study of coupled split-ring resonator arrays for circular polarization selective surface. In *Antennas and Propagation & USNC/URSI National Radio Science Meeting, 2015 IEEE International Symposium on*, pp. 362–363. IEEE, 2015.

[33] I.-Y. Tarn and S.-J. Chung. A new advance in circular polarization selective surface – A three layer CPSS without vertical conductive segments. *IEEE Trans. Antennas Propag.*, **55**(2), pp. 460–467, 2007.

[34] D. Tilston, M. Tilston, S. Tilston, W. V. Tilston, and T. Tralman. Polarization selective surface for circular polarization, 1991. US Patent 5,053,785.

[35] R. Torres and M. Catedra. Analysis and design of a two-octave polarization rotator for microwave frequency. *IEEE Trans. Antennas Propag.*, **41**(2), pp. 208–213, 1993.

[36] Y. Zhao, M. Belkin, and A. Alù. Twisted optical metamaterials for planarized ultrathin broadband circular polarizers. *Nature Communications*, **3**, pp. 870, 2012.

Experimental Characterization of Circular Polarization Selective Structures using Linearly Single-Polarized Antennas

Andreas Ericsson, Johan Lundgren and Daniel Sjöberg

Paper IV

Published as: A. Ericsson, J. Lundgren and D. Sjöberg, "Experimental Characterization of Circular Polarization Selective Structures using Linearly Single-Polarized Antennas," *IEEE Transactions on Antennas and Propagation*, Vol. 65, No. 8, pp. 4239–4249, 2017.

Abstract

We present a technique for performing high accuracy measurements of the transmission and reflection properties in circular polarizations of a test panel. By using linearly polarized antennas and measuring at four different antenna orientations, all with a relative rotation of 45 degrees, an efficient normalization of each scattering component can be utilized. This method achieves a high signal to noise ratio in all normalized linear polarization components used to synthesize the circular polarization scattering. Furthermore, a post processing scheme is introduced to compensate for measurement uncertainties due to antenna misalignments. The novel measurement and post processing techniques are utilized to characterize a manufactured wideband circular polarization selective structure, both in transmission and reflection, and the measurement results are in excellent agreement with simulation results from a commercial software. The repeatability of the measurement results is investigated, and the results are in the expected range in comparison to estimated measurement uncertainties.

1 Introduction

A strong driving force in the development of future satellite communication systems is to increase the data transfer rate [12, 25]. This has previously been achieved using frequency and polarization reuse schemes [3, 4, 12, 25, 28]. Polarization filtering can easily be achieved in linear polarization (LP) using a strip grid, where signals polarized parallel to the grid are reflected and signals polarized orthogonal to the grid are transmitted [4]. However, in future satellite communication systems, typically designed to operate in the K, K_a-bands, it is preferable to utilize circular polarization (CP) and thus eliminating the problem of aligning receiving antennas with the polarization of the incident signals.

To filter signals of orthogonal CP is not as trivial as in the case of LP. Nevertheless, a multitude of circular polarization selective structures (CPSSs) have been presented over the last 50 years [1, 2, 5, 7, 13–15, 19–22, 26, 27, 31, 32]. The most wideband CPSS presented up to date is based on cascaded anisotropic sheets of meander lines [6, 29]. This type of structure achieves a bandwidth of approximately 45 % and shows significant improvements in stability with respect to angle of incidence variations compared to previous designs. The recent performance improvement of CPSSs over the last few years make integration of these structures in an actual satellite communication system a realistic future step. This implies an increasing importance of accurately characterizing the performance of CPSSs, both through computer simulations in commercial softwares as well as through measurements of manufactured test panels. The performance of a CPSS is commonly presented as a function of frequency for a few discrete angles of incidence, and in [5] a scheme for studying the CPSS performance at fixed frequencies as a function of all possible spherical angles of incidence was presented. In a simulation software, the complete scattering matrix in CP is

easily extracted, and from this relevant scattering quantities can be determined.

The first published measurements of the transmission properties of a CPSS were presented in [32] where the relative power transmitted in right hand circular polarization (RHCP) and left hand circular polarization (LHCP) was determined. The first comprehensive experimental quantification of the transmission, reflection, and AR properties of a CPSS was presented in [9], where a Pierrot element CPSS was characterized in the X-band. However, only the scattering properties of the CPSS with a perfect electric conductor (PEC) backing was investigated in reflection. Over the last ten years, a multitude of CPSS designs have been presented and characterized through measurements in transmission only [15, 19, 20, 30, 31]. A general remark on these measurements is that the insertion loss (IL) is often accurately characterized, but the AR is commonly deviating from expected results.

Complete experimental verifications of a CPSS in transmission and reflection in CP are, to the knowledge of the authors of this work, rarely presented. Moreover, the published experimental verifications of CPSSs are, in general, not very detailed about characterization of measurement errors or the procedures of generating the presented measurement data. In [27], a CPSS was characterized both in reflection and transmission, utilizing a state of the art measurement setup. This characterization achieves low measurement errors both in reflection and transmission, but requires expensive and advanced equipment and still shows significant deviations between measured and simulated AR. To this end, we present a simple procedure for a complete experimental characterization of a CPSS using linearly single- polarized horn antennas. A post processing scheme is introduced to reduce measurement errors due to antenna misalignments, resulting in significant improvements in the accuracy of measured AR in both reflection and transmission. By normalizing the device under test (DUT) reflection and transmission data with reference measurements, the relative transmission and reflection of the structure are determined.

The paper is organized as follows: in Section 2, the theory of characterizing a DUT by synthesizing the CP scattering from LP measurements is described. The measurement setup used in this work is presented in detail in Section 3, where separate arrangements in transmission and reflection are introduced. In Section 4, the post processing scheme used to manage and calibrate the raw measurement data and synthesize the CP scattering of a DUT is presented. A measurement methodology for achieving low reference AR in transmission and reflection is introduced, where a normalization with reference measurements is utilized. Estimates of the errors associated with this type of measurements are presented in Section 5. The lower bound in AR of the measurement setup is established through measurements of a homogeneous test panel, both in reflection and transmission. In Section 6, measurement results of a non-resonant meander line CPSS, described in detail in [6], are presented and the repeatability of the measurements is investigated. Finally, Section 7 consists of concluding remarks on the work presented.

2 Theory - circular polarization measurements using linearly polarized antennas

The scattering parameters of a DUT in CP can be determined experimentally in two different ways; The first is to use CP antennas, and the CP scattering parameters are then directly determined from the co- and cross-polarization transmission and reflection properties of the DUT. This method is straightforward, but to determine the scattering parameters to high accuracy requires CP antennas of high cross polarization discrimination (XPD), which can also be interpreted as low axial ratio (AR). In [27] a CPSS was characterized using CP helix antennas with 18 dB XPD, corresponding to AR > 2.2 dB, and it was concluded that the CPSS could not be accurately characterized using antennas with such low XPD. To make a CP antenna achieve levels of XPD comparable to linear single-polarized horn antennas of $40 - 45$ dB requires careful design [10]. A number of CP antennas have been presented throughout the years with high XPD [8, 18], but to achieve this over a wide bandwidth is a difficult task.

Another way of characterizing a DUT is to use LP antennas, and acquire all co- and cross polarization scattering parameters in LP. From this data, the CP scattering parameters can be determined by using simple matrix relations for converting between LP and CP bases. The scattering matrix in CP, using the IEEE standard [11, pp.61–77] and defining the z-axis as the input direction at port 1 and the output direction at port 2, can be identified as

$$
\begin{aligned}
S^{\mathrm{CP}} &= \begin{pmatrix} S_{11}^{\mathrm{RR}} & S_{11}^{\mathrm{RL}} & S_{12}^{\mathrm{RR}} & S_{12}^{\mathrm{RL}} \\ S_{11}^{\mathrm{LR}} & S_{11}^{\mathrm{LL}} & S_{12}^{\mathrm{LR}} & S_{12}^{\mathrm{LL}} \\ S_{21}^{\mathrm{RR}} & S_{21}^{\mathrm{RL}} & S_{22}^{\mathrm{RR}} & S_{22}^{\mathrm{RL}} \\ S_{21}^{\mathrm{LR}} & S_{21}^{\mathrm{LL}} & S_{22}^{\mathrm{LR}} & S_{22}^{\mathrm{LL}} \end{pmatrix} \\
&= \frac{1}{2} \begin{pmatrix} 1 & -\mathrm{j} & 0 & 0 \\ 1 & \mathrm{j} & 0 & 0 \\ 0 & 0 & 1 & \mathrm{j} \\ 0 & 0 & 1 & -\mathrm{j} \end{pmatrix} \begin{pmatrix} S_{11}^{\mathrm{XX}} & S_{11}^{\mathrm{XY}} & S_{12}^{\mathrm{XX}} & S_{12}^{\mathrm{XY}} \\ S_{11}^{\mathrm{YX}} & S_{11}^{\mathrm{YY}} & S_{12}^{\mathrm{YX}} & S_{12}^{\mathrm{YY}} \\ S_{21}^{\mathrm{XX}} & S_{21}^{\mathrm{XY}} & S_{22}^{\mathrm{XX}} & S_{22}^{\mathrm{XY}} \\ S_{21}^{\mathrm{YX}} & S_{21}^{\mathrm{YY}} & S_{22}^{\mathrm{YX}} & S_{22}^{\mathrm{YY}} \end{pmatrix} \begin{pmatrix} 1 & 1 & 0 & 0 \\ -\mathrm{j} & \mathrm{j} & 0 & 0 \\ 0 & 0 & 1 & 1 \\ 0 & 0 & \mathrm{j} & -\mathrm{j} \end{pmatrix}, \qquad (2.1)
\end{aligned}
$$

where the two ports are located on each side of the DUT. Each entry in the scattering matrix is defined as the ratio between the outgoing electric field, E_m^k at port m with polarization state k, and the incoming electric field, E_{n0}^l at port n with polarization state l, such as $S_{mn}^{kl} = E_m^k / E_{n0}^l$, when all other ports are not excited and terminated with their characteristic impedance. The indices X, Y correspond to horizontal and vertical polarization, defined by the basis vectors $\hat{\boldsymbol{x}}$ and $\hat{\boldsymbol{y}}$ in Figure 1, and R, L correspond to RHCP and LHCP, respectively.

As long as the signal from the transmitting antenna is received in two non-parallel orientations of the receiving antenna, and the relative orientations of the transmitting and receiving antennas are known, the scattering parameters in LP

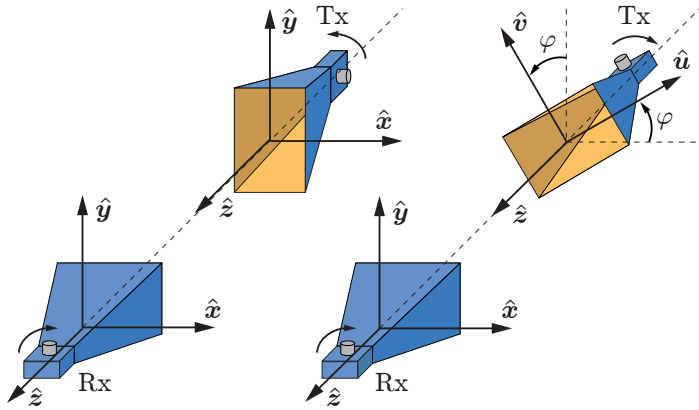

Figure 1: A principal sketch of antenna orientations in measurements of CP transmission. To the left, the main directions of the transmitting and receiving antennas are aligned, and the relative rotation between the antennas is either 0° or 90°. To the right, the main directions of the transmitting and receiving antennas are not aligned, and if the antenna orientation angle $\varphi = 45°$, the relative rotation between the transmitting and receiving antenna is always 45°.

can be extracted, and subsequently converted to CP using (2.1). If the receiving antenna is rotated around its z-axis an angle φ, as illustrated in the scenario to the right in Figure 1, the LP scattering parameters of an aligned system can be extracted through the relation

$$
\begin{aligned}
S^{\mathrm{LP}} &= \begin{pmatrix} S_{11}^{\mathrm{XX}} & S_{11}^{\mathrm{XY}} & S_{12}^{\mathrm{XX}} & S_{12}^{\mathrm{XY}} \\ S_{11}^{\mathrm{YX}} & S_{11}^{\mathrm{YY}} & S_{12}^{\mathrm{YX}} & S_{12}^{\mathrm{YY}} \\ S_{21}^{\mathrm{XX}} & S_{21}^{\mathrm{XY}} & S_{22}^{\mathrm{XX}} & S_{22}^{\mathrm{XY}} \\ S_{21}^{\mathrm{YX}} & S_{21}^{\mathrm{YY}} & S_{22}^{\mathrm{YX}} & S_{22}^{\mathrm{YY}} \end{pmatrix} \\
&= \begin{pmatrix} S_{11}^{\mathrm{XU}} & S_{11}^{\mathrm{XV}} & S_{12}^{\mathrm{XU}} & S_{12}^{\mathrm{XV}} \\ S_{11}^{\mathrm{YU}} & S_{11}^{\mathrm{YV}} & S_{12}^{\mathrm{YU}} & S_{12}^{\mathrm{YV}} \\ S_{21}^{\mathrm{XU}} & S_{21}^{\mathrm{XV}} & S_{22}^{\mathrm{XU}} & S_{22}^{\mathrm{XV}} \\ S_{21}^{\mathrm{YU}} & S_{21}^{\mathrm{YV}} & S_{22}^{\mathrm{YU}} & S_{22}^{\mathrm{YV}} \end{pmatrix} \begin{pmatrix} \cos\varphi & \sin\varphi & 0 & 0 \\ -\sin\varphi & \cos\varphi & 0 & 0 \\ 0 & 0 & \cos\varphi & \sin\varphi \\ 0 & 0 & -\sin\varphi & \cos\varphi \end{pmatrix},
\end{aligned} \tag{2.2}
$$

where the indices U, V correspond to the unit vector directions $\hat{\boldsymbol{u}}, \hat{\boldsymbol{v}}$ in Figure 1. After the rotation operation (2.2), the CP scattering matrix is determined using (2.1). Note that this holds when characterizing a DUT in both reflection and transmission. The advantage of using a relative rotation of 45° between the principal directions the transmitting and receiving antennas is described in detail in Section 5.

3 Measurement setup

All measurements in this work were carried out at the frequencies $9.5 - 20.5\,\text{GHz}$, using two rectangular standard gain horn antennas, SATIMO SGH 1240, with a XPD in LP better than 40 dB in the full band of interest. The antennas were positioned at a height of 1.4 m using tripod antenna stands. To manually rotate the antennas in a controlled manner, custom made rotation fixtures were manufactured. Relative orientations of 0°, 45° and 90° of the horns were achieved using alignment holes in the fixtures and alignment pins. The antennas were connected to an Agilent E8364b PNA Network Analyzer, which in turn was controlled by a laptop through a GPIB connection and a control script written in MATLAB. Further details on how to control Keysight (previously Agilent) instruments with MATLAB can be found in [16]. The DUT was placed on a table and fixated using poly(methyl methacrylate) (PMMA) holders, as can be seen in Figures 2–4. In order to suppress undesirable multipath signals, portable absorbing panels were placed around the setup. The absorbing panels are designed to operate at $20 - 100\,\text{GHz}$ but measurements showed them to provide a 10 dB absorption in reflection for the frequency band of interest.

Due to the fact that a two port network analyzer was used together with two single polarized antennas, the antenna placement had to be modified depending on if the transmission or reflection properties of the DUT were to be characterized. However, if a four port network analyzer had been used, either with four single polarized antennas or with two dual polarized antennas, a complete characterization could have been achieved without having to rearrange the antennas in the measurement setup.

3.1 Transmission measurements

When characterizing the transmission properties of a DUT, the antennas were separated by distances ranging from 0.7 m to 2.0 m and the DUT was placed on a table at the center of the setup, between the two antennas, as in Figure 2. The antennas were carefully aligned using a laser, spirit-level, tape measure and several strings connecting points of interest. Moreover, by utilizing the fact that the signal strength of the co-polarized transmission of the empty setup, displayed with a few seconds delay on the network analyzer, is increased as the misalignment of the setup is decreased, small fine tuning adjustments and verifications were made to the positioning and alignment of the antennas. All four co- and cross polarization scattering matrix components S_{21}^{kl} were measured in both amplitude and phase, where $k \in (\text{X}, \text{Y})$ and $l \in (\text{U}, \text{V})$ or $l \in (\text{X}, \text{Y})$ depending on if 45° or 90° relative antenna orientations were used. All measurements of different test objects were accompanied by a reference transmission measurement of the empty setup (with the DUT removed).

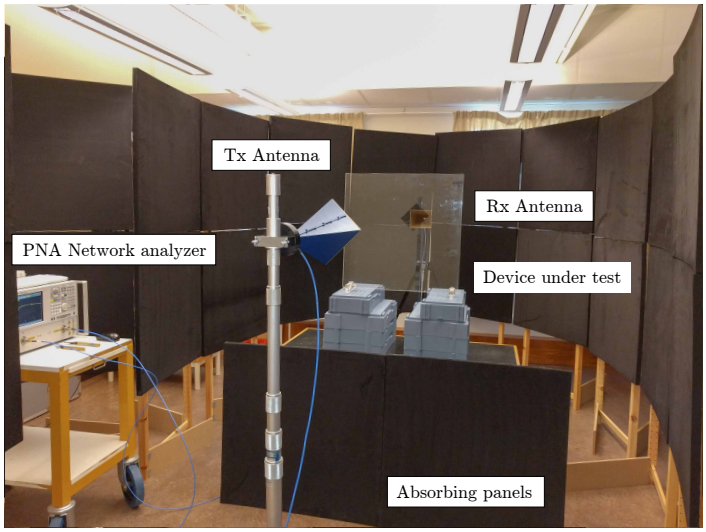

Figure 2: Measurement setup for transmission characterization of a DUT, positioned at a table centered between the transmitting and receiving antennas. The antennas are connected to a vector network analyzer and the whole setup is enclosed by portable absorbing panels.

3.2 Reflection measurements

When characterizing the reflection properties of a DUT, both antennas were placed at the same side of the DUT at distances ranging from 0.7 m to 1.8 m, and the apertures separated a distance of about 5 cm, as in Figure 3. Thus the measurement is not of normal incidence but with angles of incidence 3–8°. As in transmission, all four co- and cross polarization scattering matrix components S_{11}^{kl} were measured in both amplitude and phase, where $k \in (\mathrm{X}, \mathrm{Y})$ and $l \in (\mathrm{U}, \mathrm{V})$ or $l \in (\mathrm{X}, \mathrm{Y})$ depending on if 45° or 90° relative antenna orientations were used. All measurements of different test objects were accompanied by a reference measurement of a highly conducting panel of the same size as the DUT. In order to eliminate effects due to misalignment and different curvature of a separate highly conducting reference panel, the DUT was coated with a thin aluminum foil which was temporarily attached to the test object. A very thin layer of water was applied between the foil and the test panel, which for the panels used in this study exherted a strong adhesive bonding due to the surface tension of the water molecules [17] and the low weight of the aluminum foil. The small amount of water was applied evenly to the test panel using a water spray bottle, after that the aluminum foil was folded onto the test panel from one end to the other, and finally the structure was worked over with a plastic wallpaper scraper to remove any air bubbles or local collections of water. In Figure 4, a PMMA test panel used to characterize the measurement setup is presented with and without an aluminum foil attached.

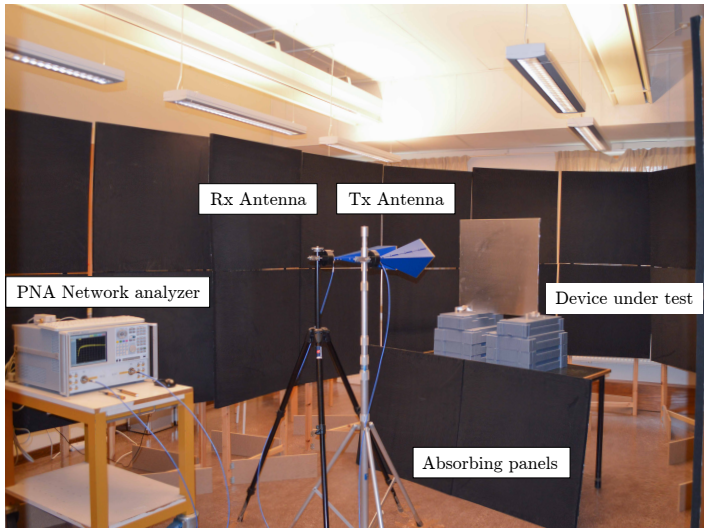

Figure 3: Measurement setup for characterization of the reflection properties of a DUT, which is positioned at a table a distance from the transmitting and receiving antennas. In order to achieve normalized reflection data of the scatterer, the test panel is coated by a conducting foil. The antennas are connected to a vector network analyzer and the whole setup is enclosed by portable absorbing panels.

4 Data post processing

All measurement data generated in this work were run through the post processing scheme defined in Figure 5, consisting of six steps of data processing. First, the four LP scattering parameters S_{ij}^{kl} were measured both for the DUT and for the reference scenario (empty setup measurement in transmission and conducting panel measurement in reflection), resulting in eight measurements in total for transmission characterization and another eight measurements for reflection characterization.

Next, if necessary, the data was zero padded symmetrically in the frequency domain in order to achieve an interpolation between the data points in time domain and thus improve the resolution of the time domain data [24]. After that, a tapered cosine window function (Tukey window) was applied to the data in the time domain to remove any unwanted multipath signals, such as reflections of the surroundings of the setup. In this step, the previously implemented interpolation is of significant use to make sure no crucial information is lost when applying the time domain window function.

When the scattering data of a test panel have been interpolated and gated in the time domain, they are transformed back to the frequency domain and normalized with the scattering data of the reference measurement, which have

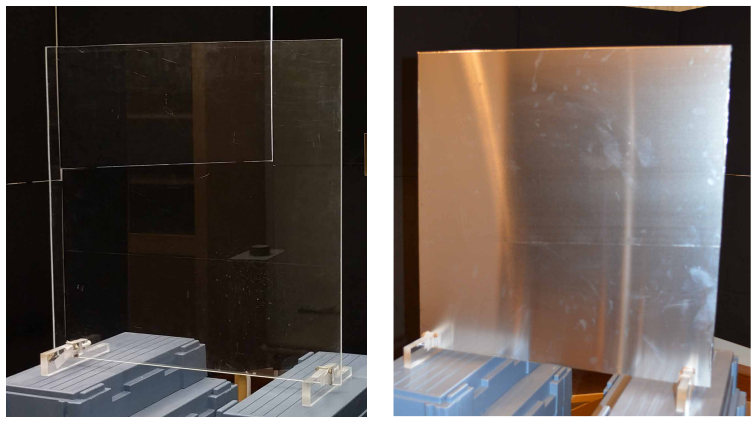

(a) (b)

Figure 4: PMMA test panel with the measures 58 cm × 58 cm used as a reference object to characterize the measurement setup. In (a) the PMMA panel is presented and in (b) the panel has been coated with a highly conductive aluminum foil, using a thin adhesive bonding layer of water, for reference measurements in reflection.

been processed similarly. Note that the normalization is performed before the scattering data is transformed to CP. The impact of normalizing the scattering data of a DUT with reference measurements is described in detail in Section 5. After the normalization, a previously computed rotation correction, based on the reference measurements, is applied to the data to reduce the impact of antenna misalignments in the parallel transmitting/receiving planes with respect to the propagating waves. This correction is described further in Section 5. The only remaining data processing is to convert the LP measurement data to CP. If $\varphi = 45°$ both expressions (2.1)–(2.2) are applied, and if $\varphi = 0°$ the rotation matrix in (2.2) reduce to the identity matrix and only (2.1) is applied.

After the CP scattering matrix components have been determined the main parameters of interest can be extracted. If for example a left hand circular polarization selective structure (LHCPSS) as in Figure 6 is studied, ideal CP filtering properties are achieved if the structure reflects LHCP signals and transmits RHCP signals, while maintaining the polarization state of the signals. The parameters of interest of an LHCPSS are defined in [3] as: the IL of transmitted RHCP, the return loss (RL) of reflected LHCP, and the corresponding AR in transmission and reflection, in this work denoted $\mathrm{AR_t}$ and $\mathrm{AR_r}$. These four

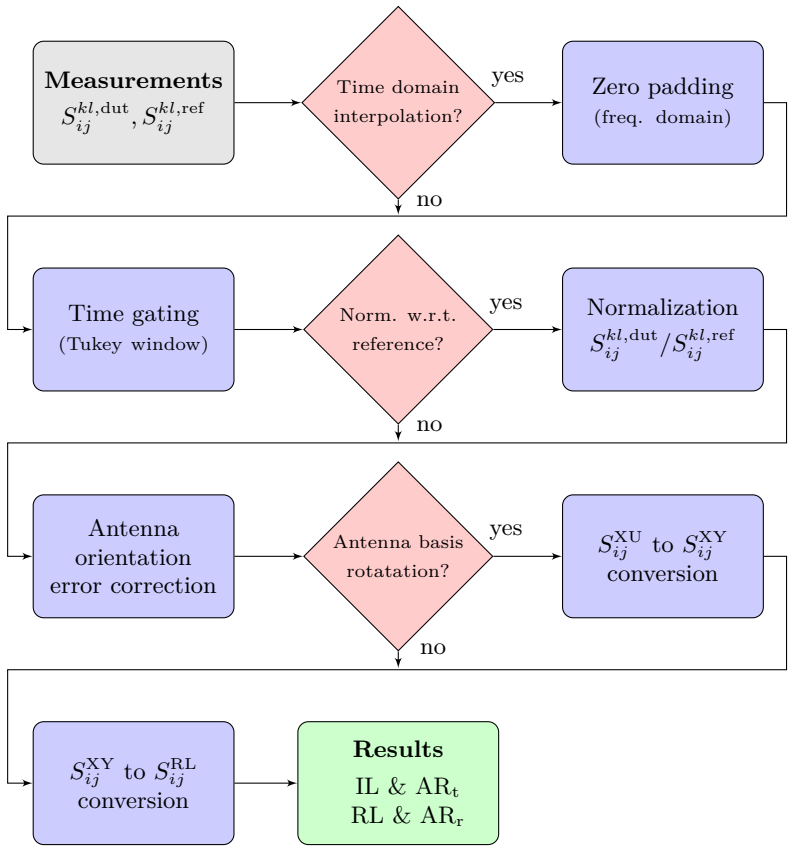

Figure 5: Post processing scheme for CP scattering measurements using LP antennas. To completely characterize the transmission and reflection of a DUT 16 measurements are required in total as input.

parameters are defined in decibels as

$$\mathrm{IL} = -20\log_{10}(|S_{21}^{\mathrm{RR}}|), \tag{4.1}$$

$$\mathrm{RL} = -20\log_{10}(|S_{11}^{\mathrm{LL}}|), \tag{4.2}$$

$$\mathrm{AR_t} = 20\log_{10}\left(\left|\frac{|S_{21}^{\mathrm{LR}}| + |S_{21}^{\mathrm{RR}}|}{|S_{21}^{\mathrm{LR}}| - |S_{21}^{\mathrm{RR}}|}\right|\right), \tag{4.3}$$

$$\mathrm{AR_r} = 20\log_{10}\left(\left|\frac{|S_{11}^{\mathrm{RL}}| + |S_{11}^{\mathrm{LL}}|}{|S_{11}^{\mathrm{RL}}| - |S_{11}^{\mathrm{LL}}|}\right|\right), \tag{4.4}$$

where it can be seen that IL is given by the ratio of the incident power and the transmitted power in co-polarization (RHCP), RL is defined as the ratio of the

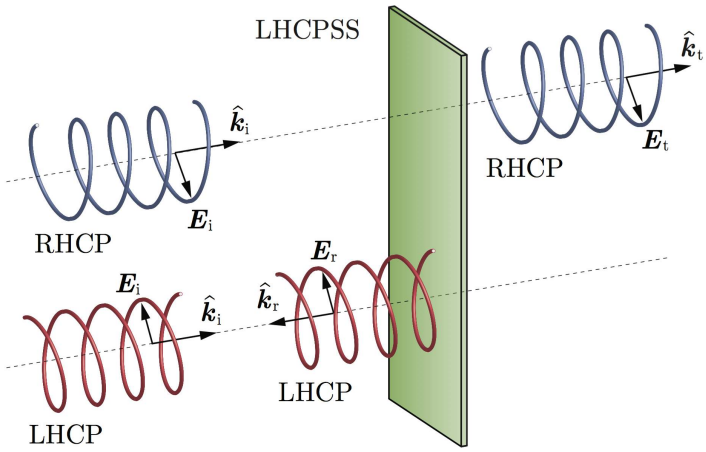

Figure 6: Operational sketch of an LHCPSS, reflecting LHCP signals in co-polarization and transmitting RHCP signals in co-polarization.

incident power and the reflected power in co-polarization (LHCP), and $\mathrm{AR_t}$, $\mathrm{AR_r}$ are given by the quotients in (4.3)-(4.4), representing the polarization purity of the transmitted and reflected signals.

Another relevant parameter is the isolation, which is defined in decibels in [23, Ch.7]. For an LHCPSS this corresponds, in transmission and reflection, to

$$\mathrm{Isolation_t} = -20\log_{10}\left(|S_{21}^{\mathrm{LL}}|\right), \tag{4.5}$$

$$\mathrm{Isolation_r} = -20\log_{10}\left(|S_{11}^{\mathrm{RR}}|\right), \tag{4.6}$$

where again the subscripts t, r indicate transmission and reflection, respectively. Having defined the parameters of interest to characterize a CPSS, we now turn to the accuracy of the measurements.

5 Measurement error estimates and calibration

In order to determine what accuracy that can be expected of the measurement setup, described in detail in Section 3, we describe the effects of finite XPD of the antennas, the orientation of the antennas, and antenna misalignments. The procedures are illustrated with measurements on a homogeneous and isotropic PMMA panel.

5.1 Measurement system XPD

One fundamental limiting factor of a measurement system for CP characterization is the XPD of the antennas. With perfectly aligned antennas and no cross-polarized scattering in the setup, the XPD of the synthesized CP for an empty setup is given by the individual antenna XPD in LP reduced by a factor of two (or 6 dB), due to the presence of two antennas in the system. Given the system XPD, the AR is given by

$$\mathrm{AR} = 20 \log_{10} \left(\left| \frac{10^{\mathrm{XPD}/20} + 1}{10^{\mathrm{XPD}/20} - 1} \right| \right). \tag{5.1}$$

The relation (5.1) is plotted in the left graph in Figure 7, where it can be noted that to determine the AR of a DUT down to levels on the order of 0.5 dB requires a measurement system with XPD $>$ 30 dB. A measurement system with XPD $=$ 20 dB is limited to characterizing AR down to 1.8 dB at best, which is not accurate enough according to the requirements of a CPSS for space applications defined in [3] as

- IL and RL better than 0.5 dB,
- AR better than 0.78 dB (corresponding to XPD $>$ 27 dB).

The simple relation (5.1) clearly identifies the need to utilize antennas with high XPD in order to determine the AR of a test panel as accurately as possible. In this work, LP antennas with boresight XPD of 40–45 dB are used (a system XPD of 34–39 dB), which implies that the lower limit of the presented measurement system is at about AR 0.2 dB.

5.2 Antenna orientations and normalization

In an ideal measurement scenario, the noise level of the setup is zero which results in an infinite signal to noise ratio (SNR). However, in a realistic measurement situation the noise level of the measurement setup is non-zero and a finite SNR of the setup can be identified. Since we make relative measurements, we need high SNR in both DUT data and data for the reference structure. If the principal directions of the transmitting and receiving antennas are aligned, as in the left part of Figure 1, the SNR:s of the reference measurements are much lower in the cross-polarized components, S_{ij}^{XY} and S_{ij}^{YX}, than in the co-polarized components, S_{ij}^{XX} and S_{ij}^{YY}, for fixed ij. But, if the principal directions of the transmitting and receiving antennas are offset by $\varphi = 45°$ as in the right part of Figure 1, the SNR:s of the reference measurements are high and equal in all four components S_{ij}^{XU}, S_{ij}^{YU}, S_{ij}^{XV}, and S_{ij}^{YV}, for fixed ij. To that end, all following measurement results in this work have been acquired using the 45° offset.

The S-parameters used when evaluating the DUT are relative to the reference measurement and ideal S-parameters, *i.e.*,

$$S_{ij}^{kl,\mathrm{rel}} = \frac{S_{ij}^{kl,\mathrm{dut}}}{S_{ij}^{kl,\mathrm{ref}}/S_{ij}^{kl,\mathrm{ideal}}}, \tag{5.2}$$

where the reference ideal LP S-parameters for 45° offset are

$$S_{21}^{\mathrm{ideal}} = -S_{11}^{\mathrm{ideal}} = \frac{1}{\sqrt{2}}\begin{pmatrix} 1 & -1 \\ 1 & 1 \end{pmatrix}. \tag{5.3}$$

Note that the normalization is made before the conversion from LP to CP. This guarantees that each component of $S^{\mathrm{dut,LP}}$ is divided with a component of $S^{\mathrm{ref,LP}}$ measured with a corresponding setup. If the normalization had been made after the conversion to CP, then the measurement errors of several different setups would be mixed together, reducing the accuracy further.

An alternative normalization could be proposed for the case of aligned principal directions of the antennas. We limit the discussion to the transmission case. All components $S_{21}^{kl,\mathrm{dut}}$ could be divided by the co-polarized reference transmission, $S_{21}^{\mathrm{XX,ref}}$ or $S_{21}^{\mathrm{YY,ref}}$, which both have a high SNR. However, this would mean the cross polarized components, $S_{21}^{\mathrm{XY,dut}}$ and $S_{21}^{\mathrm{YX,dut}}$, would have to be normalized with a factor obtained in a slightly different setup, reducing the accuracy. The reflection case follows in the same way.

5.3 Antenna misalignment errors

One source of error associated with using LP antennas for CP measurements is antenna misalignments. In the right graph in Figure 7 the simulated AR of a system, using ideal antennas, is plotted as a function of antenna misalignments, where the solid curve corresponds to a systematic misalignment in one of the components U, V, X or Y, defined in Figure 1. In order to characterize the impact of non-systematic errors associated with antenna misalignments (*i.e.* alignment errors that vary from one measurement to another) a statistical analysis was simulated. In this case, the antennas were misaligned through a rotation with respect to the axis normal to the aperture, and the angle given on the horizontal axis in the right graph in Figure 7 represents the absolute sum of all errors of the four measured components required to extract the CP scattering of a DUT. The dashed curve in the right graph in Figure 7 corresponds to the worst case scenario of this study. As can be seen, a total misalignment of 3° has a significant impact on the accuracy of the setup. This implies that to align the antennas carefully is of high importance when characterizing a DUT in CP using LP antennas.

The errors of a measurement setup due to antenna misalignments can be quantified and to some extent corrected for in post processing. For example, if the antenna orientations corresponding to $\varphi = 45°$ in Figure 1 are utilized in a transmission scenario, the ratios $S_{21}^{\mathrm{XU}}/S_{21}^{\mathrm{YU}}$, $-S_{21}^{\mathrm{XU}}/S_{21}^{\mathrm{XV}}$, $-S_{21}^{\mathrm{YV}}/S_{21}^{\mathrm{XV}}$ and

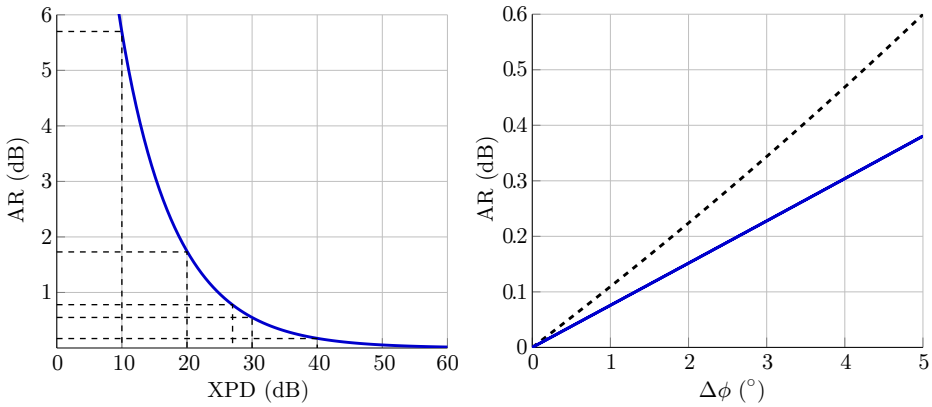

Figure 7: Simulation results of the relation between XPD and AR in a measurement system are presented to the left. The dashed lines indicate the relation at specific XPD values of interest. To the right, simulated measurement error in AR due to antenna misalignments in the plane parallel to the antenna apertures are presented. The solid curve represents a systematic error in one of the antenna orientations, and the dashed curve correspond to the worst case scenario of non-systematic errors distributed over all antenna orientations, where the angle on the horizontal axis $\Delta\phi$ here represents the absolute sum of all errors.

$S_{21}^{\mathrm{YV}}/S_{21}^{\mathrm{YU}}$ are of great interest. The same type of ratios can be evaluated in a reflection scenario. In an ideal setup, the amplitude and phase of these relations should be zero dB and 0° for the reference data, but in a realistic case errors due to antenna misalignment (and effects like phase changes due to cable bending in different setups) will result in non-zero values. In this work, the amplitude errors of the mentioned ratios, for time gated data, are on the order of ± 0.3 dB and the phase errors are about $\pm 3°$.

The amplitude errors can be reduced by utilizing rotation correction, mentioned in Section 4. Consider the following case depicted in Figure 8 with the measurements visualized as vectors. The ideal alignment corresponds to 45° angle between the basis of the receiving and transmitting antenna, indicated by the full drawn vectors and the actual alignment is shown with the dashed vectors. First the S^{YU} component is to be measured and thus the antennas are rotated for this configuration. However due to errors in alignment the assumed orientation of the vectors $\hat{\boldsymbol{y}}$ and $\hat{\boldsymbol{u}}$ does not hold, as indicated by θ_1 and θ_2 in Figure 8. The amplitude error is then given by the projection of $\hat{\boldsymbol{y}}' = R(\theta_1)\hat{\boldsymbol{y}}$ on $\hat{\boldsymbol{u}}' = R(\theta_2)\hat{\boldsymbol{u}}$, where $R(\theta_1)$ is a rotation matrix. After this measurement is completed, the antenna in the $\hat{\boldsymbol{u}}$ direction is rotated to $\hat{\boldsymbol{v}}$ in order to be able to measure S^{YV}, introducing yet another misalignment angle θ_3. For one complete

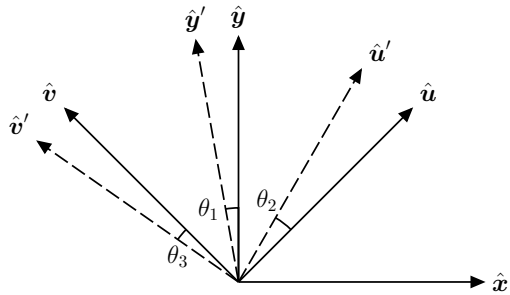

Figure 8: Error in alignment, θ introduced through the physical rotations of the antennas in the setup. The vectors $\hat{\boldsymbol{x}}$ and $\hat{\boldsymbol{y}}$ form a basis for the receiving antenna and similarly $\hat{\boldsymbol{u}}$ and $\hat{\boldsymbol{v}}$ form a basis for the transmitting antenna.

set of measurements this can be stated as,

$$S^{\mathrm{YU}} = a_1(R(\theta_1)\hat{\boldsymbol{y}})^{\mathrm{T}}R(\theta_2)\hat{\boldsymbol{u}} = a_1\cos(\pi/4+\phi_{12}), \tag{5.4}$$

$$S^{\mathrm{YV}} = a_2(R(\theta_1)\hat{\boldsymbol{y}})^{\mathrm{T}}R(\theta_3)\hat{\boldsymbol{v}} = a_2\cos(\pi/4-\phi_{13}), \tag{5.5}$$

$$S^{\mathrm{XV}} = a_3(R(\theta_4)\hat{\boldsymbol{x}})^{\mathrm{T}}R(\theta_3)\hat{\boldsymbol{v}} = a_3\cos(3\pi/4-\phi_{43}), \tag{5.6}$$

$$S^{\mathrm{XU}} = a_4(R(\theta_4)\hat{\boldsymbol{x}})^{\mathrm{T}}R(\theta_5)\hat{\boldsymbol{u}} = a_4\cos(\pi/4-\phi_{45}), \tag{5.7}$$

where R is a rotation matrix, a_i some constant and $\phi_{ij} = \theta_i - \theta_j$. In the case of the reference measurement the amplitudes should be equal, $a_i = a$, and since only differences between the angles appear in the final equations, we can set one of them to zero, for instance $\theta_1 = 0$. Since the rotations are the same for all frequencies, we find the most likely ones by minimizing the amplitude error across all frequency points. To determine these rotation errors of a measurement setup, reference measurements of the empty setup in transmission, and the reflection of a conducting plate in reflection, are utilized. This correction is then applied to the normalized scattering data of a DUT in LP. Some error due to misalignment is still expected after the correction, albeit less significant. In this work, the uncorrected data commonly resulted in θ_i on the order of 0.4° corresponding to an amplitude error of about 0.3 dB. A typical correction resulted in an absolute amplitude error of < 0.1 dB which is a significant improvement over the uncorrected data.

5.4 Verification measurements

In Figure 9, the AR in transmission and reflection of a homogeneous and isotropic PMMA test panel with the measures 58 cm × 58 cm × 2.0 cm is presented. Zero padding and time gating have been applied to the data referred to as processed, and additional rotation correction and normalization with respect to a reference measurement have been applied to the data referred to as calibrated. As was stated in Section 3, the reference scenario in transmission consists of the empty

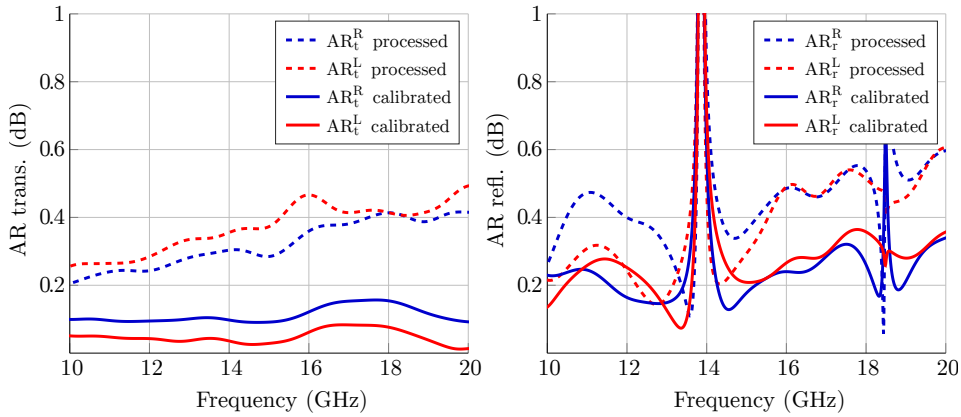

Figure 9: Measured AR of isotropic PMMA test panels, with and without calibration using $\varphi = 45°$ antenna orientations. In the top graph the transmission AR of a 58 cm × 58 cm × 2.0 cm panel is presented, and in the bottom graph the reflection AR of the same panel is presented.

setup, and the reference in reflection corresponds to a measurement of the PMMA panel coated with an aluminum foil, as in Figure 4 (b).

A significant improvement in the AR can be noticed both in the transmission and reflection results in Figure 9 when the rotation correction and normalization are applied to the DUT data, and an AR reference level better than 0.2 dB is achieved in transmission and 0.4 dB in reflection. When comparing these results to the measurement error level of 0.2–0.3 dB caused by using antennas with XPD $\approx$ 40 dB, it can be seen that in transmission the curves are below this limit and the AR curves for RHCP and LHCP diverge slightly after the normalization and rotation correction. At the same time, in reflection the curves are still above this lower limit after the normalization and error correction and the RHCP and LHCP AR curves are closer to each other after the normalization. The two spikes in the AR curve in the reflection data of Figure 9 correspond to the frequencies where the electrical thickness of the DUT is equal to $n\lambda/2$, $n = 1, 2, ..,$ resulting in almost perfect transmission and thus significantly reducing the SNR of the received reflected signal. This effect clearly indicates the importance of having a high SNR for accurate AR characterization of a DUT.

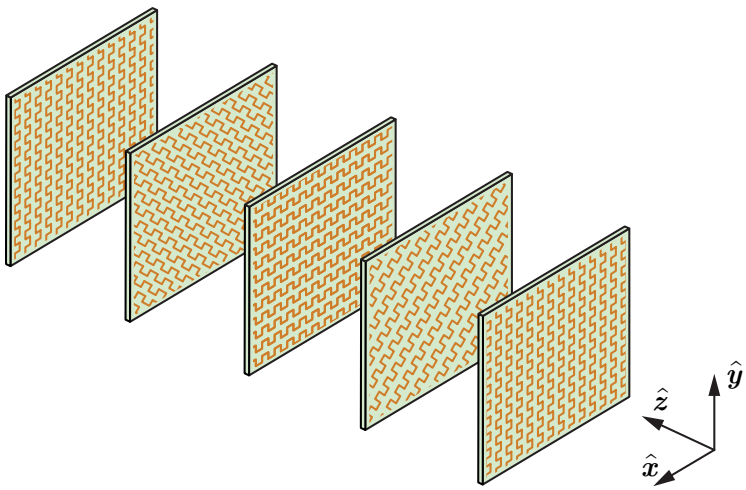

Figure 10: Concept design of the CPSS under study, consisting of meander line substrates with the pattern rotated 45 degrees with respect to the previous layer.

6 Circular polarization selective structure measurement results

The measurement scheme described in Sections 3–4, and the calibration methods and rotation error correction described in Section 5 were utilized to characterize the transmission and reflection properties of a wideband CPSS described in detail in [6]. The CPSS is based on cascaded anisotropic layers of conducting meander line patterns, as in Figure 10, where each consecutive layer is rotated 45°. A manufactured prototype of the CPSS is presented in Figure 11. The structure consists of thin Arlon DiClad 880 substrates separated by sheets of Rohacell 31 HF low permittivity foam. The total thickness of the prototype is 13.7 mm, which corresponds to 0.69 wavelengths at the center frequency 15 GHz. Specific material properties and design parameters of the CPSS are presented in [6]. Simulated and experimental results are presented in Figures 12–14, where the transparent dotted curves correspond to raw measurement data, the dashed curves referred to as processed are measurement data after time gating and zero padding, and the dash-dotted curves referred to as calibrated are the final state of the measurement results after the rotation error correction and the normalization have been applied. The solid lines correspond to simulation data from Computer Simulation Technology Microwave Studio (CST MWS), utilizing the frequency domain solver, with 16 steps per wavelength mesh setting and local mesh refinement at specific regions of the structure.

The transmission results in Figure 12 were acquired with a separation of 0.9 m between the antennas and the CPSS. All measured scattering data from the DUT

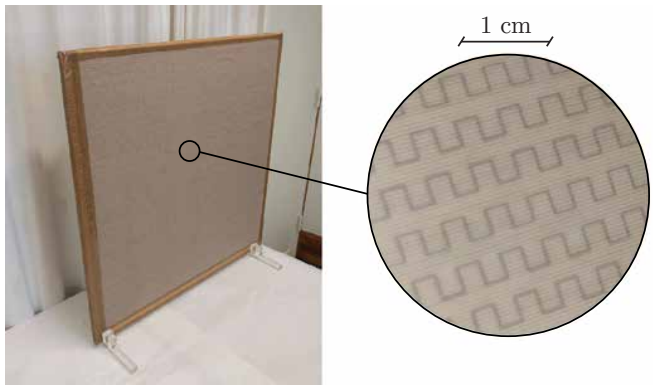

Figure 11: Manufactured CPSS prototype originally presented in [6]. To the left the 58 cm × 58 cm panel is presented and to the right a zoomed in picture of the meander line pattern on the fist substrate is shown.

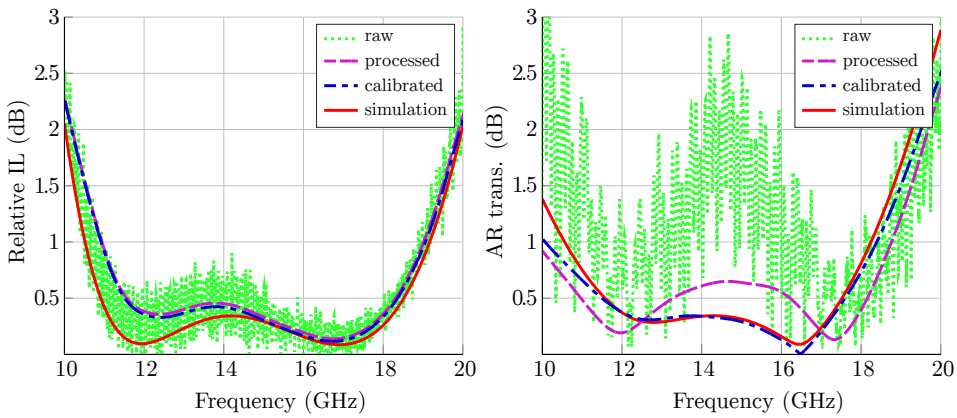

Figure 12: Transmission properties of a wideband CPSS, where the solid lines are simulation results, the dotted curves are raw measurement data, the dashed curves are processed data (after time gating and zero padding), and the dash-dotted lines correspond to data that have been calibrated and corrected for rotation errors using the scheme described in detail in Section 5. The top graph shows the relative IL for RHCP of the CPSS and the bottom graph shows the corresponding AR of the CPSS.

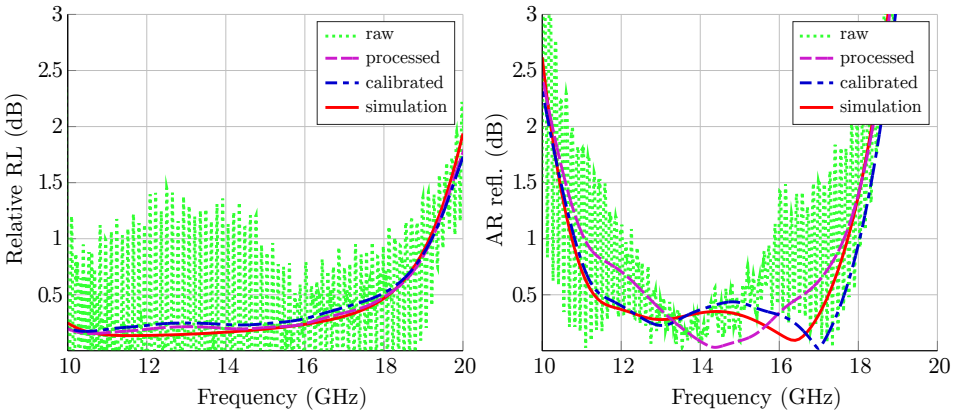

Figure 13: Reflection properties of a wideband CPSS, where the solid lines correspond to simulation results, the dotted curves to raw measurement data, the dashed curves to processed data (after time gating and zero padding), and the dash-dotted lines correspond to data that have been calibrated and corrected for rotation errors. The top graph shows the relative RL for LHCP of the CPSS and the bottom graph shows the corresponding AR of the CPSS.

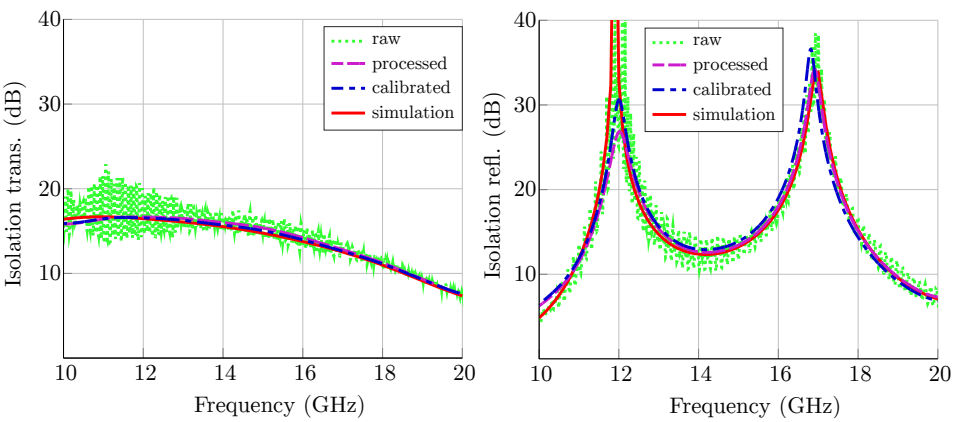

Figure 14: Isolation of the wideband CPSS, where the solid lines correspond to simulation results, the dotted curves to raw measurement data, the dashed curves to processed data (after time gating and zero padding), and the dash-dotted lines correspond to data that have been calibrated and corrected for rotation errors. The top graph shows the isolation in transmission for LHCP and the bottom graph shows the isolation in reflection for RHCP.

were normalized with a corresponding empty setup transmission measurement. The results in Figure 13 were achieved using a distance of 1.2 m between the antennas and the CPSS. All measured scattering data from the DUT were normalized with a corresponding reference reflection measurement, as described in Section 3. In Figure 14, the isolation of the CPSS, both in reflection and in transmission are presented.

In all graphs in Figures 12–14 a significant improvement can be noticed between the raw measurement data and the processed data. The reason for this improvement is the fact that the raw data are composed of signals from *all* possible paths from the transmitting antenna to the receiving antenna. Since the main signals of interest have a clearly defined trajectory (along the shortest path from the transmitting antenna, interacting with the DUT, to the receiving antenna) these signals can be separated from all undesired multipath signals.

The CPSS AR curves in Figures 12–13 indicate that, in the same manner as the results of the PMMA test panels in Figure 9, by applying the rotation error correction and the calibration scheme in Section 5 the accuracy of the measured AR is significantly improved. After calibration, the agreement between the measured and simulated AR is excellent both in transmission and reflection. At the same time, the calibration is not significantly affecting the IL, RL or isolation of the DUT, as can be seen in Figures 12–14. The agreement between simulated and measured IL, RL and isolation is also good.

In order to verify the repeatability of the measurement results of the wideband CPSS DUT, the complete setup was disassembled and reassembled five times in transmission and reflection respectively, using different distances between the antennas. In transmission, the distance from the DUT to the antennas was varied between 0.35–1.00 m, and in reflection the distance from the DUT to the antennas was varied between 0.7–1.8 m with angles of incidence 3–8° as a consequence of varying the distance from the antennas to the DUT.

When comparing the measured and simulated IL and AR in transmission in Figures 15–17, it can be seen that the agreement is very good and the repeatability from subsequent measurements is verified. A small deviation can be noted for lower frequencies, possibly caused by losses in the DUT unaccounted for in the simulations. The measured and simulated RL and AR in reflection also agree very well, but the spread between subsequent measurements is slightly larger than in the transmission parameters. This is mainly due to alignment issues associated with performing reflection measurements in general. Also, it should be noted that when varying the distance from the DUT to the antennas in reflection, the illumination angle is varied. In simulations of the CPSS, the mentioned angle variation implies a deviation smaller than 0.2 dB from the normal incidence results. The measured isolation between RHCP and LHCP is in good agreement with simulations both in transmission and reflection. Overall, the measurement results are in excellent agreement with the simulation data, and the spread between repeated measurements is in line with expectations.

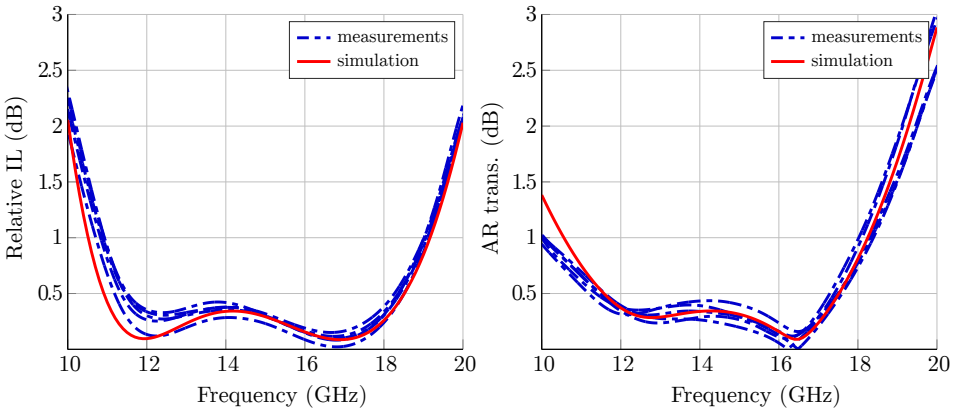

Figure 15: Multiple transmission measurements of a wideband CPSS, displaying the repeatability of the results acquired with the portable setup used in this work. The solid curves correspond to simulation data, and the dash-dotted lines correspond to measurement results acquired from five separate measurements. The top graph shows the RHCP IL and the bottom graph shows the corresponding AR.

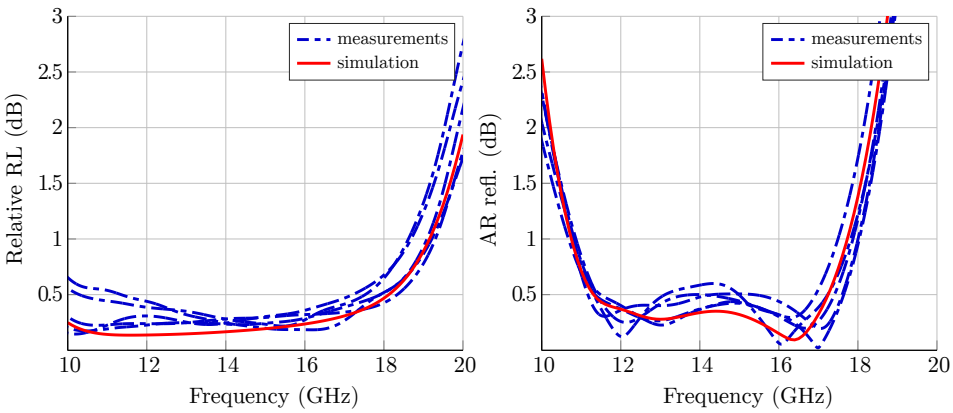

Figure 16: Multiple reflection measurements of a wideband CPSS, displaying the repeatability of the results acquired with the portable setup used in this work. The solid curves correspond to simulation data, and the dash-dotted lines correspond to measurement results acquired from five separate measurements. The top graph shows the LHCP RL and the bottom graph shows the corresponding AR.

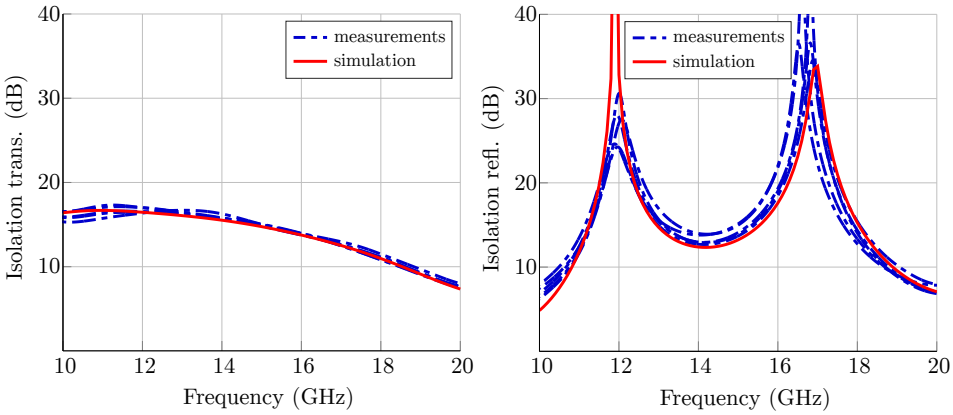

Figure 17: The isolation of a wideband CPSS from multiple transmission and reflection measurements, displaying the repeatability of the results acquired with the portable setup used in this work. The solid curves correspond to simulation data, and the dash-dotted lines correspond to measurement results acquired from five separate measurements. The top graph shows the isolation in transmission for LHCP and the bottom graph shows the isolation in reflection for RHCP.

7 Conclusions

A technique for measuring the CP transmission and reflection properties of a test panel has been presented. By utilizing LP antennas with a high XPD, the CP scattering of a test panel can be synthesized with high accuracy from LP measurements. A relative rotation of the transmitting and receiving antennas of 45° was introduced in order to achieve a high signal to noise ratio in all reference scattering matrix components. This arrangement introduces the possibility of calibrating the DUT data in an efficient manner, resulting in improved agreement in AR between measurements and simulated data. A post processing procedure was presented and utilized for characterizing a wideband CPSS. The agreement between measured and simulated data is excellent and the repeatability of the measurements was verified for the specific setup.

Acknowledgments

The authors of this paper kindly acknowledge Ron van Hoorn and Oliver Krause at Evonik for providing Rohacell samples for the manufacturing of the test panel. The work reported in this paper was partially supported by ESA Contract No. 4000108854/13/NL/MH.

References

[1] S. M. A. M. H. Abadi and N. Behdad. A broadband, circular-polarization selective surface. *Journal of Applied Physics*, **119**(24), pp. 244901, 2016.

[2] S. M. A. M. H. Abadi and N. Behdad. Wideband linear-to-circular polarization converters based on miniaturized-element frequency selective surfaces. *IEEE Trans. Antennas Propag.*, **64**(2), pp. 525–534, 2016.

[3] M. Albani, P. Balling, L. Datashvili, G. Gerini, P. Ingvarson, K. Pontoppidan, M. Sabbadini, D. Sjöberg, S. Skokic, and G. Vecchi. Concepts for polarising sheets & "dual-gridded" reflectors for circular polarisation. In *ICECom Proceedings*, pp. 1–4, 2010.

[4] M. Baunge, H. Ekström, P. Ingvarson, and M. Petersson. A new concept for dual gridded reflectors. In *Proceedings of the fourth European Conference on Antennas and Propagation (EuCAP)*, pp. 1–5. IEEE, 2010.

[5] A. Ericsson and D. Sjöberg. A performance study of circular polarization selective structures. In *Proceedings of the 9th European Conference on Antennas and Propagation (EuCAP)*. IEEE, 2015.

[6] A. Ericsson and D. Sjöberg. Design and analysis of a multilayer meander line circular polarization selective structure. *IEEE Trans. Antennas Propag.*, **65**(8), pp. 4089–4101, 2017.

[7] A. Ericsson and D. Sjöberg. A resonant circular polarization selective structure of closely spaced wire helices. *Radio Science*, **50**(8), pp. 804–812, 2015. 2014RS005641.

[8] M. J. Franco. A high-performance dual-mode feed horn for parabolic reflectors with a stepped-septum polarizer in a circular waveguide [antenna designer's notebook]. *IEEE Antennas and Propagation Magazine*, **53**(3), pp. 142–146, 2011.

[9] V. Fusco and B. Nair. Circular polarisation selective surface characterisation and advanced applications. *IEE Proceedings Microwaves Antennas and Propagation*, **153**(3), pp. 247–252, 2006.

[10] S. S. Gao, Q. Luo, and F. Zhu. *Circularly polarized antennas*. John Wiley & Sons, 2013.

[11] IEEE standard test procedures for antennas, 2008. IEEE Std 149-1979 (R2008).

[12] W. A. Imbriale, S. S. Gao, and L. Boccia, editors. *Space Antenna Handbook*. Wiley, 2012.

[13] M. Joyal and J. Laurin. A cascaded circular-polarization-selective surface at K band. In *Antennas and Propagation (APSURSI), 2011 IEEE International Symposium on*, pp. 2657–2660. IEEE, 2011.

[14] M. Joyal and J. Laurin. Analysis and design of thin circular polarizers based on meander lines. *IEEE Trans. Antennas Propag.*, **60**(6), pp. 3007–3011, 2012.

[15] M. Joyal and J. Laurin. Design and analysis of a cascade circular-polarization-selective surface at K band. *IEEE Trans. Antennas Propag.*, **62**(6), pp. 3043–3052, 2014.

[16] Keysight Instruments and MATLAB, 2017. Available at: https://se.mathworks.com/products/instrument/supported/keysight.html, accessed 2017-09-22.

[17] A. Kinloch. *Adhesion and Adhesives: Science and Technology*. Springer Science & Business Media, 2012.

[18] C. A. Leal-Sevillano, J. A. Ruiz-Cruz, J. R. Montejo-Garai, and J. M. Rebollar. Wide-band compact antenna feed for multi-beam satellite communications. In *Antennas and Propagation (EuCAP), 2015 9th European Conference on*, pp. 1–4. IEEE, 2015.

[19] I. Lopez and J. Laurin. A circular polarization selective surface implemented on a flexible substrate. *IEEE Trans. Antennas Propag.*, **62**(7), pp. 3847–3852, 2014.

[20] I. Lopez and J.-J. Laurin. Alternative topologies of circular polarization selective surfaces based on modifications of the Pierrot cell. *IEEE Trans. Antennas Propag.*, **63**(4), pp. 1465–1472, 2015.

[21] G. A. Morin. A simple circular polarization selective surface (CPSS). In *Antennas and Propagation Society International Symposium, 1990. AP-S. Merging Technologies for the 90's. Digest.*, pp. 100–103. IEEE, 1990.

[22] R. Pierrot. Reflector for circularly polarized waves, 1970. US Patent 3,500,420.

[23] D. M. Pozar. *Microwave Engineering*. John Wiley & Sons, New York, NY, third edition, 2005.

[24] K. R. Rao, D. N. Kim, and J. J. Hwang. *Fast Fourier Transform-Algorithms and Applications*. Springer Science & Business Media, 2011.

[25] S. Rao, L. Shafai, and S. K. Sharma. *Handbook of Reflector Antennas and Feed Systems Volume III: Applications of Reflectors*. Artech house, 2013.

[26] J. E. Roy and L. Shafai. Reciprocal circular-polarization-selective surface. *Antennas and Propagation Magazine, IEEE*, **38**(6), pp. 18–33, 1996.

[27] J. Sanz-Fernandez, E. Saenz, and P. de Maagt. A circular polarization selective surface for space applications. *IEEE Trans. Antennas Propag.*, **63**(6), pp. 2460–2470, 2015.

[28] J. Sanz-Fernandez, E. Saenz, P. de Maagt, and C. Mangenot. Circular polarization selective surface for dual-optics CP offset reflector antennas in Ku-band. In *Proceedings of the 6th European Conference on Antennas and Propagation (EuCAP)*, pp. 2683–2687. IEEE, 2012.

[29] D. Sjöberg and A. Ericsson. A multi layer meander line circular polarization selective structure (MLML-CPSS). In *Proceedings of the 8th European Conference on Antennas and Propagation (EuCAP)*, pp. 464–468. IEEE, 2014.

[30] W. Tang, G. Goussetis, N. J. Fonseca, H. Legay, E. Saenz, and P. de Maagt. Study of coupled split-ring resonator arrays for circular polarization selective surface. In *Antennas and Propagation & USNC/URSI National Radio Science Meeting, 2015 IEEE International Symposium on*, pp. 362–363. IEEE, 2015.

[31] I.-Y. Tarn and S.-J. Chung. A new advance in circular polarization selective surface – A three layer CPSS without vertical conductive segments. *IEEE Trans. Antennas Propag.*, **55**(2), pp. 460–467, 2007.

[32] W. V. Tilston, T. Tralman, and S. M. Khanna. A polarization selective surface for circular polarization. In *Antennas and Propagation Society International Symposium, 1988. AP-S. Digest*, pp. 762–765. IEEE, 1988.

Design and Optimization of Dual Band Circular Polarization Selective Structures

Johan Lundgren, Andreas Ericsson and Daniel Sjöberg

Paper V

To be submitted as: J. Lundgren, A. Ericsson and D. Sjöberg, "Design and Optimization of Dual Band Circular Polarization Selective Structures," *IEEE Transactions on Antennas and Propagation*, 2017.

Preprint published as: Technical Report LUTEDX/(TEAT-7257), pp. 1–21, 2017, Department of Electrical and Information Technology, Lund University, Sweden. http://www.eit.lth.se.

Abstract

We present a non-resonant, dual band circular polarization selective structure (CPSS) for satellite communication applications in the K- and K_a-band. The structure consists of multiple layers of cascaded anisotropic sheets, with printed meander lines, separated by low permittivity spacers. It reflects right hand circular polarization and transmits left hand circular polarization in the lower frequency band. In the upper frequency band the opposite polarization selectivity is achieved. The theory of dual band circular polarization selectivity from cascaded anisotropic sheets is presented, and it is concluded that the separation between the frequency bands of operation is governed by the relative rotation between subsequent layers. An optimization routine for synthesizing dual band CPSSs from predefined design requirements is introduced, where a number of different optimization algorithms are utilized. A simulated design is presented which fulfills the strict design requirements of insertion loss and return loss less than 0.5 dB, and axial ratio less than 0.78 dB, in the frequency bands 17.7–20.2 GHz and 27.5–30.0 GHz. A prototype of the optimized design has been fabricated and characterized experimentally, both in transmission and reflection, and good agreement is observed between simulated and experimental results. This type of structure is a potential candidate for implementation in dual band multiple spot beam systems utilizing frequency and polarization reuse schemes.

1 Introduction

Key components in today's interconnected world are communication satellites positioned in crowded orbits [7]. In order to utilize the available satellite aperture in a more efficient manner, frequency and polarization reuse schemes can be utilized [14]. By using dual band satellite communication (SATCOM) systems these satellites can be improved by reducing the number of reflectors needed by a factor of two [2]. An example of such a system was recently presented in [17], where a dual band polarizing surface converting linear polarization (LP) to circular polarization (CP) was used as a reflector in the K_u-band. Alternative solutions to this system can be achieved using dual band circular polarization selective structures (CPSSs), either as diplexers or reflectors. A dual band CPSS will for the lower frequency band reflect one handedness of CP while transmitting the orthogonal circular polarization, and do the converse for the higher frequency band [11].

In the last century, many different CPSS designs have been presented with various performance levels [1, 8, 12, 13, 16, 18, 20–22]. An overview of the CPSSs presented up to date is presented in [5], where these structures are evaluated with respect to relevant performance requirements. Recently, a high performing, wide band CPSS concept based on non-resonant elements was presented [3–5, 15]. These designs all consist of multiple sheets of meander lines stacked and rotated after one another. Each layer is perceived as an effective capacitance/inductance

in linear polarization by incident waves. A shortcoming of previously presented CPSSs is that the design and optimization have been carried out to obtain operation in a single frequency band. In the same manner as in a frequency selective structure, higher order resonances can be observed in a CPSS. However, the frequency separation between these resonances is generally much larger than what is desirable, and to optimize a CPSS for dual band operation is a challenging task.

To this end, we present a design procedure for dual band CPSSs consisting of multiple layers of anisotropic sheets. In the same manner as in [3–5, 15], subwavelength meander lines are used to achieve a strong anisotropic response in the sheets. The frequency bands of interest in this work are the SATCOM downlink band $17.7-20.2\,\mathrm{GHz}$ and the uplink band $27.5-30.0\,\mathrm{GHz}$, located in the K- and $\mathrm{K_a}$-bands. To the authors' knowledge, this is the first time a dual band CPSS is presented with performance levels applicable to real world configurations.

The paper is organized as follows: in Section 2 the theory of scattering in circular polarization from anisotropic sheets is presented. It is shown that the optimal number of layers of a CPSS can be found in order to achieve CP selectivity in multiple frequency bands, and to reduce the cross polarization scattering. A detailed optimization procedure is introduced in Section 3, where a dual band CPSS is designed based on predefined performance requirements. Simulation results of the optimized design are presented in Section 4. A prototype was manufactured and the details of this test panel are presented in Section 5, and experimental results of this structure are evaluated in Section 6. Finally, some concluding remarks are presented in Section 7.

2 Theory - dual band circular polarization selectivity from linear elements

The scattering matrix in circular polarization of a system with two ports, located on each side of the sample, is

$$\mathbf{S}^{\mathrm{CP}} = \begin{pmatrix} S_{11}^{\mathrm{RR}} & S_{11}^{\mathrm{RL}} & S_{12}^{\mathrm{RR}} & S_{12}^{\mathrm{RL}} \\ S_{11}^{\mathrm{LR}} & S_{11}^{\mathrm{LL}} & S_{12}^{\mathrm{LR}} & S_{12}^{\mathrm{LL}} \\ S_{21}^{\mathrm{RR}} & S_{21}^{\mathrm{RL}} & S_{22}^{\mathrm{RR}} & S_{22}^{\mathrm{RL}} \\ S_{21}^{\mathrm{LR}} & S_{21}^{\mathrm{LL}} & S_{22}^{\mathrm{LR}} & S_{22}^{\mathrm{LL}} \end{pmatrix}, \tag{2.1}$$

where the superscript R stands for right hand circular polarization (RHCP) and similarly L stands for left hand circular polarization (LHCP). The subscripts 1 and 2 indicate the number of the receiving and transmitting port. Throughout this work, the time convention $\mathrm{e}^{\mathrm{j}\omega t}$ is used, and for the definition of circular polarization the IEEE definition is followed [6]. An ideal right hand circular polarization selective structure (RHCPSS) should reflect RHCP waves and transmit LHCP waves, while maintaining the polarization state of the signals, and is de-

scribed by

$$\mathbf{S}^{\mathrm{RHCPSS}} = \begin{pmatrix} \mathrm{e}^{-\mathrm{j}\phi_\mathrm{r}} & 0 & 0 & 0 \\ 0 & 0 & 0 & \mathrm{e}^{-\mathrm{j}\phi_\mathrm{t}} \\ 0 & 0 & \mathrm{e}^{-\mathrm{j}\phi_\mathrm{r}} & 0 \\ 0 & \mathrm{e}^{-\mathrm{j}\phi_\mathrm{t}} & 0 & 0 \end{pmatrix}, \tag{2.2}$$

where ϕ_t and ϕ_r are the phases of the transmission and reflection coefficients, respectively. Similarly, an ideal left hand circular polarization selective structure (LHCPSS) is described by

$$\mathbf{S}^{\mathrm{LHCPSS}} = \begin{pmatrix} 0 & 0 & \mathrm{e}^{-\mathrm{j}\phi_\mathrm{t}} & 0 \\ 0 & \mathrm{e}^{-\mathrm{j}\phi_\mathrm{r}} & 0 & 0 \\ \mathrm{e}^{-\mathrm{j}\phi_\mathrm{t}} & 0 & 0 & 0 \\ 0 & 0 & 0 & \mathrm{e}^{-\mathrm{j}\phi_\mathrm{r}} \end{pmatrix}. \tag{2.3}$$

The scattering matrix of an ideal dual band CPSS will be represented by either (2.2) or (2.3) for a certain frequency f_1 and the other for frequency f_2.

A layer of infinite extent in the plane perpendicular to the direction of propagation, and of infinitesimal thickness, can be described by the reflection coefficients (r_x, r_y), and the transmission coefficients $(t_x = 1 + r_x, t_y = 1 + r_y)$ in LP. It can also be represented by a scattering matrix in CP [11], where the CP scattering matrix for the linear element is given by

$$\begin{aligned} \mathbf{S}^{\mathrm{CP}}_{\mathrm{Linear}} = {} & \frac{r_x + r_y}{2} \begin{pmatrix} 0 & 1 & 1 & 0 \\ 1 & 0 & 0 & 1 \\ 1 & 0 & 0 & 1 \\ 0 & 1 & 1 & 0 \end{pmatrix} + \begin{pmatrix} 0 & 0 & 1 & 0 \\ 0 & 0 & 0 & 1 \\ 1 & 0 & 0 & 0 \\ 0 & 1 & 0 & 0 \end{pmatrix} \\ & + \frac{r_x - r_y}{2} \begin{pmatrix} \mathrm{e}^{-2\mathrm{j}\theta_i} & 0 & 0 & \mathrm{e}^{-2\mathrm{j}\theta_i} \\ 0 & \mathrm{e}^{2\mathrm{j}\theta_i} & \mathrm{e}^{2\mathrm{j}\theta_i} & 0 \\ 0 & \mathrm{e}^{2\mathrm{j}\theta_i} & \mathrm{e}^{2\mathrm{j}\theta_i} & 0 \\ \mathrm{e}^{-2\mathrm{j}\theta_i} & 0 & 0 & \mathrm{e}^{-2\mathrm{j}\theta_i} \end{pmatrix}, \end{aligned} \tag{2.4}$$

where θ_i is the rotation of the element in the plane. A single layer cannot be reduced to any of the ideal cases (2.2) or (2.3), but these properties can be achieved by stacking several layers each rotated with respect to the previous layer and separated a distance d. Assuming $r_y = 0$, $r_x = r$ and using the Born approximation treating the elements as weak scatterers [10], the scattering matrix for multiple layers of linear elements can be shown to be

$$\begin{aligned} \mathbf{S}_{\mathrm{Linear}} = {} & \mathrm{e}^{-\mathrm{j}kd} \begin{pmatrix} 0 & 0 & 1 & 0 \\ 0 & 0 & 0 & 1 \\ 1 & 0 & 0 & 0 \\ 0 & 1 & 0 & 0 \end{pmatrix} \\ & + \sum_{n=1}^{N} \frac{r}{2} \begin{pmatrix} \mathrm{e}^{-2\mathrm{j}(kz_n+\theta_n)} & \mathrm{e}^{-\mathrm{j}kz_n} & \mathrm{e}^{-\mathrm{j}kd} & \mathrm{e}^{-\mathrm{j}(kd+2\theta_n)} \\ \mathrm{e}^{-2\mathrm{j}kz_n} & \mathrm{e}^{-2\mathrm{j}(kz_n-\theta_n)} & \mathrm{e}^{-\mathrm{j}(kd-2\theta_n)} & \mathrm{e}^{-\mathrm{j}kd} \\ \mathrm{e}^{-\mathrm{j}kd} & \mathrm{e}^{-\mathrm{j}(kd-2\theta_n)} & \mathrm{e}^{-2\mathrm{j}(kz_n+\theta_n)} & \mathrm{e}^{-2\mathrm{j}kz_n} \\ \mathrm{e}^{-\mathrm{j}(kd+2\theta_n)} & \mathrm{e}^{-\mathrm{j}kd} & \mathrm{e}^{-2\mathrm{j}kz_n} & \mathrm{e}^{-2\mathrm{j}(kz_n-\theta_n)} \end{pmatrix}, \end{aligned} \tag{2.5}$$

where N is the number of layers, z_n is the position of the n:th layer and θ_n is the rotation of the n:th layer. With equidistant placement and the same rotation between each layer the relevant reflection parameters in the scattering matrix can be described by

$$S_{11}^{\mathrm{RR}} = \frac{r}{2}\sum_{n=1}^{N} \mathrm{e}^{-\mathrm{j}2n(kd+\theta)}, \tag{2.6}$$

$$S_{11}^{\mathrm{LL}} = \frac{r}{2}\sum_{n=1}^{N} \mathrm{e}^{-\mathrm{j}2n(kd-\theta)}, \tag{2.7}$$

$$S_{11}^{\mathrm{RL}} = S_{11}^{\mathrm{LR}} = \frac{r}{2}\sum_{n=1}^{N} \mathrm{e}^{-\mathrm{j}2nkd}. \tag{2.8}$$

When the phase distance between two layers equals the relative rotation of the linear elements, $k_1 d = \theta$, (2.7) is maximized and LHCP waves are reflected. If the direction of rotation between the layers is mirrored, *i.e.* $\theta = -k_1 d$, (2.6) is instead maximized and thus the opposite polarization (RHCP) is reflected. Given that either (2.6) or (2.7) is maximized, the number of layers N can be chosen to minimize the reflection of the orthogonal co-polarized component as well as the cross polarization terms (2.8). A detailed derivation of the lowest optimal number of layers (N_{opt}) is presented in [11], where it is concluded that this quantity is given by the smallest denominator of θ/π when this is a rational number. To summarize, if $\theta = -k_1 d < 0$ the structure is an RHCPSS at the frequency f_1, corresponding to the wave number k_1. Another solution is achieved when $k_2 d = \pi + \theta = \pi - k_1 d$. Then (2.7) is maximized and for the previously chosen N_{opt} (2.6) and (2.8) are still minimized. This indicates that the structure is an LHCPSS at the frequency f_2, corresponding to the wave number k_2, and the relation between the two bands is given by,

$$f_2 = \frac{\pi - |\theta|}{|\theta|} f_1. \tag{2.9}$$

A physical explanation of these two solutions, and thus the dual band behavior, is as follows. At a fixed instant in time, an electromagnetic CP wave with frequency f_1 propagating in the z-direction through a multilayered CPSS will have a certain phase distribution as it interacts with each of the anisotropic layers, as in Figure 1. If the polarization of the wave rotates in a certain direction in space as a function of the distance z, and the rotation between each layer of the structure θ matches this rotation, the wave will align with the layers and be reflected. This situation is described by the relation $k_1 d = -\theta$. The orthogonal polarization will be misaligned with each layer and will thus be transmitted. However, if another wave at a different frequency f_2 rotates in the opposite direction in space it would also align with the layers the same way if the change of phase between the layers was $k_2 d = \pi + \theta = \pi - k_1 d$. Thus, dual band CP selectivity is achieved with interchanged reflection and transmission properties in the two bands, and the two reflected waves are illustrated in Figure 1.

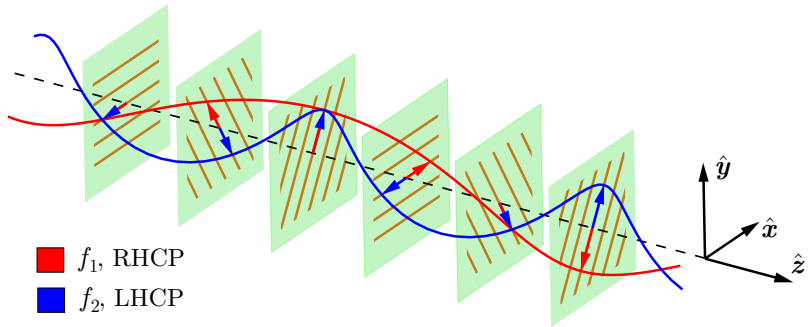

Figure 1: The principle of operation of a dual band CPSS illustrated at a fixed instant in time t, where RHCP waves at frequency f_1 rotate $\theta = -\pi/3$ radians between each layer and LHCP waves at frequency f_2 rotate $\pi + \theta = 2\pi/3$ radians (in the opposite direction).

The selectivity in transmission is not treated by the theory of weak scattering in (2.5)–(2.8), but can be motivated from a power conservation point of view. The co-polarized transmission amplitude is bounded by $|S^{ll}_{mn}|^2 \leq 1-|S^{ll}_{nn}|^2-|S^{kl}_{nn}|^2-|S^{kl}_{mn}|^2$, where $m, n \in \{1, 2\}$ are the receiving and transmitting ports, and $k, l \in \{\text{RHCP}, \text{LHCP}\}$ are the polarization state of the received and transmitted waves. If the co-polarized reflection amplitude $|S^{ll}_{nn}|$ is close to one the co-polarized transmission amplitude $|S^{ll}_{mn}|$ will be small. Conversely, if the co-polarized reflection amplitude is weak the co-polarized transmission amplitude will be strong, provided weak cross-polarization scattering and low losses.

The choice of the rotation angle θ between the CPSS layers will depend on the desired frequency separation of the bands and the optimal number of layers. In Table 1 different feasible values of θ, the corresponding lowest optimal number of layers, and the frequency separation of the two bands are shown. A general pattern that can be observed is that smaller relative rotations result in larger separations between the frequency bands, and vice versa.

For the proposed frequency bands of $17.7 - 20.2\,\text{GHz}$ and $27.5 - 30.0\,\text{GHz}$ a rotation of $\theta = 76.3°$ would be preferable. This is illustrated in Figure 2, where the reflection of a dual band CPSS consisting of five equidistantly placed layers of linear elements, each rotated $\theta = 76.3°$ with respect to the previous layer, has been simulated using the expressions (2.6)–(2.8). The cross polarization is not minimized with this number of layers but it is low. However, this choice of θ cannot be implemented in a full wave simulation model as the unit cell construction using periodic boundary conditions is infeasible if the number of layers is larger than three. For such a periodic structure consisting of connected elements, modeled with periodic boundary conditions, the feasible choices of θ are $\{45°, 60°\}$ [11]. To this end, $\theta = 60°$ is used in this work as the frequency separation of the two bands is more suitable than that of $\theta = 45°$.

Table 1: The number of layers and for what frequencies the dual band CPSS is operating for a certain rotation between layers.

Rotation - degree / (radian)	$N_{\min}$	f_2
18° / (π/10)	10	$9f_1$
20° / (π/9)	9	$8f_1$
22.5° / (π/8)	8	$7f_1$
24° / (2π/15)	15	$6.5f_1$
30° / (π/6)	6	$5f_1$
36° / (π/5)	5	$4f_1$
40° / (2π/9)	9	$3.5f_1$
45° / (π/4)	4	$3f_1$
60°/ (π/3)	3	$2f_1$
72° / (2π/5)	5	$1.5f_1$

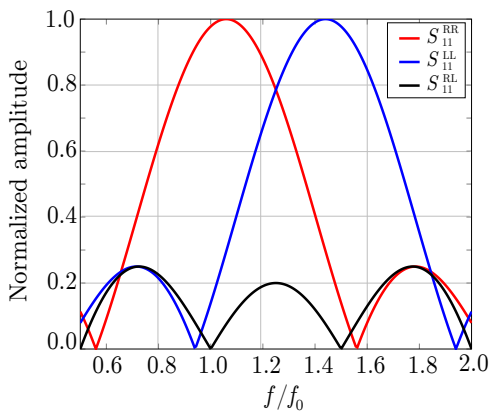

Figure 2: Reflection simulations of a five layer dual band CPSS using the weak scattering approximation. Scattering parameters of normalized magnitude are here presented as a function of normalized frequency.

3 Design and optimization

A multitude of dual band CPSS designs, consisting of different numbers of meander line sheets, were optimized and evaluated in [11]. There it was observed that adding more layers to the structure increases the potential bandwidth of the CPSS, but also increases the design complexity of the structure. It was shown that the wide bandwidth displayed in [5] can be traded for improved dual band performance by relocating the frequency bands of operation closer to each other. The study in [11] provided a starting point for designing and optimizing a dual

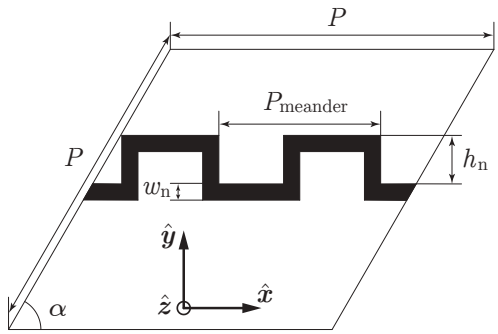

Figure 3: Geometry of a meander line unit cell. The tilt angle of the unit cell α is chosen to be equal to $\theta = 60°$.

band CPSS in this work. As was mentioned in Section 2, the rotation angle $\theta = 60°$ is used and meander lines are utilized as linear elements as they previously have been successfully used to simulate and manufacture a single band wide band CPSS [4, 5]. However, the optimization procedure presented in this section can be used to design dual band CPSS with any kind of elements. Realistic materials were implemented in the simulation model, where copper meander lines were printed on thin substrates, separated by low permittivity spacers and assembled together using thin bonding films. Further details of the materials used are presented in Sections 4–5.

The meander line geometry for a single layer is depicted in Figure 3, where a unit cell is shown and design parameters are introduced to describe the unit cell and the meander line. There are two periods of the meander line in one unit cell to achieve a desired meander line alignment in the infinite structure, see [11] for details. The three dimensional unit cell has the shape of a parallelepiped and the periodicity of the unit cell is shared between all layers. Increasing the number of layers, given $N = aN_{\text{opt}}$ ($a \in \mathbb{N}$), increases control of the polarization purity of reflected and transmitted CP waves. However, in a realistic design increasing the number of layers is problematic as the losses in the materials become more significant and the fabrication of the design becomes more challenging. Moreover, each additional layer of meander lines adds to the dimension of the parameter space, resulting in higher complexity of the optimization problem.

Due to the high number of degrees of freedom in the design, multilayer CPSS are quite complex from an optimization point of view. Thus, symmetry around the center of the structure in the $\hat{\boldsymbol{z}}$-direction is enforced in order to reduce the design complexity. This roughly reduces the dimension of the problem by half. The design parameters used are the width and height of the meander lines, the thickness of each spacer between the layers and the periodicity of the meander lines. For a design with an even number of layers this results in $\frac{3}{2}N+1$ optimization parameters where N is the number of layers, similarly for a design with an odd number of layers the number of optimization parameters are $\frac{3}{2}(N+1)$. In

this work, six layers were chosen for the design based on a compromise between performance and design complexity.

To evaluate the designs during the optimization process a number of performance parameters are introduced. For a CPSS the relevant properties to examine are the losses in transmission and reflection as well as the purity of the circular polarization in both reflection and transmission for the relevant polarization. These parameters are quantified as insertion loss (IL), return loss (RL) and axial ratio (AR). The definition of these parameters, in dB, is

$$\mathrm{IL} = -20\log 10(|S^{ll}_{mn}|), \qquad m \neq n, \tag{3.1}$$

$$\mathrm{RL} = -20\log 10(|S^{ll}_{nn}|), \tag{3.2}$$

$$\mathrm{AR_t} = 20\log 10\left(\left|\frac{|S^{kl}_{mn}| + |S^{ll}_{mn}|}{|S^{kl}_{mn}| - |S^{ll}_{mn}|}\right|\right), \qquad k \neq l, \;\; m \neq n, \tag{3.3}$$

$$\mathrm{AR_r} = 20\log 10\left(\left|\frac{|S^{kl}_{nn}| + |S^{ll}_{nn}|}{|S^{kl}_{nn}| - |S^{ll}_{nn}|}\right|\right), \qquad k \neq l, \tag{3.4}$$

where, as previously introduced in Section 2, $m, n \in \{1, 2\}$ are the receiving and transmitting ports, and $k, l \in \{\mathrm{RHCP}, \mathrm{LHCP}\}$ are the polarization state of the received and transmitted waves.

The targeted goals to be fulfilled in both frequency bands are IL and RL less than 0.5 dB for the relevant polarization, and AR less than 0.78 dB. These performance levels were previously introduced in an analogous project involving a single band CPSS [2]. For a dual band CPSS there are in total eight target goals to fulfill, summarized in Table 2. In this project, the structure was designed to reflect RHCP in the lower frequency band and LHCP in the upper frequency band, which could easily be interchanged by mirroring the structure.

From the specified performance parameters and target values a penalty function F is introduced. Finding a suitable design implies minimizing F, which has the general form

$$F = \sum_{n=1}^{2}\sum_{m=1}^{4} c_{n,m} \int_{\Omega_n} |g_{n,m}|^{k_{n,m}} \cdot \mathrm{H}(g_{n,m})\,\mathrm{d}f, \tag{3.5}$$

with

$$g_{n,m}(f) = h_{n,m}(f) - l_{n,m}, \tag{3.6}$$

where index n is for each band, index m is for the performance parameter, $c_{n,m}$ is the weight of each function, $h_{n,m}$ are the performance functions of interest (see Table 2), $l_{n,m}$ are the thresholds under which the integrand is zero, Ω_n is the integration domain specified by the frequency bands, $k_{n,m}$ are exponent weights and H is the Heaviside (or unit step) function.

The penalty function contains several local minima which is problematic for many optimization routines. To avoid these undesirable minima several opti-

Table 2: Performance parameters for each polarization and frequency band. The subscripts on AR indicate transmission (t) or reflection (r). The requirements to be fulfilled in this work are IL and RL less than 0.5 dB and AR less than 0.78 dB.

	$17.7 - 20.2\,\mathrm{GHz}$	$27.5 - 30.0\,\mathrm{GHz}$
RHCP	RL & $\mathrm{AR_r}$	IL & $\mathrm{AR_t}$
LHCP	IL & $\mathrm{AR_t}$	RL & $\mathrm{AR_r}$

mization algorithms, weight functions and thresholds were used. An initial optimization using a genetic algorithm provided a starting point, and reduced the size of the parameter space, for a Nelder-Mead simplex method algorithm to continue the optimization. If satisfactory results were not obtained, then the genetic solver was run again with changed settings and/or updated penalty functions before moving on with the Nelder-Mead simplex algorithm. Likewise, if the results after this second optimization step were non-satisfactory the penalty function and parameters were tweaked and the Nelder Mead simplex algorithm was run again. The final algorithm used was a trust region method for when the minimum was in close proximity. The described procedure can be summarized by the flowchart illustrated in Figure 4. The utilized algorithms are all available in Computer Simulation Technology Microwaves Studio (CST MWS) as built-in optimization routines. Greater flexibility can be achieved in the optimization process if the simulation software is controlled externally by MATLAB. In this case a great number of optimization algorithms can be utilized.

A six layer CPSS design was optimized for normal incidence in CST MWS using a 32 GB RAM, Intel i7-2600 3.4 GHz CPU desktop computer, using the technique in Figure 4. A coarse simulation mesh of ten steps per wavelength was initially used in the genetic algorithm optimization in order to reduce the computation time of each iteration. Typically a few thousand iterations were carried out in this part of the procedure. The mesh settings were later gradually improved during the optimization cycles when the simplex algorithm and the trust region algorithm were employed, where roughly a few hundred iterations were carried out. A mesh convergence study was executed when a final design candidate fulfilling all requirements had been achieved. This study showed that the mesh settings used in the optimization routine were satisfactory, and that almost no noticeable improvement in accuracy was achieved if a mesh finer than 16 steps per wavelength was used.

4 Simulated results

The optmized six layer CPSS, with 60° relative rotations between subsequent layers, consists of thin Arlon DiClad 880 teflon sheets with printed copper meander lines separated by low permittivity, low loss Rohacell HF31 spacers. The components of the structure were bonded together using thin bonding layers. The electrical properties and thickness of the bonding layers were estimated using the

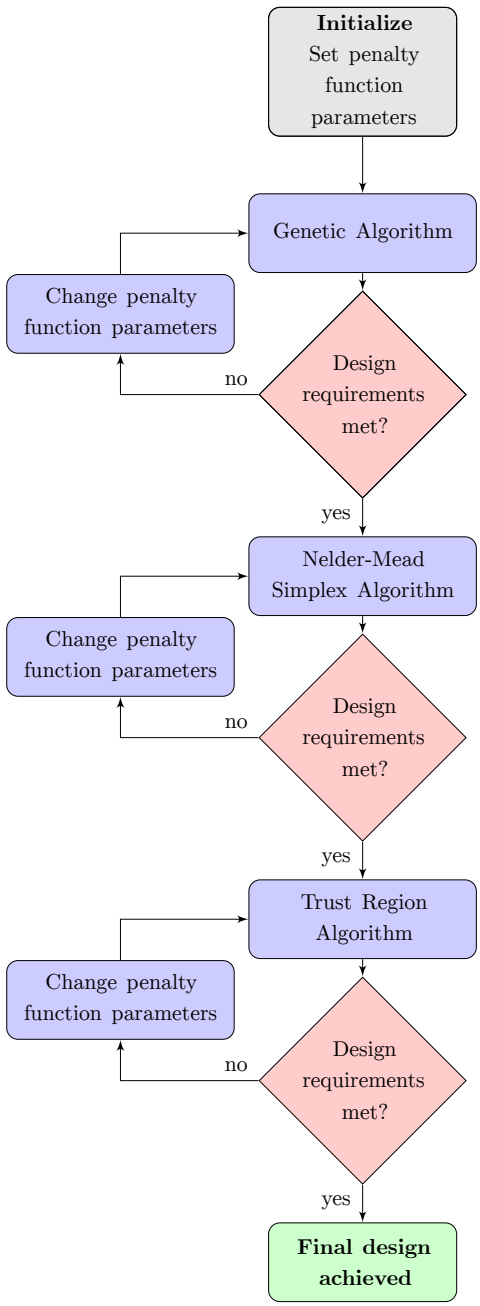

Figure 4: Flowchart for optimizing a dual band CPSS using built-in optimization algorithms in CST MWS.

Table 3: Material parameters of the meander line CPSS

Material	Rel. permittivity	Loss tangent	Thickness
Rohacell H31 spacers	1.043	0.002	d_1, d_2 and d_3
Arlon DiClad 880 substrates	2.17	0.003	0.127 mm
Copper, wires	$\sigma = 58$ MS/m		18 μm
3M Scotch-Weld bonding layers	2.32	0.001	0.05 mm

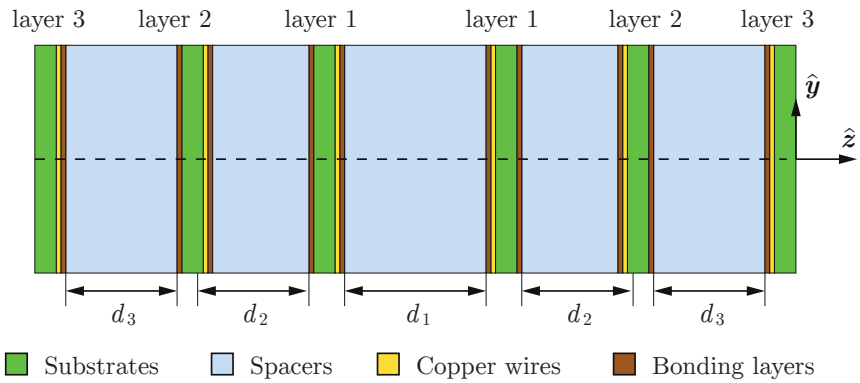

Figure 5: Side view of the dual band meander line CPSS consisting of six layers of substrates and five low permittivity spacers.

same procedure as in [5], where a similar CPSS was designed and fabricated. The material properties and the thickness of each layer of the dual band CPSS are presented in Table 3, and a side view of the CPSS can be seen in Figure 5.

The total thickness of the simulated design is 17.22 mm, which corresponds to 1.08 wavelengths at the center frequency of the lower band of operation $f = 18.95$ GHz. The meander lines of one unit cell as implemented in CST MWS can be seen in Figure 6, and the values of the meander line thickness w_i and the meandering height h_i of each layer are given in Table 4. The side length of the unit cell P and the thickness of the spacers are also presented in Table 4. Only three different meander line layers and spacer thicknesses are present in the design due to the enforced symmetry introduced in Section 3.

Simulation results are presented in Figure 7 where 16 steps per wavelength mesh setting was used, and the IL, RL and AR for transmission and reflection are presented for both bands of operation. Red curves correspond to RHCP and blue curves to LHCP and it can be seen that the eight requirements specified in Table 2 are all fulfilled. When comparing the results in Figure 7 to the wideband meander line CPSS in [5] a substantial reduction in bandwidth can be observed in the dual

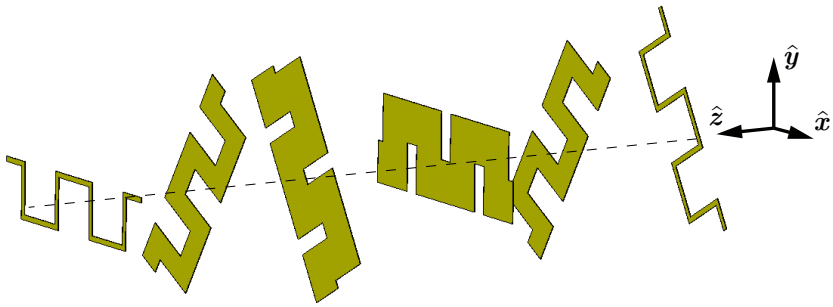

Figure 6: Meander lines of the six layers in the dual band CPSS design implemented in CST MWS. When a unit cell is defined, components extending outside of the unit cell are automatically pasted into the opposite side of the unit cell by the software.

Table 4: Design parameters of the dual band meander line CPSS.

Parameter	P	d_1	d_2	d_3	h_1
Value (mm)	5.49	3.80	2.90	3.24	1.14
Parameter	h_2	h_3	w_1	w_2	w_3
Value (mm)	1.21	1.25	0.99	0.61	0.12

band design. This is in part caused by the targeted dual band functionality as well as the relatively small frequency separation between the bands of operation.

5 Prototype manufacturing and error estimates

A prototype of the optimized six layer dual band CPSS was manufactured and can be seen in Figure 8. The dimensions of the prototype are 310 mm × 310 mm and the total thickness is 17.11 mm, which should be compared to the thickness of the optimized simulated design of 17.22 mm. As was mentioned in Section 4, copper meander lines were printed on thin Arlon DiClad 880 substrates. The Rohacell HF31 spacers of custom thickness were manufactured by Evonik. The thickness of each spacer was measured individually, using a micrometer screw gauge, before assembling the prototype and it was concluded that the deviation between simulated and fabricated values was smaller than 0.1 mm. For the bonding layers a 3M Scotch-Weld 76 adhesive spray was used. Unfortunately,

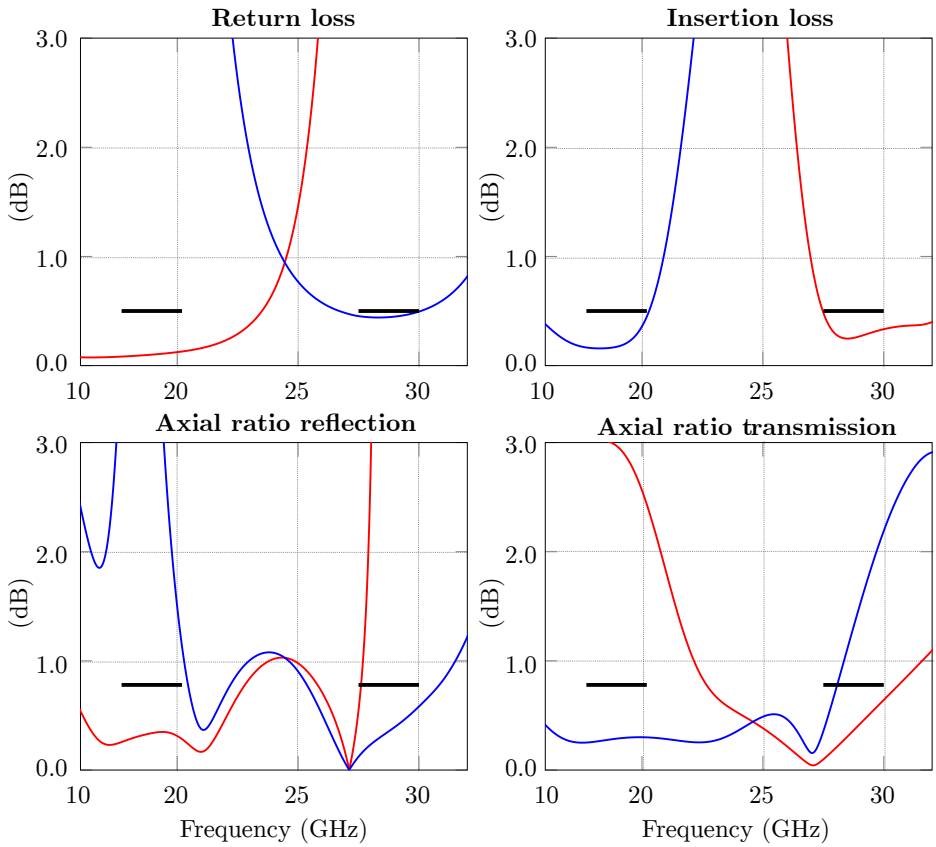

Figure 7: Simulated results of the meander line dual band CPSS, where red curves correspond to RHCP and blue curves to LHCP. The upper left plot shows the RL in both frequency bands and the lower left plot the corresponding AR. The upper right plot shows the IL in both frequency bands and the lower right plot the corresponding AR.

the actual thickness of the bonding layers proved difficult to estimate due to the Rohacell HF31 being porous and the adhesive penetrating the spacers in the process of assembly of the prototype.

In order to investigate the impact of the bonding layer thickness on the performance of the CPSS, a parametric study was carried out where the thickness of the bonding layers was varied, while the total thickness of the CPSS was kept fixed by compensating the thickness of the spacers by the same length. Simulated results are presented in Figure 9, where the solid, dashed, and dash-dotted curves correspond to the bonding layer thicknesses 0.05 mm, 0.12 mm and 0.19 mm, respectively. It can be seen that increasing the thickness of the bonding layers by a

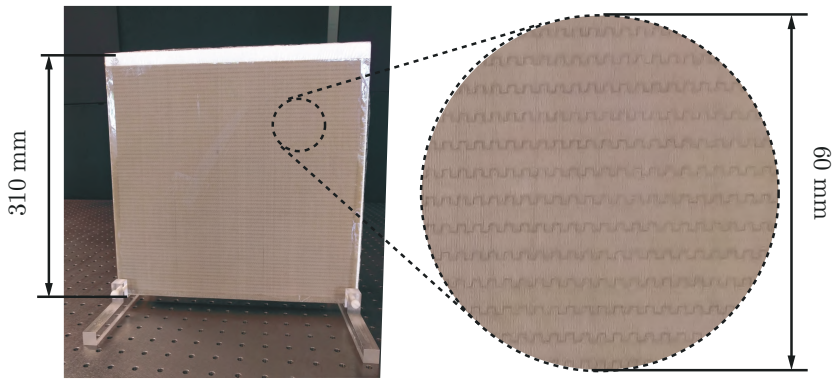

Figure 8: Manufactured dual band CPSS prototype.

factor of two implies a negative frequency shift of about 0.7 GHz in RL and IL, as well as a detuning of the corresponding AR. Another source of error associated with the assembly of the prototype is the impact of a relative displacement in the xy-plane between subsequent layers in relation to the alignment in Figure 6. This effect was investigated by simulating the properties of the CPSS where translations in the horizontal and vertical directions were introduced using random shift variables, and where the maximum shift of each layer corresponded to a complete displacement in relation to the next layer. A total of 200 such simulations were carried out and the maximum deviation of the scattering parameters for each frequency are presented as colored bands in Figure 10. Here it can be seen that the impact of displacements of the layers in transverse directions is negligible in RL and IL, and on the order of 0.05 dB in AR. Similar results were presented in [22], where relative translations of subsequent layers of a multilayer CPSS in the optical regime were investigated.

6 Experimental setup and results

Experimental characterization of the transmission and reflection properties of the dual band CPSS prototype were carried out at Lund University. The frequency range $13 - 34$ GHz was measured using two separate pairs of single-polarized, standard gain horn antennas. Two SATIMO SGH 1850 antennas were used to cover the lower frequency band, and two SATIMO SGH 2650 antennas were used for the upper frequency band. These antennas have a boresight cross-polarization discrimination better than 40 dB in their respective frequency range of interest. The experimental setup was assembled on a Newport RS2000 optical table, and the receiving and transmitting antennas were mounted on THORLABS PRMTZ8 motorized precision rotation stages. Two of such stages were used to control the yaw and the roll of each antenna, which in turn were connected to

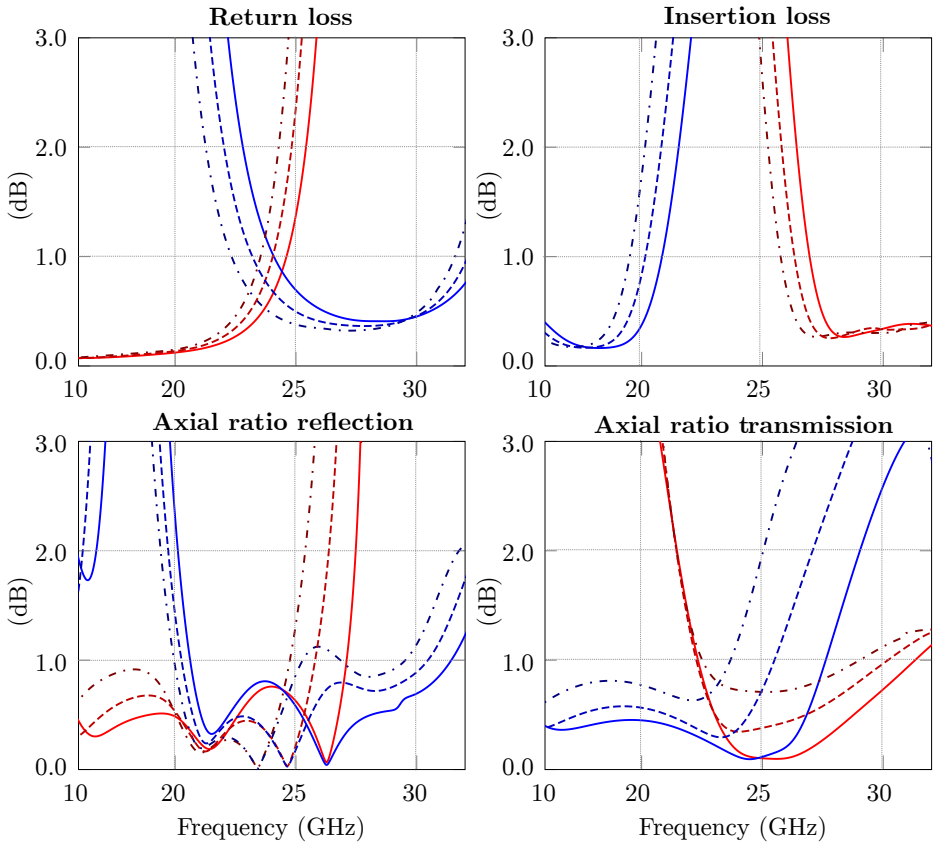

Figure 9: Parametric study of the thickness of the bonding layers in the meander line dual band CPSS. The upper left plot shows the RL in both frequency bands and the left plot the corresponding AR. The upper right plot shows the IL in both frequency bands and the lower right plot the corresponding AR. The solid, dashed, and dash-dotted curves correspond to the bonding layer thicknesses 0.05 mm, 0.12 mm and 0.19 mm, respectively.

an Agilent E8364b vector network analyzer (VNA). The VNA and the rotational stages were controlled through MATLAB scripts using USB and GPIB to USB connections [9, 19]. The CPSS prototype was placed in a custom made sample holder of adjustable height made entirely of plastic and polymethyl methacrylate (PMMA). An overview of the experimental setup is presented in Figure 11.

The high degree of control in alignment of the setup provided by the optical table, the antenna fixtures and the rotational stages implied that the setup could easily be modified to measure at different distances between the sample and the antennas. An initial coarse alignment of all components of the setup was carried

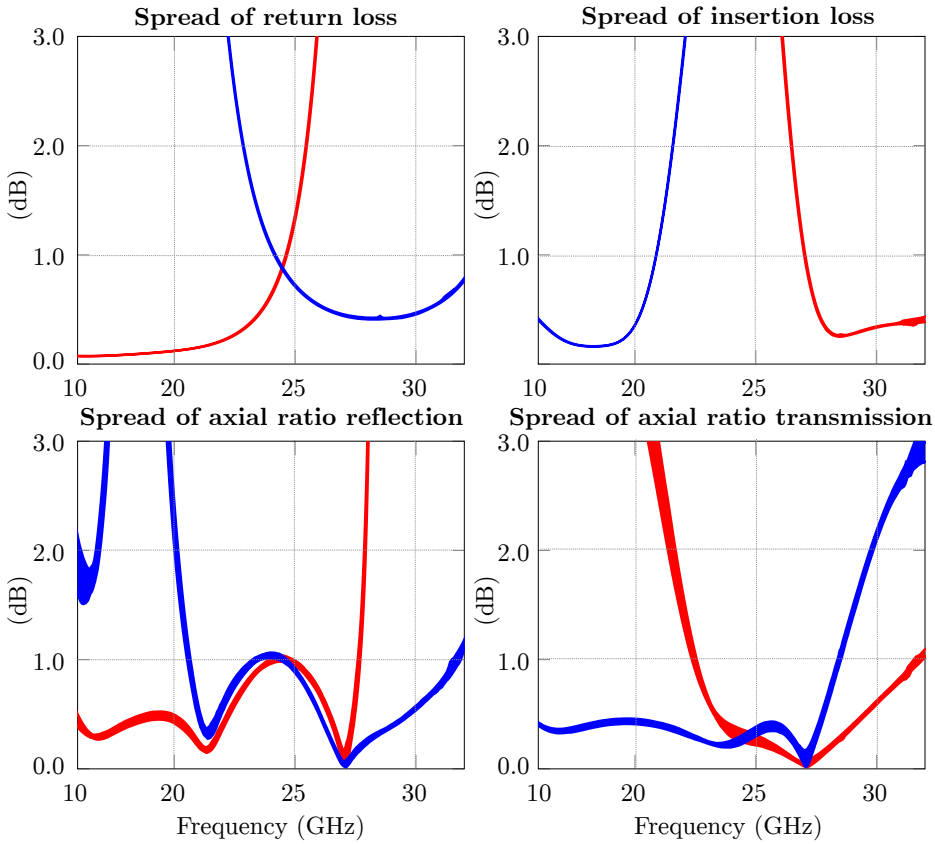

Figure 10: Simulations of relative translations of the layers of the CPSS. The maximum deviations of 200 simulations are shown.

out using cross line lasers. After that, the alignment of the rotational stages were fine-tuned using feedback from the VNA. For the transmission measurements, a golden section search was utilized to maximize power throughput of the setup, given a fixed separation between the antennas, without the prototype present. In a similar way, alignment of the setup for reflection measurements used a golden section search maximizing reflection with the reference being an aluminum foil sheet water glued to the prototype [4]. This method achieved an accuracy in antenna rotation and jaw alignment on the order of 0.1°.

When the setup had been properly aligned, the scattering matrix components of interest in linear polarization were acquired and processed using the post processing method described in detail in [4], resulting in equivalent circular polarization scattering parameters of the device under test. When characterizing the transmission properties of the CPSS, the antennas were placed on each side

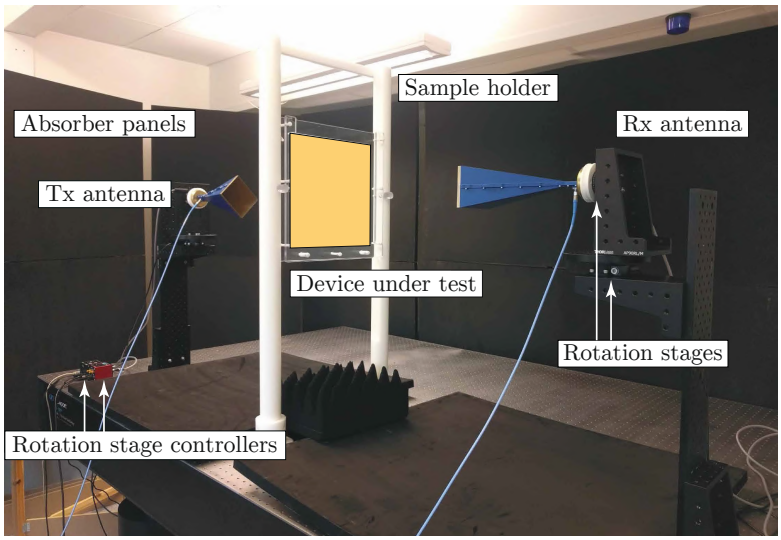

Figure 11: Experimental setup for dual/wide band characterization of a CPSS at frequencies 13-34 GHz.

of the prototype as in Figure 11. The scattering matrix components of the device under test were normalized with a corresponding reference measurement, consisting of measurements of the empty setup. In reflection, both antennas were placed on one side of the device under test at an oblique angle of about 3°. This small incidence angle variation was simulated and it was concluded that the variations in the scattering parameters of the meander line CPSS were hardly noticeable. For the reference measurements in reflection, a thin aluminum foil was attached to the device under test using a small amount of water as an adhesive.

The characterized deviations between the optimized and fabricated designs due to manufacturing errors and uncertainties, discussed in Section 5, were used to generate an updated simulation model corresponding to the realized prototype. In this design, the thickness of the spacers is $d_1 = 3.78\,\text{mm}$, $d_2 = 2.87\,\text{mm}$, $d_3 = 3.17\,\text{mm}$, and the updated bond layer thickness was set to $0.12\,\text{mm}$. A comparison between the updated simulation results and the experimental results are presented in Figure 12, were the dashed curves correspond to measurements and solid curves represent simulated results. It can be seen in the experimental data that two separate pairs of antennas were used to cover the full frequency range. The experimental AR curves are only plotted in the relevant regions of interest for each component, in order to make the figures more readable. Good agreement can be observed in general between the simulated and measured results. However, it can be noticed that the IL of the higher frequency band is about 0.2–0.3 dB larger than the simulated results. This is most likely caused by the fact that the material parameters used in the simulations are typically de-

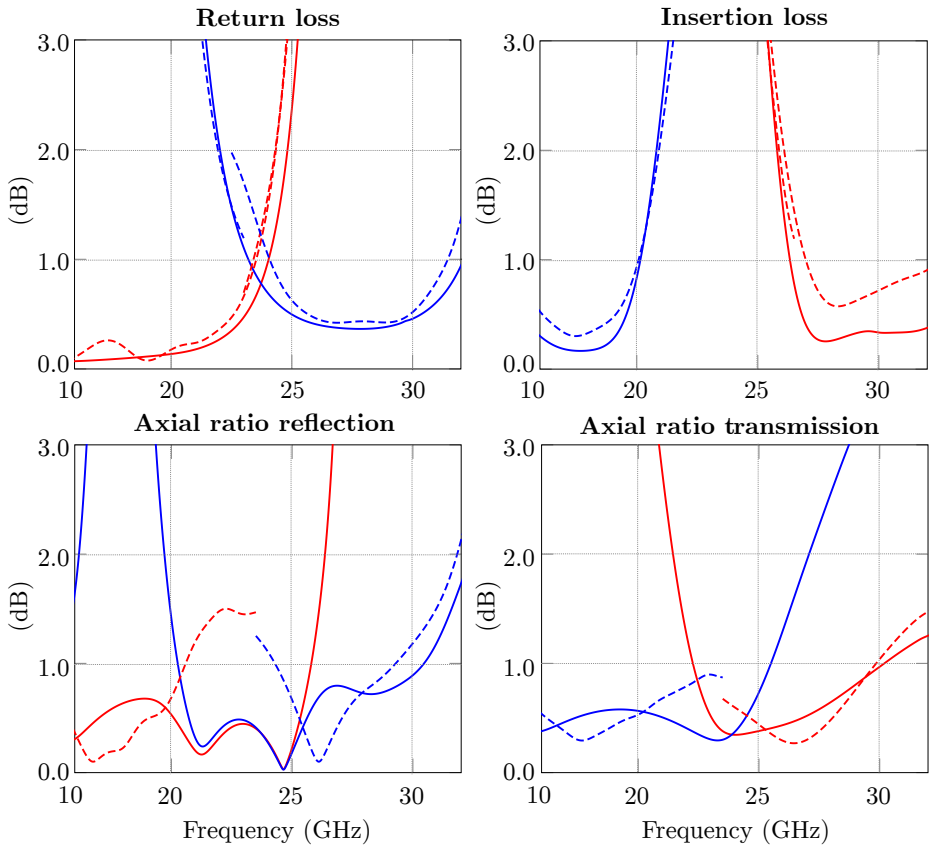

Figure 12: Experimental and simulated results of the meander line dual band CPSS. The upper left plot shows the RL in both frequency bands and the left plot the corresponding AR. The upper right plot shows the IL in both frequency bands and the lower right plot the corresponding AR. Experimental results are represented as dashed curves and simulated results as solid curves.

fined for frequencies less than 10 GHz. Both the Rohacell HF31 spacers and the adhesive layers most likely display increasing losses when higher frequencies are considered. When comparing the results in Figures 7 and 12 it is observed that the measured curves are shifted down in frequency of about 1.0 GHz in relation to the optimized simulation model. This is most likely caused by the additional thickness of the bonding layers, penetrating the Rohacell HF31 spacers.

7 Conclusions

A dual band circular polarization selective structure for K- and K_a-band applications has been presented. The structure consists of six cascaded layers of meander lines, separated by low permittivity spacers. Simulations of the design fulfill the strict design requirements of return loss and insertion loss better than 0.5 dB, and axial ratio better than 0.78 dB over the frequency bands 17.7–20.2 GHz and 27.5-30.0 GHz, with alternating circular polarizations in the two bands. A prototype was fabricated and characterized experimentally and good agreement has been observed between simulated and measured results. This type of cascaded circular polarization selective structures has been shown to possess great potential to achieve both wideband and multi-band filtering properties, and constitutes an interesting design concept for future ideas.

Acknowledgments

The authors of this paper kindly acknowledge Ron van Hoorn and Oliver Krause at Evonik for providing Rohacell HF31 samples for the manufacturing of the test panel, and the Royal Physiographic Society of Lund for funding the experimental setup used in this work.

References

[1] S. M. A. M. H. Abadi and N. Behdad. A broadband, circular-polarization selective surface. *Journal of Applied Physics*, **119**(24), pp. 244901, 2016.

[2] M. Albani, P. Balling, L. Datashvili, G. Gerini, P. Ingvarson, K. Pontoppidan, M. Sabbadini, D. Sjöberg, S. Skokic, and G. Vecchi. Concepts for polarising sheets & "dual-gridded" reflectors for circular polarisation. In *ICECom Proceedings*, pp. 1–4, 2010.

[3] C. Cappellin, D. Sjöberg, A. Ericsson, P. Balling, G. Gerini, N. J. G. Fonseca, and P. D. Maagt. Design and analysis of a reflector antenna system based on doubly curved circular polarization selective surfaces. In *2016 10th European Conference on Antennas and Propagation (EuCAP)*, pp. 1–5, 2016.

[4] A. Ericsson, J. Lundgren, and D. Sjöberg. Experimental characterization of circular polarization selective structures using linearly single-polarized antennas. *IEEE Trans. Antennas Propag.*, **65**(8), pp. 4239–4249, 2017.

[5] A. Ericsson and D. Sjöberg. Design and analysis of a multilayer meander line circular polarization selective structure. *IEEE Trans. Antennas Propag.*, **65**(8), pp. 4089–4101, 2017.

[6] IEEE standard test procedures for antennas, 2008. IEEE Std 149-1979 (R2008).

[7] W. A. Imbriale, S. S. Gao, and L. Boccia, editors. *Space Antenna Handbook*. Wiley, 2012.

[8] M. Joyal and J. Laurin. Design and analysis of a cascade circular-polarization-selective surface at K band. *IEEE Trans. Antennas Propag.*, **62**(6), pp. 3043–3052, 2014.

[9] Keysight Instruments and MATLAB, 2017. Available at: https://se.mathworks.com/products/instrument/supported/keysight.html, accessed 2017-09-22.

[10] G. Kristensson. *Scattering of Electromagnetic Waves by Obstacles*. SciTech Publishing, an imprint of the IET, Edison, NJ, 2016.

[11] J. Lundgren. Dual band circular polarization selective structures for space applications. Master's thesis, Lund University, Department of Electrical and Information Technology, P.O. Box 118, SE-221 00 Lund, Sweden, 2016. Rep. No. LU/LTH-EIT 2016-540.

[12] G. A. Morin. A simple circular polarization selective surface (CPSS). In *Antennas and Propagation Society International Symposium, 1990. AP-S. Merging Technologies for the 90's. Digest.*, pp. 100–103. IEEE, 1990.

[13] R. Pierrot. Reflector for circularly polarized waves, 1970. US Patent 3,500,420.

[14] S. Rao, L. Shafai, and S. K. Sharma. *Handbook of Reflector Antennas and Feed Systems Volume III: Applications of Reflectors*. Artech house, 2013.

[15] D. Sjöberg and A. Ericsson. A multi layer meander line circular polarization selective structure (MLML-CPSS). In *Proceedings of the 8th European Conference on Antennas and Propagation (EuCAP)*, pp. 464–468. IEEE, 2014.

[16] W. Tang, G. Goussetis, N. J. G. Fonseca, H. Legay, E. Sáenz, and P. de Maagt. Coupled split-ring resonator circular polarization selective surface. *IEEE Trans. Antennas Propag.*, **65**(9), pp. 4664–4675, 2017.

[17] W. Tang, S. Mercader-Pellicer, G. Goussetis, H. Legay, and N. J. G. Fonseca. Low-profile compact dual-band unit cell for polarizing surfaces operating in orthogonal polarizations. *IEEE Trans. Antennas Propag.*, **65**(3), pp. 1472–1477, 2017.

[18] I.-Y. Tarn and S.-J. Chung. A new advance in circular polarization selective surface – A three layer CPSS without vertical conductive segments. *IEEE Trans. Antennas Propag.*, **55**(2), pp. 460–467, 2007.

[19] Thorlabs PRMTZ8 motorized precision rotation stage, 2017. Available at: https://www.thorlabs.com/newgrouppage9.cfm?objectgroup_id=4134, accessed 2017-09-22.

[20] W. V. Tilston, T. Tralman, and S. M. Khanna. A polarization selective surface for circular polarization. In *Antennas and Propagation Society International Symposium, 1988. AP-S. Digest*, pp. 762–765. IEEE, 1988.

[21] J. Wang, Z. Shen, and W. Wu. Broadband and high-efficiency circular polarizer based on planar-helix chiral metamaterials. *Applied Physics Letters*, **111**(11), pp. 113503, 2017.

[22] Y. Zhao, M. Belkin, and A. Alù. Twisted optical metamaterials for planarized ultrathin broadband circular polarizers. *Nature Communications*, **3**, pp. 870, 2012.

A Combined Electromagnetic and Acoustic Analysis of a Triaxial Carbon Fiber Weave for Reflector Antenna Applications

Andreas Ericsson, Romain Rumpler, Daniel Sjöberg,
Peter Göransson, Niklas Wellander and Joakim Johansson

Paper VI

Published as: A. Ericsson, R. Rumpler, D. Sjöberg, P. Göransson, N. Wellander and J. Johansson, "A combined electromagnetic and acoustic analysis of a triaxial carbon fiber weave for reflector antenna applications," *Aerospace Science and Technology*, Vol. 58, pp. 401–417, 2016.

Abstract

Fiber composites are widely used for space applications such as antennas, solar panels and spacecraft support structures. This paper presents a combined electromagnetic and acoustic analysis of a triaxial carbon fiber weave structure, designed for ultra lightweight reflector antennas in satellite communication systems. The electromagnetic and acoustic performance of the structure are analyzed over a wide range of parametric studies, both at a microscopic and mesoscopic length scale. The electromagnetic study indicates that the main parameter governing the electromagnetic reflection performance of the weave is the electric conductivity of the carbon fibers, given that the weave structure is significantly smaller than the wavelength of the incident signals. The acoustic study identifies a critical threshold in the mesoscale geometry in order to avoid a critically high resistive behavior of the weave structure, driven by viscous effects. Design guidelines are drawn from these analyses in order to achieve a trade-off between the electromagnetic reflection properties and the resistance to acoustic loading of such composite materials. These combined analyses allow to deepen the understanding from both an electromagnetic and acoustic perspective in order to open for some new design possibilities.

1 Introduction

For many years, reflector antennas have been widely used in satellite communication applications. The conditions in space are very harsh with significant temperature effects and thermal cycling, radiation and vacuum, at the same time satellite reparations are very hard to perform. This implies that designing a space antenna is a very delicate matter where aspects such as the weight and size of the antenna are very important to take into consideration [8, Ch. 4]. The current satellite communication situation consists of high demands of increasing communication data rates between satellites and ground stations. To this end, large aperture reflector antennas are mounted on the satellites, typically with a diameter of a few meters up to 30 meters [8, 22]. To reduce the satellite payload, components such as reflectors, solar panels and satellite support structures are made of carbon fiber composites [16], where the reflectors commonly consist of multi-layer carbon fiber laminates. However, a reflector with a large aperture to mass ratio may suffer from high acoustic loads at take-off due to a wide range of airborne acoustics and structure-borne vibration interactions, potentially causing fractures. One way to overcome this problem is to utilize ultra light weight reflectors [3, 19, 20, 22], which typically consist of a porous carbon fiber weave structure kept in place by a stabilizing rim. This type of "mesh reflector surface" is also commonly used in large aperture unfurlable reflectors [10, 23], with a diameter up to 30 meters, that are unfolded and deployed when the satellite is in position in space.

The high porosity of this type of reflectors implies a slight degradation of the electromagnetic reflection performance, but also provides a significant im-

provement of the payload and reduced acoustic loads of the structure at take-off compared to traditional reflectors. This property of triaxial carbon fiber weaves has been utilized in other applications such as face sheets in acoustic absorbing panels for aircraft engines [27]. The mechanical and thermodynamic properties of triaxial woven fabrics have previously been studied extensively [7,10,17]. However, to the knowledge of the authors, there are few previously published works where the acoustic and electromagnetic properties of this type of structures are analyzed in parallel, resulting in common design guidelines for triaxial weaves in satellite communication applications.

The outline of this paper is as follows: in Section 2 the general properties of the studied structure, the triaxial composite weave, are described. In Section 3 the electromagnetic reflection properties of the weave structure are investigated. In the low frequency limit the electromagnetic properties of the structure can be modeled using homogenization methods, while at the main frequencies of interest for satellite communication applications (the K_u and K bands at 10 GHz−30 GHz), the electromagnetic response of the structure is analyzed using full wave finite element method (FEM) simulation models. In Section 4 the acoustic properties of the weave structure are studied. A numerical model is established in order to study the impact of the mesoscale geometry, *i.e.* of a geometrical unit cell, on the fluid-structure coupling. Although fluid-structure interactions due to macro-scale properties play an important role, the study of flow resistance of the triaxial composite weave provides a major starting point linking the design parameters (unit cell geometry), the acoustic loading, and the acoustic excitation level. A parametric study of this flow resistance is thus presented, leading to a non-linear law accounting for medium to high sound pressure levels. In Section 5 design guidelines are presented based on the multiphysics considerations and the necessary tradeoff between the electromagnetic and acoustic performance of the structure. Finally, in Section 6 some concluding remarks are presented.

2 Triaxial weave structure

A porous weave reflector can be analyzed at different length scales, see Figure 1. The microscopic fine structure of the weave consists of carbon fiber bundles (commonly referred to as fiber tows) in a background resin material, typically epoxy. Each fiber bundle is coated by an insulating resin coating such that the weave fiber tows are not in electric contact with each other. This further means that the weave fiber tows are only conductive along the fiber direction. The triaxial weave reflector surface used as a reference design in this study is manufactured by Tencate advanced composites [30]. The carbon fiber fabric consists of a pitch based high modulus fiber material made by Sakase Adtech in Japan, with the product reference YSH-70A 1K, and with a weight of $85\,\mathrm{g/m^2}$ and a density of $0.59\,\mathrm{g/cm^3}$ [24], see Figure 2. The period of the weave pattern is approximately 3.5 mm and the side length of the perforations is about 1.2 mm, which corresponds to a perforation rate of 44 %. The insulating resin is a cyanate

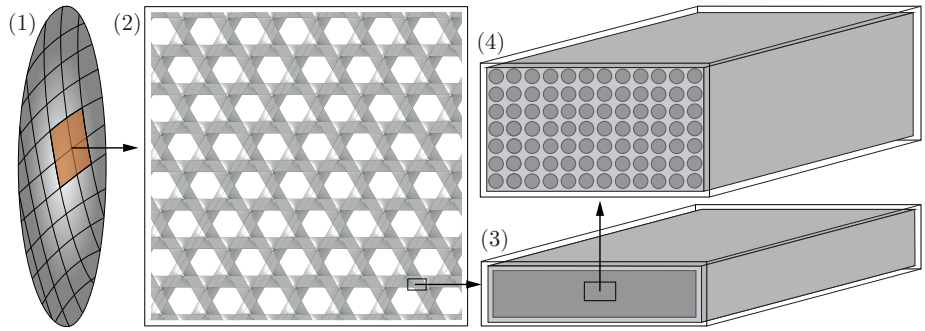

Figure 1: Different length scales of an ultra lightweight weave reflector. The reflector surface (1) consist of a composite triaxial weave (2), where each of the weave fiber tows consist of a conducting core and an insulating coating (3). The conductive core is composed by many conductive microscopic fibers held in place by an insulating resin background material (4).

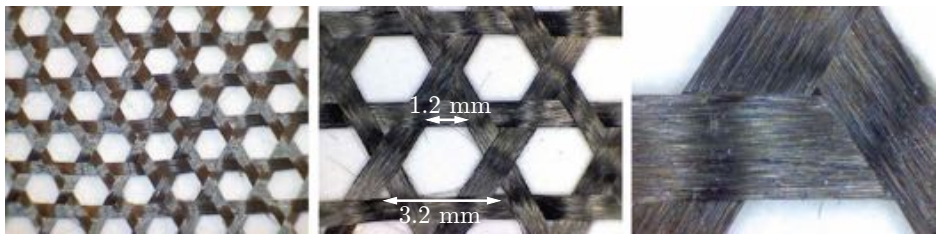

Figure 2: The weave fabric under study, manufactured by Sakase Adtech [24], presented on three length scales.

ester RS-3C with low electromagnetic loss tangent [31], and the resin content of the reflector surface is approximately 28 %. The manufacturing procedure of the triaxial weave fabric is based on braiding of multiple carbon fiber tows in three principal directions [28], and the manufacturing of the porous reflector surface from a braided weave is described in detail in [10].

The weave structure and its external loads are periodic and can thus be modeled by a unit cell geometry with periodic boundaries in the plane of the structure. In this paper two simulation models have been implemented to analyze the electromagnetic and acoustic properties of the weave: a detailed anisotropic weave model, taking into account the structure of the weave fiber tows, as in Figure 3, and a simplified homogeneous slab model, as can be seen in Figure 4. The size of the smallest possible unit cell that can be used to model the weave depends on the weave geometry and the nature of the considered problem. For example, when modeling the electromagnetic response of the structure, the vector-valued nature of the problem implies extra constraints to the unit cell modeling, compared to the analysis of scalar-valued acoustic interactions.

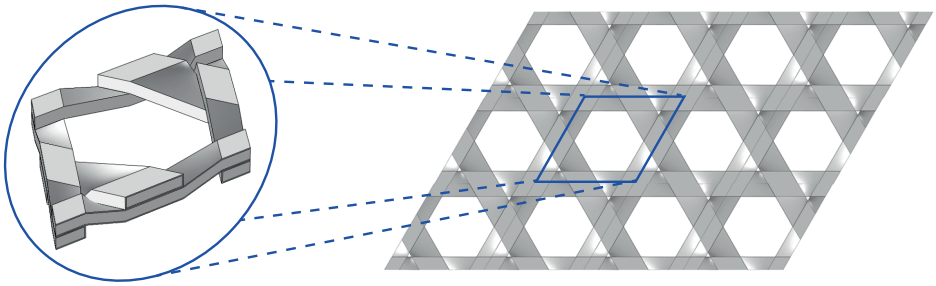

Figure 3: Fine structure model of the triaxial carbon fiber weave, where each fiber consists of a conductive core and an insulating coating.

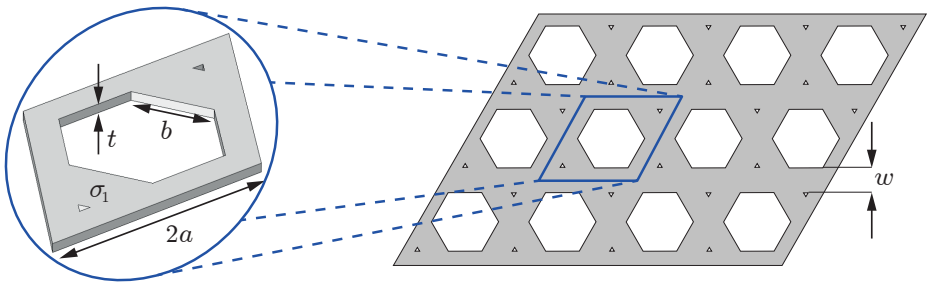

Figure 4: Simplified homogeneous slab model of the triaxial carbon fiber weave.

The width of the fiber tows is related to the unit cell parameters a and b in Figure 4 as $w = \sqrt{3}(a-b)$, which implies that by either varying the ratio b/a, or keeping b/a fixed and varying both b and a simultaneously, the width of the fiber tows and the shape of the unit cell geometry may be studied. The expression b/a is constrained by the relation

$$2/3 < b/a < 1 \tag{2.1}$$

due to manufacturing constraints, such that $b = 2a/3$ corresponds to tightly woven fabrics with the largest possible fiber tow width with respect to a given unit cell size, and $b = a$ corresponds to the limit case where $w = 0$. This implies that, for a given unit cell size, the width of the fiber tows is bounded by the expression

$$0 < w < a/\sqrt{3}. \tag{2.2}$$

In addition to the width of the fiber tows, the perforation rate ϕ (sometimes also referred to as porosity, *i.e.* the void fraction of the permeable structure) is also directly linked to the parameters a and b through the relation

$$\phi = \frac{3b}{a}\left(\frac{b}{a} - 1\right) + 1, \tag{2.3}$$

where the minimum value of b/a in (2.1) corresponds to a perforation rate of 33 %.

3 Electromagnetic analysis

The electromagnetic properties of the weave were modeled using the commercial simulation softwares Comsol Multiphysics and Computer Simulation Technology Microwave Studio (CST MWS). The main goal of the electromagnetic study was to analyze how the reflection performance of the weave structure depends on the weave design parameters, such as the width, thickness and conductivity of the weave fiber tows, as well as the size of the weave unit cell. A general observation from previous studies [19, 20] is that the performance of a porous carbon fiber reflector surface deteriorates at high frequencies, which indicates that a low frequency analysis can give information regarding the optimum reflection performance to be expected of the structure.

3.1 Low frequency limit analysis

In the low frequency limit, the fine structure of the porous weave becomes very small with respect to the wavelength of the incident signal. The weave can then be modeled as a homogeneous slab with effective material parameters that are extracted by using homogenization methods described in detail for bulk materials in [15], and for conductive sheets in [26].

To quantify the low frequency limit, we need to consider three different scales, corresponding to the time scales discussed in [34, p. 707]. First, the thickness t of the sheet should be much less than the free space wavelength $\lambda = c_0/f$, where f is the frequency and $c_0 = 1/\sqrt{\epsilon_0\mu_0}$ is the speed of light in vacuum, with ϵ_0 and μ_0 being the permittivity and permeability of vacuum, respectively. This requirement is usually stated as $kt \ll 1$, where $k = 2\pi f/c_0$ is the free space wave number. Second, the conductive properties of the sheet should dominate over the capacitive properties, so that $\sigma \gg 2\pi f\epsilon$, where σ and ϵ are the conductivity and the permittivity of the sheet, respectively. Third, the thickness should be much smaller than the skin depth $\delta = 1/\sqrt{\pi f\sigma\mu}$, where μ is the magnetic permeability of the sheet. Introducing the refractive index $n = \sqrt{\epsilon\mu/(\epsilon_0\mu_0)}$ and wave impedance $\eta = \sqrt{\mu/\epsilon}$, we can then formulate all the requirements in terms of the thickness of the structure in relation to the wavelength (kt) as

$kt \ll 1$,	weave thickness smaller than the center wavelength.
$nkt \ll \eta\sigma t$,	conductive properties dominate over capacitive.
$nkt \ll 2/(\eta\sigma t)$,	weave thickness smaller than the weave skin depth.

For our particular weave, we assume that: the fiber tow conductivity and relative permittivity are of the order of $\sigma = 10^4\,\mathrm{S/m}$, $\epsilon = 2\epsilon_0$, the weave is nonmagnetic

($\mu = \mu_0$), and it has a thickness of $t \approx 80\,\mu$m. This implies $\eta\sigma t = 210$, which demonstrates that the third requirement is the most conservative. It requires $kt \ll 2/(n\eta\sigma t) = 3.3 \cdot 10^{-3}$, or $f \ll 2.0\,$GHz. Thus, the low frequency limit is not strictly applicable to frequencies in the range $10 - 30\,$GHz. However, it still provides valuable physical insight into the conductive processes in the weave, which makes it a relevant model to consider in more detail.

When the conductive properties dominate over the capacitive ones, the constitutive relation for the material is

$$\boldsymbol{J} = \boldsymbol{\sigma} \cdot \boldsymbol{E}, \tag{3.1}$$

where $\boldsymbol{J}$ is the current density, $\boldsymbol{\sigma}$ is the (possibly anisotropic) conductivity, and $\boldsymbol{E}$ is the electric field intensity. In the low frequency limit, the electric field is irrotational ($\nabla \times \boldsymbol{E}(\boldsymbol{r}) = \boldsymbol{0}$) and can be written as $\boldsymbol{E}(\boldsymbol{r}) = \boldsymbol{E}_0 - \nabla V(\boldsymbol{r})$, where $\boldsymbol{E}_0$ corresponds to an applied constant field, and the potential V is the response from the material structure. The non-divergent nature of the low-frequency current, $\nabla \cdot \boldsymbol{J} = 0$, then implies

$$\nabla \cdot [\boldsymbol{\sigma}(\boldsymbol{r}) \cdot (\boldsymbol{E}_0 - \nabla V(\boldsymbol{r}))] = 0 \tag{3.2}$$

with periodic boundary conditions in the plane of the sheet, and isolating boundary conditions in the normal direction, $\hat{\boldsymbol{n}} \cdot \boldsymbol{J} = 0$. In Figure 5 the induced potential V is plotted when a constant external electric field $\boldsymbol{E}_0 = E_0\hat{\boldsymbol{y}}$ is applied to the structure in Comsol Multiphysics. In order for the model not to be underdetermined by a constant potential, a reference potential $V = 0$ is defined in one point of the unit cell. Once the electric field intensity $\boldsymbol{E}$ and the electric current density $\boldsymbol{J}$ are known, the effective conductance of the weave can be determined through the relation

$$\boldsymbol{i} = \mathbf{G}_{\text{eff}} \cdot \boldsymbol{E}_0, \tag{3.3}$$

where $\boldsymbol{i}$ is the net current in the structure defined as

$$\boldsymbol{i} = \frac{1}{A} \iiint_U \boldsymbol{J}(\boldsymbol{r})\,\mathrm{d}x\,\mathrm{d}y\,\mathrm{d}z = \frac{1}{A} \iiint_U \boldsymbol{\sigma}(\boldsymbol{r}) \cdot (\boldsymbol{E}_0 - \nabla V(\boldsymbol{r}))\,\mathrm{d}x\,\mathrm{d}y\,\mathrm{d}z, \tag{3.4}$$

where U denotes the unit cell volume, and A is its area in the plane of periodicity. Due to the isolating boundary condition $\hat{\boldsymbol{n}} \cdot \boldsymbol{J} = 0$ in the normal direction, the effective conductance dyadic is

$$\mathbf{G}_{\text{eff}} = \begin{pmatrix} G_{xx} & 0 & 0 \\ 0 & G_{yy} & 0 \\ 0 & 0 & 0 \end{pmatrix}. \tag{3.5}$$

When the triaxial weave is modeled as a homogeneous slab, as in Figure 5, the conductance dyadic in (3.5) is isotropic in the xy-plane, resulting in $G_{xx} = G_{yy}$. By normalizing the effective conductance of the weave in Figure 5 with

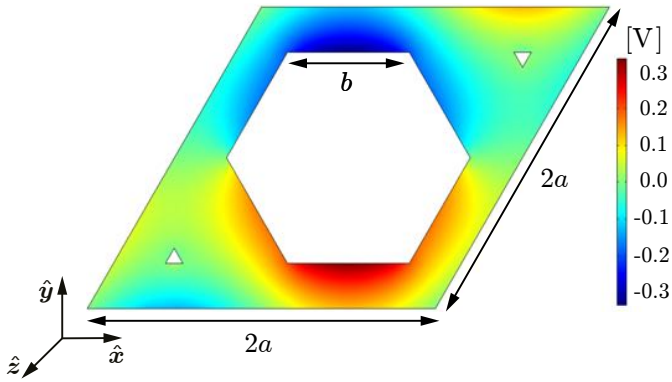

Figure 5: Two dimensional low frequency model of the triaxial weave. The induced electric potential at the surface of the slab is given by the color map when an external constant electric field of strength 1 V/m is applied in the $\hat{\boldsymbol{y}}$-direction.

the fiber conductance, defined as $G_1 = \sigma_1 t$, the relative effective conductance is determined as

$$G_{yy,\mathrm{rel}} = \frac{G_{yy}}{\sigma_1 t}. \tag{3.6}$$

This quantity is plotted as a function of the relative side length of the hexagon shaped hole in Figure 6a together with the bounds on the effective conductance of the unit cell given by the Wiener bounds [32] defined as

$$\left\langle (\sigma(\boldsymbol{r})t)^{-1} \right\rangle^{-1} \mathbf{I} \leq \mathbf{G}_{\mathrm{eff}} \leq \langle \sigma(\boldsymbol{r})t \rangle \mathbf{I}, \tag{3.7}$$

where the brackets represent the average of the evaluated function, $\mathbf{I}$ is the identity dyadic, $\sigma(\boldsymbol{r})$ is the conductivity of the unit cell and t is the weave thickness. In our specific case this corresponds to a bounded effective conductance G_{yy} such that

$$\frac{1}{\frac{A_1}{\sigma_1 t} + \frac{A_2}{\sigma_2 t}} \leq G_{yy} \leq A_1 \sigma_1 t + A_2 \sigma_2 t, \tag{3.8}$$

where A_1 and σ_1 are the relative area and the conductivity of the weave, and A_2 and $\sigma_2 = 0$ are the relative area and conductivity of the perforations in the weave. Since the free space conductivity is zero, the lower bound is equal to zero over the full range of b/a. The side length of the hexagon shaped hole in the unit cell is in practice bounded according to (2.1) but was varied in the range $b \in (0, a)$ for verification. This homogenization method can also be implemented to determine the effective conductivity of the carbon fiber tows from the microscopic material parameters of the carbon fibers and the background resin material. A connection is then established between the microscopic material properties of the weave fiber tows and the return loss of the full weave structure.

To determine the reflection and transmission of the homogenized structure the weave is modeled as a lumped impedance in a transmission line as in [25], where

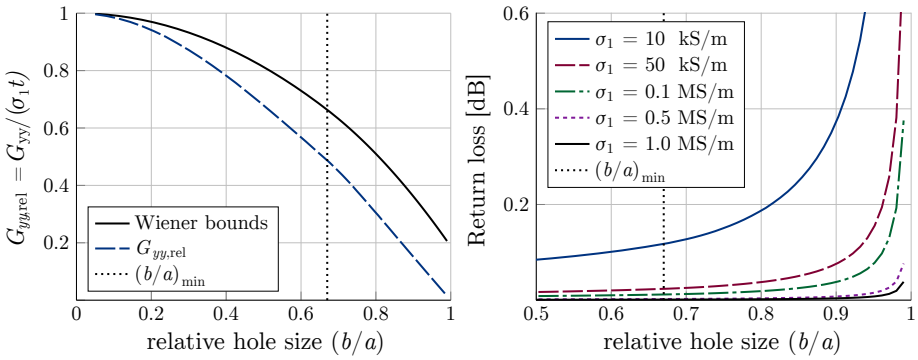

(a) (b)

Figure 6: Homogeneous low frequency limit model implemented in Comsol Multiphysics. In (a) the relative conductivity of the weave is plotted as a function of the relative hole size (b/a). The thickness of the slab is 80 μm, the dashed line represents the lower bound of b/a and the solid black line correspond to the upper Wiener bound of the effective conductivity of the weave. The lower Wiener bound is zero for all relative hole sizes. In (b) the low frequency limit return loss (defined as $\mathrm{RL} = -20\log_{10}(|S_{11}|)$) of the weave is plotted as a function of the relative hole size for different weave fiber conductivities.

in this case the characteristic impedance of the line is the free space impedance $Z_0 = \eta_0 \approx 377\,\Omega$. The low frequency reflection coefficient is then calculated as

$$S_{11} = \frac{-Z_0 G_{yy}/2}{1 + Z_0 G_{yy}/2}, \tag{3.9}$$

where S_{11} is the reflection coefficient of the weave and G_{yy} is the effective conductance of the slab. The return loss of the homogenized structure is plotted, for different weave fiber conductivities, as a function of the side length of the hexagon shaped hole in Figure 6b, for a thickness of the weave of 80 μm and an effective conductance of the slab extracted from Comsol Multiphysics. The results indicate that if the conductivity of the weave fiber tows is 50 kS/m or higher, and the relative hole size is minimized ($b/a \approx 0.7$), the return loss of a reflected signal is lower than 0.05 dB in the low frequency limit.

3.2 Full wave analysis

To study the reflection and transmission properties of the weave at the frequencies of main interest in satellite communication systems, 10–30 GHz, the unit cell models in Figures 3–4 were implemented in commercial simulation softwares, where pillars of air were added above and below the periodic structure, as in Figure 7. Two Floquet ports were defined on both sides of the device under test (DUT), where ports 1 and 3 correspond to signals of $\hat{\boldsymbol{x}}$-polarization and ports 2

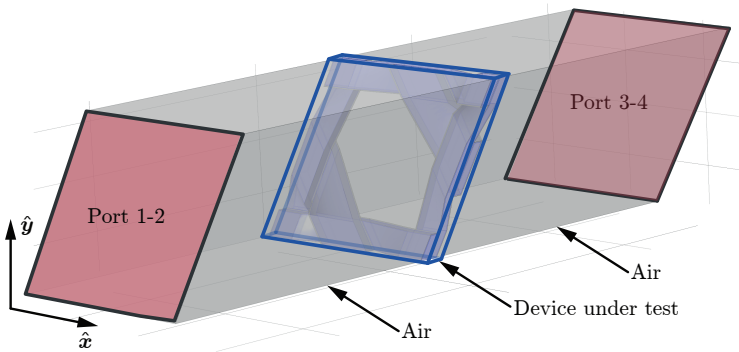

Figure 7: Simulation model implemented in Comsol Multiphysics and CST MWS.

and 4 correspond to signals of $\hat{\boldsymbol{y}}$-polarization. The interaction of a device under test with incoming linearly polarized signals from the four ports is fully described by the scattering matrix S [21, p. 178]. By exciting an incident signal at one of the ports and collecting the output signals at each port, and repeating this process for all four ports, a 4×4 scattering matrix is achieved as in (3.10), where each element $S_{ij} = E_i/E_j$ corresponds to a signal excited at port j and received at port i. The fact that the structure has a high degree of symmetry in the xy-plane implies that all the cross polarization terms in the S-matrix are almost identically zero, resulting in

$$S = \begin{pmatrix} S_{11} & S_{12} & S_{13} & S_{14} \\ S_{21} & S_{22} & S_{23} & S_{24} \\ S_{31} & S_{32} & S_{33} & S_{34} \\ S_{41} & S_{42} & S_{43} & S_{44} \end{pmatrix} \approx \begin{pmatrix} S_{11} & 0 & S_{13} & 0 \\ 0 & S_{22} & 0 & S_{24} \\ S_{31} & 0 & S_{33} & 0 \\ 0 & S_{42} & 0 & S_{44} \end{pmatrix}. \tag{3.10}$$

Since the weave consists of conductive fibers of three principal directions, and the weave periodicity is small in comparison to the wavelength of incident signals, the electromagnetic scattering from the structure is practically independent of the polarization direction of the incident signal, which further implies that the weave appears to be isotropic and that

$$\begin{aligned} S_{11} &\approx S_{22}, \quad S_{31} \approx S_{42}, \\ S_{33} &\approx S_{44}, \quad S_{13} \approx S_{24}. \end{aligned} \tag{3.11}$$

A material that is isotropic and passive has a reciprocal response to incident signals, resulting in the relations

$$S_{24} = S_{42}, \qquad S_{31} = S_{13}. \tag{3.12}$$

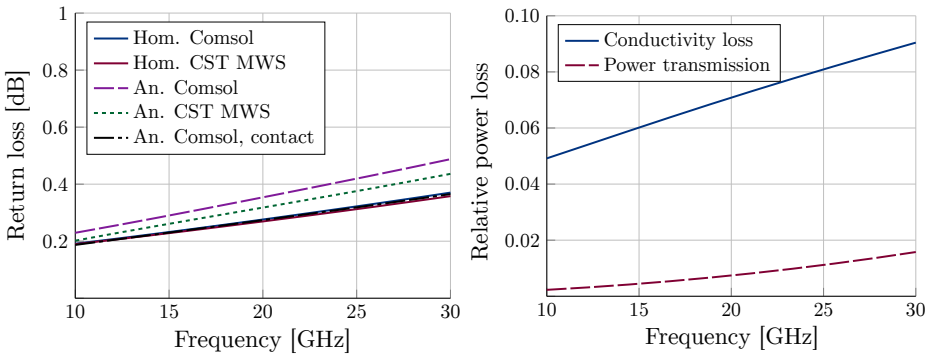

(a) (b)

Figure 8: Simulation models implemented in Comsol Multiphysics and CST MWS. In (a) simulation results are compared of the homogeneous slab model and the anisotropic fine structure model in both simulation softwares. In (b) the relative power losses due to transmission and the finite conductivity of the structure are presented.

Also, due to the symmetry of the structure, the reflection properties of the structure are identical when the structure is illuminated from the front or back side

$$S_{11} = S_{33}, \qquad S_{22} = S_{44}. \tag{3.13}$$

In conclusion, the outcome of this analysis is that S_{11} and S_{31} are the only influential independent scattering parameters to be analyzed. A common measure of the reflection performance of a structure is the return loss (RL), defined as the ratio in decibels of the power of a wave incident to a discontinuity relative to the power of the wave reflected by the discontinuity [21]. Using S-parameters the return loss is defined as

$$\mathrm{RL} = -20\log_{10}(|S_{jj}|). \tag{3.14}$$

As can be seen in the definition above, the return loss is always a positive value unless the reflected wave has more power than the incident wave, which is only possible in an active system.

The weave structures in Figures 3–4 were simulated both in CST MWS and Comsol Multiphysics for verification, with the unit cell size $2a = 2\,\mathrm{mm}$, corresponding to $2a \in (\lambda/15, \lambda/5)$ at the frequencies of main interest, the weave thickness $t = 80\ \mu\mathrm{m}$, the weave conductivity $\sigma = 10^4$ S/m, and the side length of the perforations $b = 0.7a$ (corresponding to a perforation rate of 37%). The design parameters of the anisotropic model are presented in Table 2, and the number of mesh elements, required RAM memory, and simulation times of the different models are presented in Table 3. In Figure 8a the simulation curves of the two softwares almost coincide, and when the insulating coating of the fiber tows is removed from the anisotropic model the return loss is almost identical to

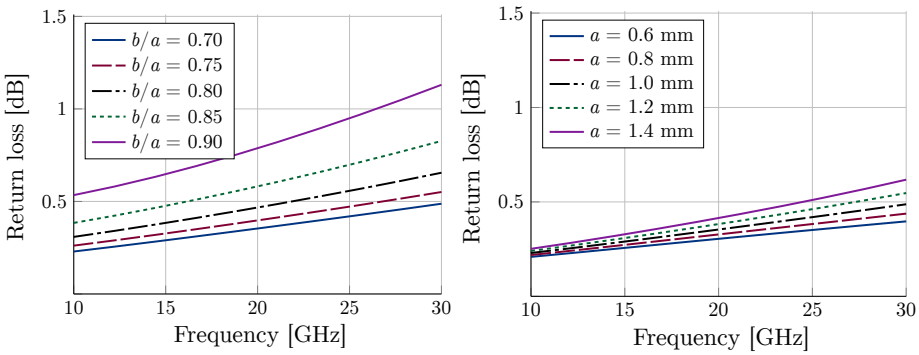

Figure 9: Anisotropic simulation model implemented in Comsol Multiphysics. In (a) the width of the fiber tows has been varied for a fixed unit cell size ($a = 1\,\text{mm}$) and in (b) the size of the unit cell has been varied for a fixed unit cell shape ($b/a = 0.7$).

that of the homogeneous model; this indicates that the anisotropy of the structure introduces a small increase in the return loss of the weave.

In Figure 8b the relative power loss due to transmission ($P_{\text{transmitted}}/P_{\text{incident}}$) and the finite conductivity of the weave, ($P_{\text{dissipated}}/P_{\text{incident}}$) are plotted separately, where it can be seen that most of the losses are caused by conductivity losses inside the weave fibers. This is an interesting result considering current research on highly conductive carbon nanotubes with a conductivity of up to 10^8 S/m [13, 36]. A weave with fibers of very high conductivity would have a significantly improved performance in comparison to a weave of ordinary carbon fibers, typically with a conductivity of approximately 10^4 S/m.

Upon varying the width of the fiber tows for a fixed unit cell size, $a = 1\,\text{mm}$, it can be seen in Figure 9a that when the fiber tows are made thinner, the return loss of the structure increases. In Figure 9b the size of the unit cell is varied for a fixed unit cell shape, $b/a = 0.7$, which indicates that making the weave structure finer improves the return loss. This corresponds to shrinking the fine structure of the weave with respect to the wavelength of the incident signal.

The conductivity of the fiber tows is varied in Figure 10a, where the results indicate that by increasing the fiber conductivity the return loss is significantly improved. Also, when comparing the results of the full wave simulations in Figure 10a to the low frequency limit model in Figure 6b, it can be seen that the low frequency limit return loss is slightly lower than the return loss at 10 GHz. The low frequency limit return loss thus serves as a lower bound on the return loss of the weave, $\text{RL}(f) \geq \text{RL}(f \to 0)$, so it gives an indication of the maximum reflection performance of a weave with given material and design characteristics. If, on the other hand, the conductivity of the weave is made infinite, $\sigma \to \infty$, the minimum return loss for a specified unit cell and perforation size is achieved. The results in Figure 10a indicate that, given a periodicity of $2a = 2\,\text{mm}$ and

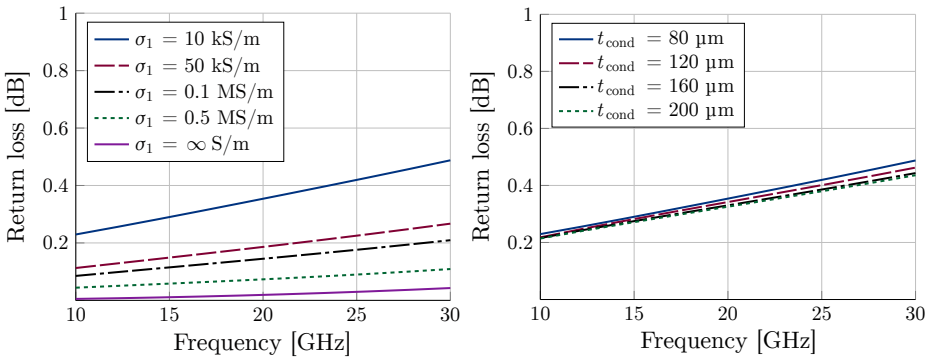

(a) (b)

Figure 10: Anisotropic simulation model implemented in Comsol Multiphysics. In (a) the conductivity of the fiber tows has been varied and in (b) the thickness of the fibers tows has been varied.

a perforation side length of $b = 0.7\,\text{mm}$, the lower bound on the return loss is approximately 0.04 dB in the frequency band of interest.

The last design parameter to be analyzed is the thickness of the weave fiber tows, and the results are presented in Figure 10b. When the fiber tows are made thicker the return loss is slightly improved, but the gain in return loss is too small to make up for the increase in weight of the structure. This indicates that, the fiber tow thickness is not a relevant design parameter if the goal is to minimize the product between return loss and weight of the structure.

3.3 Fiber tow cross section homogenization

To this point, the material parameters of the carbon fiber tows have been treated as homogeneous quantities. But on a microscopic length scale, each of the carbon fiber tows in the weave consist of a great number of conducting fibers ($\sigma_c \approx 14\,\text{kS/m}$) oriented in a periodic manner in an insulating resin material ($\sigma_{ins} \approx 0$), as in Figure 1. Determining an effective conductivity of the fiber tows from the microscopic material properties would open for a relevant connection between these microscopic material parameters and the return loss of the macroscopic reflector surface.

The microscopic structure of the fiber tows can be modeled as a periodic array of cylindrical rods as in Figure 11. By defining a two dimensional homogenization model of the microscopic fiber cross section in Figure 11, and applying an external current, $\boldsymbol{J}_e$, the effective conductivity of the fiber tows in Figure 1 can be determined from the microscopic response of the structure [15]. The fields associated with this problem satisfy the conductivity equations in (3.1)–(3.2). A requirement for the low frequency model to be valid is that the period of the unit cell should be much smaller than the wavelength of the incident signal, which is

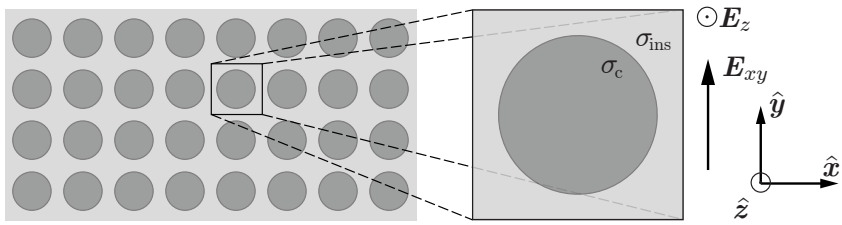

Figure 11: Microscopic cross section of a carbon fiber tow, the dark area consists of conducting carbon fibers, with conductivity σ_{c}, and the light area represent an insulating resin material, with conductivity $\sigma_{\text{ins}} \approx 0$.

the case in this problem since the diameter of a carbon fiber is of the order of 5–10 μm [28] and the wavelength of the incident signal is 1 cm at 30 GHz.

Once the microscopic response of the device under test is known, the transverse and longitudinal homogenization parameters ($\sigma_{\text{eff},xy}$ and $\sigma_{\text{eff},z}$) can be determined from the expression

$$\langle \boldsymbol{J}(\boldsymbol{r}) \rangle = \frac{1}{A} \iint\limits_{\Omega} \left[\sigma(\boldsymbol{r}) (\boldsymbol{E}_0 - \nabla V(\boldsymbol{r})) \right] \, \mathrm{d}x \, \mathrm{d}y = \boldsymbol{\sigma}_{\text{eff}} \cdot \langle \boldsymbol{E}(\boldsymbol{r}) \rangle \tag{3.15}$$

where A is the area of the two dimensional unit cell in Figure 11, Ω is denoting the conductive part of the unit cell, and the effective conductivity tensor can be written as

$$\boldsymbol{\sigma}_{\text{eff}} = \begin{pmatrix} \sigma_{\text{eff},xy} & 0 & 0 \\ 0 & \sigma_{\text{eff},xy} & 0 \\ 0 & 0 & \sigma_{\text{eff},z} \end{pmatrix}. \tag{3.16}$$

Due to the translational symmetry of the fiber tow cross section, the homogenization problem of finding the transverse and longitudinal conductivity decouple and can be solved independently of each other. If the external applied electric field in Figure 11 is oriented in the xy-plane, orthogonal to the fiber direction, the transverse component of the effective conductivity ($\sigma_{\text{eff},xy}$) is determined. Since the insulating resin material in the unit cell is non-conductive, the effective conductivity in the transverse direction is zero, *i.e.* ($\sigma_{\text{eff},xy} \approx 0$). On the other hand, if the external applied electric field in Figure 11 is oriented in the z-direction, parallel to the fiber direction, the longitudinal component of the effective conductivity ($\sigma_{\text{eff},z}$) is determined. In this case, the applied electric field $\boldsymbol{E} = E_0 \hat{\boldsymbol{z}}$ is parallel to all boundaries of the structure in the unit cell in Figure 11, and thus the effective conductivity $\sigma_{\text{eff,z}}$ can be calculated analytically through the expression

$$\langle \boldsymbol{J} \rangle = \sigma_{\text{c}} A_{\text{c}} E_0 \hat{\boldsymbol{z}} = \boldsymbol{\sigma}_{\text{eff,z}} \cdot \langle \boldsymbol{E} \rangle = \sigma_{\text{eff,z}} E_0 \hat{\boldsymbol{z}}, \tag{3.17}$$

where A_{c} is the surface fraction of the conducting part of the unit cell. The effective material parameters of the fiber tows are thus given by $\sigma_{\text{eff},z} = \sigma_{\text{c}} A_{\text{c}}$

and $\sigma_{\text{eff},xy} \approx 0$. These parameters can then be used as input parameters in the full wave simulation models in Section 3.2. For example, if the conductivity of the carbon fibers is approximately 14 kS/m, and the resin content of the fiber tows is 28 %, which is the case of the reference weave of this study in Fig 2, this corresponds to the fiber tows having an effective conductivity of 10 kS/m.

4 Acoustic analysis

Few studies have been reported regarding the impact of high levels of acoustic excitation on the lightweight triaxial carbon fiber weaves considered here. In such conditions, for which required qualification test levels may be well above 140 dB, non-linear effects, such as vorticity-related dissipation in the vicinity of the orifices, may have to be taken into account. In [11], a global approach was considered using a full-sized acoustic model composed of an equivalent shell structure of the antenna, connected to a semi-infinite fluid on both sides, modeled with either a Statistical Energy Analysis (SEA) or Boundary Elements. The focus was more on the modelling aspects than the actual design parameters. More details may be found in works focusing on Micro-Perforated Panels (MPPs), such as recently in [18], where an equivalent acoustic impedance approach was used in order to study a sandwich structure including MPPs such as those of interest here. The resulting model, building upon milestone studies on the acoustic properties of orifices such as in [9,12,14], is however limited to a study of the linear regime even though the contribution is initially positioned in the context of high vibro-acoustic excitation levels. Recently, in [29], an extension of a porous-model formulation from [1] to this non-linear regime of interest was proposed. This extension is based upon a Forchheimer law [6] (quadratic law) for the air flow resistivity parameter, acknowledged to be the most influencial parameter for the non-linear behaviour of such materials at high sound pressure levels [2,33,35]. In particular, considering a modelling of the triaxial carbon fiber weaves in the form of a non-linear impedance, these studies show that the resistive part, *i.e.* the real part of the impedance, is the most affected by the non-linear behaviour [4, 5, 9, 14, 29]. The analysis conducted here, in order to estimate the influence of the meso-scale design of these weaves on their local acoustic loading, is therefore especially focused on the study of the flow resistance. The approach considered in the following is, in line with the electromagnetic analysis, to conduct a parametric study of the static flow resistance in a range of realistic design parameters. In this range, it is shown that a critical transition in the behavior of the perforated structure takes place for a threshold size of the unit cell.

4.1 Assumptions and acoustic numerical model

4.1.1 The flow resistance: the viscous and inertia regimes

The flow resistance, or flow resistivity depending on its definition, quantifies the physical resistance by a permeable structure in opposition to a traversing flow. In the low frequency range of interest here, the static flow resistance, generally identified in steady-state conditions, provides a relation between the pressure drop (pressure increase at the flow inlet due to the flow resistance) and the mean velocity flow. In turn, for the problem of interest, this may be linked to a relation between the acoustic loading (pressure drop) and the acoustic excitation (acoustic velocity). Two situations may be distinguished: *i)* a flow dominated by viscous forces, further referred to as the viscous regime, and *ii)* a situation where these are dominated by inertial and convective acceleration forces, further referred to as the inertia regime. In both cases, a set of common assumptions allow to consider a simplified description of the physics.

First, for a study involving an airflow under ordinary conditions, the pressure and velocity fields are described by the reduced set of Navier-Stokes equations —momentum and mass continuity equations—,

$$\rho\left(\frac{\partial \boldsymbol{v}}{\partial t} + \boldsymbol{v}\cdot\nabla\boldsymbol{v}\right) = -\nabla P + \nabla\cdot\mathbf{T} + \boldsymbol{f}, \tag{4.1}$$

$$\frac{\partial \rho}{\partial t} + \nabla\cdot(\rho\boldsymbol{v}) = 0, \tag{4.2}$$

where ρ is the fluid density, $\boldsymbol{v}$ is the fluid velocity [m.s^{-1}], P is the pressure [Pa], $\mathbf{T}$ is the deviatoric stress tensor, corresponding to a Newtonian fluid in the present study, and $\mathbf{f}$ are the body forces (neglected here). For the low frequency range of interest, the acoustic wavelength being much larger than the typical dimensions of the orifices, the flow is assumed to be incompressible, thus reducing the mass continuity equation (4.2) to

$$\nabla\cdot\boldsymbol{v} = 0. \tag{4.3}$$

While the reduced set of equations (4.1) and (4.3) are sufficient to describe the problem of interest in order to estimate the flow resistance, the two phenomenological situations mentioned above may be identified from the momentum equation (4.1) in relation to the Reynolds number of the flow in the flow restriction of the permeable structure. The Reynolds number Re, quantifying the ratio of inertial forces over viscous forces in the flow, thus allows to distinguish:

- $Re \ll 1$: the viscous forces (corresponding to the term $\nabla\cdot\mathbf{T}$ in (4.1)) dominate over the convective acceleration forces (corresponding to the term $\boldsymbol{v}\cdot\nabla\boldsymbol{v}$ in (4.1)) which can thus be neglected. This corresponds to the **viscous regime**.

- $Re \sim 1$ (and greater): the convective acceleration forces dominate over the viscous forces, this corresponds to the **inertia regime**.

The viscous regime, corresponding to a Stokes flow, is thus described by a linearised form of the Navier-Stokes equations, here written for the steady-state case, *i.e.* $\dfrac{\partial \boldsymbol{v}}{\partial t} = 0$,

$$-\nabla P + \nabla \cdot \mathbf{T} = 0. \tag{4.4}$$

Phenomenologically, the emerging linear relation between the pressure drop δP from one side of the permeable structure to the other, and the mean particle velocity in the flow may be described by Darcy's law, which for a unidimensional flow, is of the form

$$\delta P = k_1 v, \tag{4.5}$$

v being the one dimensional mean velocity of the input (or output) flow through the permeable surface, away from the surface. The coefficient k_1 is dependent on the fluid properties (dynamic viscosity, density, ...) and the geometry of the orifices (surface restriction, typical dimension of the orifice(s), thickness of the permeable structure, shape of the holes, ...). This coefficient may be identified by measuring the input/output pressure difference from one side to the other of a permeable structure, for an imposed steady-state flow with normal incidence.

The inertia regime, in addition to the viscous regime description, includes the term corresponding to the convective acceleration forces. Thus for the steady-state case, the Navier-Stokes equations read

$$\rho \boldsymbol{v} \cdot \nabla \boldsymbol{v} = -\nabla P + \nabla \cdot \mathbf{T}. \tag{4.6}$$

Phenomenologically, the non-linear relation between the pressure drop mean particle velocity in the flow may be described by a Forchheimer's law [6, 29], *e.g.* in its quadratic form for a unidimensional flow,

$$\delta P = k_1 v + k_2 v^2, \tag{4.7}$$

k_1 being the same as for Darcy's law in (4.5). Forchheimer's law is often described as Darcy's law with a correction for Reynolds number from the order of unity, where inertial effects start to become dominant, in the transition from a laminar to turbulent flow. In order to establish a basis for a design methodology, a parametric study is performed, in the following, determining the dependence of these Forchheimer's coefficients with respect to the most influential parameters.

4.2 Parametric study, and identification of a Forchheimer-like law

For the problem of interest, the manufacturing constraints are assumed to impose tightly woven fiber tows, *i.e.* a ratio b/a close to its minimum of 2/3. In agreement with the electromagnetic study, b/a is set to a reference value of 0.7. The parametric study is subsequently mostly dependent on either of the unit

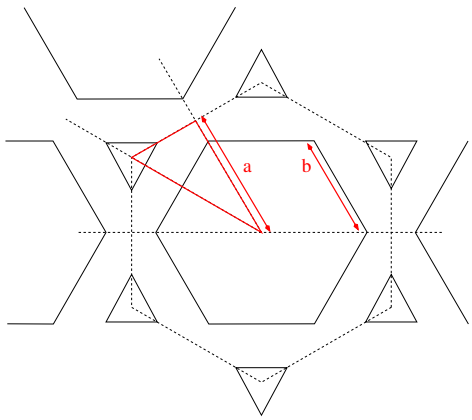

Figure 12: Geometry: unit-cell for the simulation of normal flow through the permeable structure.

cell characteristic lengths a or b. The thickness, while also being influential, is considered to be secondary due to its very limited range of variation, and to the fact that the presumably linear increase in flow resistance may be compensated by a linear increase in mechanical strength of the yarns (note that the inertial impact of the added thickness may be of interest, but is left out of the scope of this study at a meso-scale level). Furthermore, it is shown in the electromagnetic study in Section 3 that an increased thickness is of little benefit for the return loss (see *e.g.* Figure 10b).

The numerical model is intended to enable an efficient numerical characterization of Darcy's and Forchheimer's laws by calculating k_1 and k_2. For this purpose, a meso-scale geometry (of the order of the orifices) of the antenna and the surrounding air is established, assuming a normal airflow through the permeable structure, corresponding to the conditions of experimental characterization of these laws. It is assumed that the interaction between the flow through one orifice and the neighboring orifices, potentially breaking the periodicity of the problem, can be neglected, thus limiting the study to a unit cell (see Appendix B for a numerical validation of this assumption for the Forchheimer-like law characterization).

From a normal flow perspective, the unit cell consists of a hexagonal shape with a 30-degree rotation with respect to a unit hexagonal shape of the orifices, assuming that the influence of the in-plane geometry of the structure due to the weaving of the yards is neglected (see Figures 3 and 4 with the associated discussion). This unit cell, presented in dotted lines in Figure 12, contains all the streamlines associated with the orifices located within its boundaries, *i.e.* no streamline generated by the normal incident flow is crossing the unit cell boundaries. This implies a symmetry at the unit cell boundaries in terms of both geometry and loads; an acceptable unit cell is thus defined.

This unit cell can be further downsized to a triangular unit cell, correspond-

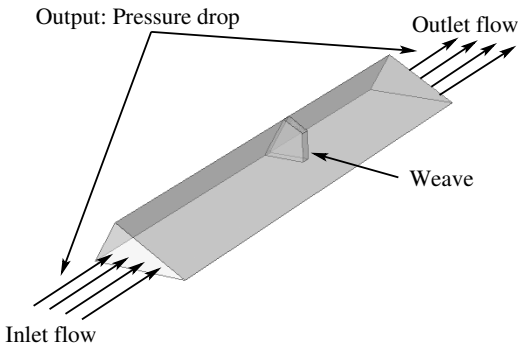

Figure 13: Numerical model for the flow resistance analysis of triaxial woven fabrics: $1/12^{\text{th}}$ of a fluid unit cell, normal incidence steady-state air flow on the permeable structure.

ing to $1/12^{\text{th}}$ of the original cell, if the internal symmetries of the hexagon are taken into account and respected by the flow. Figure 12 shows this final triangular unit cell, together with its parametric dimensions in agreement with the notations presented in Section 2. The assumed value of $b/a = 0.7$ corresponds to a perforation rate $\phi = 0.37$, which is noticeably higher than the range usually considered in the literature [6, 29].

The finite element (FE) model corresponding to the unit cell of Figure 12 for the study of flow resistance is presented in Figure 13. It consists of a unit cell of fluid (normal extrusion of the 2D fluid cell geometry presented in Figure 12), including the permeable structure modeled as a rigid body. A steady-state airflow is imposed on the boundary planes parallel to the structure, as a fixed velocity boundary condition on both the "inlet" and "outlet" surfaces. The side surfaces of the fluid cell may either be applied "slip" rigid wall boundary conditions (no viscous layer on the wall), or symmetry boundary conditions. The former option is only possible because no streamline is assumed to cross the side boundaries of the fluid cell.

4.3 Parametric study, and identification of a Forchheimer-like law

4.3.1 The viscous regime: Darcy's linear law

Darcy's law may be determined via numerical experiments involving a Stokes flow such as presented in Figure 14. This viscous-dominated nature of the flow is reflected by the streamlines, especially close to the surface at the outlet side, where the viscous drag ensures that the streamlines follow closely the sharp

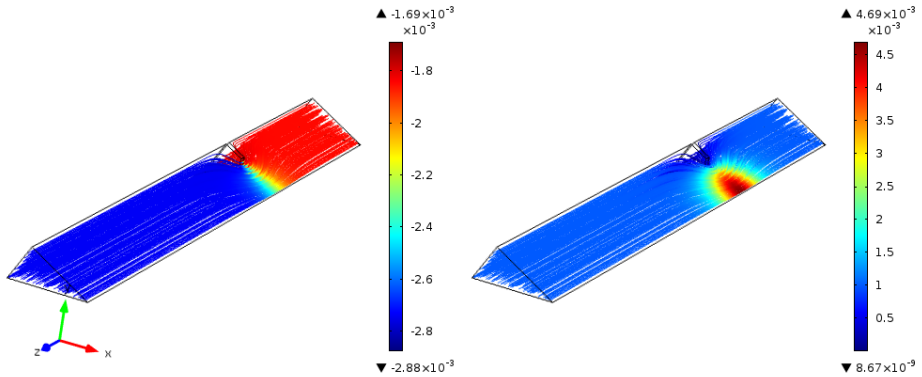

(a) (b)

Figure 14: Stokes flow for the identification of Darcy's law ($a = 1 \cdot 10^{-3}$ m, inlet flux $1 \cdot 10^{-3}$ m.s^{-1}, $Re_{\text{orifice}} \approx 0.210$); (a): Streamlines and pressure field (Pa); (b): Streamlines and velocity field m.s^{-1}. Flow in the **z** direction.

variations in the geometry. The resulting velocity field (Figure 14b) is mostly affected in the close vicinity of the permeable structure, with a sharp increase of the velocity at the restriction, followed by an almost symmetric decrease, such that the velocity distribution may be assumed constant in parallel planes close to the permeable structure. The pressure field (Figure 14a) follows with a sharp drop at the restriction and quasi uniform distribution of the pressure within planes parallel to the permeable structure in its close vicinity.

The linear coefficient $k_1(a)$ for the Darcy's law may be identified at a given low velocity (*i.e.* for which the Reynolds number associated with the flow in the orifice is typically lower than unity) and from a range of values for a. Figure 15a presents the evolution of the pressure drop with respect to the mean flow velocity for apertures corresponding to a ranging from $1 \cdot 10^{-4}$ m to $1 \cdot 10^{-3}$ m.

The linearity expected from Darcy's law seems to be verified in the range of velocity considered, *i.e.* the values here taken at $v = 5 \cdot 10^{-4}$ m.s^{-1} and $v = 1 \cdot 10^{-3}$ m.s^{-1}. Figure 15b subsequently presents the power-law fit of $k_1(a)$, from the numerical experiments at $v = 5 \cdot 10^{-4}$ m.s^{-1}. An excellent fit is found with a two-parameter power law fit (q_1 and q_2), such that Darcy's law for the triaxial woven fabrics of interest is given by

$$\delta P = \frac{q_1 + a}{q_2 a^2} v, \tag{4.8}$$

where q_1 and q_2 are dependent on fluid properties (*e.g.* viscosity) and the geometry (*e.g.* orifice shape factor, thickness of the permeable structure, porosity of the structure, *etc.*), and can be identified from the one-point numerical experiment and curve fit presented above.

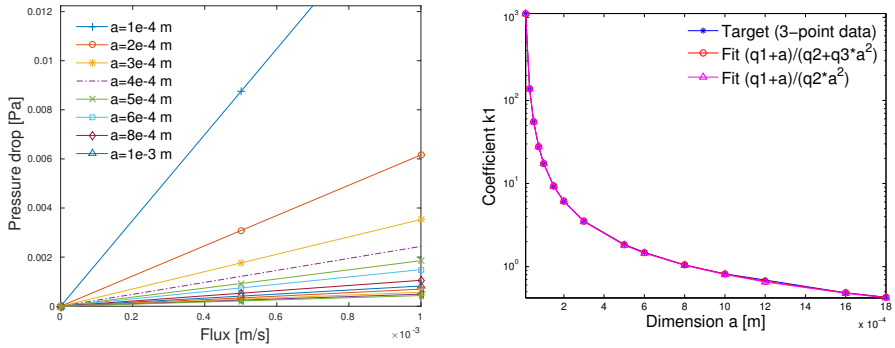

(a) (b)

Figure 15: (a): Multiple aperture (dimension a) analysis for the identification of Darcy's law; (b): Analytical fit (semi-log scale) with a power law, data at $v = 5 \cdot 10^{-4}$ m.s^{-1}.

4.3.2 The inertia regime: Forchheimer's quadratic law

Forchheimer's quadratic law may be constructed as an augmentation to Darcy's law, with numerical experiments involving a flow whose convective accelerations become dominant over viscous effects. This corresponds to a flow where geometrical irregularities have a stronger impact on the flow, as illustrated in Figure 16. As can be seen with the streamlines in Figure 16a and Figure 16b, a recirculation appears downstream (flow in opposite direction compared to Figure 13) due to the inertial effects overcoming the viscous drag and its tendency to have the streamline closely follow the geometry variations. This implies, contrary to the viscous case in Figures 14, a velocity gradient in planes parallel to the permeable structure downstream. The pressure field is also affected, and eventually evolves to a quasi-constant pressure within planes further away from the permeable structure. This implies, for the purpose of determining Forchheimer's law, a need to have a variable length of fluid downstream in the numerical model, increasing with the Reynolds number. Consequently, the Forchheimer's law model is more computationally costly, and its reduction to the minimum geometry is here critical.

The quadratic coefficient $k_2(a)$ for the Forchheimer law may be identified, after the determination of the linear coefficient from Darcy's law, at a given velocity such that $Re \gg 1$, and from a range of values for a. Figure 17 presents the evolution of the pressure drop with respect to the mean flow velocity for apertures corresponding to a ranging from $1 \cdot 10^{-4}$ m to $1.6 \cdot 10^{-3}$ m. From these plots, it appears that the point at v_{Forch}, introduced previously such that $Re(a, v_{\text{Forch}}) \gg 1$, *i.e.* that the pressure drop behaviour would be quadratic with respect to the mean flow velocity, is to be chosen such that $v_{\text{Forch}} > 1\,\text{m.s}^{-1}$. The preliminary identification of Darcy's law allows the pressure drop to be decomposed into its linear (or viscous induced) and its quadratic (or inertia

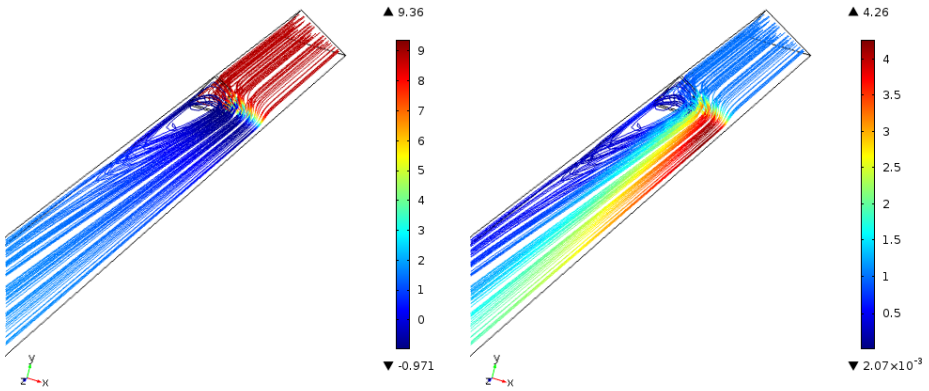

(a) (b)

Figure 16: Inertia-driven flow for the identification of Forchheimer's law ($a = 1 \cdot 10^{-3}$ m, inlet flux 1 m.s^{-1}, $Re_{\text{orifice}} \approx 210$); (a): Streamlines and pressure field (Pa); (b): Streamlines and velocity field (m.s^{-1}). Flow in the **z** direction.

induced) parts. Figure 18 presents this separation for the apertures $a = 2 \cdot 10^{-4}$ m and $a = 8 \cdot 10^{-4}$ m. In a combined analysis with the results from Figure 17, the following conclusions are drawn:

- After a sharp decrease of the pressure drop with increasing orifice sizes a, this dependence on the aperture seems to reach an asymptotic behaviour where this dependence becomes negligible, for the range of velocities considered.
- As expected, above an orifice size threshold, the viscous contribution to the pressure drop becomes negligible compared to the inertia contribution. This is well explained by the fact that as the orifice size increases, the ratio of fluid within the viscous layer along the boundaries vs. outside this viscous layer (and hence dominated by inertial effects) decreases.
- It may be noticed at this stage that the inertia contribution being very similar for the range of apertures considered —an observation confirmed for plots at additional aperture sizes—, this pressure drop dependence on the orifice size is mostly driven by the viscous contribution.

In an attempt to propose a fit for the explicit dependence of the Forchheimer coefficient k_2 on the aperture a, it appeared that a velocity-dependence remains. This is well illustrated in Figure 19, where it is shown that the coefficient k_2 exhibits an explicit dependence on $a\sqrt{v}$ in the range of velocities of interest. A good fit for this dependence is achieved with a 4-parameter power law with exponential cutoff and offset, such that

$$k_2(a\sqrt{v}) = q_3 \left(a\sqrt{v}\right)^{-q_4} \mathrm{e}^{-\frac{(a\sqrt{v})}{q_5}} + q_6. \tag{4.9}$$

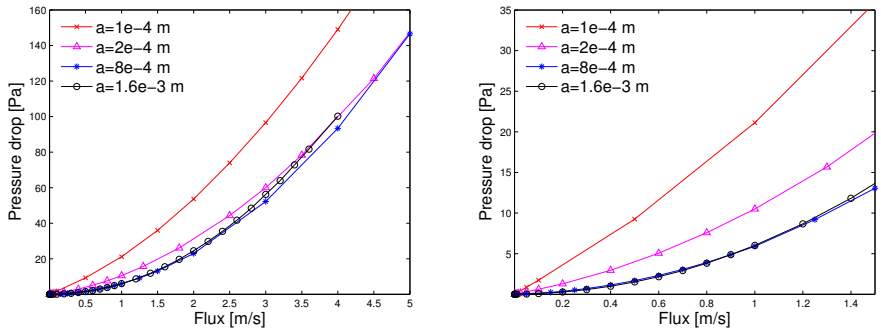

(a) (b)

Figure 17: Multiple aperture (dimension a) analysis for the identification of Forchheimer's law; (a): $v \in [0, 5]$ m.s^{-1}; (b): Zoom in for $v \in [0, 1.5]$ m.s^{-1}.

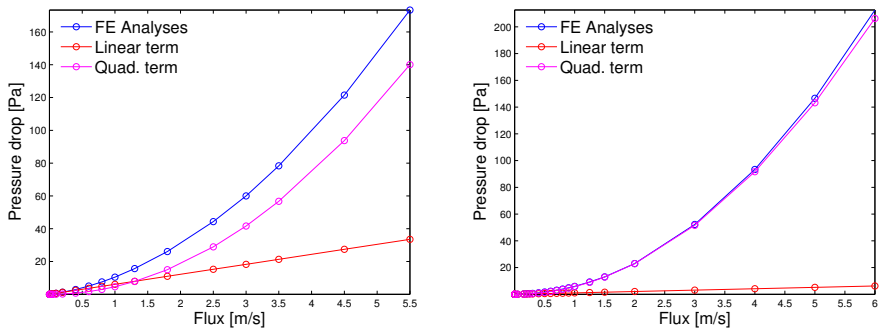

(a) (b)

Figure 18: Illustration of the separation of the pressure drop into the viscous and inertial contributions: (a) $a = 2 \cdot 10^{-4}$ m; (b) $a = 8 \cdot 10^{-4}$ m.

This leads to a Forchheimer-like law identified numerically for the triaxial woven fabrics of interest,

$$\Delta P\left(a, v\right) = \left[\frac{q_1 + a}{q_2 a^2}\right] v + \left[q_3 \left(a\sqrt{v}\right)^{-q_4} \mathrm{e}^{-\frac{\left(a\sqrt{v}\right)}{q_5}} + q_6\right] v^2 \tag{4.10}$$

where $q_1, \cdots, q_6$ may be determined in a two-step procedure, first involving q_1 and q_2 in the viscous regime alone, and then $q_3 \cdots q_6$ by adding data from the inertia regime. Table 1 presents the values of these coefficients for the case of interest. This Forchheimer-like law is checked at six different velocities covering the entire range of interest, confirming the validity of the Forchheimer-like law identified for the triaxial woven fabrics of interest under the current assumptions (See Figure 24 in Appendix C).

The complete surface fit corresponding to the identified Forchheimer-like law is plotted in Figure 20 for the range of aperture $a \in (0, 2)$ mm and mean flow

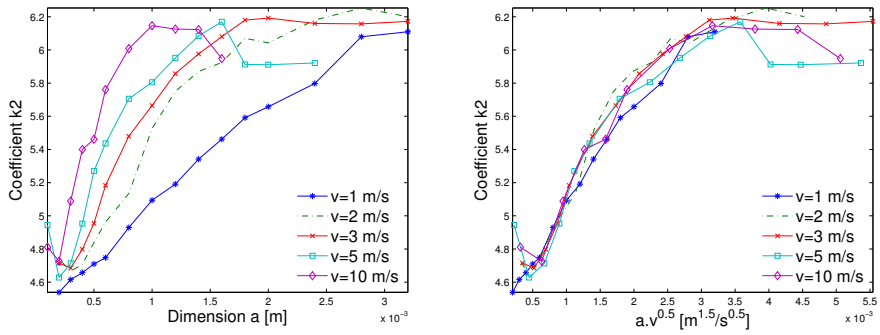

(a) (b)

Figure 19: Illustration of the dependence of k_2 on the flow velocity, ranging from $v = 1$ m.s^{-1} to $v = 10$ m.s^{-1}: (a) k_2 vs. orifice dimension a; (b) k_2 vs. orifice dimension a and $\sqrt{v}$.

Table 1: Values for coefficients $q_1, \cdots, q_6$ of the Forchheimer-like law identified.

q_1	q_2	q_3	q_4	q_5	q_6
$1.48 \cdot 10^{-4}$	$1.43 \cdot 10^{3}$	$-1.82 \cdot 10^{2}$	$-5.226 \cdot 10^{-1}$	$6.09 \cdot 10^{-4}$	6.1

velocity $v \in (0, 10)$ m.s^{-1}. The superimposed red line represents a velocity-dependent pressure drop minimum, which corresponds to the transition from viscous-driven to inertia-driven flow. Figure 21 presents a separation between the viscous contribution and inertia contribution to the overall pressure drop. Interestingly, the viscous contribution and its associated design constraints are evidently orifice-dimension dependent, while the inertia contribution and its associated design constraints are primarily flow-velocity dependent (and thus sensitive to acoustic excitation levels).

4.4 Other parametric dependence

In order to further detail the results in connection with the electromagnetic study, a parametric analysis focusing on the influence of the perforation rate is performed, *i.e.* allowing for a variation of the ratio b/a. As previously mentioned, the impact of the variation of the thickness is not detailed considering its negligible impact from an electromagnetic perspective, and its similarly minor impact at the level of the meso-scale acoustic study presented here. In particular, the thickness mostly impacts the viscous-related flow resistance, whose contribution is to be minimized for the design of antenna reflectors. On the other hand, even though the perforation rate is considered to be constrained by manufacturing requirements in the present study (assumed such that $b/a = 0.7$), its variation may open the possibility for a trade-off between acoustic and electromagnetic

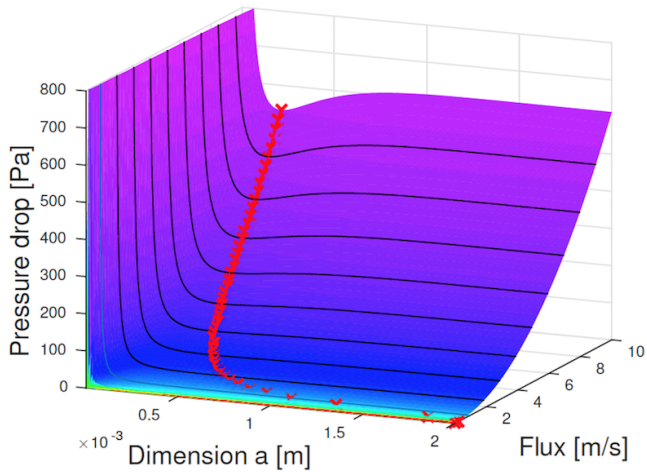

Figure 20: Complete Forchheimer-like law for 1 mm thick triaxial woven fabrics, with $\frac{b}{a} = 0.7$.

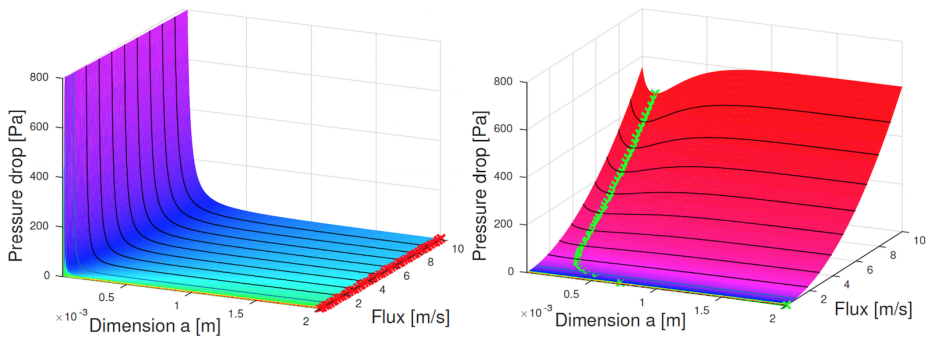

(a) (b)

Figure 21: Forchheimer-like law: separation into the viscous contribution (left) and the inertia contribution (right) to the pressure drop.

performance.

Figure 22 presents the influence of the porosity for a low mean flow velocity in Figure 22a, and higher velocity in Figure 22b, both including points in the viscous regime (lower values of a) and in the inertia regime. Figure 22c presents a synthesis of the influence of the porosity for each of the five points considered in the design space, normalized with respect to the reference value at $b/a = 0.7$ as used in the previous sections (this reference configuration is highlighted with a dotted line in Figures 22a and 22b). Two main observations may be extracted from these plots: *i)* the pressure drop is highly sensitive to the porosity, exhibiting a rapid decrease for even a small increase of the porosity, and *ii)* this applies to both the viscous and inertia regimes, at low or high velocities. Furthermore,

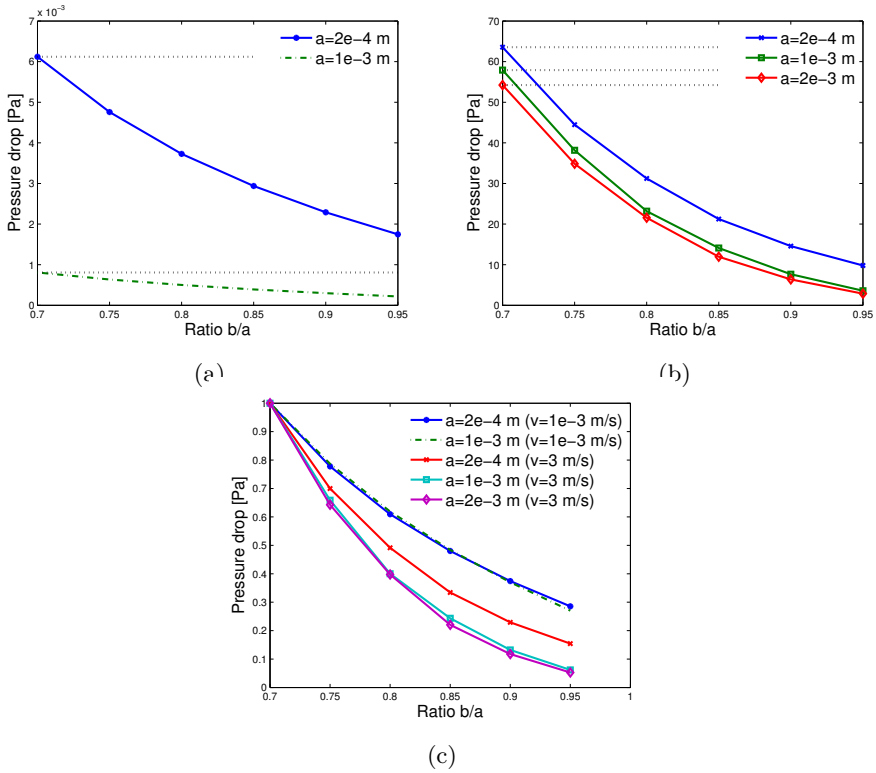

Figure 22: Influence of the porosity in both the viscous and inertia regimes: (a) $v = 1 \cdot 10^{-3}$ m.s^{-1}; (b) $v = 3$ m.s^{-1}; (c) $v = 1 \cdot 10^{-3}$ m.s^{-1} and $v = 3$ m.s^{-1}.

Figure 22c shows that the perforation rate is particularly influential at higher levels of acoustic excitation (higher mean flow velocities). This confirms that the porosity may open a wide range of design possibilities in order to reduce the acoustic load. In particular, a tradeoff may be found with the electromagnetic requirement of minimizing the porosity.

5 Design guidelines

The motivation of using the currently investigated type of porous weave structure as a reflector antenna surface is to increase the durability of the reflector, at the cost of a slightly reduced electromagnetic reflection performance. The simulation results in Section 3 indicate that, for a weave structure with a perforation rate of 37%, the period $2a \approx 2$ mm, corresponding to $2a \in (\lambda/15, \lambda/5)$ at the frequency range of interest, and conductivity $\sigma \approx 10$ kS/m, the reflection performance is still high, with a return loss in the order of 0.5 dB. Furthermore, both full wave simulations and the low frequency limit analysis indicate that the main parameter

governing the reflection performance of the structure is the fiber conductivity. If the size of the weave perforations is increased, the reflection performance is reduced. However, this effect could efficiently be mitigated by increasing the fiber conductivity, for example by either coating the weave with a conductive paint, decreasing the relative resin content in the fiber tows, or possibly in the future, by using highly conducting carbon nanotube fibers in the manufacturing process.

From an acoustic perspective, the results in Section 4 have highlighted a critical dimension for the perforations of the reflector antenna, below which the porous weave structure is dominated by a very flow-resistive behavior. This behavior is due to fluid-structure interactions being driven by the viscous drag, and should be avoided in the context of the design of reflector antennas because of the strong coupling induced with external acoustic excitation such as during takeoff. On the basis of the Forchheimer-like law identified, plotted in Figure 20, this threshold is located at the transition between the viscous-driven and inertia-driven resistance of the antenna material. According to the readings on Figure 20, it may arguably be such that a is in the range $a \approx 0.25\,\text{mm}$ and $a \approx 0.5\,\text{mm}$, with very little dependence on the level of excitation (*i.e.* the particle velocity). Interestingly, with the steady-state resistive study conducted here, marginal variations of the resistance are observed for perforations sizes beyond this critical size. This point, combined with the results from the electromagnetic study, opens a design window for the periodicity of the weave structure to be in the range $2a \in (1, 2)\,\text{mm}$. From a structural-acoustic point of view, further insight may be gained by performing a transient (or frequency-dependent) set of analyses, in order to quantify the impact of the inertial behavior which dominates the fluid-structure interactions in this range.

Additionally, the high sensitivity of the flow resistance of the triaxial weave to its porosity (or the ratio b/a) offers additional possibilities, provided that the manufacturing processes allow for such a change in the design. Indeed, a small increase in the porosity implies an equally important reduction of the flow resistance in both the viscous and inertial regimes, and a small impact on the return loss of a reflected signal (see Figure 6b and 9). This suggests that the design of panels with higher or non-uniform porosities may provide improved design tradeoffs between the electromagnetic and acoustic constraints.

In summary, the synthesis of the study performed in the current work leads to the following design guidelines, applicable to a triaxial weave for a reflector:

- The fiber conductivity should be as high as possible.
- The weave periodicity ($2a$) should be larger than 1.0 mm, given a perforation rate of 37 %, in order to conservatively ensure a flow resistance dominated by inertial fluid-structure interactions.
- The weave periodicity should however be smaller than 2.0 mm ($\lambda/5$ at 30 GHz) in order to have an electromagnetic return loss better than 0.5 dB in the frequency range of interest, given a fiber conductivity of $10^4\,\text{S/m}$.
- Larger weave perforations, or a higher frequency of operation, implies an increase in the electromagnetic return loss.

- The weave fiber tow thickness does not significantly affect the performance of the structure.
- Depending on the manufacturing possibilities, a small increase of the porosity (or perforation rate) may offer better overall performances.

This implies that the weave used as a reference in this study, as can be seen in Figure 2, has a higher perforation rate (44 %) than recommended, and the periodicity of the weave pattern ($2a = 3.5\,\mathrm{mm}$) is too large to achieve a low electromagnetic return loss in the frequency band of interest at 10–30 GHz.

6 Conclusions

A combined electromagnetic and acoustic analysis of a triaxial carbon fiber weave structure, designed for ultra lightweight reflector antennas in satellite communication systems, has been presented. The structure was analyzed for its electromagnetic performance over a wide range of frequencies at both microscopic and mesoscopic length scales, completed by a mesoscopic analysis of its acoustic performance. Design guidelines were drawn from these analyses in order to reach a trade-off between the electromagnetic reflection properties and the resistance to acoustic loading of such composite materials. It was found that the typical unit cell size should be of the order of $2a \in (1, 2)\,\mathrm{mm}$, for a perforation rate of 37 % (*i.e.* $b/a = 0.7$), with the largest conductivity possible. The electromagnetic return loss of a weave with the mentioned geometrical properties, and a fiber tow conductivity of $10^4\,\mathrm{S/m}$, is around 0.2–0.5 dB in the frequency range of main interest at 10–30 GHz, where $2a \in (\lambda/15, \lambda/5)$. However, if the conductivity of the fiber tows could be increased, for example by coating the weave with a conductive paint, decreasing the relative resin content in the fiber tows, or by increasing the conductivity of the microscopic carbon fibers, either the return loss could be brought down to at most 0.04 dB, or a larger mesoscopic weave periodicity and a higher perforation rate could be utilized, to further increase the resistance to acoustic loading.

Due to the fact that the fiber tow thickness is not significantly affecting the performance whereas small variations of the perforation rate are, multilayer weaves may offer promising performances. The study of such multilayer weaves, and the effect of moiré patterns on the acoustic and electromagnetic performance of the structure, are therefore interesting extensions for future works.

Acknowledgements

The support provided by Rymdstyrelsen, the Swedish National Space Board, through the NRFP research program, is gratefully acknowledged, together with the contribution of RUAG Space.

Appendix A Design parameters and computational resources for the electromagnetic simulations

Table 2: Design parameters modeling the anisotropic weave design.

Parameter	Description	Value
a	half side length of unit cell	1 mm
b	side length of hexagon shaped perforations	0.7 mm
w	width of fiber tows	$\sqrt{3}(a-b)$
t	thickness of fiber tows	80 μm
t_{ins}	thickness of insulating layer of fiber tows	10 μm
t_{cond}	thickness of conducting core of fiber tows	80 μm
σ_1	conductivity of fiber tows	10^4 S/m
$\epsilon_{\text{r},1}$	relative permittivity of fiber core	2
$\mu_{\text{r},1}$	relative permeability of fiber core	1
σ_{ins}	conductivity of insulating material	10^{-12} S/m
$\epsilon_{\text{r,ins}}$	relative permittivity of insulating material	2
$\mu_{\text{r,ins}}$	relative permeability of insulating material	1
z_{dist}	distance from weave to ports	3 mm

Table 3: Specifications of the simulation models in CST MWS and Comsol Multiphysics.

Simulation model	Number of mesh elements	Allocated RAM memory	Simulation time
Homogeneous model, Comsol M.	35 000	6 GB	30 min.
Anisotropic model, Comsol M.	63 000	15 GB	42 min.
Homogeneous model, CST MWS	33 000	2 GB	10 min.
Anisotropic model, CST MWS	171 000	8 GB	50 min.

Appendix B On the multi-hole interactions impact on the flow resistance simulations

The impact of a potentially broken symmetry of the flow when inertial effects start to become prevalent is checked by comparing the flow resistance on a seven-cell model (one cell and its six closest neighbours) with the Forchheimer-like law in (4.10). Due to the limitations in computational resources with respect to the size of the model, the study is limited to a mean flow velocity up to $v = 3$ m.s^{-1}.The results in Figures 23a–23b clearly demonstrate the validity of

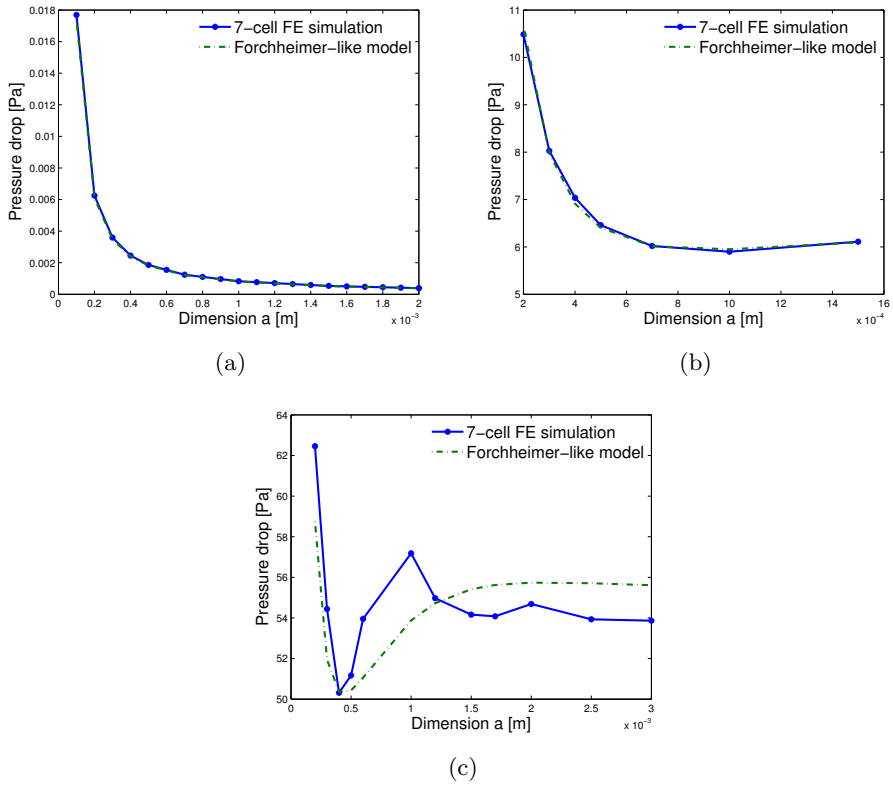

Figure 23: Validation of the Forchheimer-like law against a 7-cell model with potential interactions: (a) $v = 1 \cdot 10^{-3}$ m.s^{-1}; (b) $v = 1$ m.s^{-1}; (c) $v = 3$ m.s^{-1}.

the unit cell model for low mean flow velocities where viscous effects are prevalent. In Figure 23c, the impact of potential flow interactions between neighbour cells is shown to be minor in the range considered. The deviation from the Forchheimer-like law is indeed contained within a variation of 5 %, here attributed for the greater part to the difficulties for the calculations to converge due to the mesh size limitations. Overall, this confirms the ability of the identified law in (4.10) to qualitatively estimate the interaction between structural loading, acoustic excitation level, and geometry of the cells.

Appendix C Verification of the Forchheimer-like law in the velocity range of interest

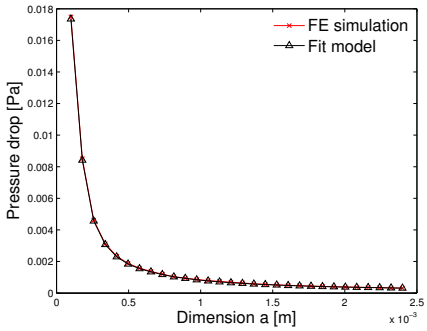

(a)

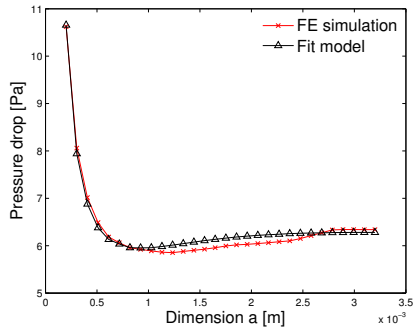

(b)

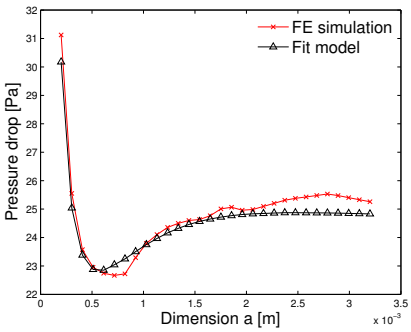

(c)

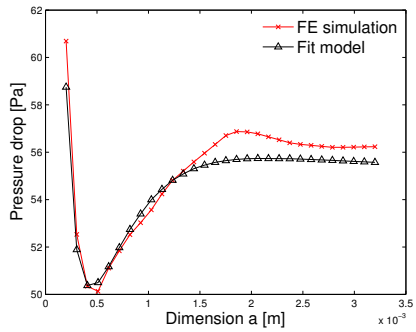

(d)

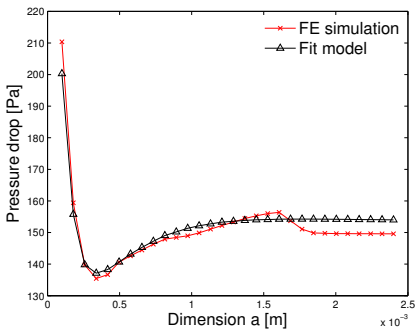

(e)

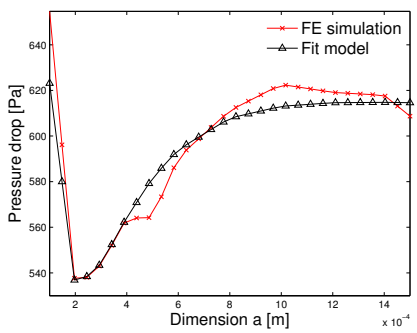

(f)

Figure 24: Validation of Forchheimer's law fit with $k_1(a)$ and $k_2(a\sqrt{v})$ from numerical experiments at 6 different velocities: (a) $v = 1 \cdot 10^{-3}$ m.s^{-1}; (b) $v = 1$ m.s^{-1}; (c) $v = 2$ m.s^{-1}; (d) $v = 3$ m.s^{-1}; (e) $v = 5$ m.s^{-1}; (f) $v = 10$ m.s^{-1}.

References

[1] N. Atalla and F. Sgard. Modeling of perforated plates and screens using rigid frame porous models. *Journal of Sound and Vibration*, **303**(1), pp. 195–208, 2007.

[2] Y. Auregan and M. Pachebat. Measurement of the nonlinear behavior of acoustical rigid porous materials. *Physics of Fluids (1994-present)*, **11**(6), pp. 1342–1345, 1999.

[3] L. Brydon. Ultra lightweight thin membrane antenna reflector, 1999. EP Patent 0,741,435.

[4] A. Cummings. Acoustic nonlinearities and power losses at orifices. *AIAA journal*, **22**(6), pp. 786–792, 1984.

[5] A. Cummings. The effects of grazing turbulent pipe-flow on the impedance of an orifice. *Acta Acustica United with Acustica*, **61**(4), pp. 233–242, 1986.

[6] P. Forchheimer. Wasserbewegung durch boden. *Z. Ver. Deutsch. Ing*, **45**(1782), pp. 1788, 1901.

[7] A. Fujita, H. Hamada, and Z. Maekawa. Tensile properties of carbon fiber triaxial woven fabric composites. *Journal of composite materials*, **27**(15), pp. 1428–1442, 1993.

[8] W. A. Imbriale, S. S. Gao, and L. Boccia, editors. *Space Antenna Handbook*. Wiley, 2012.

[9] U. Ingard. On the theory and design of acoustic resonators. *The Journal of the acoustical society of America*, **25**(6), pp. 1037–1061, 1953.

[10] A. Kueh and S. Pellegrino. *Triaxial weave fabric composites*. Department of Engineering, University of Cambridge, 2007.

[11] J. M. Larko and V. Cotoni. Vibroacousitc response of the nasa acts spacecraft antenna to launch acoustic excitation. *Proceedings ICSV*, **14**, 2008.

[12] D.-Y. Maa. Potential of microperforated panel absorber. *the Journal of the Acoustical Society of America*, **104**(5), pp. 2861–2866, 1998.

[13] P. L. McEuen, M. S. Fuhrer, and H. Park. Single-walled carbon nanotube electronics. *IEEE Transactions on Nanotechnology*, **1**(1), pp. 78–85, 2002.

[14] T. H. Melling. The acoustic impendance of perforates at medium and high sound pressure levels. *Journal of Sound and Vibration*, **29**(1), pp. 1–65, 1973.

[15] G. W. Milton. *The Theory of Composites*. Cambridge University Press, Cambridge, 2002.

[16] P. Morgan. *Carbon Fibers and Their Composites*, volume 1. Taylor & Francis Boca Raton, FL, 2005.

[17] R. A. Naik. Analysis of woven and braided fabric reinforced composites, 1994.

[18] A. Omrani and I. Tawfiq. Vibro-acoustic analysis of micro-perforated sandwich structure used in space craft industry. *Mechanical Systems and Signal Processing*, **25**(2), pp. 657–666, 2011.

[19] E. Pfeiffer, A. Ihle, M. Klebor, O. Reichmann, S. Linke, C. Tschepe, N. Nathrath, A. Grillenbeck, J. S. Prowald, P. Rinous, et al. Highly stable antenna structure technologies. In *Proceedings of 32nd ESA Antenna Workshop on Antennas for Space Applications, Noordwijk, The Netherlands*, 2010.

[20] E. K. Pfeiffer, T. Ernst, and A. Ihle. Highly stable lightweight antennas for ka/q/v-band and other advanced telecom structure concepts. In *Antennas and Propagation, 2009. EuCAP 2009. 3rd European Conference on*, pp. 745–749. IEEE, 2009.

[21] D. M. Pozar. *Microwave Engineering*. John Wiley & Sons, New York, NY, third edition, 2005.

[22] S. Rao, L. Shafai, and S. K. Sharma. *Handbook of Reflector Antennas and Feed Systems Volume III: Applications of Reflectors*. Artech house, 2013.

[23] A. G. Roederer and Y. Rahmat-Samii. Unfurlable satellite antennas: A review. *Annales des Telecommunications*, **44**(9-10), pp. 475–488, 1989.

[24] Sakase adtech co., ltd. Available at: http://sakase.co.jp/home_en/, accessed 2016-04-25.

[25] D. Sjöberg. Circuit analogs for wave propagation in stratified structures. In A. Petrin, editor, *Wave Propagation in Materials for Modern Applications*, pp. 489–508. InTech, 2010.

[26] D. Sjöberg, N. Wellander, and A. Ericsson. A Homogenization Procedure for Microstructured Resistive Sheets. In *URSI General Assembly and Scientific Symposium, 2014-08-16/2014-08-23*. IEEE, 2014.

[27] G. Stephens. Method of making an acoustic panel with a triaxial open-weave face sheet, 1987. US Patent 4,671,841.

[28] A. B. Strong. *Fundamentals of composites manufacturing: materials, methods and applications*. Society of Manufacturing Engineers, 2008.

[29] R. B. Tayong, T. Dupont, and P. Leclaire. Sound absorption of a micro-perforated plate backed by a porous material under high sound excitation: measurement and prediction. *International Journal of Engineering & Technology*, **2**(4), pp. 281–292, 2013.

[30] Tencate advanced composites. Available at: http://www.tencate.com/advancedcomposites/default.aspx, accessed 2016-04-25.

[31] Tencate rs-3 cyanate ester data sheet. Available at: http://www.tencate.com/advancedcomposites/product-compare-tool/RS-3.aspx, accessed 2016-04-25.

[32] S. Torquato. *Random Heterogeneous Materials: Microstructure and Microscopic Properties*. Springer-Verlag, Berlin, 2002.

[33] O. Umnova, K. Attenborough, E. Standley, and A. Cummings. Behavior of rigid-porous layers at high levels of continuous acoustic excitation: Theory and experiment. *The Journal of the Acoustical Society of America*, **114**(3), pp. 1346–1356, 2003.

[34] J. G. van Bladel. *Electromagnetic Fields*. IEEE Press, Piscataway, NJ, second edition edition, 2007.

[35] D. K. Wilson, J. D. McIntosh, and R. F. Lambert. Forchheimer-type nonlinearities for high-intensity propagation of pure tones in air-saturated porous media. *The Journal of the Acoustical Society of America*, **84**(1), pp. 350–359, 1988.

[36] B. Zhao, H. Qi, and D. Xu. Resistance measurement of isolated single-walled carbon nanotubes. *Measurement*, **45**(5), pp. 1297–1300, 2012.

Scattering from a Multilayered Sphere - Applications to Electromagnetic Absorbers on Double Curved Surfaces

Andreas Ericsson, Daniel Sjöberg, Christer Larsson
and Torleif Martin

Paper VII

Submitted as: A. Ericsson, D. Sjöberg, C. Larsson and T. Martin, "Scattering from a multilayered sphere - Applications to electromagnetic absorbers on double curved surfaces," *Progress In Electromagnetics Research B*, pp. 1–23, 2017, under review.

Preprint published as: Technical Report LUTEDX/(TEAT-7249), pp. 1–32, 2017, Department of Electrical and Information Technology, Lund University, Sweden. http://www.eit.lth.se.

Abstract

The scattering from a layered sphere with any number of layers and admittance sheets at the interfaces is calculated in this work. By utilizing spherical vector wave expansion and matching of the tangential fields at each interface, and introducing a surface admittance to the magnetic field boundary condition, the transition matrix components are determined. A numerical implementation of the derived analytic expressions is utilized to determine the monostatic radar cross section from a sphere, of varying radius, coated with a number of different electromagnetic absorbers. When the monostatic scattering from a sphere coated with an absorber is normalized with the monostatic scattering, either from the uncoated structure or from an enclosing perfect electric conductor, a comparison can be made to the planar absorber performance. The impact of curvature on the absorber performance is evaluated from these results. It is concluded that absorbers based on bulk losses are less sensitive to curvature than absorbers based on single or multiple layers of thin sheets.

1 Introduction

Electromagnetic scattering from a sphere is a subject with a long and distinguished history. It can be argued who was first in presenting a solution to the problem, but today it is commonly referred to as the Mie series, named after Gustav Mie from his work in [15]. Since then the topic has been studied extensively, and the results are summarized in many textbooks [2,3,13,21,27]. The Mie series is used in a wide variety of applications such as optics, climate modelling, astro physics, nano science and biomedical imaging [2, 9, 16, 19, 24, 29].

When the spherical scatterer is much smaller than the wavelength of the incident wave, the Rayleigh scattering approximation can be applied [28]. When the size of the scatterer exceeds about 10 % of the wavelength of the incident wave, this approximation breaks down and the Mie series solution has to be applied. Since the advent of modern computers, much work has been done on implementing stable and reliable algorithms of Mie series calculations [5, 7, 8, 14, 23, 31]. This has resulted in efficient calculations of Mie series with size parameters on the order of 10 000. Some examples of scenarios that have been considered are: spheres of different dielectric and magnetic materials, layered spheres, anisotropic spheres, distorted spheres and spheres in an absorbing medium [9]. Recently, a summarizing article was presented [24] where the history of the Mie series is presented in detail. Analytic expressions for scattering from a layered sphere and the numerical implementation of the problem was presented in [24]. The authors of this report were surprised to find no reference to prior work that considers the scattering from a layered sphere with an arbitrary number of layers, and with admittance sheets at the interfaces. This type of problem has much use in the analysis of electromagnetic absorbers, which commonly consists of single or multiple layers of dielectric or magnetic materials, resistive sheets and circuit analog structures [17].

Electromagnetic absorbers are commonly used to attenuate electromagnetic signals and reduce the reflection and transmission from particular objects. Examples of areas where absorbers are used are in free space measurement setups for electromagnetic characterization of antennas or other objects [30], and in defense applications such as radar cross section (RCS) reduction [12, 21]. Most absorbers are designed for a planar structure of infinite extent, while most real applications involve that the absorber is applied to a curved structure, such as the body of an aircraft. Surprisingly little work exists with respect to the degradation of the absorber performance due to curvature. In [4] a Luneberg-Kliene expansion of the scattered field from a cylinder and a sphere is carried out to identify a correction term proportional to the radius of curvature of the scatterer, and in [11] the performance degradation of a five layer Jaumann absorber applied to a cylinder is calculated. In [26] a series of different absorbers are evaluated when applied to a perfect electric conductor (PEC) cylinder, and a conclusion in this work is that by normalizing the monostatic scattering from a coated cylinder with either the scattering from the uncoated structure, or the scattering from an enclosing PEC structure, a comparison can be made to a corresponding planar absorber design.

In this work, the scattering from a multilayered sphere is calculated by expanding the electric and magnetic fields in spherical vector waves. The structure of the specific scattering problem implies that all information of the scattered fields are stored in the transition matrix (or T-matrix), the mapping matrix between the incident and scattered fields. Once this mapping has been determined, the scattered fields are easily calculated. In the special case of scattering of a linearly polarized plane wave from a layered sphere with isotropic materials the T-matrix is diagonal, which greatly simplifies the solution of calculating the scattered fields. We use the T-matrix to determine the monostatic RCS of a PEC sphere coated with different types of classical electromagnetic absorbers, such as the Salisbury screen [22], Jaumann absorber [11], Chambers-Tennant absorber [6], conductive dielectric absorber, thin magnetic absorber and different types of circuit analog absorbers (CAA). By utilizing the normalization scheme that was first presented in [26] the monostatic RCS of the coated spheres can be compared to the corresponding planar design of the absorber under test. This study gives information of the performance degradation of absorbers due to curvature, and it is observed that electromagnetic absorbers of the same type display similar behavior when exposed to curvature.

This report is organized as follows: in Section 2 the theory of spherical vector waves is presented and in Section 3 the theory of scattering from layered spheres with admittance sheets at the interfaces is presented. This content is based on the notation and approach used in [13], where scattering from a PEC sphere, dielectric sphere, and layered spheres without thin sheets at the interfaces are considered. A numerical implementation of the theory in Sections 2–3 is presented in Section 4. In Section 5 simulation results of the implementation in Section 4 are presented, where the monostatic RCS of different electromagnetic absorbers applied to a sphere is calculated, and some concluding remarks are presented in Section 6. In Appendix A a detailed analytic derivation is presented of the

scattering from a layered sphere with admittance sheets at the interfaces, and in Appendix B the implemented code is benchmarked against different commercial software.

2 Spherical vector waves

The theory and notation presented in Sections 2–3 are based on the work in [13], and the time convention $e^{j\omega t}$ is used throughout this report.

2.1 Expansion of fields

In order to construct an orthogonal set of spherical vector waves with the right properties one needs to introduce a vector valued version of the ordinary scalar spherical harmonics [13]

$$Y_{\sigma ml}(\theta,\phi) = \sqrt{\frac{\varepsilon_m}{2\pi}}\sqrt{\frac{2l+1}{2}\frac{(l-m)!}{(l+m)!}}P_l^m(\cos\theta)\begin{Bmatrix}\cos m\phi\\ \sin m\phi\end{Bmatrix}, \tag{2.1}$$

where the Neumann factor ε_m is defined as

$$\varepsilon_m = 2-\delta_{m0}, \qquad i.e.\ \varepsilon_0 = 1,\ \varepsilon_m = 2,\ m>0. \tag{2.2}$$

The spherical vector harmonics are here denoted $\boldsymbol{A}_{\tau\sigma ml}(\hat{\boldsymbol{r}})$, where $\tau = 1,2,3$ is the spherical vector wave index, σ is the even/odd mode index, $m = 0,1,2,..,l-1,l$ is the azimuthal mode index, and $l = 0,1,2,...,\infty$ is the spherical harmonics index. In order to simplify the notation, we introduce a multiindex $n = (\sigma,m,l)$ which results in the spherical vector harmonics being denoted $\boldsymbol{A}_{\tau n}(\hat{\boldsymbol{r}})$. The spherical vector harmonics are generated from the relations

$$\begin{cases} \boldsymbol{A}_{1n}(\hat{\boldsymbol{r}}) = \dfrac{1}{\sqrt{l(l+1)}}\nabla Y_n(\hat{\boldsymbol{r}})\times\hat{\boldsymbol{r}} \\ \boldsymbol{A}_{2n}(\hat{\boldsymbol{r}}) = \dfrac{1}{\sqrt{l(l+1)}}r\nabla Y_n(\hat{\boldsymbol{r}}) \\ \boldsymbol{A}_{3n}(\hat{\boldsymbol{r}}) = \hat{\boldsymbol{r}}Y_n(\hat{\boldsymbol{r}}), \end{cases} \tag{2.3}$$

where $\boldsymbol{A}_{1n}$, $\boldsymbol{A}_{2n}$, and $\boldsymbol{A}_{3n}$ are orthogonal, and $\boldsymbol{A}_{1n}$ and $\boldsymbol{A}_{2n}$ are tangential to spherical surfaces. A far field vector can be expanded in spherical vector waves using the Fourier expansion

$$\boldsymbol{F}(\hat{\boldsymbol{r}}) = \sum_{\tau=1}^{3}\sum_{n=\sigma,m,l} a_{\tau n}\boldsymbol{A}_{\tau n}(\hat{\boldsymbol{r}}), \tag{2.4}$$

where the Fourier coefficients $a_{\tau n}$ are determined through the relation

$$a_{\tau n} = \int_{\Omega} \boldsymbol{F}(\hat{\boldsymbol{r}}) \cdot \boldsymbol{A}_{\tau n}(\hat{\boldsymbol{r}}) \, \mathrm{d}\Omega. \tag{2.5}$$

We are now ready to introduce the spherical vector waves used to describe the electric- and magnetic field on a spherical surface. The out-going spherical vector waves are given by

$$\begin{cases} \boldsymbol{u}_{1n}(k\boldsymbol{r}) = h_l^{(2)}(kr)\boldsymbol{A}_{1n}(\hat{\boldsymbol{r}}) \\ \\ \boldsymbol{u}_{2n}(k\boldsymbol{r}) = \dfrac{(krh_l^{(2)}(kr))'}{kr}\boldsymbol{A}_{2n}(\hat{\boldsymbol{r}}) + \sqrt{l(l+1)}\dfrac{h_l^{(2)}(kr)}{kr}\boldsymbol{A}_{3n}(\hat{\boldsymbol{r}}). \end{cases} \tag{2.6}$$

and the regular spherical vector waves are

$$\begin{cases} \boldsymbol{v}_{1n}(k\boldsymbol{r}) = j_l(kr)\boldsymbol{A}_{1n}(\hat{\boldsymbol{r}}) \\ \\ \boldsymbol{v}_{2n}(k\boldsymbol{r}) = \dfrac{(krj_l(kr))'}{kr}\boldsymbol{A}_{2n}(\hat{\boldsymbol{r}}) + \sqrt{l(l+1)}\dfrac{j_l(kr)}{kr}\boldsymbol{A}_{3n}(\hat{\boldsymbol{r}}), \end{cases} \tag{2.7}$$

where $j_l(kr)$ is the spherical Bessel function, $h_l^{(2)}(kr)$ is the spherical Hankel function, defined as $h_l^{(2)}(kr) = j_l(kr) - \mathrm{j}y_l(kr)$, and $y_l(ka)$ is the spherical Neumann function. We construct a sphere enclosing the scatterer and expand the total electric field outside the sphere as

$$\begin{aligned} \boldsymbol{E}(\boldsymbol{r},\omega) = \boldsymbol{E}_{\mathrm{i}}(\boldsymbol{r},\omega) + \boldsymbol{E}_{\mathrm{s}}(\boldsymbol{r},\omega) = \sum_{\tau=1}^{3}\sum_{l=0}^{\infty}\sum_{m=0}^{l}\sum_{\sigma=\mathrm{e,o}} (a_{\tau\sigma ml}\boldsymbol{v}_{\tau\sigma ml}(k\boldsymbol{r}) \\ + f_{\tau\sigma ml}\boldsymbol{u}_{\tau\sigma ml}(k\boldsymbol{r})) = \sum_{\tau=1}^{3}\sum_{n}\left(a_{\tau n}\boldsymbol{v}_{\tau}(k\boldsymbol{r}) + f_{\tau n}\boldsymbol{u}_{\tau n}(k\boldsymbol{r})\right), \end{aligned} \tag{2.8}$$

where $a_{\tau n}$ are the incident field coefficients and $f_{\tau n}$ are the scattered field coefficients.

3 Sphere scattering

3.1 Solution method

To solve a Mie series scattering problem, we use the boundary conditions of the electric and magnetic fields at each side of an interface

$$\hat{\boldsymbol{n}} \times (\boldsymbol{E}_2 - \boldsymbol{E}_1) = 0, \qquad \hat{\boldsymbol{n}} \times (\boldsymbol{H}_2 - \boldsymbol{H}_1) = \boldsymbol{J}_{\mathrm{S}}, \tag{3.1}$$

where $\boldsymbol{E}_1$, $\boldsymbol{H}_1$ are the fields in region 1, $\boldsymbol{E}_2$, $\boldsymbol{H}_2$ are the fields in region 2, $\boldsymbol{J}_{\mathrm{S}}$ is the surface current at the interface, and $\hat{\boldsymbol{n}}$ is the normal vector of the surface

pointing from region 1 towards region 2. If the materials in the two regions are linear, a linear mapping exists between the incident field coefficients $a_{\tau n}$ and the scattered field coefficients $f_{\tau n}$

$$f_{\tau n} = t_{\tau l} a_{\tau n}, \qquad \tau = 1, 2. \tag{3.2}$$

The mapping matrix between the incident and scattered field coefficients in (3.2) is called the transition matrix or the T-matrix, and its coefficients $t_{\tau l}$ are determined from the boundary conditions of the specific problem, as is shown in Sections 3.3–3.5. An incident, monochromatic, plane wave is represented in spherical vector waves as

$$\begin{cases} \boldsymbol{E}_{\mathrm{i}}(\boldsymbol{r}, \omega) = \boldsymbol{E}_0 \mathrm{e}^{-\mathrm{j}\hat{\boldsymbol{k}}_{\mathrm{i}} \cdot \boldsymbol{r}} = \displaystyle\sum_{\tau=1}^{2} \sum_{n} a_{\tau n} \boldsymbol{v}_{\tau n}(k\boldsymbol{r}) \\ \boldsymbol{H}_{\mathrm{i}}(\boldsymbol{r}, \omega) = \boldsymbol{H}_0 \mathrm{e}^{-\mathrm{j}\hat{\boldsymbol{k}}_{\mathrm{i}} \cdot \boldsymbol{r}} = \dfrac{\mathrm{j}}{\eta_0 \eta} \displaystyle\sum_{\tau=1}^{2} \sum_{n} a_{\tau n} \boldsymbol{v}_{\bar{\tau} n}(k\boldsymbol{r}), \end{cases} \tag{3.3}$$

where η_0, η are the free space and relative wave impedance. The expansion coefficients are

$$\begin{cases} a_{1n} = 4\pi(-\mathrm{j})^l \boldsymbol{E}_0 \cdot \boldsymbol{A}_{1n}(\hat{\boldsymbol{k}}_{\mathrm{i}}) \\ a_{2n} = 4\pi(-\mathrm{j})^{l-1} \boldsymbol{E}_0 \cdot \boldsymbol{A}_{2n}(\hat{\boldsymbol{k}}_{\mathrm{i}}) \\ a_{3n} = 4\pi(-\mathrm{j})^{l-1} \boldsymbol{E}_0 \cdot \boldsymbol{A}_{3n}(\hat{\boldsymbol{k}}_{\mathrm{i}}) = 0, \end{cases} \tag{3.4}$$

where since $a_{3n} = 0$ the $\tau = 3$ terms in (3.3) does not contribute and have been excluded. The dual index $\bar{\tau}$ is indicating that $\tau = 1 \to \bar{\tau} = 2$, and $\tau = 2 \to \bar{\tau} = 1$. If the plane wave is incident along the z-axis, *i.e.* $= \hat{\boldsymbol{k}}_{\mathrm{i}} = \hat{\boldsymbol{z}}$, the expansion coefficients are

$$\begin{cases} a_{1n} = (-\mathrm{j})^l \delta_{m1} \sqrt{2\pi(2l+1)} \boldsymbol{E}_0 \cdot (\delta_{\sigma \mathrm{o}} \hat{\boldsymbol{x}} - \delta_{\sigma \mathrm{e}} \hat{\boldsymbol{y}}) \\ a_{2n} = (-\mathrm{j})^{l-1} \delta_{m1} \sqrt{2\pi(2l+1)} \boldsymbol{E}_0 \cdot (\delta_{\sigma \mathrm{e}} \hat{\boldsymbol{x}} + \delta_{\sigma \mathrm{o}} \hat{\boldsymbol{y}}) \\ a_{3n} = 0, \end{cases} \tag{3.5}$$

where $\delta_{\sigma o} = 1$ if $\sigma = o$ and $\delta_{\sigma o} = 0$ if $\sigma \neq \mathrm{o}$, and in the same manner $\delta_{m1} = 1$ if $m = 1$ and $\delta_{m1} = 0$ if $m \neq 1$. Using this representation of the incident field, the scattered field can be determined.

3.2 The scattering parameters

The scattering dyadic is given by

$$\mathbf{S}(\hat{\boldsymbol{r}}, \hat{\boldsymbol{k}}_{\mathrm{i}}) = -\frac{4\pi}{\mathrm{j}k} \sum_{nn'} \boldsymbol{a}_n^*(\hat{\boldsymbol{r}}) T_{nn'} \boldsymbol{a}_{n'}(\hat{\boldsymbol{r}}), \tag{3.6}$$

where in this context the multiindex $n = (\tau, \sigma, m, l)$ is used (as opposed to $n = (\sigma, m, l)$ which is used in the rest of the report), and where $T_{nn'}$ is the T-matrix defined as

$$f_n = \sum_{nn'} T_{nn'} a_{n'}, \tag{3.7}$$

and where the complex vector spherical harmonics $\boldsymbol{a}_n(\hat{\boldsymbol{r}})$ are defined as

$$\boldsymbol{a}_n(\hat{\boldsymbol{r}}) = \mathrm{j}^{\tau-l-1}\boldsymbol{A}_n(\hat{\boldsymbol{r}}), \tag{3.8}$$

with the parity condition $\boldsymbol{a}_n^*(\hat{\boldsymbol{r}}) = \boldsymbol{a}_n(-\hat{\boldsymbol{r}})$. From the T-matrix, and thus alternatively from the scattering matrix, specific scattering properties of an object can be calculated. For example, the differential cross section of a scatterer is defined as

$$\frac{\mathrm{d}\sigma}{\mathrm{d}\Omega}(\hat{\boldsymbol{r}}, \hat{\boldsymbol{k}}_\mathrm{i}) = \frac{|\boldsymbol{F}(\hat{\boldsymbol{r}})|^2}{k^2|\boldsymbol{E}_0|^2} = 4\pi|\mathbf{S}(\hat{\boldsymbol{r}}, \hat{\boldsymbol{k}}_\mathrm{i}) \cdot \hat{\boldsymbol{p}}_\mathrm{e}|^2, \tag{3.9}$$

where $\hat{\boldsymbol{p}}_\mathrm{e} = \boldsymbol{E}_0/|\boldsymbol{E}_0|$, $\boldsymbol{E}_0$ is the incident field, and $\boldsymbol{F}(\hat{\boldsymbol{r}})$ is the scattered farfield. From the differential cross section, the scattering cross section is defined as

$$\sigma_\mathrm{s} = \frac{1}{4\pi}\int \frac{\mathrm{d}\sigma}{\mathrm{d}\Omega}(\hat{\boldsymbol{r}}, \hat{\boldsymbol{k}}_\mathrm{i})\ \mathrm{d}\Omega = \sum_{nn'n''} b^*_{n''}(\hat{\boldsymbol{k}}_\mathrm{i})T^\dagger_{n''n}T_{nn'}b_{n'}(\hat{\boldsymbol{k}}_\mathrm{i}), \tag{3.10}$$

where $b_n(\hat{\boldsymbol{k}}_\mathrm{i}) = -\mathrm{j}4\pi\boldsymbol{a}_n(\hat{\boldsymbol{k}}_\mathrm{i}) \cdot \hat{\boldsymbol{p}}_\mathrm{e}$, and from the scattering cross section, σ_s, the total cross section of a scatterer is defined as

$$\sigma_\mathrm{t} = \sigma_\mathrm{s} + \sigma_\mathrm{a}, \tag{3.11}$$

where σ_a is the absorption cross section of the scatterer. In this work, we are especially interested in the monostatic scattering properties of the object under study. The scattering dyadic in the backscattering direction, $\hat{\boldsymbol{r}} = -\hat{\boldsymbol{k}}_\mathrm{i}$, is

$$\mathbf{S}(-\hat{\boldsymbol{k}}_\mathrm{i}, \hat{\boldsymbol{k}}_\mathrm{i}) = -\frac{4\pi}{\mathrm{j}k}\sum_{nn'} \boldsymbol{a}^*_n(\hat{\boldsymbol{k}}_\mathrm{i})T_{nn'}\boldsymbol{a}_{n'}(\hat{\boldsymbol{k}}_\mathrm{i}), \tag{3.12}$$

and the differential cross section is

$$\frac{\mathrm{d}\sigma}{\mathrm{d}\Omega}(-\hat{\boldsymbol{k}}_\mathrm{i}, \hat{\boldsymbol{k}}_\mathrm{i}) = \frac{64\pi^3}{k^2}\left|\sum_{nn'} \boldsymbol{a}_n(\hat{\boldsymbol{k}}_\mathrm{i})T_{nn'}\boldsymbol{a}_{n'}(\hat{\boldsymbol{k}}_\mathrm{i}) \cdot \hat{\boldsymbol{p}}_\mathrm{e}\right|^2. \tag{3.13}$$

For a spherical scatterer, the T-matrix is diagonal with respect to all indices $n = (\tau, \sigma, m, l)$, and (3.10) simplifies to

$$\sigma_\mathrm{s} = \frac{2\pi}{k^2}\sum_{l=1}^{\infty}(2l+1)(|t_{1l}|^2 + |t_{2l}|^2), \tag{3.14}$$

the scattered farfield $\boldsymbol{F}(\hat{\boldsymbol{r}})$ is in this case given by

$$\boldsymbol{F}(\hat{\boldsymbol{r}}) = \sum_{\tau=1}^{2}\sum_{n} \mathrm{j}^{\tau-l-1}f_{\tau n}\boldsymbol{A}_{\tau n}(\hat{\boldsymbol{r}}), \tag{3.15}$$

and the monostatic RCS of a spherical scatterer simplifies from (3.13) to

$$\frac{\mathrm{d}\sigma}{\mathrm{d}\Omega}(-\hat{\boldsymbol{k}}_\mathrm{i}, \hat{\boldsymbol{k}}_\mathrm{i}) = \frac{\pi}{k^2}\left|\sum_{l=1}^{\infty}(-1)^l(2l+1)(t_{1l} - t_{2l})\right|^2 \tag{3.16}$$

which is the main scattering quantity of interest in this work.

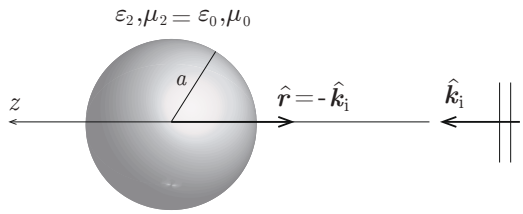

Figure 1: Electromagnetic scattering of a plane wave from a PEC sphere with radius a. In this work the main focus is on finding the monostatic scattering, which corresponds to $\hat{\boldsymbol{r}} = -\hat{\boldsymbol{k}}_\mathrm{i}$.

3.3 Scattering from a perfectly conducting sphere

The most simple case of Mie scattering is the scattering from a PEC sphere, see Figure 1. The total electric field outside of the scatterer is expanded in the regular and out-going spherical vector waves as in (2.8), where the coefficients of the incident plane wave $a_{\tau n}$ are known, see (3.5), and the coefficients of the scattered field $f_{\tau n}$ are unknown. This field representation is inserted into the boundary conditions in (3.1) where inside the conducting sphere the electric field is zero, resulting in the relations

$$\begin{cases} a_{1n} j_l(ka) + f_{1n} h_l^{(2)}(ka) = 0 \\ a_{2n} (kaj_l(ka))' + f_{1n} (kah_l^{(2)}(ka))' = 0, \end{cases} \tag{3.17}$$

where a is the radius of the scatterer. The expression (3.17) can be rewritten as

$$f_{\tau n} = t_{\tau l} a_{\tau n}, \qquad \tau = 1, 2 \tag{3.18}$$

which is a linear mapping between $a_{\tau n}$ and $f_{\tau n}$, where

$$t_{1l} = -\frac{j_l(ka)}{h_l^{(2)}(ka)}, \qquad t_{2l} = -\frac{(kaj_l(ka))'}{(kah_l^{(2)}(ka))'}. \tag{3.19}$$

From the T-matrix elements in (3.19) the scattered monostatic RCS is given by the expression in (3.16). The scattered electric field outside of the scatterer is given by

$$\boldsymbol{E}_\mathrm{s}(\boldsymbol{r}, \omega) = \sum_{\tau=1}^{2} \sum_{n} f_{\tau n} \boldsymbol{u}_{\tau n}(k\boldsymbol{r}). \tag{3.20}$$

3.4 Scattering from a dielectric sphere

The scattering from a dielectric sphere is calculated using the same approach as for the PEC sphere, the main difference being that in this case the continuity of

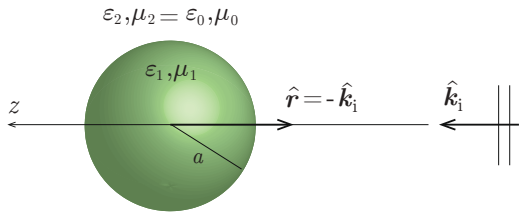

Figure 2: Electromagnetic scattering of a plane wave from a dielectric sphere with radius a.

both the electric and magnetic fields at the surface of the scatterer are utilized in the calculation of the scattered field coefficients, see Figure 2. As in Section 3.3, the incident field is given by

$$\boldsymbol{E}_\mathrm{i}(\boldsymbol{r},\omega)=\boldsymbol{E}_0\mathrm{e}^{-\mathrm{j}kz}=\sum_{\tau=1}^{2}\sum_{n}a_{\tau n}\boldsymbol{v}_{\tau n}(k\boldsymbol{r}), \tag{3.21}$$

where the coefficients $a_{\tau n}$ for a plane wave, incident in the z-direction, are given in (3.5) as

$$\begin{cases} a_{1n}=(-\mathrm{j})^l\sqrt{2\pi(2l+1)}\boldsymbol{E}_0\cdot(\delta_{\sigma\mathrm{o}}\hat{\boldsymbol{x}}-\delta_{\sigma\mathrm{e}}\hat{\boldsymbol{y}}) \\ a_{2n}=-(-\mathrm{j})^{l+1}\sqrt{2\pi(2l+1)}\boldsymbol{E}_0\cdot(\delta_{\sigma\mathrm{e}}\hat{\boldsymbol{x}}+\delta_{\sigma\mathrm{o}}\hat{\boldsymbol{y}}) \\ a_{3n}=0. \end{cases}$$

The unknown scattered field is given by

$$\boldsymbol{E}_\mathrm{s}(\boldsymbol{r},\omega)=\sum_{\tau=1}^{2}\sum_{n}f_{\tau n}\boldsymbol{u}_{\tau n}(k\boldsymbol{r}),\qquad r>a, \tag{3.22}$$

and the total fields outside the scatterer are

$$\begin{cases} \boldsymbol{E}(\boldsymbol{r},\omega)=\displaystyle\sum_{\tau=1}^{2}\sum_{n}(a_{\tau n}\boldsymbol{v}_{\tau n}(k\boldsymbol{r})+f_{\tau n}\boldsymbol{u}_{\tau n}(k\boldsymbol{r})) \\ \boldsymbol{H}(\boldsymbol{r},\omega)=\dfrac{\mathrm{j}}{\eta_0\eta}\displaystyle\sum_{\tau=1}^{2}\sum_{n}(a_{\tau n}\boldsymbol{v}_{\bar{\tau}n}(k\boldsymbol{r})+f_{\tau n}\boldsymbol{u}_{\bar{\tau}n}(k\boldsymbol{r})) \end{cases} \tag{3.23}$$

while the total fields inside the scatterer, which we denote $\boldsymbol{E}_1$ and $\boldsymbol{H}_1$, are

$$\begin{cases} \boldsymbol{E}_1(\boldsymbol{r},\omega)=\displaystyle\sum_{\tau=1}^{2}\sum_{n}\alpha_{\tau n}\boldsymbol{v}_{\tau n}(k_1\boldsymbol{r}) \\ \boldsymbol{H}_1(\boldsymbol{r},\omega)=\dfrac{\mathrm{j}}{\eta_0\eta_1}\displaystyle\sum_{\tau=1}^{2}\sum_{n}\alpha_{\tau n}\boldsymbol{v}_{\bar{\tau}n}(k_1\boldsymbol{r}). \end{cases} \tag{3.24}$$

The boundary conditions at the surface of the sphere are

$$\begin{cases} \hat{\boldsymbol{r}} \times \boldsymbol{E}_1(\boldsymbol{r},\omega)|_{r=a} = \hat{\boldsymbol{r}} \times \boldsymbol{E}_2(\boldsymbol{r},\omega)|_{r=a} \\ \hat{\boldsymbol{r}} \times \boldsymbol{H}_1(\boldsymbol{r},\omega)|_{r=a} = \hat{\boldsymbol{r}} \times \boldsymbol{H}_2(\boldsymbol{r},\omega)|_{r=a} \end{cases} \tag{3.25}$$

which result in the system of equations

$$\begin{cases} \alpha_{1n} j_l(k_1 a) = a_{1n} j_l(ka) + f_{1n} h_l^{(2)}(ka) \\ \alpha_{2n} \dfrac{(k_1 a j_l(k_1 a))'}{k_1 a} = a_{2n} \dfrac{(k a j_l(ka))'}{ka} + f_{2n} \dfrac{(k a h_l^{(2)}(ka))'}{ka} \\ \dfrac{1}{\eta_1} \alpha_{1n} \dfrac{(k_1 a j_l(k_1 a))'}{k_1 a} = \dfrac{1}{\eta} \left(a_{1n} \dfrac{(k a j_l(ka))'}{ka} + f_{1n} \dfrac{(k a h_l^{(2)}(ka))'}{ka} \right) \\ \dfrac{1}{\eta_1} \alpha_{2n} j_l(k_1 a) = \dfrac{1}{\eta} \big(a_{2n} j_l(k_1 a) + f_{2n} h_l^{(2)}(ka) \big). \end{cases} \tag{3.26}$$

The expression (3.26) can be written as a T-matrix relation

$$f_{\tau l} = t_{\tau l} a_{\tau n} = \begin{pmatrix} t_{1l} & 0 \\ 0 & t_{2l} \end{pmatrix} \begin{pmatrix} a_{1n} \\ a_{2n} \end{pmatrix}. \tag{3.27}$$

If the terms in (3.26) are rearranged, and the coefficients $\alpha_{\tau n}$ are eliminated, the final expression of the T-matrix elements is

$$t_{\tau l} = \frac{j_l(ka)(k_1 a j_l(k_1 a))' - \gamma_\tau j_l(ka)(k a j_l(ka))'}{h_l^{(2)}(ka)(k_1 a j_l(k_1 a))' - \gamma_\tau j_l(k_1 a)(k a j_l(ka))'}, \tag{3.28}$$

where $\gamma_\tau = \delta_{\tau 1}(\mu_1/\mu) + \delta_{\tau 2}(\epsilon_1/\epsilon)$, and where ϵ_1, ϵ, μ_1, μ are the relative permittivity and permeability of the scatterer and the surrounding medium, respectively. The result (3.28) implies that the scattered field looks as if it comes from an electric multipole ($\tau = 1$), and a magnetic multipole ($\tau = 2$).

3.5 Scattering from layered spheres with resistive sheets

We are now ready to treat the more general scattering case of multilayered spheres with resistive sheets at the interfaces, such as the structure in Figure 3. Let $r_1 \le r_2 \le ... \le r_N$ be the radii of the N layers of the sphere, and let ϵ_i and μ_i, $i = 1, 2, ..., N$ be the (relative) permittivity and permeability, respectively, of the layers. The outmost radius is r_N, and outside this sphere we have free space, *i.e.* $\epsilon_{N+1} = \epsilon_0$ and $\mu_{N+1} = \mu_0$. The total fields in each region are given by

$$\begin{cases} \boldsymbol{E}^{(i)}(\boldsymbol{r},\omega) = \displaystyle\sum_{\tau=1}^{2} \sum_n A_{\tau n}^{(i)} (\boldsymbol{v}_{\tau n}(k_i \boldsymbol{r}) + t_{\tau n}^{(i-1)} \boldsymbol{u}_{\tau n}(k_i \boldsymbol{r})) \\ \boldsymbol{H}^{(i)}(\boldsymbol{r},\omega) = \dfrac{\mathrm{j}}{\eta_0 \eta_i} \displaystyle\sum_{\tau=1}^{2} \sum_n A_{\tau n}^{(i)} (\boldsymbol{v}_{\bar{\tau} n}(k_i \boldsymbol{r}) + t_{\tau n}^{(i-1)} \boldsymbol{u}_{\bar{\tau} n}(k_i \boldsymbol{r})) \end{cases} \quad r_{i-1} < r < r_i, \tag{3.29}$$

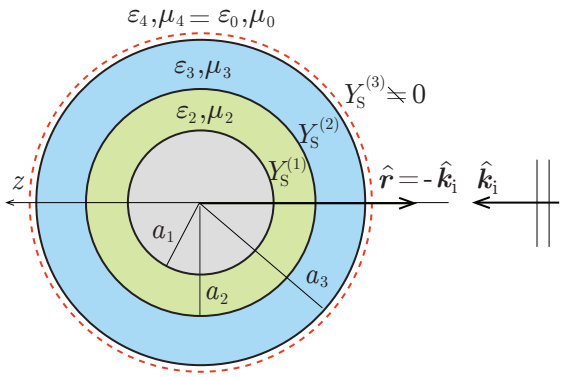

Figure 3: Electromagnetic scattering from a layered sphere with a PEC core and possibly with admittance sheets at the interfaces. In this example, a PEC sphere with radius a_1 is coated with two dielectric/magnetic layers with thicknesses $a_2 - a_1$, $a_3 - a_2$, and an infinitely thin admittance sheet $Y_S^{(3)}$ is located at the outer boundary.

where $i = 1, 2, ..., N+1$ correspond to each region in space, N is the number of layers of the scatterer, $k_i = k_0\sqrt{\epsilon_i\mu_i}$, $\eta_i = \sqrt{\mu_i/\epsilon_i}$, $\eta_{N+1} = \sqrt{\mu_0/\epsilon_0}$, and $t_{\tau l}^{(i)}$ are the unknowns. We define $t_{\tau l}^{(0)} = 0$ since $\boldsymbol{E}^{(0)}(\boldsymbol{r},\omega)$ is non-singular at $r_0 = 0$. The boundary conditions at the interfaces are in this case

$$\begin{cases} \hat{\boldsymbol{n}} \times \boldsymbol{E}^{(i)}(\boldsymbol{r},\omega)|_{r=a_i} = \hat{\boldsymbol{n}} \times \boldsymbol{E}^{(i+1)}(\boldsymbol{r},\omega)|_{r=a_i} \\ \hat{\boldsymbol{n}} \times \boldsymbol{H}^{(i)}(\boldsymbol{r},\omega)|_{r=a_i} - \hat{\boldsymbol{n}} \times \boldsymbol{H}^{(i+1)}(\boldsymbol{r},\omega)|_{r=a_i} = \boldsymbol{J}_s^{(i)}(\boldsymbol{r},\omega)|_{r=a_i}, \end{cases} \tag{3.30}$$

where $\boldsymbol{J}_s^{(i)} = Y_S^{(i)}\hat{\boldsymbol{n}} \times (\boldsymbol{E}^{(i)} \times \hat{\boldsymbol{n}})|_{r=a_i} = Y_S^{(i)}\hat{\boldsymbol{n}} \times (\boldsymbol{E}^{(i+1)} \times \hat{\boldsymbol{n}})|_{r=a_i}$. In the same manner as in Section 3.4, the boundary conditions (3.30) result in a system of equations for each interface of the layered sphere. The solution to this system is found by first finding the T-matrix elements of the innermost interface, and then iterating through each interface of the layered sphere. This results in a recursion relation of the T-matrix elements, see Appendix A for a detailed derivation, in form of a Möbius transform

$$t_{\tau l}^{(i)} = -\frac{a_\tau^{(i)} t_{\tau l}^{(i-1)} + b_\tau^{(i)}}{c_\tau^{(i)} t_{\tau l}^{(i-1)} + d_\tau^{(i)}}. \tag{3.31}$$

To simplify the expressions of the coefficients in (3.31), we introduce the Riccati-Bessel functions and their derivatives [1, 18]

$$\begin{aligned} \psi_l(z) &= z j_l(z), & \xi_l(z) &= z h_l^{(2)}(z), \\ \psi_l'(z) &= j_l(z) + z j_l'(z), & \xi_l'(z) &= h_l^{(2)}(z) + z h_l'^{(2)}(z). \end{aligned} \tag{3.32}$$

For $\tau = 1$ the coefficients are

$$\begin{cases} a_1^{(i)} = \dfrac{\eta_i}{\eta_{i+1}}\xi_l(k_i r_i)\psi_l'(k_{i+1}r_i) - \xi_l'(k_i r_i)\psi_l(k_{i+1}r_i) - \mathrm{j}\eta_i Y_{\mathrm{S}}^{(i)}\xi_l(k_i r_i)\psi_l(k_{i+1}r_i) \\ b_1^{(i)} = \dfrac{\eta_i}{\eta_{i+1}}\psi_l(k_i r_i)\psi_l'(k_{i+1}r_i) - \psi_l'(k_i r_i)\psi_l(k_{i+1}r_i) - \mathrm{j}\eta_i Y_{\mathrm{S}}^{(i)}\psi_l(k_i r_i)\psi_l(k_{i+1}r_i) \\ c_1^{(i)} = \dfrac{\eta_i}{\eta_{i+1}}\xi_l(k_i r_i)\xi_l'(k_{i+1}r_i) - \xi_l'(k_i r_i)\xi_l(k_{i+1}r_i) - \mathrm{j}\eta_i Y_{\mathrm{S}}^{(i)}\xi_l(k_i r_i)\xi_l(k_{i+1}r_i) \\ d_1^{(i)} = \dfrac{\eta_i}{\eta_{i+1}}\psi_l(k_i r_i)\xi_l'(k_{i+1}r_i) - \psi_l'(k_i r_i)\xi_l(k_{i+1}r_i) - \mathrm{j}\eta_i Y_{\mathrm{S}}^{(i)}\psi_l(k_i r_i)\xi_l(k_{i+1}r_i), \end{cases} \tag{3.33}$$

and for $\tau = 2$ the coefficients are

$$\begin{cases} a_2^{(i)} = \dfrac{\eta_{i+1}}{\eta_i}\xi_l(k_i r_i)\psi_l'(k_{i+1}r_i) - \xi_l'(k_i r_i)\psi_l(k_{i+1}r_i) - \mathrm{j}\eta_{i+1} Y_{\mathrm{S}}^{(i)}\xi_l'(k_i r_i)\psi_l'(k_{i+1}r_i) \\ b_2^{(i)} = \dfrac{\eta_{i+1}}{\eta_i}\psi_l(k_i r_i)\psi_l'(k_{i+1}r_i) - \psi_l'(k_i r_i)\psi_l(k_{i+1}r_i) - \mathrm{j}\eta_{i+1} Y_{\mathrm{S}}^{(i)}\psi_l'(k_i r_i)\psi_l'(k_{i+1}r_i) \\ c_2^{(i)} = \dfrac{\eta_{i+1}}{\eta_i}\xi_l(k_i r_i)\xi_l'(k_{i+1}r_i) - \xi_l'(k_i r_i)\xi_l(k_{i+1}r_i) - \mathrm{j}\eta_{i+1} Y_{\mathrm{S}}^{(i)}\xi_l'(k_i r_i)\xi_l'(k_{i+1}r_i) \\ d_2^{(i)} = \dfrac{\eta_{i+1}}{\eta_i}\psi_l(k_i r_i)\xi_l'(k_{i+1}r_i) - \psi_l'(k_i r_i)\xi_l(k_{i+1}r_i) - \mathrm{j}\eta_{i+1} Y_{\mathrm{S}}^{(i)}\psi_l'(k_i r_i)\xi_l'(k_{i+1}r_i). \end{cases} \tag{3.34}$$

It can be seen that the expressions in (3.33)–(3.34) reduce to the same recursive relations presented in [13, Ch. 8] if no surface currents are present at the interfaces. If a general homogeneous material is located at the center of the scatterer, the iteration starts by $i = 1$. However, if the innermost layer is a PEC then the iteration starts at $i = 2$, and it is initialized by

$$t_{1l}^{(1)} = \frac{\psi_l(k_2 r_1)}{\xi_l(k_2 r_1)}, \qquad t_{2l}^{(1)} = \frac{\psi_l'(k_2 r_1)}{\xi_l'(k_2 r_1)}. \tag{3.35}$$

4 Numerical implementation

4.1 Python code

The theory described in Sections 2–3 was implemented in Python as a function that calculates the scattered fields of a multilayer sphere with N layers of dielectric/magnetic materials, possibly with resistive sheets at the interfaces. The input parameters to the code are:

$$\texttt{material} = [[\epsilon_1, \mu_1], [\epsilon_2, \mu_2], ..., [\epsilon_{N+1}, \mu_{N+1}]], \qquad \texttt{d} = [d_1, d_2, ..., d_{N+1}],$$
$$\texttt{adm} = [Y_{\mathrm{S}1}, Y_{\mathrm{S}2}, ..., Y_{\mathrm{S}N+1}], \qquad \texttt{f} = \mathrm{linspace}(f_1, f_2, N_{\mathrm{f}}),$$

where `material` is an array consisting of $N + 1$ vectors containing the material parameters of the layered sphere, the material parameters of the medium at the center (which in this work is replaced by PEC boundary conditions) are $[\epsilon_1, \mu_1]$,

and $[\epsilon_{N+1}, \mu_{N+1}]$ are the material parameters of the surrounding medium. The thickness of each layer is defined by the vector `d` and the surface admittance at each interface is given by the vector `adm`. The code was also specifically modified to treat dispersive materials and reactive surfaces, such as capacitive and/or inductive sheets, using extended input arguments for each frequency:

$$\texttt{Material} = [\texttt{material}(f_1), \texttt{material}(f_2), ..., \texttt{material}(f_{N_f})],$$
$$\texttt{Adm} = [\texttt{adm}(f_1), \texttt{adm}(f_2), ..., \texttt{adm}(f_{N_f})],$$

where the parameters `adm` and `material` are defined as in the previous, non-dispersive case.

The numerical implementation is organized as follows: the spherical Bessel and Hankel functions are imported from standard packages in Python. The `mathcal` package is used for higher accuracy (float precision of the special functions). A function called `Mobius`() is defined that takes the input parameters listed above, uses the expressions (3.31)–(3.34) to iterate through the T-matrix coefficients from the center layer outwards one layer at a time, and returns the T-matrix coefficients of the outermost layer of the scatterer. When these T-matrix coefficients have been extracted, all scattering information of the layered sphere can be calculated from the relations presented in Section 3.2, such as the scattering cross section, the extinction cross section and the monostatic cross section.

The numerical implementation was verified through a number of benchmarking simulations in Comsol Multiphysics, Computer Simulation Technology Microwave Studio (CST MWS), and FEKO. The results, presented in Appendix B, indicate good agreement between the code and the full wave simulation software. It was concluded that the finite element solver of Comsol Multiphysics and the finite integration technique solver in CST MWS are not well suited for scattering simulations of object larger than a few wavelengths in size due to high memory requirements. Due to the aforementioned reasons, out of the three software FEKO seems to be the best suited for RCS simulations of three dimensional structures larger than a few wavelengths in size, with lossy dielectric/magnetic materials and resistive sheets. Although, all numerical software used for benchmarking displayed a significant increase in memory and computation time requirements in comparison to the analytic in-house simulation code.

Emphasis is put on the truncation of the l-index in the numerical implementation. An expression for this truncation was presented by Wiscombe in [31] to achieve convergence on the order of 10^{-14} for the sum of the squared Mie scattering coefficients. It states that

$$l_{\max} = \begin{cases} x + 4x^{1/3} + 1, & 0.02 \leq x \leq 8, \\ x + 4.05x^{1/3} + 2, & 8 < x < 4200, \\ x + 4x^{1/3} + 2, & 4200 < x < 20000, \end{cases} \tag{4.1}$$

where $x = ka$ is the electric size of the scatterer. This truncation relation has been used for all scatterers under study in this work.

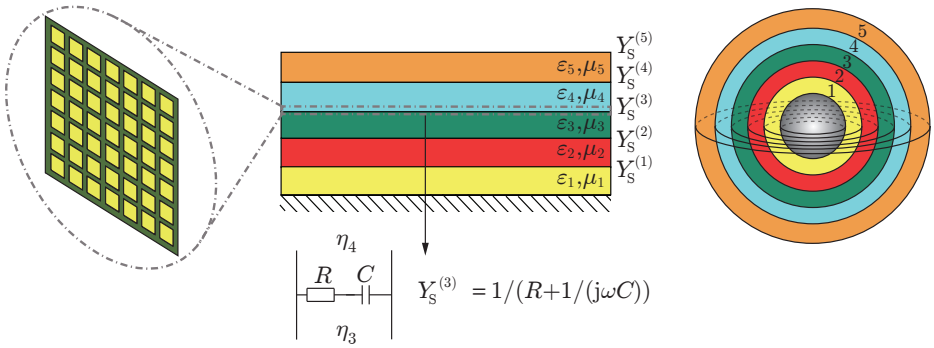

Figure 4: A planar multilayer absorber above a ground plane, consisting of different materials in the layers and possibly with admittance sheets $Y_S^{(i)}$ at the interfaces is presented in the middle. An example of a surface admittance consisting of a lattice of resistive patches is presented to the left, and to the right a multilayer sphere corresponding to the planar structure is presented.

5 Absorbers on doubly curved surfaces

5.1 RCS simulations and normalizations

The expressions (3.31)–(3.34) are used specifically to evaluate the monostatic RCS from a PEC sphere coated with different types of electromagnetic absorbers, as in Figure 4. The absorbers under study consist of multiple layers of homogeneous, isotropic, dielectric and/or magnetic materials with or without losses and dispersion. Resistive sheets and frequency selective structures at the interfaces are treated, using equivalent circuit parameters, as a surface admittance, which can also be frequency dependent, see Figure 4. Three different simulations were carried out for each absorber scenario:

1. scattering from a PEC sphere,
2. scattering from a PEC sphere coated with an absorber,
3. scattering from a PEC sphere enclosing the coated structure,

see Figure 5. The two PEC simulations were then used to normalize the absorber RCS, and then make a comparison between the performance of the curved absorber and a corresponding planar design.

5.2 Salisbury screen

The first absorber under test is a classical Salisbury screen [22] consisting of a resistive sheet placed quarter of a wavelength, at the design frequency, from a

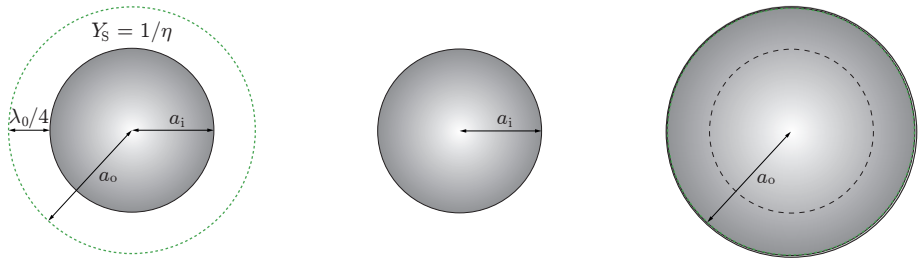

Figure 5: A PEC sphere with a coating Salisbury screen matched to the free space impedance (left), and the two normalization cases: A PEC sphere with the center radius a_i (center), an enclosing PEC sphere with the outer radius a_o (right).

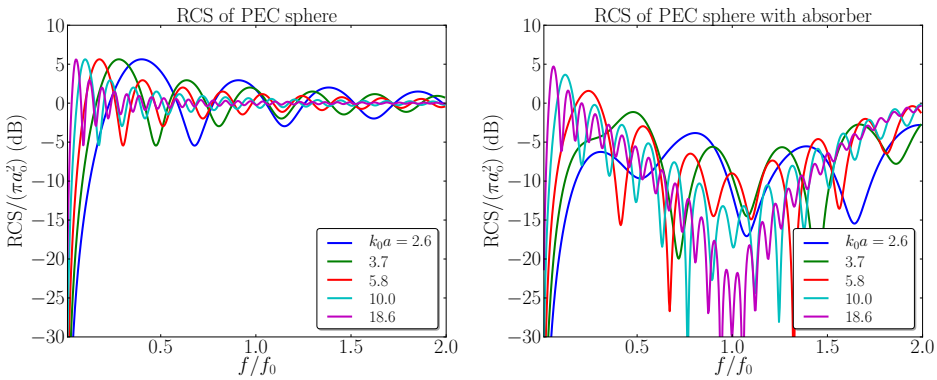

Figure 6: Monostatic RCS from a PEC sphere with a Salisbury screen (right) and the monostatic RCS from a PEC sphere (left).

ground plane. For the best possible performance the impedance of the resistive sheet should be matched to the free space impedance, *i.e.* $Y_S = 1/\eta$, where $\eta = 377\ \Omega$. The three scenarios that are evaluated are presented in Figure 5, namely a PEC sphere coated with a resistive sheet, the same sphere without the absorber, and a PEC sphere enclosing the inner sphere and the absorber.

The monostatic RCS of a PEC sphere with radius a_o is presented to the left in Figure 6, and the monostatic RCS of a PEC sphere with radius a_i with a Salisbury screen is presented to the right in Figure 6, where all results are normalized with the cross section area of the scatterer. The radius of the PEC core was varied, both in the scenario with and without the Salisbury screen, corresponding to the different curves in Figure 6. It can be seen that the normalized monostatic RCS of a PEC sphere goes to 0 dB for higher frequencies, which is a familiar result. When comparing the two graphs in Figure 6 it can be seen that the Salisbury absorber reduces the RCS of the PEC sphere. However, in order to

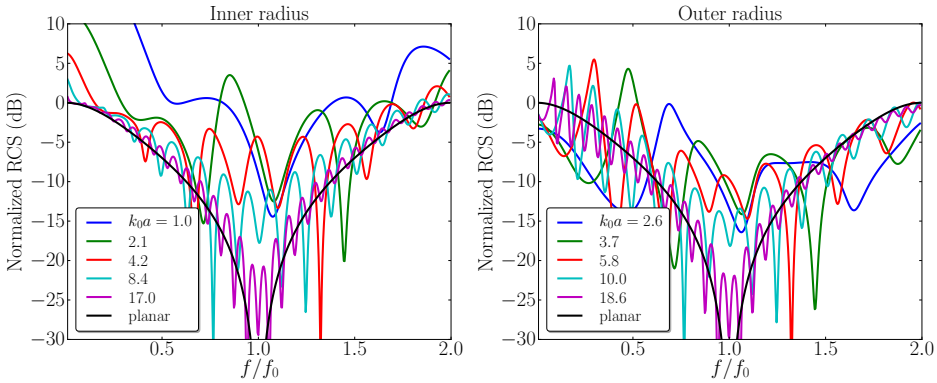

Figure 7: Monostatic RCS from a PEC sphere with a Salisbury screen, to the left normalized with the RCS of the inner PEC scatterer, and to the right normalized with the RCS of an enclosing PEC scatterer.

properly evaluate the performance of the spherical absorber, the RCS from the PEC sphere with a coating absorber is henceforth normalized according to the theory presented in Section 5.1.

Normalized scattering data of the spherical Salisbury screen are presented in Figure 7, where the left plot is normalized with the RCS of the uncoated PEC scatterer, and the right plot is normalized with the RCS of an enclosing PEC. The colored curves correspond to different radii of the uncoated PEC scatterer, where in the plots labeled "inner radius" $k_0a = 2\pi(a_\mathrm{i}/\lambda_0)$ indicate the size of the uncoated structure with respect to the center wavelength of the absorber, and in the plots labeled "outer radius" $k_0a = 2\pi(a_\mathrm{o}/\lambda_0)$ indicate the size of the enclosing structure. This implies that all pairs of graphs of RCS data presented, using the two different normalizations, have been evaluated using the same size of scatterers corresponding to each color of the curves in the two graphs. In Figure 7 it can be seen that the absorber performance converges towards the planar result, indicated by the black curve, for large enough scatterers ($k_0a \approx 17$). There is no significant difference between the results with the two different normalizations in Figure 7.

5.3 Jaumann absorber

The next absorber under study is a multilayered version of the salisbury screen, commonly referred to as a Jaumann absorber, see Figure 8. The specific design of the implemented absorber was presented in [11], where the performance degradation of Jaumann absorbers when applied to a cylinder is studied. This structure consists of five layers of resistive sheets with successively increasing admittance, seen from the incident wave, $Y_\mathrm{S}^{(5)} = 1/1885$, $Y_\mathrm{S}^{(4)} = 1/1205$, $Y_\mathrm{S}^{(3)} = 1/679$, $Y_\mathrm{S}^{(2)} = 1/302.1$, $Y_\mathrm{S}^{(1)} = 1/71.40$ [Ω^{-1}], with the distance $d = \lambda_0/4$ between the

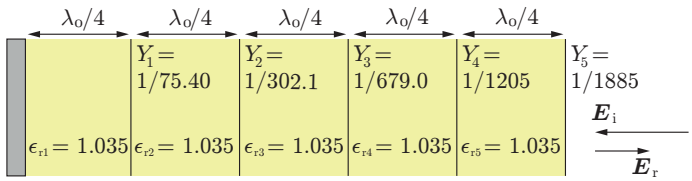

Figure 8: Jaumann absorber consisting of five resistive sheets with tuned impedances.

sheets, and a spacer material with relative permittivity $\epsilon_r = 1.035$.

The results in Figure 9 indicate that the performance of this type of absorber also converges towards the planar curve, but at a slower rate than the single layer Salisbury screen. Also, the results for large scatterers seem to oscillate with the mean value given by the planar curve. This is most likely due to a surface wave at the center of the structure. A significant difference can be noticed between the results being normalized with respect to the inner, uncoated, scatterer, and the data that is normalized with respect to an enclosing PEC sphere. The curves in Figure 9 indicate that, for thick absorbing structures, the normalization with respect to the enclosing PEC structure might overestimate the performance of the absorber.

5.4 Capacitive Salisbury screen

For practical reasons it is commonly desirable to design absorbers with as small thickness as possible, while not significantly reducing the bandwidth of the absorber. In [20] it is shown that the maximum bandwidth B of an absorber backed by a PEC ground plane is bounded by the thickness of the structure d, where a thinner absorber implies lower maximum bandwidth. One way to achieve B/d close to this physical limit is to add capacitive sheets to the absorber. In [10] a thin, ultra-wideband absorber based on multiple capacitive resistive sheets was presented which achieves a significant increase B/d in comparison to a traditional multilayer Jaumann absorber.

To investigate this effect, a Salisbury screen is modified to achieve similar performance from a thinner structure. In practice, this corresponds to constructing a thin sheet with a lattice of resistive patches, equivalent to a shunt resistance and capacitance in series as in Figure 4. The capacitance and conductance of this structure are given by

$$\alpha = \tan(k_0 d), \qquad C = \frac{1}{\eta\omega_0}\left(\alpha + \frac{1}{\alpha}\right), \qquad G = \frac{1}{\eta}\left(1 + \frac{1}{\alpha^2}\right), \tag{5.1}$$

where ω_0 is the frequency of maximum absorption. The parameter α can be varied to control the response from the structure, as can be seen in Figure 10. As α decreases, the resonance of the absorber is shifted down in frequency, which

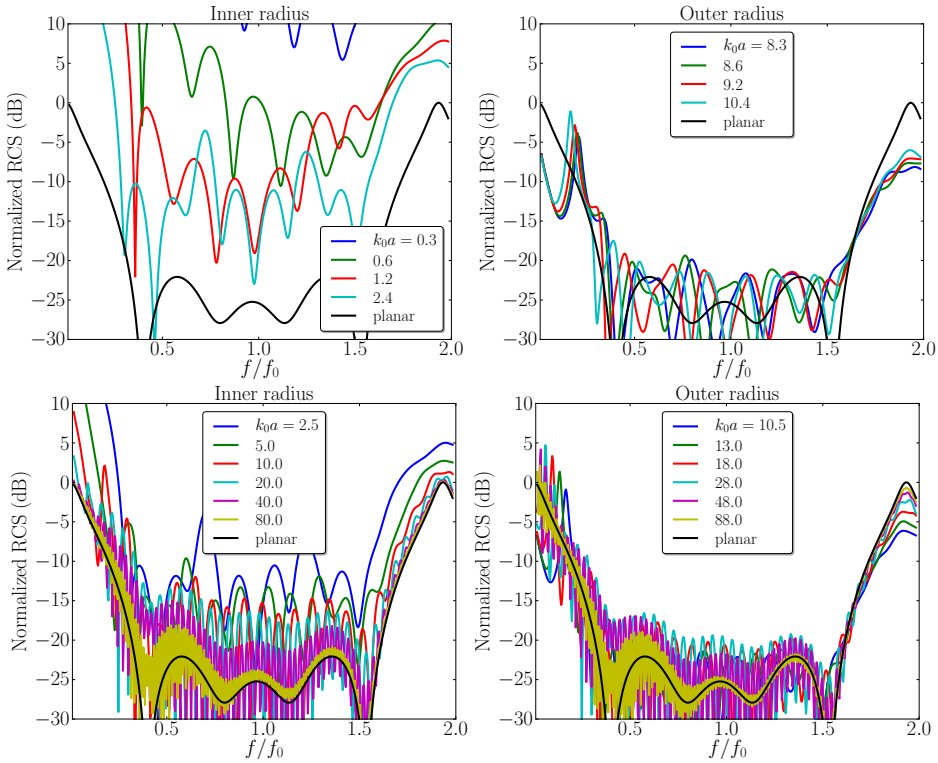

Figure 9: Monostatic RCS from a PEC sphere with a Jaumann absorber. The plots to the left are normalized with the RCS of the inner PEC scatterer, and the plots to the right are normalized with the RCS of an enclosing PEC scatterer. The upper plots show smaller radii of curvature and the lower plots show larger radii of curvature.

corresponds to achieving similar performance as in the case of a regular Salisbury screen, but for a thinner absorber. As α decreases the bandwidth is slightly decreased. The curves in Figure 10 converge toward the planar case at approximately the same rate as the Salisbury screen in Figure 7, and there is no significant difference between the two normalizations. This indicates that both the original and the capacitively loaded Salisbury screen show a similar response with respect to curvature.

5.5 Circuit analog absorber

A simple case of a circuit analog absorber presented in [25] consists of a shunt series resistance, capacitance, and inductance, which could be realized as a periodic lattice of resistive patches. In this particular design, the circuit parameters

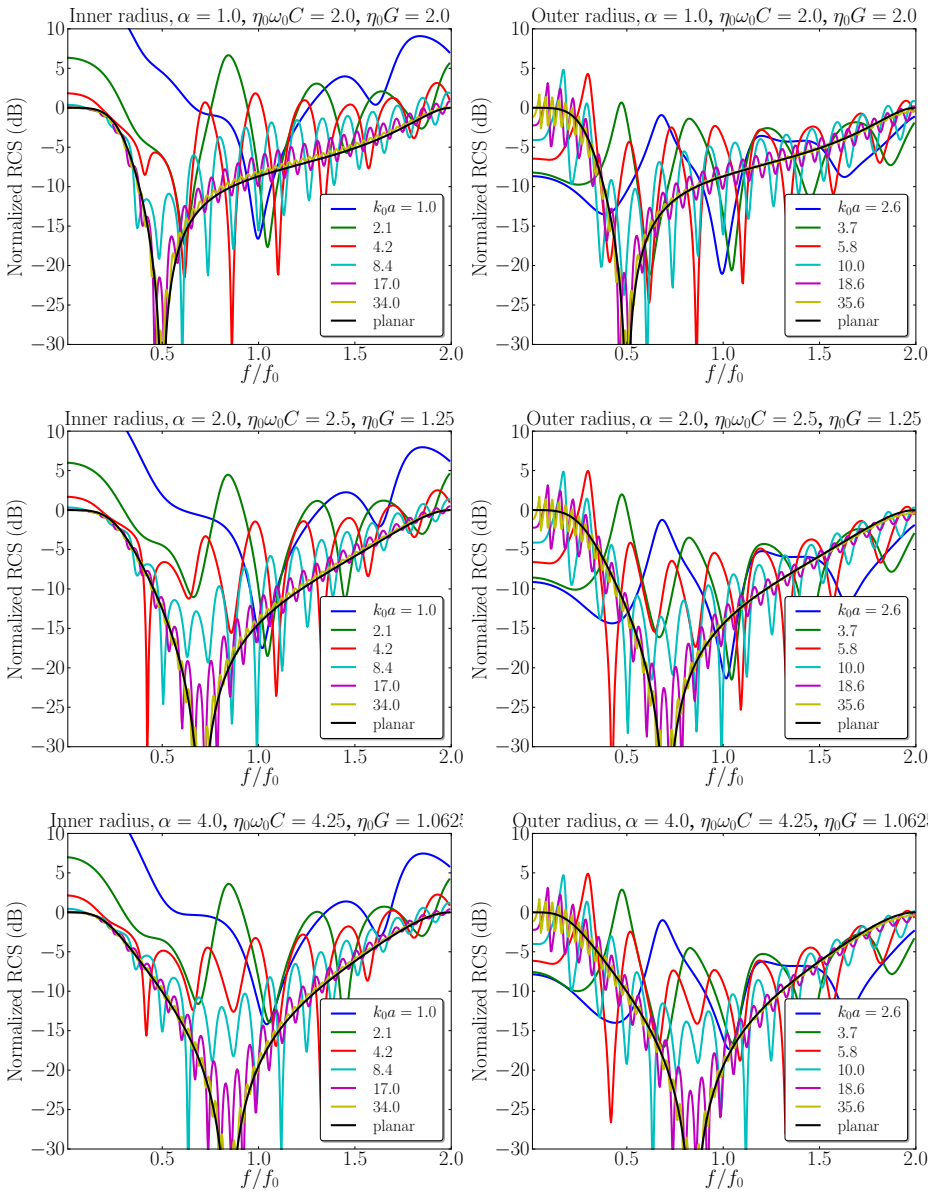

Figure 10: Monostatic RCS from a PEC sphere with a capacitive Salisbury screen, to the left normalized with the RCS of the inner PEC scatterer, and to the right normalized with the RCS of an enclosing PEC scatterer.

are $R = 308\,\Omega$, $X = 30.8\,\text{fF}$, and $L = 3.16\,\text{nH}$, and the resistive sheet is placed a distance $\lambda_0/4$ from the ground plane, see [25] for further details on the specific

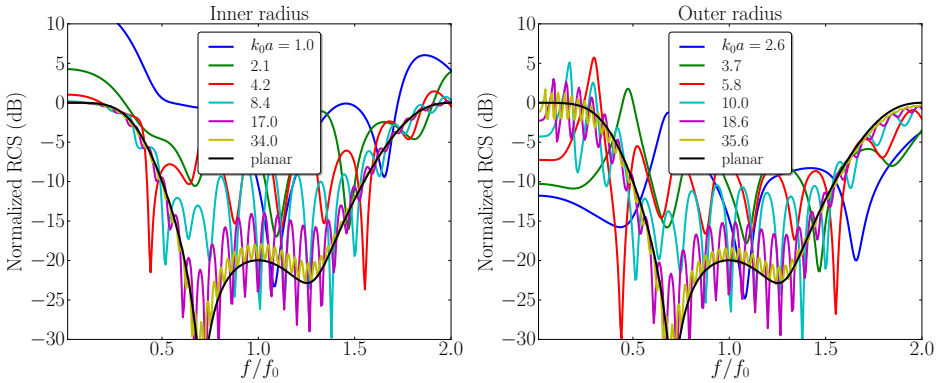

Figure 11: Monostatic RCS from a PEC sphere with a CAA screen from [25], to the left normalized with the RCS of the inner PEC scatterer, and to the right normalized with the RCS of an enclosing PEC scatterer.

absorber geometry and how to extract the circuit parameters from unit cell simulations. The results presented in Figure 11 indicate, compared to Figure 10, that the bandwidth is significantly improved by adding an inductive element L to the structure. However, this type of absorber might be quite difficult to manufacture in such a manner that the resistivity and reactance of the resistive sheet have the desired values.

5.6 Salisbury screen with a skin

In [6] it was shown that if a dielectric skin of a high dielectric constant is added outside of a Salisbury screen a double resonance occurs and the bandwidth of the absorber is improved. A planar absorber was designed in [6] according to the parameters in Figure 12, where a resistive sheet with $R = 225\ \Omega$ is placed a distance $d_1 = 6.8\,\text{mm}$ above a ground plane, and a dielectric skin of thickness 1 mm, and relative permittivity $\epsilon_\text{r} = 4$, is located a distance $d_2 = 2.3\,\text{mm}$ from the resistive sheet. The total thickness of the absorber is 10.1 mm, which at the center frequency 7.42 GHz corresponds to approximately $\lambda_0/4$.

This absorber design, henceforth referred to as a Chambers-Tennant absorber, was implemented as a coating for a spherical scatterer, and the results in Figure 13 indicate that, in conjecture to the previous absorber designs under study, the performance of the absorber does not converge towards that of the corresponding planar design for large scatterers. However, if losses are added to the spacer material the results in Figure 14 are achieved, where it can be seen that the results now converge better toward the planar curve. This is an indication of energy being stored in the spacer region as the structure acts as a spherical cavity, that resonates for the polarization component normal to the inner sphere surface.

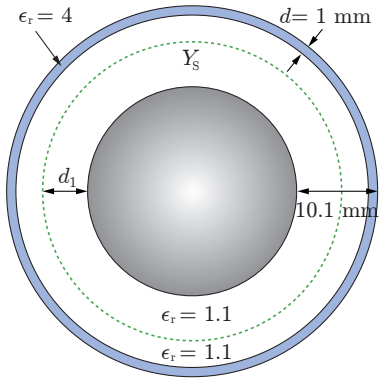

Figure 12: A PEC sphere coated with a resistive sheet and a dielectric skin commonly referred to as a Chambers-Tennant absorber.

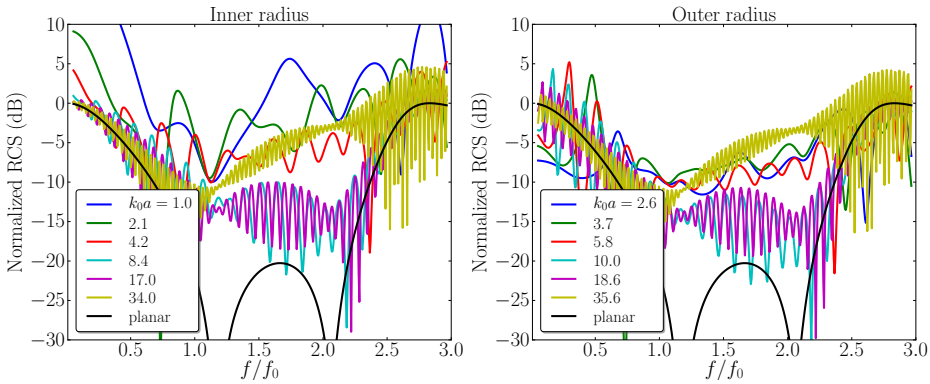

Figure 13: Monostatic RCS from a PEC sphere with a resistive sheet and a dielectric skin, to the left normalized with the RCS of the inner PEC scatterer, and to the right normalized with the RCS of an enclosing PEC scatterer.

5.7 Conductive volume absorber

In order to extent the study to absorbers based on bulk material losses, the resistive sheet and the spacer material inside the skin in Section 5.6 are replaced by a conducting bulk material with a relative permittivity on the form

$$\epsilon_r(\omega) = \epsilon_r' - j\epsilon_r''(\omega), \qquad \epsilon_r' = A, \qquad \epsilon_r''(\omega) = B\frac{\omega_0}{\omega}. \tag{5.2}$$

The material parameters were chosen to be $A = 1.1$, $B = 2.39$ after a quick run in a simple optimization of the material parameters. The reflection coefficient was optimized of a planar absorber with respect to the threshold level -20 dB. This absorber was implemented in a spherical scenario as in see Figure 15 where

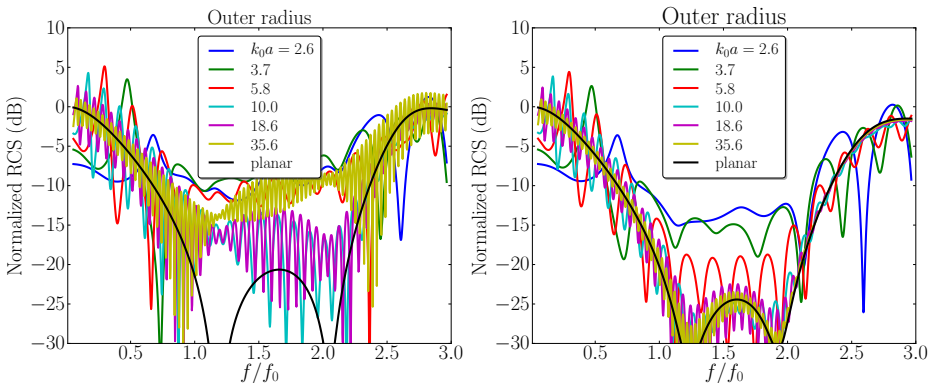

Figure 14: Monostatic RCS from a PEC sphere with a resistive sheet and a dielectric skin, where losses has been added to the spacer material, $\epsilon_{\mathrm{r}} = 1.1 - \mathrm{j}0.01$ (left) and $\epsilon_{\mathrm{r}} = 1.1 - \mathrm{j}0.1$ (right).

the simulated geometry and the material parameters are presented. This type of volume (or bulk) absorber is seen in Figure 16 to perform very well when applied to a curved scatterer. This is an indication of the fact that the planar performance of this absorber can be used to anticipate the response from applying the absorber to a curved structure.

5.8 Debye volume absorber

Now, we consider the geometry in Figure 17, which is the same setup as in the previous design, but with a Debye bulk material with a relative permittivity on the form

$$\epsilon_{\mathrm{r}}(\omega) = \epsilon'_{\mathrm{r}}(\omega) - \mathrm{j}\epsilon''_{\mathrm{r}}(\omega) = A + \frac{B}{\mathrm{j}\omega/\omega_0 + C}, \tag{5.3}$$

where $A = 1$, $B = 2.39$, and $C = 0.13$ after performing the same type of optimization as in Section 5.7. The results in Figure 18 are very similar to those of the conductive bulk absorber in Figure 16, even though the material parameters in Figure 15 and Figure 17 can be seen to differ. The result curves in Figure 18 show a very good agreement to the planar design, even for relatively small spherical scatterers, where $k_0a \approx 5$.

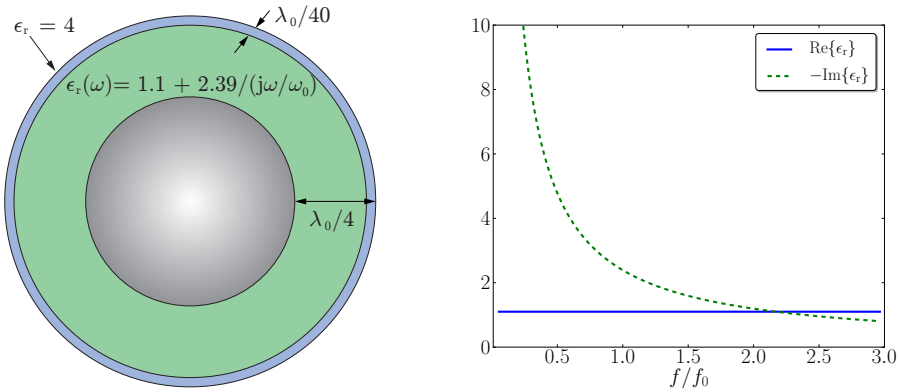

Figure 15: A PEC sphere coated with a volume absorber with a conducting bulk material and a skin (left) and the material parameters of the bulk material (right).

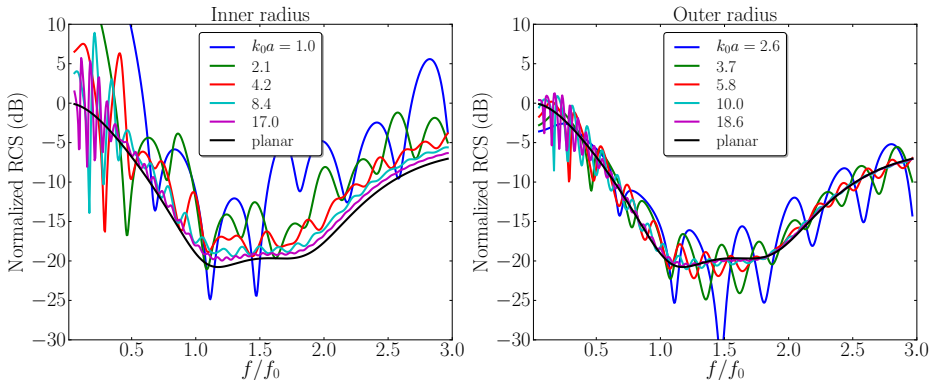

Figure 16: Monostatic RCS from a PEC sphere coated with a bulk absorber of a conducting material and a dielectric coating. To the left normalized with the RCS of the inner PEC scatterer, and to the right normalized with the RCS of an enclosing PEC scatterer.

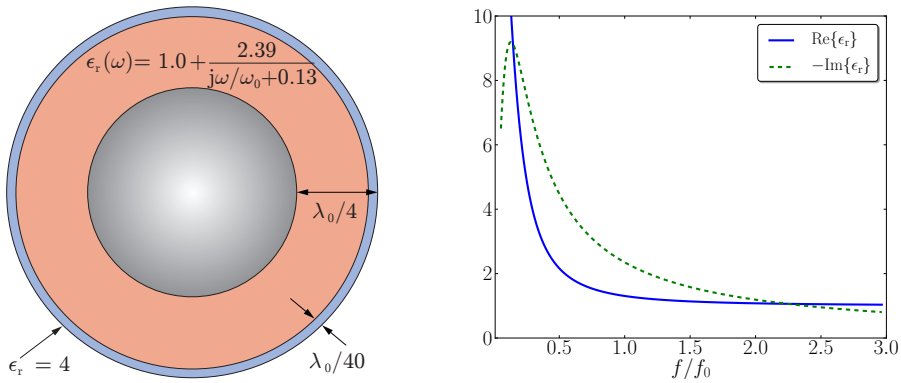

Figure 17: A PEC sphere coated with a volume absorber with a Debye bulk material and a skin (left) and the material parameters of the bulk material (right).

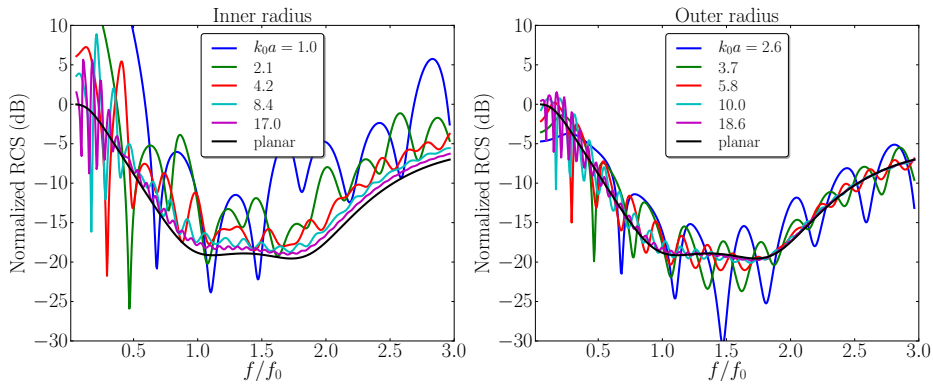

Figure 18: Monostatic RCS from a PEC sphere coated with a bulk absorber of a Debye material, and a dielectric coating. To the left normalized with the RCS of the inner PEC scatterer, and to the right normalized with the RCS of an enclosing PEC scatterer.

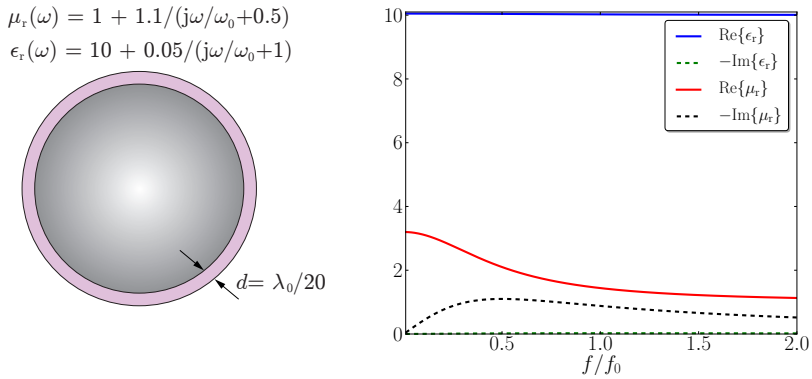

Figure 19: A PEC sphere coated with a thin magnetic absorber (left) and the material parameters of the absorber (right).

5.9 Thin magnetic sheet absorber

The final absorber under study is a thin magnetic sheet absorber, as in Figure 19. The absorber has a thickness of $d = \lambda_0/20$ and relative permittivity and relative permeability

$$\epsilon_r(\omega) = \epsilon_r'(\omega) - j\epsilon_r''(\omega) = 10 + \frac{0.05}{j\omega/\omega_0 + 1.0},$$
$$\mu_r(\omega) = \mu_r'(\omega) - j\mu_r''(\omega) = 1.0 + \frac{1.1}{j\omega/\omega_0 + 0.5}$$

were achieved after performing the same type of optimization as in Section 5.7. The results presented in Figure 20 indicate that this absorber is well suited for applications of cloaking curved surfaces, as the curves converge to the planar results for relatively small radii of curvature, $k_0 a \approx 5$. The resonance in Figure 20 can be seen to be shifted up in frequency compared to the Salisbury screen, although B/d quite large for this type of absorber in relation to the previous designs in this work.

5.10 Evaluation of absorber performance

The results in Section 5 are summarized in Table 1, where the values of ka for the different types of absorbers correspond to a rough estimate of when the difference in absorber performance of the spherical and planar scenario is $< 3\,\text{dB}$, in the case of normalization with enclosing PEC. A general observation of the results are that the normalized RCS of a PEC sphere coated with an absorber converges to the planar scattering parameter of the absorber backed by a ground plane, when the radius of the PEC sphere is increased to a few wavelengths in size. This is true for all absorbers in this study except for the Chambers-Tennant absorber in

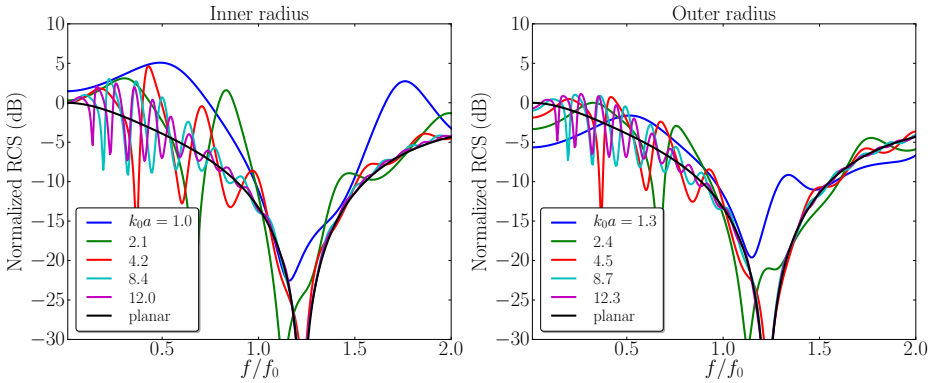

Figure 20: Monostatic RCS from a PEC sphere coated with thin magnetic material absorber. To the left normalized with the RCS of the inner PEC scatterer, and to the right normalized with the RCS of an enclosing PEC scatterer.

Table 1: Summary of when the monostatic scattering of a sphere coated with an absorber has converged to the planar scattering parameter. The size parameters ka for the different absorbers correspond to a rough estimate of when the difference in absorber performance of the spherical and planar scenario is < 3 dB.

Absorber	Sphere size (ka)
Salisbury	17
Capacitive Salisbury	17
CAA	25
Jaumann	60
Chambers-Tennant	-
Conductive bulk	5
Debye bulk	5
Thin magnetic	6

Section 5.6, where it was observed that the PEC sphere and absorber act as a spherical cavity which reduces the absorber performance.

When comparing the results in Table 1 to the similar analysis presented in [26] it is noted that the convergence of the absorber performance in a sphere scattering scenario is comparable to that of the TM component of an absorber applied to a cylinder of infinite extent in the axial direction. At the same time, the TE component in the cylinder scattering scenario in [26] converges significantly faster when ka is increased. This conclusion implies that the performance of electromagnetic absorbers is relatively insensitive to curvature in the TE-direction of the incident signal, while curvature in the TM direction with respect to the incident signal has a more significant effect on the absorber performance.

When comparing the results in Section 5 using the "inner" or "outer" normalization scheme it can be seen that the outer normalization seems to overestimate the absorber performance, while the inner normalization underestimates the absorber performance. This effect is especially noticeable for the Jaumann absorber in Section 5.3. Which normalization technique that is preferable depends on the application where the absorber is used. For example, in some applications the outer dimensions of the object, with an absorber applied, are predetermined and in these cases the outer normalization is most relevant. On the other hand, if the inner dimensions of the scatterer are predefined the inner normalization gives a more realistic evaluation of the absorber performance in the current scenario.

6 Conclusions

A method for calculating the electromagnetic scattering from a multilayer spherical scatterer, possibly resistive sheets at the interfaces, has been presented. The solution to the specific scattering problem is a recursion relation of the transition matrix elements, on the form of a Möbius transform. From the transition matrix components the scattered fields can be calculated in any direction. A numerical implementation of the solution has been implemented, resulting in a code that can handle any number of layers, resistive sheets, lossy electric and magnetic materials, and dispersive materials and sheets.

A number of different electromagnetic absorbers have been applied to spherical scatterers of different size, and the effect of curvature on the absorber performance was evaluated. By normalizing the scattering from a coated scatterer with, either the scattering from the uncoated structure, or an enclosing PEC structure, a comparison can be made between the absorber performance of the curved application and a corresponding planar design. It is concluded that absorbers based on resistive sheets or circuit analog layers, are more sensitive to curvature than bulk absorbers, based on volume losses, such as thin magnetic absorbers or carbon doped dielectric absorbers.

It has also been observed that the convergence of the absorber performance in a sphere scattering scenario is comparable to that of the TM component of an absorber applied to a cylinder of infinite extent in the axial direction [26], while the TE component converges much faster when ka is increased. This implies that the performance of electromagnetic absorbers is relatively insensitive to curvature in the TE direction of the incident signal, while curvature in the TM direction with respect to the incident signal has a more significant effect on the absorber performance.

Appendix A Derivation of T-matrix components for plane wave illumination of a layered sphere

As was stated in Section 3.5, the total fields in each region of a layered sphere are given by (3.29) and the boundary conditions at each interfaces of the layered sphere are presented in (3.30). If the fields in (3.29) are inserted in (3.30), the first expression in (3.30) results in the relations

$$A_{1n}^{(i)}(j_l(k_i r_i)+t_{1l}^{(i-1)}h_l^{(2)}(k_i r_i)) = A_{1n}^{(i+1)}(j_l(k_{i+1} r_i)+t_{1l}^{(i)}h_l^{(2)}(k_{i+1} r_i)), \tag{A.1}$$

$$A_{2n}^{(i)}\left(\frac{(k_i r_i j_l(k_i r_i))'}{k_i r_i}+t_{2l}^{(i-1)}\frac{(k_i r_i h_l^{(2)}(k_i r_i))'}{k_i r_i}\right) = A_{2n}^{(i+1)}\left(\frac{(k_{i+1} r_i j_l(k_{i+1} r_i))'}{k_{i+1} r_i}+t_{2l}^{(i)}\frac{(k_{i+1} r_i h_l^{(2)}(k_{i+1} r_i))'}{k_{i+1} r_i}\right), \tag{A.2}$$

and the second relation in (3.30) results in the expressions

$$A_{1n}^{(i)}\frac{1}{\eta_i}\left(\frac{(k_i r_i j_l(k_i r_i))'}{k_i r_i}+t_{2l}^{(i-1)}\frac{(k_i r_i h_l^{(2)}(k_i r_i))'}{k_i r_i}\right) - A_{1n}^{(i+1)}\frac{1}{\eta_{i+1}}\left(\frac{(k_{i+1} r_i j_l(k_{i+1} r_i))'}{k_{i+1} r_i}+t_{2l}^{(i)}\frac{(k_{i+1} r_i h_l^{(2)}(k_{i+1} r_i))'}{k_{i+1} r_i}\right) = -\mathrm{j}Y_{\mathrm{S}}^{(i)}A_{1n}^{(i)}(j_l(k_i r_i)+t_{1l}^{(i)}h_l^{(2)}(k_i r_i)), \tag{A.3}$$

$$A_{2n}^{(i)}\frac{1}{\eta_i}\left(j_l(k_i r_i)+t_{2l}^{(i-1)}h_l^{(2)}(k_i r_i)\right) - A_{2n}^{(i+1)}\frac{1}{\eta_{i+1}}\left(j_l(k_{i+1} r_i)+t_{2l}^{(i)}h_l^{(2)}(k_{i+1} r_i)\right) = \mathrm{j}Y_{\mathrm{S}}^{(i)}A_{2n}^{(i)}\left(\frac{(k_i r_i j_l(k_i r_i))'}{k_i r_i}+t_{2l}^{(i-1)}\frac{(k_i r_i h_l^{(2)}(k_i r_i))'}{k_i r_i}\right), \tag{A.4}$$

where we have used the relations

$$\hat{\boldsymbol{r}}\times\boldsymbol{A}_{3n}(\hat{\boldsymbol{r}})=\boldsymbol{0},\qquad \boldsymbol{A}_{2n}(\hat{\boldsymbol{r}})=\hat{\boldsymbol{r}}\times\boldsymbol{A}_{1n}(\hat{\boldsymbol{r}}),\qquad \boldsymbol{A}_{1n}(\hat{\boldsymbol{r}})=\boldsymbol{A}_{2n}(\hat{\boldsymbol{r}})\times\hat{\boldsymbol{r}}. \tag{A.5}$$

The goal from here is to eliminate all the the coefficients $A_{\tau n}$, and to find recursion expressions for the unknown T-matrix coefficients $t_{\tau l}^{(i)}$. To simplify the notation further, introduce the Riccati-Bessel functions and their derivatives [1, 18]

$$\begin{aligned} \psi_l(z) &= z j_l(z), & \xi_l(z) &= z h_l^{(2)}(z),\\ \psi_l'(z) &= j_l(z)+z j_l'(z), & \xi_l'(z) &= h_l^{(2)}(z)+z h_l'^{(2)}(z), \end{aligned} \tag{A.6}$$

and divide (A.4) by (A.2) to get the expression

$$\frac{\frac{1}{\eta_i}(\psi_l(k_i r_i) + t_{2l}^{(i-1)}\xi_l(k_i r_i)) - \mathrm{j}Y_{\mathrm{S}}^{(i)}(\psi_l'(k_i r_i) + t_{2l}^{(i-1)}\xi_l'(k_i r_i))}{\psi_l'(k_i r_i) + t_{2l}^{(i-1)}\xi_l'(k_i r_i)} = \frac{1}{\eta_{i+1}}\left(\frac{\psi_l(k_{i+1} r_i) + t_{2l}^{(i)}\xi_l(k_{i+1} r_i)}{\psi_l'(k_{i+1} r_i) + t_{2l}^{(i)}\xi_l'(k_{i+1} r_i)}\right). \quad \text{(A.7)}$$

Now, divide (A.3) by (A.1), to get

$$\frac{\frac{1}{\eta_i}(\psi_l'(k_i r_i) + t_{1l}^{(i-1)}\xi_l'(k_i r_i)) + \mathrm{j}\eta_i Y_{\mathrm{S}}^{(i)}(\psi_l(k_i r_i) + t_{1l}^{(i-1)}\xi_l(k_i r_i))}{\psi_l(k_i r_i) + t_{1l}^{(i-1)}\xi_l(k_i r_i)} = \frac{1}{\eta_{i+1}}\left(\frac{\psi_l'(k_{i+1} r_i) + t_{1l}^{(i)}\xi_l'(k_{i+1} r_i)}{\psi_l(k_{i+1} r_i) + t_{1l}^{(i)}\xi_l(k_{i+1} r_i)}\right), \quad \text{(A.8)}$$

where it can be seen that (A.7) only contain the T-matrix components $t_{1l}^{(i-1)}$, $t_{1l}^{(i)}$, and (A.8) only contain the T-matrix component $t_{2l}^{(i-1)}$, $t_{2l}^{(i)}$. Furthermore, the expressions (A.7)–(A.8) describe recursion relations where the unknown T-matrix components are updated for each layer through linear mappings $A(\cdot)$, $B(\cdot)$

$$\begin{cases} t_{1l}^{(i)} = A(t_{1l}^{(i-1)}) \\ t_{2l}^{(i)} = B(t_{2l}^{(i-1)}) \end{cases} \qquad i = 1, 2, ..., n+1. \quad \text{(A.9)}$$

These mappings can be seen to have the general structure

$$\frac{a' + b'x_1}{c' + d'x_1} = \frac{e' + f'x_2}{g' + h'x_2}, \quad \text{(A.10)}$$

where $a', b', c', d', e', f', g'$ and h' are known coefficients, and x_1 is a known parameter and x_2 is unknown. A rearrangement of (A.10) results in the familiar Möbius transform

$$x_2 = \frac{(e'd' - b'g')x_1 + e'c' - a'g'}{(b'h' - f'd')x_1 + a'h' - f'c'} = -\frac{ax_1 + b}{cx_1 + d}, \quad \text{(A.11)}$$

where

$$\begin{aligned} a &= b'g' - e'd', \quad b = a'g' - e'c', \\ c &= b'h' - f'd', \quad d = a'h' - f'c'. \end{aligned} \quad \text{(A.12)}$$

This implies that by identifying the exact expressions of $a', b', c', d', e', f', g'$ and h' for our two expressions (A.7)–(A.8), we have a final expression for the solution

to the problem. In (A.7) the mapping coefficients are

$$\begin{aligned} a' &= \frac{\eta_{i+1}}{\eta_i}\psi_l(k_i r_i) - \mathrm{j}Y_{\mathrm{S}}^{(i)}\psi_l'(k_i r_i)\eta_{i+1}, & b' &= \frac{\eta_{i+1}}{\eta_i}\xi_l(k_i r_i) - \mathrm{j}Y_{\mathrm{S}}^{(i)}\xi_l'(k_i r_i)\eta_{i+1}, \\ c' &= \psi_l'(k_i r_i), & d' &= \xi_l'(k_i r_i), \\ e' &= \psi_l(k_{i+1} r_i), & f' &= \xi_l(k_{i+1} r_i), \\ g' &= \psi_l'(k_{i+1} r_i), & h' &= \xi_l'(k_{i+1} r_i), \end{aligned} \tag{A.13}$$

and in (A.8) the mapping coefficients are

$$\begin{aligned} a' &= \frac{\eta_{i+1}}{\eta_i}\psi_l'(k_i r_i) - \mathrm{j}Y_{\mathrm{S}}^{(i)}\psi_l(k_i r_i)\eta_{i+1}, & b' &= \frac{\eta_{i+1}}{\eta_i}\xi_l'(k_i r_i) - \mathrm{j}Y_{\mathrm{S}}^{(i)}\xi_l(k_i r_i)\eta_{i+1}, \\ c' &= \psi_l(k_i r_i), & d' &= \xi_l(k_i r_i), \\ e' &= \psi_l'(k_{i+1} r_i), & f' &= \xi_l'(k_{i+1} r_i), \\ g' &= \psi_l(k_{i+1} r_i), & h' &= \xi_l(k_{i+1} r_i). \end{aligned} \tag{A.14}$$

Finally, the recursive expression for the T-matrix coefficients can be formulated as

$$t_{\tau l}^{(i)} = -\frac{a_\tau^{(i)} t_{\tau l}^{(i-1)} + b_\tau^{(i)}}{c_\tau^{(i)} t_{\tau l}^{(i-1)} + d_\tau^{(i)}}, \tag{A.15}$$

where for $\tau = 1$ the coefficients are

$$\begin{cases} a_1^{(i)} = \dfrac{\eta_i}{\eta_{i+1}}\xi_l(k_i r_i)\psi_l'(k_{i+1} r_i) - \xi_l'(k_i r_i)\psi_l(k_{i+1} r_i) - \mathrm{j}\eta_i Y_{\mathrm{S}}^{(i)}\xi_l(k_i r_i)\psi_l(k_{i+1} r_i) \\ b_1^{(i)} = \dfrac{\eta_i}{\eta_{i+1}}\psi_l(k_i r_i)\psi_l'(k_{i+1} r_i) - \psi_l'(k_i r_i)\psi_l(k_{i+1} r_i) - \mathrm{j}\eta_i Y_{\mathrm{S}}^{(i)}\psi_l(k_i r_i)\psi_l(k_{i+1} r_i) \\ c_1^{(i)} = \dfrac{\eta_i}{\eta_{i+1}}\xi_l(k_i r_i)\xi_l'(k_{i+1} r_i) - \xi_l'(k_i r_i)\xi_l(k_{i+1} r_i) - \mathrm{j}\eta_i Y_{\mathrm{S}}^{(i)}\xi_l(k_i r_i)\xi_l(k_{i+1} r_i) \\ d_1^{(i)} = \dfrac{\eta_i}{\eta_{i+1}}\psi_l(k_i r_i)\xi_l'(k_{i+1} r_i) - \psi_l'(k_i r_i)\xi_l(k_{i+1} r_i) - \mathrm{j}\eta_i Y_{\mathrm{S}}^{(i)}\psi_l(k_i r_i)\xi_l(k_{i+1} r_i), \end{cases} \tag{A.16}$$

and for $\tau = 2$ the coefficients are

$$\begin{cases} a_2^{(i)} = \dfrac{\eta_{i+1}}{\eta_i}\xi_l(k_i r_i)\psi_l'(k_{i+1} r_i) - \xi_l'(k_i r_i)\psi_l(k_{i+1} r_i) - \mathrm{j}\eta_{i+1} Y_{\mathrm{S}}^{(i)}\xi_l'(k_i r_i)\psi_l'(k_{i+1} r_i) \\ b_2^{(i)} = \dfrac{\eta_{i+1}}{\eta_i}\psi_l(k_i r_i)\psi_l'(k_{i+1} r_i) - \psi_l'(k_i r_i)\psi_l(k_{i+1} r_i) - \mathrm{j}\eta_{i+1} Y_{\mathrm{S}}^{(i)}\psi_l'(k_i r_i)\psi_l'(k_{i+1} r_i) \\ c_2^{(i)} = \dfrac{\eta_{i+1}}{\eta_i}\xi_l(k_i r_i)\xi_l'(k_{i+1} r_i) - \xi_l'(k_i r_i)\xi_l(k_{i+1} r_i) - \mathrm{j}\eta_{i+1} Y_{\mathrm{S}}^{(i)}\xi_l'(k_i r_i)\xi_l'(k_{i+1} r_i) \\ d_2^{(i)} = \dfrac{\eta_{i+1}}{\eta_i}\psi_l(k_i r_i)\xi_l'(k_{i+1} r_i) - \psi_l'(k_i r_i)\xi_l(k_{i+1} r_i) - \mathrm{j}\eta_{i+1} Y_{\mathrm{S}}^{(i)}\psi_l'(k_i r_i)\xi_l'(k_{i+1} r_i). \end{cases} \tag{A.17}$$

For the case of a general material at the center of the scatterer, the iteration starts by $i = 1$. However, If the innermost layer is a PEC then the iteration starts at $i = 2$, and it is initialized by

$$t_{1l}^{(i)} = \frac{\psi_l(k_2 r_1)}{\xi_l(k_2 r_1)}, \qquad t_{2l}^{(i)} = \frac{\psi_l'(k_2 r_1)}{\xi_l'(k_2 r_1)}. \tag{A.18}$$

Appendix B Verification of the numerical implementation

In this section the monostatic RCS of differerent scatterers is calculated using the analytic in-house Python code, developed in this work, and a number of commercial software. The MoM solver in FEKO, the frequency domain solver in CST MWS and the finite element method solver in Comsol Multiphysics were all used for bencmarking.

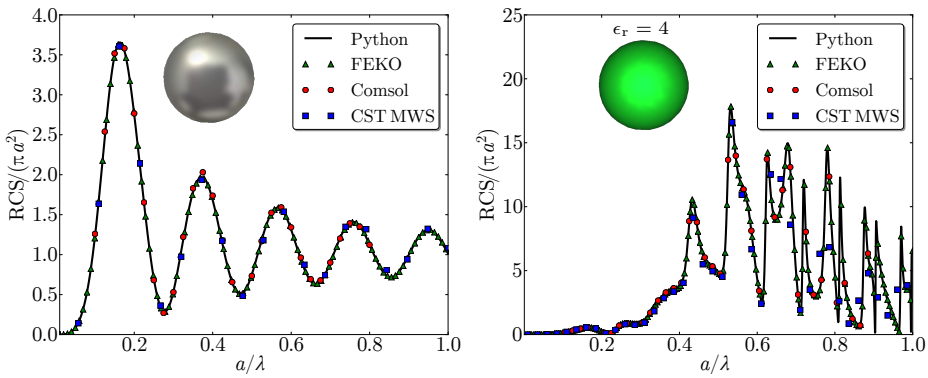

Figure 21: Verification simulations of the monostatic RCS of a PEC sphere (left) and a dielectric sphere of relative permittivity $\epsilon_r = 4$ (right).

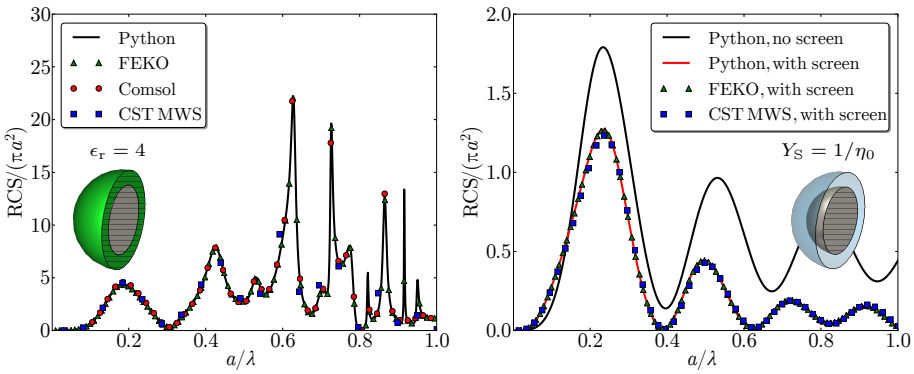

Figure 22: Verification simulations of the monostatic RCS of a PEC sphere coated with a dielectric shell (left) and a PEC sphere with a resistive sheet (right). The outer radius of the spheres is a. In the left scenario the PEC sphere radius is $0.7a$, the dielectric shell has a relative permittivity $\epsilon_r = 4$ and thickness $d = 0.3a$. In the right scenario the PEC sphere has the radius $0.7a$ and the resistive coating is located a distance $d = 0.3a$ from the sphere.

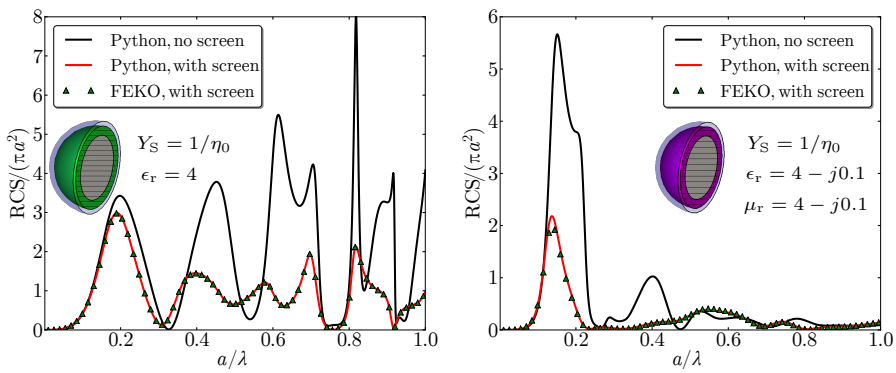

Figure 23: Verification simulations of the monostatic RCS for a PEC sphere with a dielectric coating and a resistive sheet (left), and a PEC sphere with a magnetic lossy coating and a resistive sheet (right). The outer radius of the spheres is a. In the left scenario the PEC sphere has radius $0.7a$, the dielectric shell has a relative permittivity $\epsilon_r = 4$ and thickness $d = 0.2a$ and the resistive coating is located a distance $d = 0.1a$ from the dielectric layer. In the right scenario the PEC sphere has radius $0.7a$, the magnetic shell has the relative permeability $\mu_r = 4 - 0.1$j, relative permittivity $\epsilon_r = 4 - 0.1$j and thickness $d = 0.2a$ and the resistive coating is located a distance $d = 0.1a$ from the magnetic layer.

References

[1] M. Abramowitz and I. A. Stegun, editors. *Handbook of Mathematical Functions*. Applied Mathematics Series No. 55. National Bureau of Standards, Washington DC, 1970.

[2] C. F. Bohren and D. R. Huffman. *Absorption and Scattering of Light by Small Particles*. John Wiley & Sons, New York, NY, 1983.

[3] J. J. Bowman, T. B. A. Senior, and P. L. E. Uslenghi. *Electromagnetic and Acoustic Scattering by Simple Shapes*. North-Holland, Amsterdam, 1969.

[4] J. J. Bowman and V. H. Weston. The effect of curvature on the reflection coefficient of layered absorbers. *IEEE Trans. Antennas Propag.*, **14**(6), pp. 760–767, 1966.

[5] C. Cantrell. Numerical methods for the accurate calculation of spherical bessel functions and the location of mie resonances, 2013. Available at: http://www.utdallas.edu/cantrell/ee6481/lectures/bessres1.pdf, accessed 2016-05-20.

[6] B. Chambers and A. Tennant. Design of wideband Jaumann radar absorbers with optimum oblique incidence performance. *Electronics Letters*, **30**(18), pp. 1530–1532, September 1994.

[7] J. Dave. Subroutines for computing the parameters of the electromagnetic radiation scattered by a sphere. Technical Report No. 320-3237, IBM Palo Alto Scientific Center, Calif., 1968.

[8] A. Gogoi, A. Choudhury, and G. A. Ahmed. Mie scattering computation of spherical particles with very large size parameters using an improved program with variable speed and accuracy. *Journal of Modern Optics*, **57**(21), pp. 2192–2202, 2010.

[9] W. Hergert and T. Wriedt. *The Mie Theory: Basics and Applications*, volume 169. Springer, 2012.

[10] A. Kazemzadeh and A. Karlsson. Multilayered wideband absorbers for oblique angle of incidence. *IEEE Trans. Antennas Propag.*, **58**(11), pp. 3637–3646, 2010.

[11] E. F. Knott and K.Langseth. Performance degardation of Jaumann absorbers due to curvature. *IEEE Trans. Antennas Propag.*, **28**(1), pp. 137–139, 1980.

[12] E. F. Knott, J. F. Shaeffer, and M. T. Tuley. *Radar Cross Section*. SciTech Publishing Inc., 5601 N. Hawthorne Way, Raleigh, NC 27613, 2004.

[13] G. Kristensson. *Scattering of Electromagnetic Waves by Obstacles*. SciTech Publishing, an imprint of the IET, Edison, NJ, 2016.

[14] W. J. Lentz. Generating Bessel functions in Mie scattering calculations using continued fractions. *Applied Optics*, **15**(3), pp. 668–671, 1976.

[15] G. Mie. Beiträge zur Optik trüber Medien, speziell kolloidaler Metallösungen. *Ann. Phys. Leipzig*, **25**, pp. 377–445, 1908.

[16] M. I. Mishchenko and L. D. Travis. Gustav mie and the evolving discipline of electromagnetic scattering by particles. *Bulletin of the American Meteorological Society*, **89**(12), pp. 1853–1861, 2008.

[17] B. Munk. *Frequency Selective Surfaces: Theory and Design*. John Wiley & Sons, New York, NY, 2000.

[18] F. W. J. Olver, D. W. Lozier, R. F. Boisvert, and C. W. Clark. *NIST Handbook of mathematical functions*. Cambridge University Press, New York, 2010.

[19] M. Rostami, D. Ansari Oghol Beig, and H. Mosallaei. Dispersion diagram analysis of arrays of multishell multimaterial nanospheres. *Progress In Electromagnetics Research B*, **48**, pp. 77–98, 2013.

[20] K. N. Rozanov. Ultimate thickness to bandwidth ratio of radar absorbers. *IEEE Trans. Antennas Propag.*, **48**(8), pp. 1230–1234, August 2000.

[21] G. T. Ruck, D. E. Barrick, W. D. Stuart, and C. K. Krichbaum. *Radar Cross-Section Handbook*, volume 1 and 2. Plenum Press, New York, 1970.

[22] W. Salisbury. Absorbent body for electromagnetic waves, 1952. Patent number 2,599,944.

[23] J. Shen and X. Cai. Algorithm of numerical calculation on Lorentz Mie theory. *PIERS Online*, **1**(6), pp. 691–694, 2005.

[24] R. A. Shore. Scattering of an electromagnetic linearly polarized plane wave by a multilayered sphere: Obtaining a computational form of mie coefficients for the scattered field. *Antennas and Propagation Magazine, IEEE*, **57**(6), pp. 69–116, 2015.

[25] D. Sjöberg. Circuit analogs for wave propagation in stratified structures. In A. Petrin, editor, *Wave Propagation in Materials for Modern Applications*, pp. 489–508. InTech, 2010.

[26] D. Sjöberg. Scattering for singly curved functional surfaces and corresponding planar designs. In *Antennas and Propagation (EuCAP), 2013 7th European Conference on*, pp. 3339–3342. IEEE, 2013.

[27] J. A. Stratton. *Electromagnetic Theory*. McGraw-Hill, New York, NY, 1941.

[28] J. W. Strutt. Lviii. on the scattering of light by small particles. *The London, Edinburgh, and Dublin Philosophical Magazine and Journal of Science*, **41**(275), pp. 447–454, 1871.

[29] V. V. Tikhonov, D. A. Boyarskii, E. Sharkov, M. Raev, I. A. Repina, V. Ivanov, T. A. Alexeeva, and N. Y. Komarova. Microwave model of radiation from the multilayer“ocean-atmosphere”system for remote sensing studies of the polar regions. *Progress In Electromagnetics Research B*, **59**, pp. 123–133, 2014.

[30] H. E. William. Electromagnetic wave absorbers and anechoic chambers through the years. *IEEE Trans. Antennas Propag.*, **21**(4), 1973.

[31] W. J. Wiscombe. Improved Mie scattering algorithms. *Applied optics*, **19**(9), pp. 1505–1509, 1980.

Approximative Computation Methods for Monostatic Scattering from Axially Symmetric Objects

Andreas Ericsson, Daniel Sjöberg, Christer Larsson
and Torleif Martin

Paper VIII

Submitted as: A. Ericsson, D. Sjöberg, C. Larsson and T. Martin, "Approximative computation methods for monostatic scattering from axially symmetric objects," *Progress In Electromagnetics Research B*, pp. 1–24, 2017, under review.

Preprint published as: Technical Report LUTEDX/(TEAT-7256), pp. 1–36, 2017, Department of Electrical and Information Technology, Lund University, Sweden. http://www.eit.lth.se.

Abstract

Two approximation methods are presented for fast calculations of the monostatic scattering from axial-symmetric scatterers coated with electromagnetic absorbers. The methods are designed for plane wave illumination parallel to the axis of rotation of the scatterer. The first method is based on simulating the scattering of a perfect electric conductor (PEC) enclosing the absorber coated scatterer, and multiplying the result with the squared magnitude of the absorber reflection coefficient in a planar scenario. The second method is based on simulating the scattering scenario in a physical optics (PO) solver, where the electromagnetic absorber is treated as reflection dyadic at the outer surface of the scatterer. Both methods result in a significant acceleration in computation speed in comparison to full wave methods, where the PO method carries out the computations in a number of seconds. The monostatic scattering from different geometries have been investigated, and parametric sweeps were carried out to test the limits where the methods yield accurate results. For specular reflections, the approximation methods yield very accurate results compared to full wave simulations when the radius of curvature is on the order of half a wavelength or larger of the incident signal. It is also concluded that the accuracy of the two methods vary depending on what type of absorber is applied to the scatterer, and that absorbers based on "volume losses" such as carbon doped foam absorber and thin magnetic absorbers yield better results than absorbers based on resistive sheets, such as a Salisbury absorber.

1 Introduction

In many applications it is of great interest to characterize how electromagnetic waves interact with objects [32]. In some scenarios this interaction should be as significant as possible, such as for antennas [2], while in other scenarios this interaction is to be minimized, such as in defense applications [24]. In order to minimize the electromagnetic scattering from an object one can either shape the object to direct the signals in desired directions, or use electromagnetic absorbers that reduce the electromagnetic scattering in a desired frequency band of operation [19].

When numerically calculating the scattered fields of an object, accurate results can be achieved using full wave methods such as the method of moments (MoM), finite element method (FEM), or finite difference time domain method (FDTD) [6, 15]. However, the computational requirements increase rapidly as the size of the scatterer is made larger than a few wavelengths in size [6]. In [3] it is shown that, in a simulation at the wave frequency f of a 3D system of fixed spatial extent, the number of floating point operations and the memory requirements scales as $\mathcal{O}(f^4)$ in all of the above mentioned methods. If a 2D simulation system is considered the MoM scales as $\mathcal{O}(f^2)$ and the FEM and FDTD scales as $\mathcal{O}(f^3)$ [3]. It should be noted that time-domain difference methods give a complete frequency spectrum, as compared to a standard frequency-domain method

that requires one computation for a single frequency. This means that for wideband problems a time domain method can lead to reduced simulation complexity. In order to reduce the requirements and accelerate simulations a number of numerical acceleration methods have been presented in the last decades. For MoM two such methods well suided for simulating electrically large scattering problems are the multilevel fast multipole method (MLFMM) [5, 7, 23] and the characteristic basis function method (CBFM) [14, 20, 21]. The MLFMM scales in 3D as $\mathcal{O}(f^2\log(f))$ [3] which is a significant improvement, but can still result in heavy computations for complicated structures.

If for example an electromagnetic absorber consisting of single/multiple layers of different materials are applied to a scatterer under test the computational requirements increase even further, resulting in even higher memory requirements and longer simulation times [19]. A different approach to further reduce the computational requirements is to utilize high frequency approximation methods. This type of methods are commonly utilized when simulating very large objects, but can be useful for smaller scatterers as well. A high frequency approximation method used in many applications such as optics, electrical engineering and applied physics is physical optics (PO) [27]. It is an intermediate method between geometrical optics, which treats electromagnetic waves as rays, and full wave electromagnetism [6, 16]. The approximation consists of estimating the field on a surface using ray optics and then integrating the field over the surface to calculate the transmitted or scattered field. This resembles the Born approximation from the fact that details of the problem are treated as a perturbation [4]. A strong advantage of this method is the fact that the simulation complexity and computation time does not significantly increase with frequency as in the previous methods [1,12,28]. Drawback with PO is that it does not consider edge diffraction and the accuracy of the method is decreased for scattering in directions other than the specular direction [1]. Modified versions of PO have been presented throughout the years where these problem have been successfully addressed, utilizing physical theory of diffraction (PTD) or other techniques [22, 25, 29–31].

In this work, two approximation methods are presented for calculating the monostatic scattering from absorber coated axially-symmetric scatterers illuminated by a plane wave propagating along the axis of rotation of the scatterer. The methods are based on the work presented in [10, 11] where the effect of curvature on electromagnetic absorbers was evaluated using analytic recursion expressions. The first method consists in multiplying the scattering from a perfect electric conductor (PEC) enclosing the scatterer with the squared magnitude of the reflection coefficient of the absorber in a planar scenario. The second consists of calculating the monostatic scattering using the PO approximation, where the absorber is treated as an angle of incidence dependent reflection dyadic at the surface of the scatterer. An in-house solver presented in [26] is utilized for generating the PO simulation data, and is benchmarked against full wave simulations in Comsol Multiphysics. The time convention $\mathrm{e}^{\mathrm{j}\omega t}$ is used throughout this work.

This work is organized as follows: simplified integral expressions for calculating the monostatic far field in a full wave- or PO solver are presented in Section 2.

In Section 3 the approximation methods are introduced in detail and in Section 4 simulation results are presented for different electromagnetic absorbers used in this work. The two approximation methods are compared to a corresponding full wave simulation for different electromagnetic absorbers applied to scatterers of different geometrical shapes in Section 5. Finally, a short summary and evaluation of the performance of the approximation methods are presented in Section 6, followed by some concluding remarks in Section 7.

2 Monostatic RCS from axially symmetric scatterers

2.1 General formulation

In this work the main focus is on characterizing the monostatic radar cross section (RCS) from axially symmetric scatterers, illuminated along the axis of rotation. The RCS can be determined from the far field amplitude in the backscattering direction through the relation

$$\sigma = 4\pi \frac{|\boldsymbol{F}(-\hat{\boldsymbol{z}})|^2}{|E_0|^2}, \tag{2.1}$$

where σ is the RCS and E_0 is the amplitude of the incident electric field. In [26] a method was presented to determine the far field amplitude in the backscattering direction from a axially symmetric scatterer, illuminated by a linearly polarized (LP) plane wave $\boldsymbol{E}_0 = E_0 \mathrm{e}^{-\mathrm{j}kz}\hat{\boldsymbol{x}}$ propagating along the axis of rotation of the scatterer, as in Figure 1. There it was shown that by exciting the structure with a circularly polarized (CP) plane wave $\boldsymbol{E}_0 = E_0 \mathrm{e}^{-\mathrm{j}kz}\mathrm{e}^{\mp m\mathrm{j}\varphi}(\hat{\boldsymbol{\rho}} - \mathrm{j}\hat{\boldsymbol{\varphi}})$ of one of the two azimutal modes $m = \pm 1$, the backscattered farfield $\boldsymbol{F}(-\hat{\boldsymbol{z}})$ from the scatterer, illuminated by a LP plane wave, can be determined through the expression

$$\begin{aligned}\boldsymbol{F}(-\hat{\boldsymbol{z}}) = \hat{\boldsymbol{x}}\frac{\mathrm{j}k}{4}\int_\gamma \Big[& n_\rho E_z(\rho,z) - n_z E_\rho(\rho,z) + \eta_0 n_z H_\varphi(\rho,z) \\ & - \mathrm{j}n_z E_\varphi(\rho,z) + \mathrm{j}\eta_0(n_\rho H_z(\rho,z) - n_z H_\rho(\rho,z))\Big]\mathrm{e}^{-\mathrm{j}kz}\rho\,\mathrm{d}\ell, \end{aligned} \tag{2.2}$$

where the index $m = \pm 1$ has been dropped for brevity, k is the wave number, η_0 is the wave impedance in vacuum, $\hat{\boldsymbol{n}} = n_\rho\hat{\boldsymbol{\rho}} + n_z\hat{\boldsymbol{z}}$ is the normal vector of the scatterer, and the field components $(E_\rho, E_\varphi, E_z, H_\rho, H_\varphi, H_z)$ are computed in a numerical software and integrated over any given line segment γ enclosing the scatterer. In the following, we show how the electric and magnetic field components can be determined in the physical optics (PO) approximation, and how the expression (2.2) is reformulated in the PO scheme.

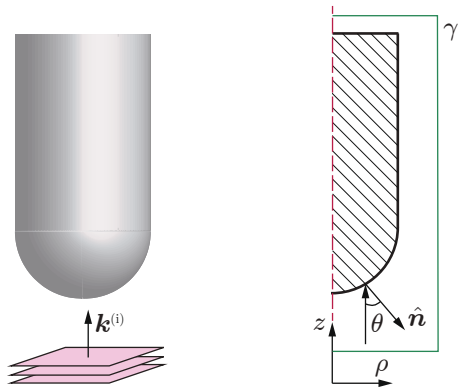

Figure 1: Principle sketch of a scattering scenario considered in this work. To the left a axially symmetric scatterer is illuminated by a plane wave along its axis of rotation. To the right a sketch of the numerical modeling of the scatterer is depicted, where the backscattered far field amplitude is calculated by calculating (2.2) along any line segment γ enclosing the scatterer.

2.2 Physical optics formulation

In the PO approximation, the scattering surface is assumed to be locally flat [1,28] and described by a reflection dyadic so that the tangential electric and magnetic fields are given by

$$\boldsymbol{E}_{\mathrm{t}} = (\mathbf{I} + \mathbf{R}) \cdot \boldsymbol{E}_{\mathrm{t}}^{(\mathrm{i})}, \tag{2.3}$$

$$\boldsymbol{H}_{\mathrm{t}} = \mathbf{Y}_{\mathrm{w}} \cdot (\mathbf{I} - \mathbf{R}) \cdot \boldsymbol{E}_{\mathrm{t}}^{(\mathrm{i})}. \tag{2.4}$$

By defining the unit vectors $\hat{\boldsymbol{p}}$ and $\hat{\boldsymbol{s}}$ spanning the surface, the identity dyadic in the tangential plane of the surface can be written as $\mathbf{I} = \hat{\boldsymbol{p}}\hat{\boldsymbol{p}} + \hat{\boldsymbol{s}}\hat{\boldsymbol{s}}$ and $\mathbf{R}$ denotes the reflection dyadic. The wave admittance dyadic of the surrounding medium $\mathbf{Y}_{\mathrm{w}}$ is defined as follows. A plane wave propagating in free space in the $\hat{\boldsymbol{k}}$ direction is given by the right-hand rule as $\boldsymbol{E} = \boldsymbol{E}_0 \mathrm{e}^{-\mathrm{j}k\hat{\boldsymbol{k}}\cdot\boldsymbol{r}}$ and $\boldsymbol{H} = \eta_0^{-1}\hat{\boldsymbol{k}} \times \boldsymbol{E}_0 \mathrm{e}^{-\mathrm{j}k\hat{\boldsymbol{k}}\cdot\boldsymbol{r}}$. Now fix a different direction $\hat{\boldsymbol{u}}$, and consider the components of $\boldsymbol{E}$ and $\boldsymbol{H}$ orthogonal to $\hat{\boldsymbol{u}}$ (the transverse parts, $\boldsymbol{E}_{\mathrm{t}}$ and $\boldsymbol{H}_{\mathrm{t}}$). The wave admittance is then defined by the relation $\boldsymbol{H}_{\mathrm{t}} = \mathrm{sign}(\hat{\boldsymbol{u}} \cdot \hat{\boldsymbol{k}})\mathbf{Y}_{\mathrm{w}} \cdot \boldsymbol{E}_{\mathrm{t}}$. In this case, it can be represented as (with $\hat{\boldsymbol{u}} = -\hat{\boldsymbol{n}}$ and assuming $(\hat{\boldsymbol{p}}, \hat{\boldsymbol{s}}, \hat{\boldsymbol{n}})$ is a right-handed system and $\hat{\boldsymbol{n}}$ is the outward pointing normal)

$$\mathbf{Y}_{\mathrm{w}} = -\hat{\boldsymbol{n}} \times \eta_0^{-1} \left(\frac{1}{\cos\theta} \hat{\boldsymbol{p}}\hat{\boldsymbol{p}} + \cos\theta \hat{\boldsymbol{s}}\hat{\boldsymbol{s}} \right) = \eta_0^{-1} \left(\frac{-1}{\cos\theta} \hat{\boldsymbol{s}}\hat{\boldsymbol{p}} + \cos\theta \hat{\boldsymbol{p}}\hat{\boldsymbol{s}} \right). \tag{2.5}$$

Here, θ is the angle of incidence. For an isotropic case, the reflection dyadic can be represented as

$$\mathbf{R} = R_{\mathrm{TM}}(\theta)\hat{\boldsymbol{p}}\hat{\boldsymbol{p}} + R_{\mathrm{TE}}(\theta)\hat{\boldsymbol{s}}\hat{\boldsymbol{s}} \tag{2.6}$$

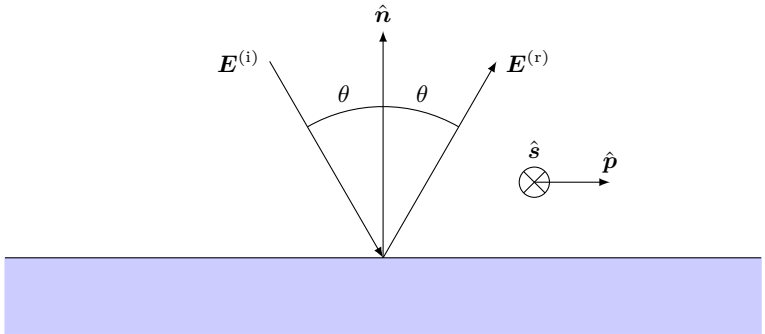

Figure 2: Local geometry of the plane of incidence, defining the unit vectors $\hat{\boldsymbol{p}}$ (corresponding to TM polarization) and $\hat{\boldsymbol{s}}$ (corresponding to TE polarization).

and we have the result

$$\boldsymbol{E}_{\mathrm{t}} = (1 + R_{\mathrm{TM}}(\theta))E^{(\mathrm{i})}_{\mathrm{TM}}\hat{\boldsymbol{p}} + (1 + R_{\mathrm{TE}}(\theta))E^{(\mathrm{i})}_{\mathrm{TE}}\hat{\boldsymbol{s}}, \tag{2.7}$$

$$\boldsymbol{H}_{\mathrm{t}} = -\frac{\eta_0^{-1}}{\cos\theta}(1 - R_{\mathrm{TM}}(\theta))E^{(\mathrm{i})}_{\mathrm{TM}}\hat{\boldsymbol{s}} + \eta_0^{-1}\cos\theta(1 - R_{\mathrm{TE}}(\theta))E^{(\mathrm{i})}_{\mathrm{TE}}\hat{\boldsymbol{p}}. \tag{2.8}$$

In [26] the tangential field components in the PO approximation in (2.7)–(2.8) are identified and reformulated on the form of the components in the integral (2.2), and the final result for the backscattered far field from a axially symmetric scatterer illuminated by a plane wave in the axial direction is

$$\boldsymbol{F}(-\hat{\boldsymbol{z}}) = -\hat{\boldsymbol{x}}\frac{\mathrm{j}k}{4}\int_\gamma \Bigg[(1 + R_{\mathrm{TM}})n_z + \frac{1 - R_{\mathrm{TM}}}{\cos\theta}n_z^2 + (1 + R_{\mathrm{TE}})n_z + \cos\theta(1 - R_{\mathrm{TE}})\Bigg]E_0\mathrm{e}^{-2\mathrm{j}kz}\rho\,\mathrm{d}\ell. \tag{2.9}$$

All parameters inside the integral can be parametrized along the curve γ. It is immediately seen that sections of a straight circular cylinder, where $n_z = 0$ and $\cos\theta = 0$, give zero contribution regardless of the reflection coefficients. In the next section, the relations (2.2) and (2.9) are used to calculate approximative results of the RCS of a scatterer coated by an electromagnetic absorber.

3 Approximative computation methods for coated scatterers

Two approximative computation methods for calculating the RCS from axially symmetric scatterers coated with an electromagnetic absorber are presented in this work. Both methods are based on the results presented in [10]. There it

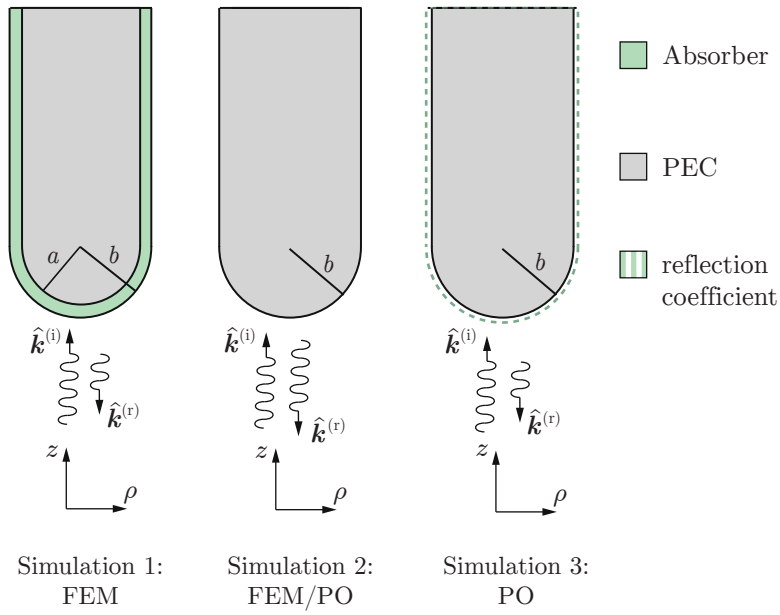

Figure 3: Three different RCS simulation cases evaluated for each geometry coated with a specific absorber. The left scenario shows the RCS of a full wave simulation model where the absorber is completely resolved in the meshing of the scatterer. The middle scenario depicts the RCS from a PEC enclosing the coated scatterer, which could be evaluated either using a full wave software or a PO solver. To the right the RCS of the coated scatterer is evaluated using a PO solver, where the absorber is treated as a reflection coefficient at the enclosing surface of the scatterer.

is shown that for a PEC sphere coated with an electromagnetic absorber an approximative relation is observed as the radius of the inner sphere is increased to a few wavelengths in size

$$\frac{\sigma^{\text{coated}}}{\sigma^{\text{PEC}}} \approx |S_{11}^{\text{planar}}|^2, \tag{3.1}$$

where σ^{coated} is the RCS of the PEC sphere with an absorber, σ^{PEC} is the is the RCS from either the uncoated PEC sphere or a PEC sphere enclosing the coated scatterer, and S_{11}^{planar} is the reflection coefficient of the absorber, illuminated by a plane wave at normal incidence, in a planar scenario of infinite extent backed by ground plane, *i.e.* $S_{11}^{\text{planar}} = \Gamma^{\text{planar}}$. In [10] this relation was used to evaluate the effect of curvature on the performance of different types of absorbers, and it was concluded that absorbers based on bulk loss, such as thin magnetic absorbers or carbon loaded foam absorbers, are less sensitive to curvature than absorbers based on single or multiple layers of resistive sheets.

However, if (3.1) is rearranged we get the expression

$$\sigma^{\text{coated}} \approx \sigma^{\text{PEC}} |S_{11}^{\text{planar}}|^2, \tag{3.2}$$

which can be interpreted in the following way: the RCS from a PEC scatterer coated with an absorber can be approximated by the RCS from an enclosing PEC scatterer multiplied by the squared reflection coefficient of the absorber in a planar scenario. This relation is the first RCS approximation method used in this work, where the parameter σ^{PEC} could be determined either using a full wave simulation software, or a PO solver. This is depicted in the center illustration in Figure 3.

The second approximation method for calculating RCS in this work is based on evaluating (2.9) using an in-house PO code. The electromagnetic absorber applied to the scatterer is treated as a reflection coefficient at the surface enclosing the scatterer, as in the rightmost illustration in Figure 3. This implies that for each absorber the reflection coefficient of the planar absorber has to be evaluated for a number of discrete angles of incidence in the range $0 \leq \theta \leq 90°$, both for TE and TM polarization. Further details on how this was carried out are presented in Section 4. Both the presented approximation methods are compared to a corresponding full wave simulation as in the left illustration in Figure 3.

4 Simulation results - planar electromagnetic absorbers

Three different types of absorbers have been investigated to evaluate the RCS approximation methods introduced in the previous section. The design procedure of the absorbers is presented in detail in [10], where the performance degradation of the absorbers with respect to double curvature was evaluated. The absorbers under study are:

1. A Salisbury absorber, consisting of a resistive sheet with the surface impedance $Z_{\text{S}} = \eta_0 = 376.7\,\Omega$, located a distance $\lambda_0/4$ from a PEC ground plane.

2. A foam absorber consisting of a conductivity loaded low permittivity material with thickness $9\lambda_0/40$ and relative permittivity $\epsilon_{\text{r}} = 1 - \text{j}2.39 f_0/f$, coated with a thin dielectric skin with thickness $\lambda_0/40$ and relative permittivity $\epsilon_{\text{r}} = 4$. The total thickness of the absorber is $\lambda_0/4$. This type of absorber could be realized by utilizing a carbon doped foam [19].

3. A thin magnetic absorber with a thickness of $\lambda_0/20$, relative permeability $\mu_{\text{r}} = 1 + 1.1/(\text{j}f/f_0 + 0.5)$ and a relative permittivity $\epsilon_{\text{r}} = 10 + 0.05/(\text{j}f/f_0 + 1)$. This type of absorber could be realized by componds of iron introducing a magnetic dipole moment [19].

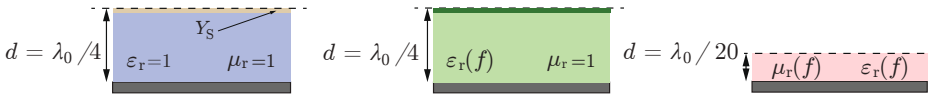

Figure 4: Electromagnetic absorbers used in this work. To the left a Salisbury screen is presented, in the center is a carbon doped foam absorber with a thin dielectric coating, and to the right is a thin magnetic absorber.

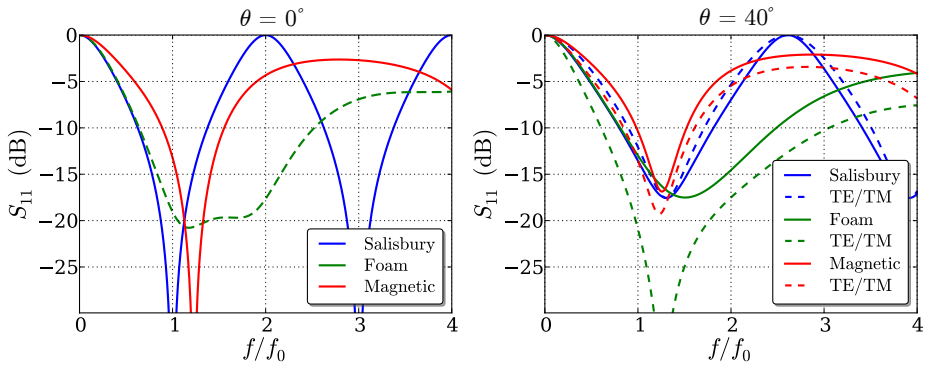

Figure 5: Simulation results of the three absorbers used in this study. To the left, the reflection coefficient of the absorbers are presented ,in dB, for normal incidence. To the right, the reflection coefficient is presented, in dB, for $\theta = 40°$ angle of incidence for TE polarization (solid curves) and TM polarization (dashed curves).

The parameter λ_0 is the design wavelength of operation of the absorbers and the geometries can be seen in Figure 4. Simulation results of the three absorbers are presented in Figure 5, where it can be seen that the foam absorber has a wider bandwidth than the other two, but it also a shows larger deviation in performance between TE and TM illumination at oblique angles of incidence.

5 Simulation results - electromagnetic absorbers on axially symmetric scatterers

The approximate computation methods for calculating the RCS from axially symmetric scatterers, presented in Section 3, were evaluated for different scatterers with and without different electromagnetic absorbers applied. The RCS of the

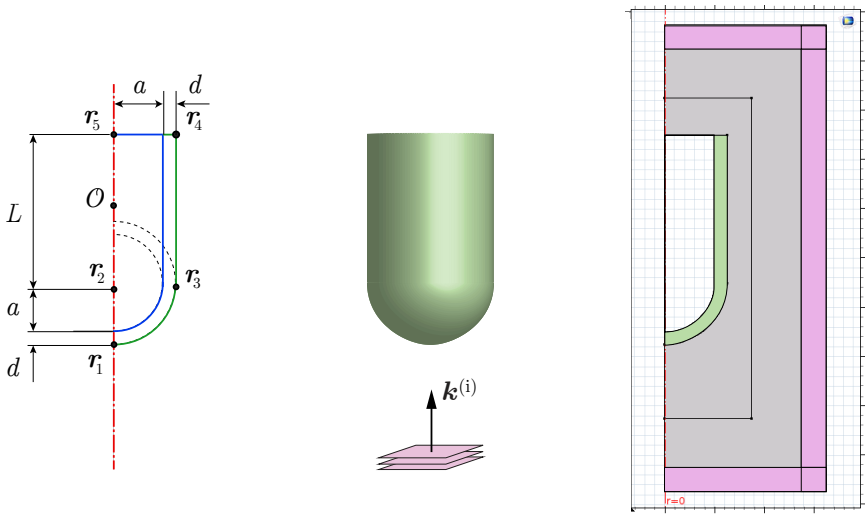

Figure 6: An example of a scattering scenario under test (center), where a scatterer coated with an absorber is illuminated by a plane wave from below the scatterer. Identical simulation models are evaluated in a PO solver (left) and a full wave solver (right). In the PO model the line segment defining the scatterer is parametrized with respect to a predefined coordinate system, and in the full wave model the geometry is generated in a graphical editor.

scatterers under test was determined for on-axis illumination both in a 2D axial symmetric full wave FEM in Comsol Multiphysics, and in an in-house PO solver, written in python using the SciPy package for scientific computing [17]. The electric and magnetic fields were evaluated at 501 frequency points in the range $f_0/200 \leq f \leq 3f_0$ in both solvers, where f_0 is the center frequency of operation of the applied absorbers. Verification simulations and a mesh convergence study of the 2D axial-symmetric full wave solver in Comsol Multiphysics are presented in Appendix C, where simulation results from FEKO are used as a benchmark.

In the full wave model, the maximum mesh size was defined as $\lambda_2/10$, where λ_2 is the wavelength at the highest frequency of the study. In the right illustration in Figure 6 a conical scatterer with a rounded nose and a single layer absorber has been implemented in Comsol Multiphysics. The outer cyan area represent a perfectly matched layer, providing a boundary condition for the numerical solver, the grey area is free space, the rectangle enclosing the scatterer is the line segment γ along which the integral (2.2) is carried out for extracting the monostatic far-field amplitude, and the green area correspond to an electromagnetic absorber coating the scatterer. The structure is illuminated by a plane wave propagating in the upward direction. The simulations were carried out on a Supermicro 2028GR-TR 2U computation server with 2 Intel Xeon E5 8-Core 2.40 GHz processors and 8 Samsung 16GB DDR4 2133MHz RAM. A typical simulation consisted of about

200 000–500 000 mesh elements, required about 20-40 GB RAM, and finished in about $12 - 24$ h, depending on the size of the scatterer under study.

In the PO simulations the backscattered far field was determined by evaluation of (2.9) over the line segment defining the surface of the scatterer, using a simple Riemann integral with 10000 elements along the line. Simulations were carried out over the same frequency range as in the full wave software, but this type of approximation method can easily be used for much higher frequencies without a significant increase in computation time. In order to carry out this integral each scatterer under study was parametrized as can be seen in Appendix B. An example of a scatterer under test in this work is presented in the left illustration in Figure 6, where the design parameters of the scatterer are marked and $\boldsymbol{r}_i = (\rho_i, z_i)$, $i = 1, 2, .., 5$ are key points used in the parametrization, see Appendix B for details. A typical PO simulation, evaluating the RCS through the relation (2.9), was carried out in about 5–10 seconds.

In Section 2.2 we mention that the PO far field expression (2.9) will be identically zero for all incidence angles $\theta \leq 0$, resulting in that a PO solver will not catch scattering from the back edge of objects. This type of scattering can be accounted for by utilizing geometrical theory of diffraction (GTD) [13, 18]. However, to compare the two approximation methods in this work the back edge scattering in the full wave simulations is removed by utilizing time gating. This is a well established method commonly used in electromagnetic measurements to filter out multipath reflections and other unwanted scattering components [8, 9]. By performing a discrete inverse Fourier transform on frequency domain data, multiplying the data with a time domain window function, and finally transforming the data back to the frequency domain, the filtered data is acquired. In order to achieve the desired results, without introducing spurious oscillations in the data, a tapered cosine window function is utilized (commonly referred to as tukey window) [17].

5.1 Hemispherically capped cylinder

The first scatterer under study is a cylinder with a spherical cap, as in Figure 6. The radius of the nose is denoted a and the length of the cylinder L is defined as $L = 3a$, which implies that the total length of the scatterer is $L_{\text{tot}} = 4a$ and the total width is $w_{\text{tot}} = 2a$. Simulation results of a PEC scatterer with $a = 8\lambda_0/3$, are presented in Figure 7. In the top left plot the raw RCS is presented both from a full wave simulation and a PO simulation, where all results are normalized with the gemetrical cross section of the scatterer πa^2. Here it can be seen that the full wave data oscillates rapidly due to the interference of the scattering component from the nose and the back of the scatterer. To compare the two methods the scattering off the back is gated out from the full wave data, and the resulting comparison is made in the upper right plot in Figure 7. Here it can be seen that the agreement between the PO and full wave data is excellent. In the lower left and right plots the full wave and PO data are presented in the time

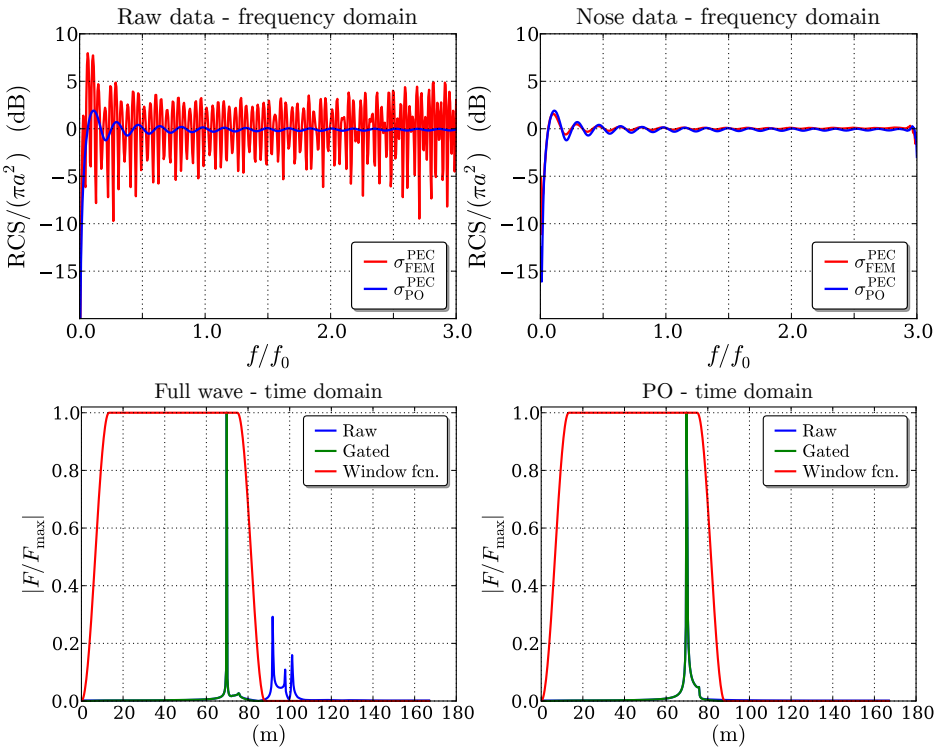

Figure 7: Simulation results of a PEC hemispherically capped cylinder evaluated both in a full wave solver and in a PO solver. The top left plot shows the RCS of the scatterer normalized with its geometrical cross section, presented in the frequency domain. The top right plot shows the normalized RCS when the scattering from the back edge has been gated out in the time domain. The bottom left plot shows the full wave simulation far-field data in the time domain and the bottom right plot is the corresponding PO data, both with the corresponding window function.

domain, alongside with the tapered cosine window function used to separate the two scattering components. Here it can be seen that the right peak in the full wave data in the lower left plot (corresponding to the back edge scattering) is absent in the PO data in the lower right plot. Still, the same window function is applied to both data sets for consistency.

The RCS from the hemispherically capped cylinder coated with the three different absorbers, introduced in Section 4, was evaluated for different sizes of the scatterer. By varying the parameter a the electrical size of the scatterer was varied while keeping the length to width ratio of the PEC scatterer and the thickness of the absorber fixed. Simulation results of the scatterer coated with the foam absorber are presented in Figure 8 and simulation results of the thin magnetic absorber and the Salisbury absorber are presented in Appendix A.

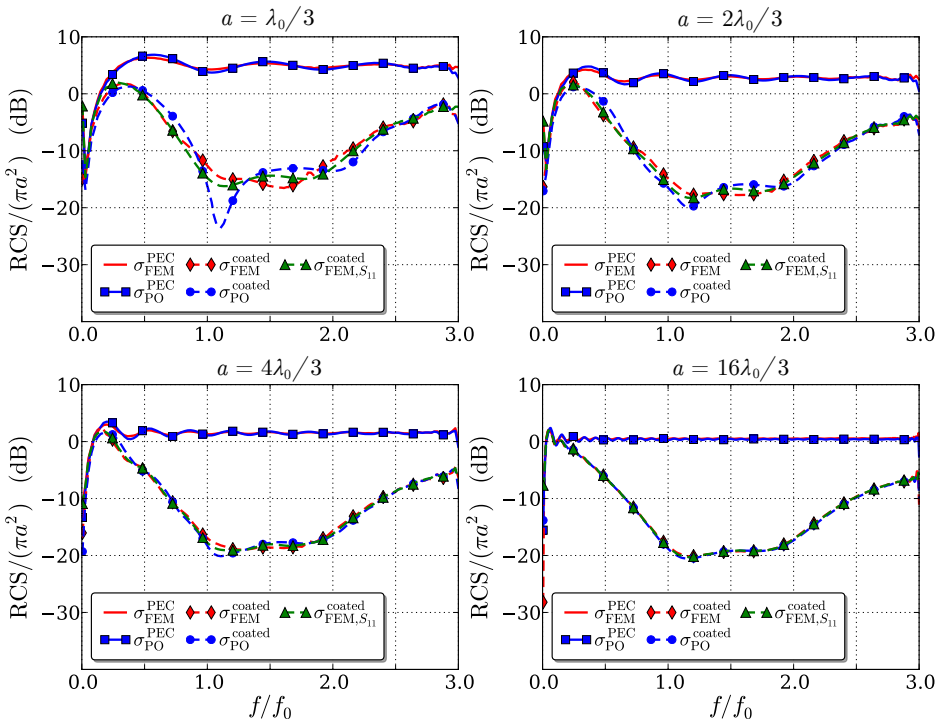

Figure 8: Simulation results of hemispherically capped cylinder scatterers of different sizes, coated with a foam absorber. In the upper left plot the radius of the scatterer is $a = \lambda_0/3$, in the upper right plot $a = 2\lambda_0/3$, in the lower left plot $a = 4\lambda_0/3$, and in the lower right plot $a = 16\lambda_0/3$. The solid curves represent the RCS of a PEC enclosing the coated scatterer and the dashed curves correspond to the RCS of the coated scatterer. The dashed red curve is the full wave simulation, the dashed green curve is the first approximation method and the dashed blue curve is the PO approximation method.

Note that the time gating scheme previously described has been utilized in all simulations henceforth presented in this work. In the top left plot in Figure 8, $a = \lambda_0/3$ which corresponds to $L_{\mathrm{tot}} = 4\lambda_0/3$ and $w_{\mathrm{tot}} = 2\lambda_0/3$. In the top right plot $a = 2\lambda_0/3$ which corresponds to $L_{\mathrm{tot}} = 8\lambda_0/3$ and $w_{\mathrm{tot}} = 4\lambda_0/3$. In the lower left plot $a = 4\lambda_0/3$ which corresponds to $L_{\mathrm{tot}} = 16\lambda_0/3$ and $w_{\mathrm{tot}} = 8\lambda_0/3$. Finally, in the lower right plot $a = 16\lambda_0/3$ which corresponds to $L_{\mathrm{tot}} = 64\lambda_0/3$ and $w_{\mathrm{tot}} = 32\lambda_0/3$. Full wave simulation results are marked in red, PO results are marked in blue and results calculated from the first approximation method ($\sigma_{\mathrm{coated}}^{\mathrm{FEM}} \approx \sigma_{\mathrm{PEC}}^{\mathrm{FEM}} |S_{11}^{\mathrm{planar}}|$) are marked in green. Solid curves correspond to simulations of a PEC enclosing the scatterer with absorber coating, denoted with the superscript "PEC". Dashed curves correspond to simulations of the scatterer with the absorber, denoted with the superscript "coated". All results

are normalized with the geometrical cross section of the PEC scatterer without the absorber, *i.e.* $A = \pi a^2$.

In Figure 8 it can be seen that the PEC results from the full wave- and PO simulations agree very well for all sizes of the scatterer. In the case where the scatterer is coated with a foam absorber it can be seen that for the smallest scatterer, in the upper right graph, the approximation methods represented by the blue and green dashed curves deviate from the full wave simulation, represented by the red dashed curve. When the size of the scatterer is increased this deviation is reduced and in the largest case, where the radius of curvature of the scatterer is about $5.3\lambda_0$, the approximation methods yield almost identical results as the full wave simulation.

The same geometry was simulated with a thin magnetic absorber in Figure 15, and with a Salisbury absorber in Figure 16. When comparing the results of the capped cylinder with these three different types of absorbers it can be seen that the accuracy of the RCS approximation methods varies between the different absorbers. The thin magnetic absorber seems to yield the best agreement, closely followed by the foam absorber. The Salisbury absorber also shows good agreement for the larger scatterers, but relatively poor agreement for radii of curvature $\lesssim 2\lambda_0$. This effect was investigated in great detail in [10], where it was concluded that absorbers based on "volume losses" such as in foam absorbers or thin magnetic absorbers are less sensitive to curvature than absorbers based on single or multiple layers of thin resistive sheets. Both approximation methods used in this work assume "local flatness" and this approximation is thus valid for smaller radii of curvature for absorbers that utilize volume losses.

5.2 Rounded cone

The next geometry under test is a cone with a rounded nose, as in the middle illustration in Figure 9. To the left in Figure 9 the PO geometry of the cone is presented and to the right is the corresponding full wave simulation model in Comsol Multiphysics. The radius of curvature of the nose of the scatterer is denoted a_{n1}, and the length to width ratio of the cone is the same as for the capped cylinder in Figure 6 resulting in the cone half angle $\alpha = \tan^{-1}(1/4) \approx 14°$. The angle defining the intersection between the spherical nose and the straight cone segment β is calculated as a function of a_{n1} tp achieve a smooth transition. The scattering contribution from the back edge of the scatterer is gated out in all simulations of this geometry.

This geometry is of interest for evaluating the accuracy of the RCS approximation methods for radii of curvature smaller than λ_0. A general rule of thumb for achieving high accuracy using a PO solver is to avoid simulating geometries with radii of curvature smaller than a few wavelengths in size, which indicates that we might see deviations between full wave simulations and the approximation methods. The length and width of the underlying cone are now fixed as $w = 4\lambda_0$, $L_{\mathrm{tot}} = 8\lambda_0$ while the radius of curvature of the nose is varied

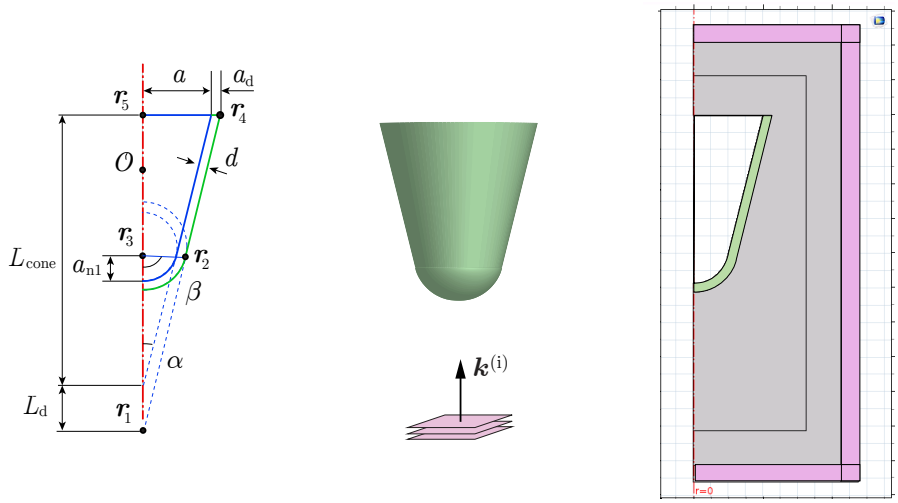

Figure 9: An example of a scattering scenario under test (center), where a scatterer coated with an absorber is illuminated by a plane wave from below the scatterer. Identical simulation models are evaluated in a PO solver (left) and a full wave solver (right). In the PO model the line segment defining the scatterer is parametrized with respect to a predefined coordinate system, and in the full wave model the geometry is generated in a graphical editor.

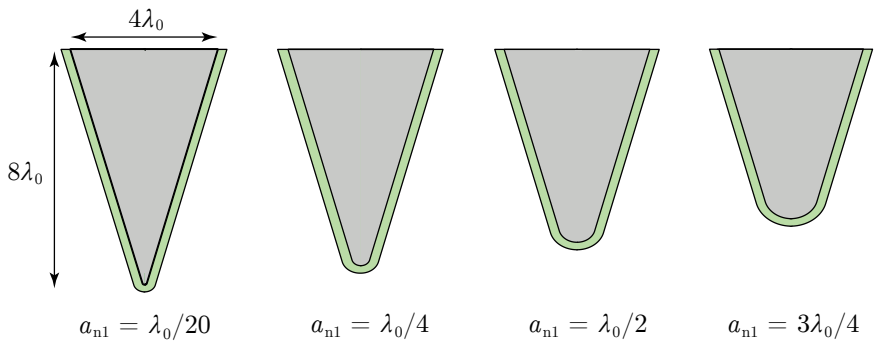

Figure 10: Cone scatterers with a spherically rounded nose. The radius of curvature of the PEC scatterers, denoted a_n1, is increasing from left to right.

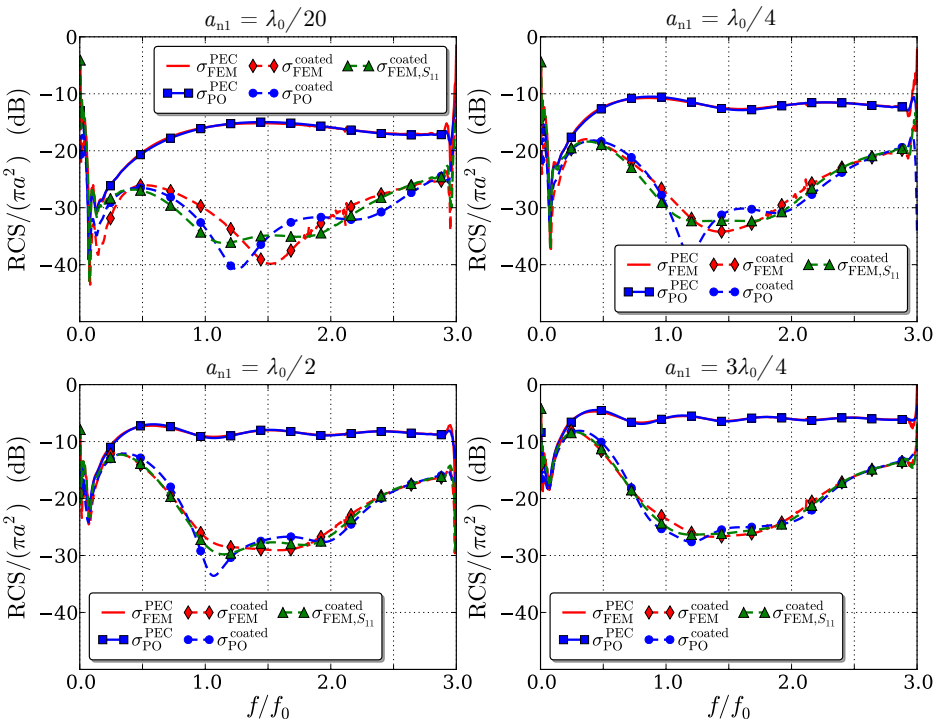

Figure 11: Simulation results of rounded cone scatterers of the same underlying size and with a varying radius of curvature in the nose, coated with a foam absorber. In the upper left plot the radius of the nose of the scatterer is $a_{n1} = \lambda_0/20$, in the upper right plot $a_{n1} = \lambda_0/4$, in the lower left plot $a_{n1} = \lambda_0/2$, and in the lower right plot $a_{n1} = 3\lambda_0/4$. The solid curves represent the RCS of a PEC enclosing the coated scatterer and the dashed curves correspond to the RCS of the coated scatterer. The dashed red curve is the full wave simulation, the dashed green curve is the first approximation method and the dashed blue curve is the PO approximation method.

$a_{n1} = [\lambda_0/20, \lambda_0/4, \lambda_0/2, 3\lambda_0/4]$, see Figure 10. The results in Figure 11 show simulations of the rounded cone scatterer with the nose radius increasing from the upper right to the lower left graph. Here it can be seen that for a radius of curvature on the order of $\lambda_0/2$ the RCS from the approximation methods and the full wave simulations deviate, but for a_{n1} in the lower right plot in Figure 11 the approximation methods yield accurate results.

In the same manner as for the previous geometry, the rounded cone scatterer was simulated with a thin magnetic absorber and a Salisbury absorber, for different radii of curvature of the nose, and the results are presented in Figures 17, 18. When comparing the results of the different absorbers a similar behavior is observed as for the capped cylinder, *i.e.* that the agreement of the approximation

methods and the full wave simulations is best for the thin magnetic absorber, slightly worse for the foam absorber and noticeably less accurate for the Salisbury absorber. In the magnetic absorber case the agreement is very good already at $a_{n1} = \lambda_0/4$. A peculiar behavior is observed in the Salisbury results, where in the PO simulations the absorber actually imply a larger RCS than the uncoated scatterer. This is most likely a result of the uncertainty of the method, and it can be seen that this effect is reduced as the radius of curvature of the scatterer is increased. It can also be seen that the agreement between the PO simulations and the full wave simulations of the uncoated scatterer is excellent for all cases evaluated, even when the radius of curvature is $\ll \lambda$.

In Appendix A.4, simulation results are presented for a sharp cone tip, with and without a Salisbury absorber. As in the previous simulated cases, the scattering from the back edge of the structure has been removed by using time gating. In Figure 21 it can be seen that the agreement between PO and full wave simulations is good for a PEC scatterer. However, it can also be seen that the proposed approximation method, using the PO solver, is not at all accurate when the cone tip is coated with an absorber. This is expected since the PO uses the interaction of the incident signal with the PEc cone and the absorber is more complicated than what can be modeled with a local reflection coefficient on a planar surface.

5.3 Rounded cone-cylinder

The final geometry under study in this work is a combination of the scatterers in Sections 5.1–5.2. A cone with a spherically rounded nose and a cylinder are merged, and a rounding of the same radius of curvature as at the nose is introduced at the joint. In Figure 12 an example of the scatterer is presented in the center illustration, and the corresponding simulation model implemented in Comsol Multiphysics and in the PO solver are presented to the right and left, respectively. The half angle of the cone segment is given by $\alpha \approx 14°$, as was the case in the rounded cone scatterer in the previous section. The size of the scatterer was defined as $w = 8\lambda_0/3$, $L_{\text{tot}} = 32\lambda_0/3$ to avoid very long simulation times when generating the full wave simulation results. Just as for the previous geometries the scattering from the back edge of the cylinder is gated out.

A parametric sweep was carried out were the radius of curvature of the nose and the rounded joint was varied as $A_{n1} = [\lambda_0/10, \lambda_0/4, \lambda_0/2, \lambda_0, 4\lambda_0/3]$. When the radius of curvature of the nose and joint take the value of half the width of the scatterer, as in the rightmost illustration in Figure 13, the center of the two spherical components coincide and structure takes the same form as the hemispherically capped cylinder in Section 5.1. The results of this scenario is presented for the three different absorbers in the lower left plot in Figure 8 and Figures 15–16.

Simulation results of the rounded cone-cylinder are presented in Figure 14, where the radius of curvature of the nose is increased in the order from the upper left plot, to the upper right, to the lower left and finally the lower right plot. For

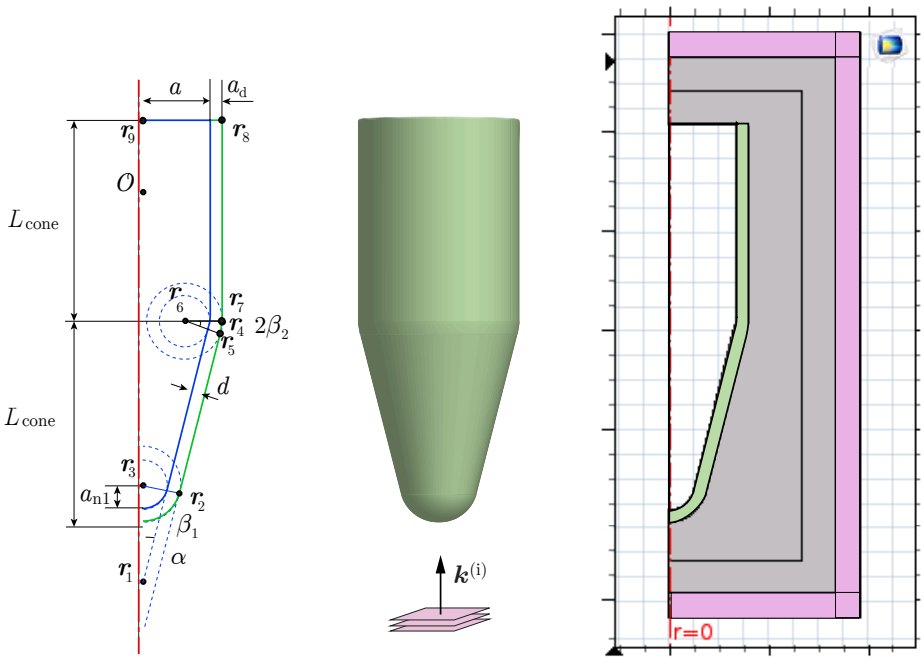

Figure 12: An example of a scattering scenario under test (center), where a scatterer coated with an absorber is illuminated by a plane wave from below the scatterer. Identical simulation models are evaluated in a PO solver (left) and a full wave solver (right).

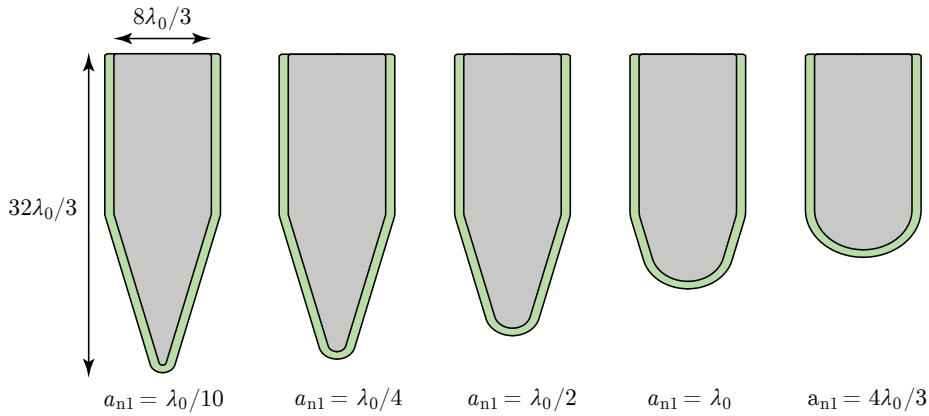

Figure 13: Cone-cylinder scatterers with a spherically rounded nose and middle edge. The radius of curvature of the PEC scatterers, denoted a_{n1}, is increasing from left to right.

the smallest nose curvature in the upper left plot all curves are oscillating quite rapidly due to interference between the signals scattered from the nose and the joint between the cone and the cylinder parts of the scatterer. It can be seen that the agreement between PO- and full wave simulations is still very good in the PEC scenario, but in the absorber case the approximation methods are showing much larger oscillations than the full wave simulations. As the radius of curvature of the nose is increased the oscillations of the absorber coated curves are reduced and the approximation methods yield better results. When comparing the results in Figure 14 with the results of the rounded cone in Figure 11 it is observed that the approximation methods yield better results for the cone scatterer. This is most likely due to the fact that both methods are based on a "local flatness" assumption, which is very accurate for specular reflections, but not as accurate for non-specular (or diffused) reflections. The second type of reflections are often a result on diffraction, which is not fully incorporated in PO.

The geometries in Figure 13 were also evaluated for the thin magnetic absorber and the Salisbury absorber and the results are presented in Figures 19–20. Here it can be seen that the approximation methods yield similar accuracy for the foam absorber and the magnetic absorber, where reasonably accuracy is achieved when $a_{n1} \geq \lambda_0/2$. For the Salisbury absorber the accuracy is significantly worse and good agreement is not achieved in any of the scenarios evaluated.

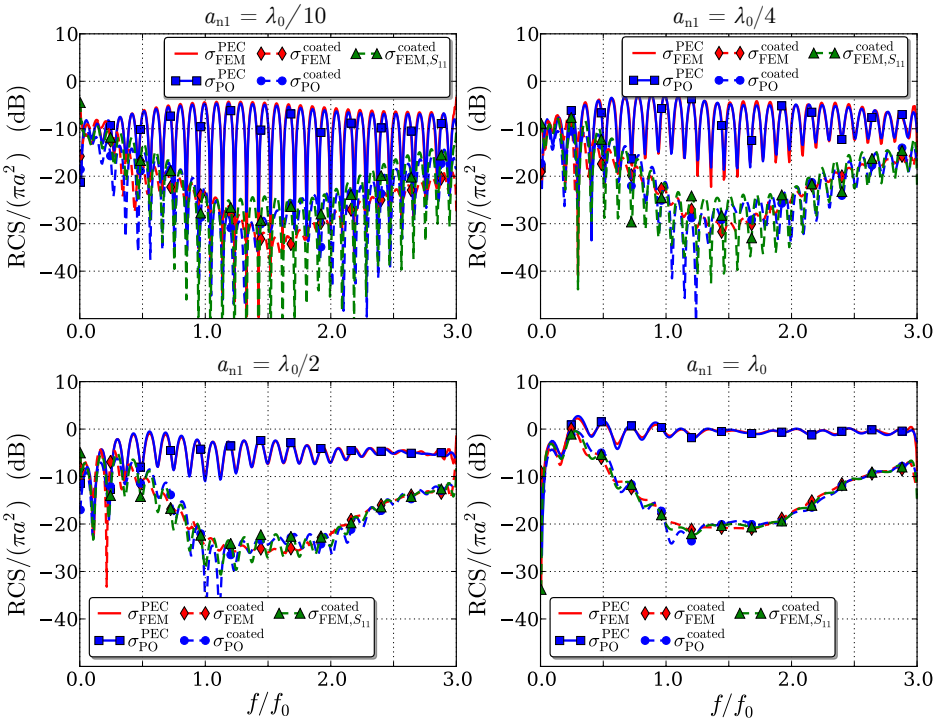

Figure 14: Simulation results of rounded cone-cylinder scatterers of the same underlying size and with a varying radius of curvature in the nose, coated with a foam absorber. In the upper left plot the radius of the nose of the scatterer is $a_{n1} = \lambda_0/10$, in the upper right plot $a_{n1} = \lambda_0/4$, in the lower left plot $a_{n1} = \lambda_0/2$, and in the lower right plot $a_{n1} = \lambda_0$. The solid curves represent the RCS of a PEC enclosing the coated scatterer and the dashed curves correspond to the RCS of the coated scatterer. The dashed red curve is the full wave simulation, the dashed green curve is the first approximation method and the dashed blue curve is the PO approximation method.

6 Evaluation of approximation methods

The two approximation methods introduced in this work have been thoroughly evaluated and it has been shown that in most cases they yield similar results. This is most likely due to the fact that the PO- and full wave simulations of a PEC enclosing the scatterer show excellent agreement for all geometries evaluated, as long as the diffraction scattering from the back edge is gated out. The first method is relatively fast if simulated in a full wave solver, since the absorber is not meshed in the simulation model. However, if a PO solver is used, as in the second approximation method, the simulations are carried out in a few seconds since only a line integral describing the scatterer is required.

It has been shown that for specular reflections the approximation methods yield accurate results for scatterers coated with an absorber, when the radius of curvature of the scatterer is larger that about $\lambda_0/2 - \lambda_0$. But it has also been observed that both methods yield significantly better agreement for the foam absorber and the magnetic absorber than the Salisbury absorber. This behavior was described in detail for spherical scatterers in [10], where it was concluded that absorbers based on single or multiple layers of resistive sheets are more sensitive to curvature than absorbers based on "volume losses". Since the approximation methods used in this work are derived from the work in [10] it was expected that the same behavior is observed for the scatterers under study. The agreement between the approximation methods and the full wave simulations was not as good for the final geometry under study as for the previous two geometries. This is most likely due to the fact that the scattering from the joint between the cylinder and the cone components of the scatterer is causing non-specular reflections that are not as accurately modeled by PO as ordinary specular reflections.

7 Conclusions

Two approximation methods have been presented for calculating monostatic RCS from axial-symmetric scatterers coated with electromagnetic absorbers. The methods are designed for plane wave illumination parallel to the axis of rotation of the scatterer. The first methods is based on simulating the scattering of a PEC enclosing the absorber coated scatterer, and multiplying the result with the squared magnitude of the absorber reflection coefficient in a planar scenario. The second method is based on simulating the scattering scenario in a PO solver, where the electromagnetic absorber is treated as a reflection dyadic at the outer surface of the scatterer. Both methods result in a significant acceleration in computation speed, where the PO method carries out the computations in a number of seconds.

The monostatic scattering from three different geometries have been investigated, and parametric sweeps were carried out to test the limits where the methods yield accurate results. The two methods yield similar results in most cases evaluated in this study. This is due to the fact that the agreement between PO- and full wave simulations of a PEC scatterer is excellent, even for radii of curvature much smaller that the wavelength of incident signals. For specular reflections, the approximation methods yield very accurate results compared to full wave simulations when the radius of curvature is on the order of 1/2-1 wavelength of the signal. It is also concluded that the accuracy of the two methods vary depending on what type of absorber is applied to the scatterer, and that absorbers based on "volume losses" such as carbon doped foam absorber and thin magnetic absorbers yield better results than for absorbers based on resistive sheets, such as a Salisbury absorber.

Appendix A Simulation results

In this appendix, a collection of simulation results are presented. All geometries introduced in Section 5 have been coated with a thin magnetic absorber or a Salisbury absorber, defined in Section 4, and the monostatic scattering results are presented in Figures 15–20. In Section A.4, simulation results are presented for a sharp cone tip, with and without an absorber.

A.1 Hemispherically capped cylinder

A.1.1 Thin magnetic absorber

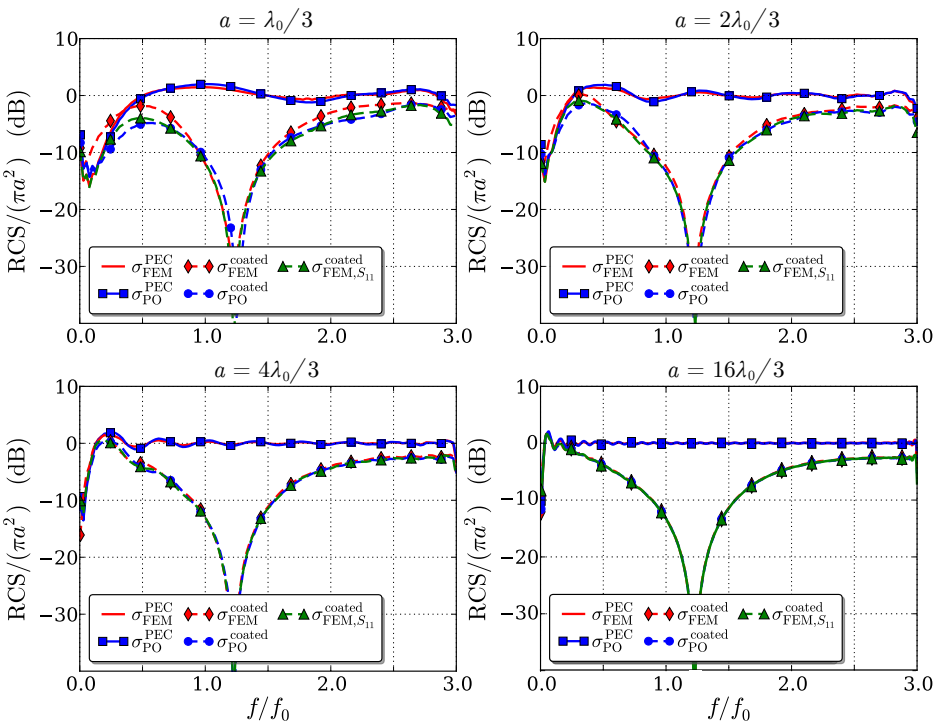

Figure 15: Simulation results of capped cylinder scatterers of different sizes, coated with a thin magnetic absorber. In the upper left plot the radius of the scatterer is $a = \lambda_0/3$, in the upper right plot $a = 2\lambda_0/3$, in the lower left plot $a = 4\lambda_0/3$, and in the lower right plot $a = 16\lambda_0/3$. The solid curves represent the RCS of a PEC enclosing the coated scatterer and the dashed curves correspond to the RCS of the coated scatterer. The dashed red curve is the full wave simulation, the dashed green curve is the first approximation method and the dashed blue curve is the PO approximation method.

A.1.2 Salisbury absorber

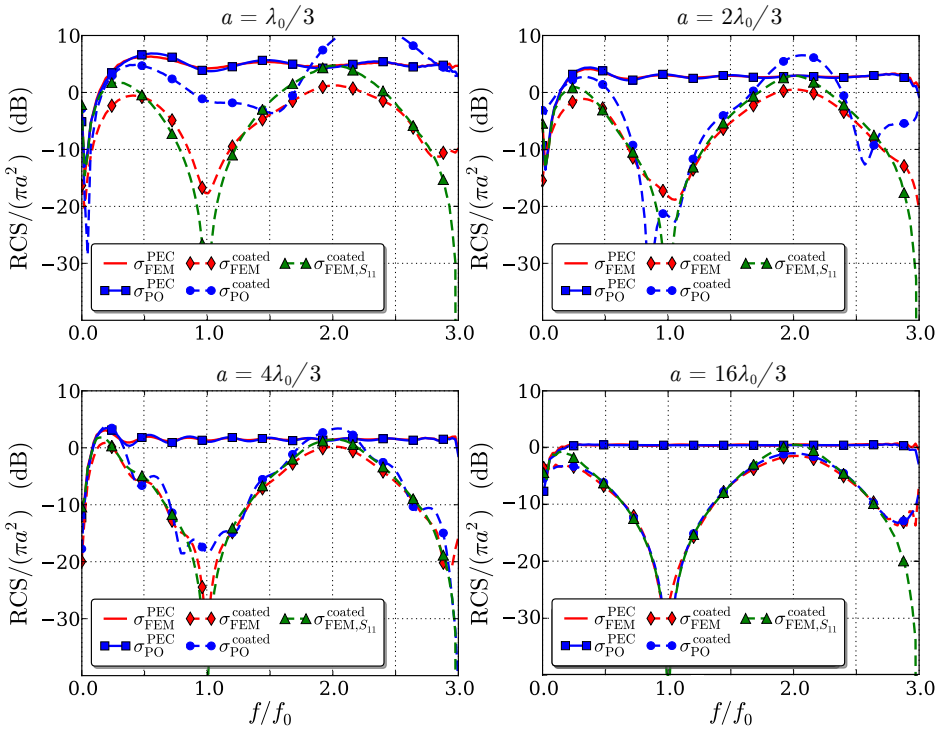

Figure 16: Simulation results of capped cylinder scatterers of different sizes, coated with a Salisbury absorber. In the upper left plot the radius of the scatterer is $a = \lambda_0/3$, in the upper right plot $a = 2\lambda_0/3$, in the lower left plot $a = 4\lambda_0/3$, and in the lower right plot $a = 16\lambda_0/3$. The solid curves represent the RCS of a PEC enclosing the coated scatterer and the dashed curves correspond to the RCS of the coated scatterer. The dashed red curve is the full wave simulation, the dashed green curve is the first approximation method and the dashed blue curve is the PO approximation method.

A.2 Rounded cone

A.2.1 Thin magnetic absorber

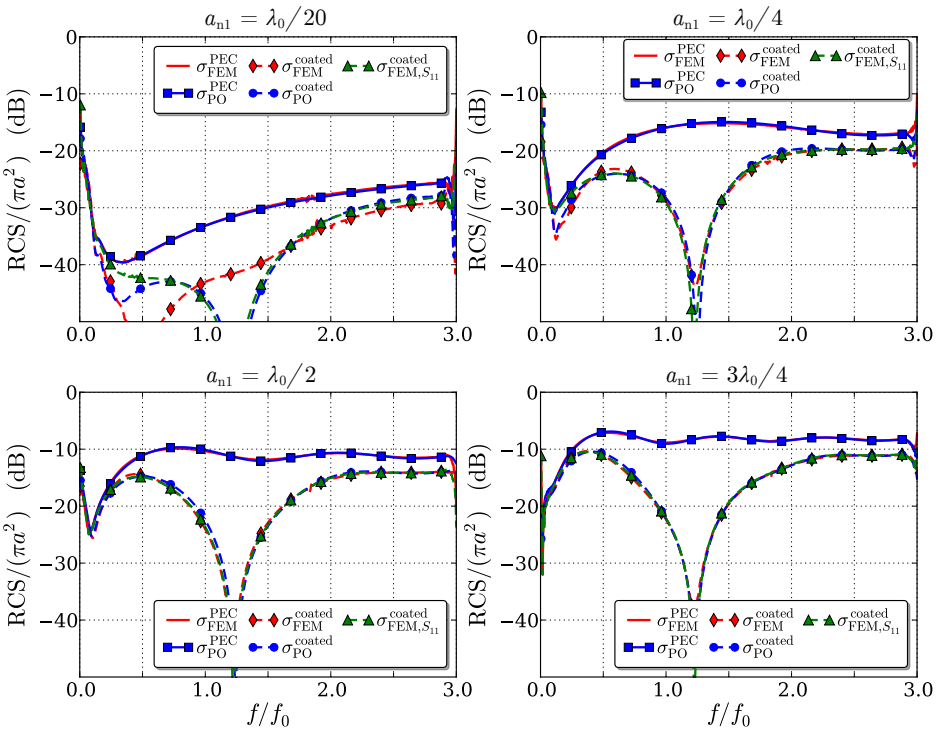

Figure 17: Simulation results of rounded cone scatterers of the same underlying size and with a varying radius of curvature in the nose, coated with a thin magnetic absorber. In the upper left plot the radius of the nose of the scatterer is $a_{n1} = \lambda_0/20$, in the upper right plot $a_{n1} = \lambda_0/4$, in the lower left plot $a_{n1} = \lambda_0/2$, and in the lower right plot $a_{n1} = 3\lambda_0/4$. The solid curves represent the RCS of a PEC enclosing the coated scatterer and the dashed curves correspond to the RCS of the coated scatterer. The dashed red curve is the full wave simulation, the dashed green curve is the first approximation method and the dashed blue curve is the PO approximation method.

A.2.2 Salisbury absorber

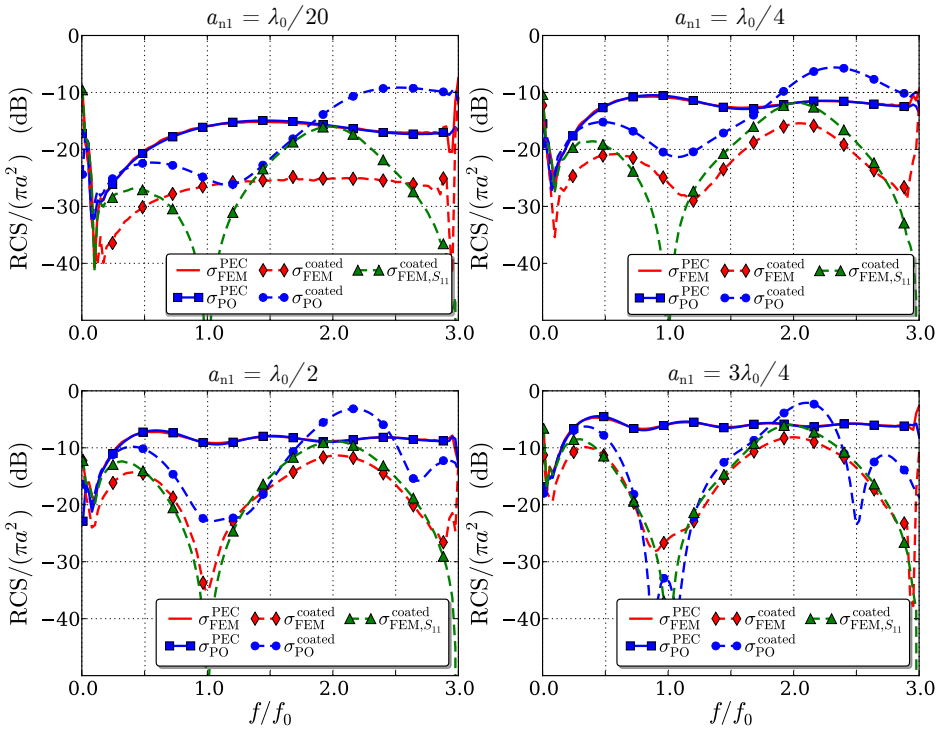

Figure 18: Simulation results of rounded cone scatterers of the same underlying size and with a varying radius of curvature in the nose, coated with a Salisbury absorber. In the upper left plot the radius of the nose of the scatterer is $a_{n1} = \lambda_0/20$, in the upper right plot $a_{n1} = \lambda_0/4$, in the lower left plot $a_{n1} = \lambda_0/2$, and in the lower right plot $a_{n1} = 3\lambda_0/4$. The solid curves represent the RCS of a PEC enclosing the coated scatterer and the dashed curves correspond to the RCS of the coated scatterer. The dashed red curve is the full wave simulation, the dashed green curve is the first approximation method and the dashed blue curve is the PO approximation method.

A.3 Rounded cone-cylinder

A.3.1 Magnetic absorber

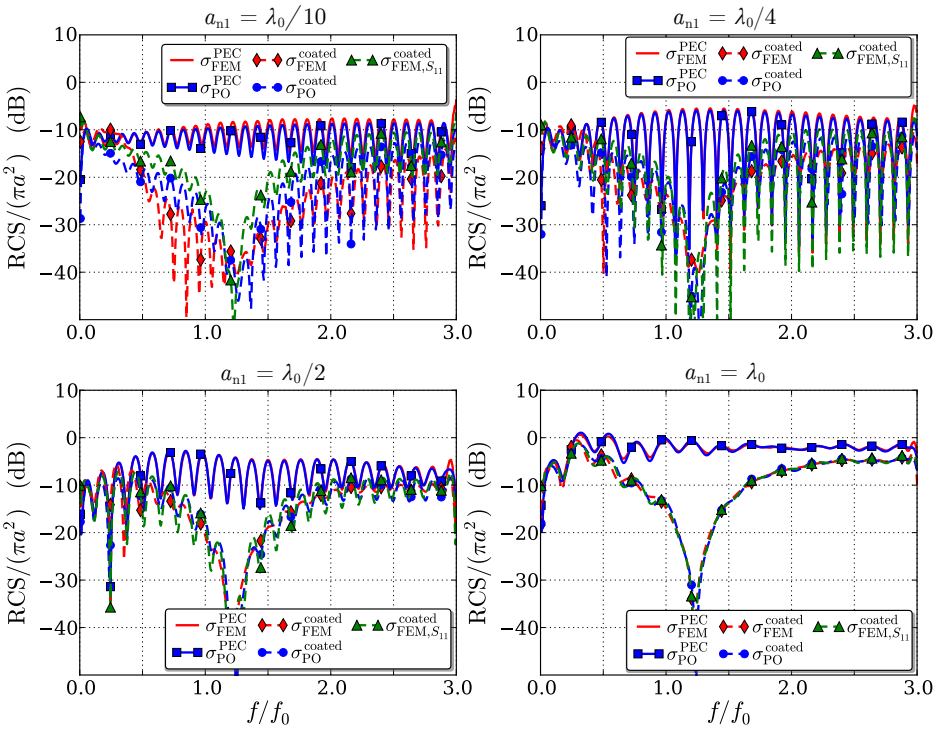

Figure 19: Simulation results of rounded cone-cylinder scatterers of the same underlying size and with a varying radius of curvature in the nose, coated with a thin magnetic absorber. In the upper left plot the radius of the nose of the scatterer is $a_{n1} = \lambda_0/10$, in the upper right plot $a_{n1} = \lambda_0/4$, in the lower left plot $a_{n1} = \lambda_0/2$, and in the lower right plot $a_{n1} = \lambda_0$. The solid curves represent the RCS of a PEC enclosing the coated scatterer and the dashed curves correspond to the RCS of the coated scatterer. The dashed red curve is the full wave simulation, the dashed green curve is the first approximation method and the dashed blue curve is the PO approximation method.

A.3.2 Salisbury absorber

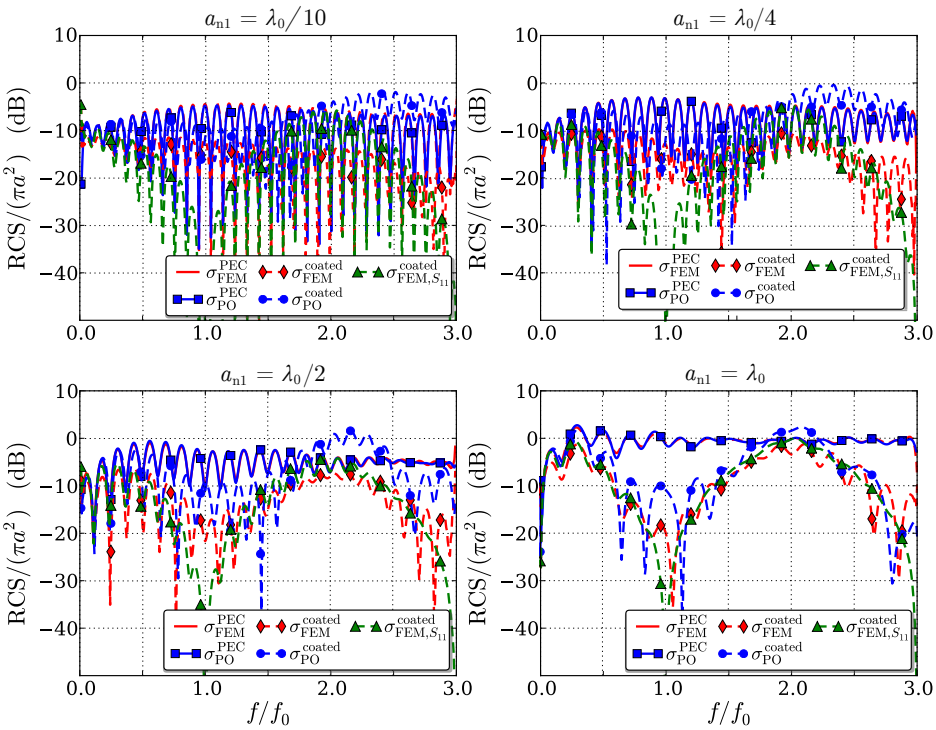

Figure 20: Simulation results of rounded cone-cylinder scatterers of the same underlying size and with a varying radius of curvature in the nose, coated with a Salisbury absorber. In the upper left plot the radius of the nose of the scatterer is $a_{n1} = \lambda_0/10$, in the upper right plot $a_{n1} = \lambda_0/4$, in the lower left plot $a_{n1} = \lambda_0/2$, and in the lower right plot $a_{n1} = \lambda_0$. The solid curves represent the RCS of a PEC enclosing the coated scatterer and the dashed curves correspond to the RCS of the coated scatterer. The dashed red curve is the full wave simulation, the dashed green curve is the first approximation method and the dashed blue curve is the PO approximation method.

A.4 Sharp cone tip

For the sake of completeness, the scattering from a sharp cone tip was simulated, both using a full wave solver and the in-house code. The geometry of the scatterer can be seen in B.3, the size of the scatterer was defined as $a = 4\lambda_0/3$, and the same frequency range was used as in previous simulations. In [19, p.255], the monostatic scattering from a cone tip is stated to be approximately related to

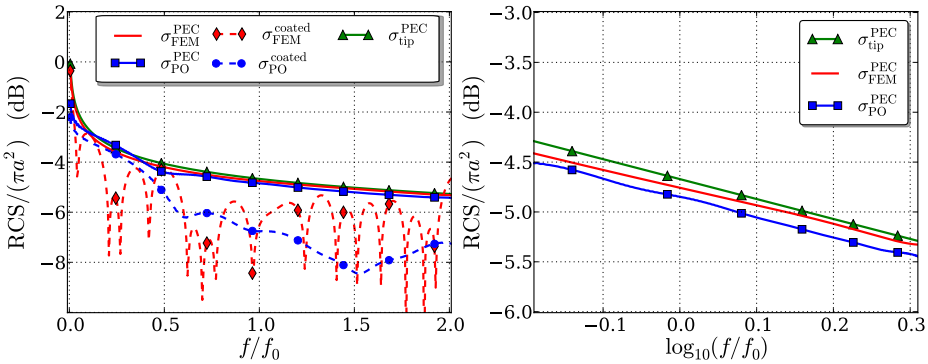

Figure 21: Simulation results of a PEC cone tip, with and without a foam absorber applied. To the left, simulation results from the in-house PO solver and a full wave solver are compared to the asymptotic scattering from a cone tip in (A.1). To the right, the PO scattering data is plotted in log-log scale and the simulated results are compared to the asymptotic relation.

the opening angle of the cone 2α, and the frequency f as

$$\sigma_{\text{tip}}^{\text{PEC}} \approx (0.256 \cdot 2\alpha)^{4.3} \left(\frac{c_0}{f}\right)^2. \tag{A.1}$$

This result is verified in Figure 21 where simulation results are presented for the scattering from a cone tip. In order to evaluate if the approximation method based on PO simulations is accurate in this type of scenario, a foam absorber was also added to the structure, see the dashed lines in Figure 21. The scattering data from the cone is truncated using time gating, but to extract the desired information a small modification is applied to the time gating procedure. Due to the frequency dependency of the cone tip scattering contribution (A.1), the spectrum of the scattered far field was weighted before transformation into the time domain. The spectrum of a differentiated Gaussian pulse was here used as a weighting function. This weight function, operating on the scattered far field, have a linear frequency slope which was used to compensate for the $1/f^2$-dependency in the RCS of (A.1). Without this operation, it is not possible to separate the scattered contributions from the cone tip and the rest of the structure the in time domain. This weighting operation was compensated for after the signal had been gated and transformed back to the frequency domain.

In the left plot in Figure 21, simulation results are compared to the asymptotic relation (A.1) and it can be seen that the PO and full wave simulation results agree very well with the asymptotic relation. In the case with a foam absorber applied it can be seen that the approximative results acquired using PO deviate from the full wave simulation results. This indicates that the proposed approximation methods are not suitable for calculating scattering from sharp edges coated with an electromagnetic absorber. In the right plot in Figure 21, the scattering from a PEC cone tip is calculated using FEM, PO and the ex-

pression (A.1) and plotted in log-log scale. Here it can be seen that the slope of the three curves, corresponding to the frequency dependency of $1/f^2$ is almost identical in the three curves. The slight vertical shift that can be seen is most likely caused by the gating procedure.

Appendix B Parametrization of axially symmetric objects

A detailed parametrization of each scatterer under study is presented in this appendix.

B.1 General theory

A curve γ defining a axially symmetric scatterer can be parametrized by a real scalar q:

$$\gamma = \{\boldsymbol{r}(q) : \ 0 \leq q \leq 1\}, \tag{B.1}$$

where $\boldsymbol{r}(q) = \rho(q)\hat{\boldsymbol{\rho}} + z(q)\hat{\boldsymbol{z}}$. The start point $\boldsymbol{r}(0)$ is chosen at the bottom of each scatterer and the end point $\boldsymbol{r}(1)$ is at the top. Defining the unit vector as

$$\hat{\boldsymbol{n}}(q) = \frac{z'(q)\hat{\boldsymbol{\rho}} - \rho'(q)\hat{\boldsymbol{z}}}{\sqrt{(z'(q))^2 + (\rho'(q))^2}} \tag{B.2}$$

then makes it point out of the object (in the typical case, we have $z'(q) \geq 0$). The angle of incidence is given by

$$\cos\theta = -\hat{\boldsymbol{z}} \cdot \hat{\boldsymbol{n}}(q) = \frac{\rho'(q)}{\sqrt{(z'(q))^2 + (\rho'(q))^2}}. \tag{B.3}$$

Finally, the length element is $\mathrm{d}\ell = (\mathrm{d}\ell/\,\mathrm{d}q)\,\mathrm{d}q$, where

$$\frac{\mathrm{d}\ell}{\mathrm{d}q} = \sqrt{(z'(q))^2 + (\rho'(q))^2}. \tag{B.4}$$

In special cases it may be easier to do the parametrization more explicitly. The approach that is used here is to identify the location of key points of the geometry in a global coordinate system $\boldsymbol{r}_i = (\rho_i, z_i)$, break down the parametrization in separate regions, and from these points determine the parametrization of the scatterer.

B.2 Hemispherically capped cylinder

To parametrize a hemispherically capped cylinder coated with an absorber as in Figure 22 the parametrization is broken down to three regions. Key points of the geometry are identified and marked in Figure 22, and the coordinates of these

points are defined in Table 1 where L is the length of the cylinder, a is the radius of the hemispherical nose and $a_\mathrm{n} = a + d$ is the radius of the absorber coated hemispherical nose. Here, it is clearly seen that the straight part of the cylinder and the flat top do not satisfy $\cos\theta > 0$, and hence are in the shadow region in the physical optics approximation.

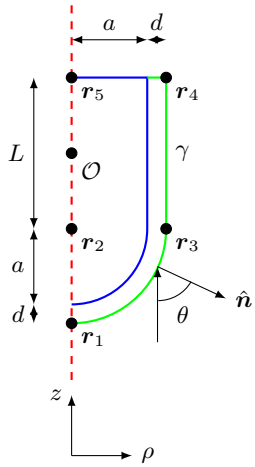

Figure 22: A typical geometry, with a hemispherically capped right circular cylinder of height L and radius a. The total height is $L + a$.

Table 1: Key points of interest for parametrization of a hemispherically capped cylinder coated with an absorber.

	$\boldsymbol{r}_1$	$\boldsymbol{r}_2$	$\boldsymbol{r}_3$	$\boldsymbol{r}_4$	$\boldsymbol{r}_5$
ρ_i	0	0	a_n	a_n	0
z_i	$-L/2 - a_\mathrm{n}$	$-L/2$	$-L/2$	$L/2$	$L/2$

Table 2: Parametrization of hemispherically capped cylinder coated with an absorber.

	Spherical nose	Straight cylinder	Flat top
q	$0 \le q < 1/3$	$1/3 \le q < 2/3$	$2/3 \le q \le 1$
$\rho(q)$	$a_\mathrm{n}\sin(q3\pi/2)$	ρ_3	$\rho_4 - \rho_4(3q-2)$
$z(q)$	$z_2 - a_\mathrm{n}\cos(q3\pi/2)$	$z_3 + (z_4 - z_3)(3q-1)$	z_5
$\hat{\boldsymbol{n}}(q)$	$\sin(q3\pi/2)\hat{\boldsymbol{\rho}} - \cos(q3\pi/2)\hat{\boldsymbol{z}}$	$\hat{\boldsymbol{\rho}}$	$\hat{\boldsymbol{z}}$
$\mathrm{d}\ell/\,\mathrm{d}q$	$\lvert a_\mathrm{n} 3\pi/2\rvert$	$\lvert 3(z_4 - z_3)\rvert$	$\lvert 3(\rho_5 - \rho_4)\rvert$
$\cos\theta(q)$	$\cos(q3\pi/2)$	0	-1

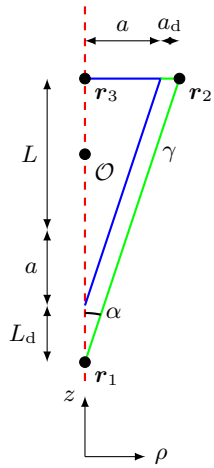

Figure 23: A cone scatterer with total height $L + a$ and width a, coated with an absorber with thickness d.

B.3 Cone

A cone with the same width and length as the capped cylinder in Section B.2 is presented in Figure 23 and is defined by the points $\boldsymbol{r}_1, \boldsymbol{r}_2, \boldsymbol{r}_3$ specified in Table 3. The thickness of the absorber is dented d and the parameters $L_\mathrm{d} = d/\sin(\alpha)$, $a_\mathrm{d} = d/\cos(\alpha)$ are introduced to take this into consideration. The cone is parametrized according to the expressions in Table 4.

Table 3: Key points of interest for parametrization of a cone scatterer coated with an absorber.

	$\boldsymbol{r}_1$	$\boldsymbol{r}_2$	$\boldsymbol{r}_3$
ρ_i	0	$a + a_\mathrm{d}$	0
z_i	$-L/2 - a - L_\mathrm{d}$	$L/2$	$L/2$

B.4 Rounded cone

Next we consider a cone with a spherically rounded nose. The underlying cone has the same width and length as the capped cylinder in Section B.2, but the total length of the rounded cone depends on the radius of curvature of the nose. The geometry is presented in Figure 24 and is parametrized through the key points $\boldsymbol{r}_i$, $i = 1, 2, .., 5$. The thickness of the applied absorber is denoted d and the parameters $L_\mathrm{d} = d/\sin(\alpha)$, $a_\mathrm{d} = d/\cos(\alpha)$ are introduced to maintain the absorber thickness along the surface of the scatterer.

Table 4: Parametrization of cone coated with an absorber.

	Cone segment	Flat top
q	$0 \le q < 1/2$	$1/2 \le q \le 1$
$\rho(q)$	$\rho_1 + (\rho_2 - \rho_1)2q$	$\rho_2 + (\rho_3 - \rho_2)(2q-1)$
$z(q)$	$z_1 + (z_2 - z_1)2q$	z_2
$\hat{\boldsymbol{n}}(q)$	$\dfrac{(z_2 - z_1)\hat{\boldsymbol{\rho}} - (\rho_2 - \rho_1)\hat{\boldsymbol{z}}}{\sqrt{(z_2 - z_1)^2 + (\rho_2 - \rho_1)^2}}$	$\hat{\boldsymbol{z}}$
$\mathrm{d}\ell/\,\mathrm{d}q$	$2\sqrt{(z_2 - z_1)^2 + (\rho_2 - \rho_1)^2}$	$2\lvert\rho_3 - \rho_2\rvert$
$\cos\theta(q)$	$\dfrac{\rho_2 - \rho_1}{\sqrt{(z_2 - z_1)^2 + (\rho_2 - \rho_1)^2}}$	-1

Table 5: Key points of interest for parametrization of a rounded cone scatterer coated with an absorber.

	$\boldsymbol{r}_1$	$\boldsymbol{r}_2$	$\boldsymbol{r}_3$	$\boldsymbol{r}_4$	$\boldsymbol{r}_5$
ρ_i	0	ρ_2	0	$a + a_\mathrm{d}$	0
z_i	$-L/2 - a - L_\mathrm{d}$	z_2	z_3	$L/2$	$L/2$

In order to parametrize the scatterer we need to determine the coordinates of the center of the spherical nose, as well as the intersecting point between the spherical nose and the cone in such a way that the first order derivative is continuous at this point. This point, denoted $\boldsymbol{r}_2$, is given by the relations

$$\rho_2 = \sqrt{\frac{a_{\mathrm{n}2}^2}{\tan(\alpha)^2 + 1}}, \qquad z_2 = z_1 + \frac{1}{\tan(\alpha)}\sqrt{\frac{a_{\mathrm{n}2}^2}{\tan(\alpha)^2 + 1}}, \tag{B.5}$$

where $a_{\mathrm{n}2} = a_{\mathrm{n}1} + d$ is the radius of the nose including the absorber coating. From $\boldsymbol{r}_2$ the location of the center of the nose, denoted $\boldsymbol{r}_3$, is calculated using the relations

$$\rho_3 = 0, \qquad z_3 = z_2 + \sqrt{a_{\mathrm{n}2}^2 - \rho_2^2}. \tag{B.6}$$

The angle β in Figure 24 defining the nose is given by $\beta = \arcsin(\rho_2/a_{\mathrm{n}2})$, and the key points of the geometry is summarized in Table 5. To parametrize a rounded capped cone as in Figure 24, the parametrization is broken down to three regions

Figure 24: A capped cone scatterer with total height $L+a$ and width a, coated with an absorber with thickness d.

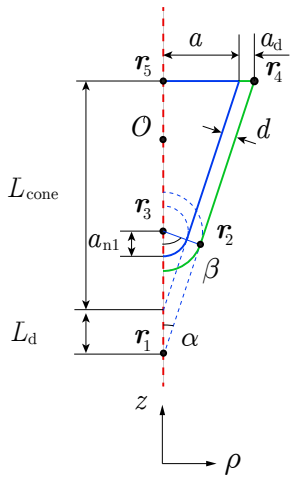

B.5 Capped cone-cylinder

A slightly more complicated structure consisting of a cone and a cylinder is parametrized. The same rounding is introduced in the nose and at the wedge in the middle of the structure, see Figure 25. The nose is parametrized in the same way as in Section B.4 where the spherical nose has the maximum parametrization angle β_1. To determine the location of the center of the upper rounding $\boldsymbol{r}_6$ and the spherical parametrization angle of the upper rounding $2\beta_2$, a number of trigonometric expressions are introduced:

$$\gamma_1 = \alpha - \pi/2, \qquad \gamma_2 = \alpha/2, \qquad \beta_1 = \arcsin(\rho_2/a_{\mathrm{n}2}), \qquad \beta_2 = \pi/2 - \alpha/2,$$

$$x = a_{\mathrm{n}2}\sqrt{\frac{1}{\tan(\gamma_2)^2+1}\left(1+\frac{1}{\tan(\gamma_2)^2}\right)} = \frac{a_{\mathrm{n}2}}{|\tan\gamma_2|}, \tag{B.7}$$

where γ_1, γ_2 are relevant angles related to the rounding of the edges, and $x = |\boldsymbol{r}_7 - \boldsymbol{r}_4| = |\boldsymbol{r}_5 - \boldsymbol{r}_4|$ is the distance between points of interest. After some calculations, the key coordinates of the geometry in Figure 25 were identified and are summarized in Table 7 where (ρ_1, z_1), (ρ_2, z_2), (ρ_3, z_3) are defined as in (B.5)–(B.6) and in Table 5. From these coordinates is is relatively straightforward to parametrize the scatterer in Figure 25, and the key parameters are presented in Table 8.

Table 6: Parametrization of the scatterer in Figure 24.

	Spherical nose	Cone segment	Flat top
q	$0 < q < 1/3$	$1/3 < q < 2/3$	$2/3 < q < 1$
$\rho(q)$	$a_{\mathrm{n}2} \sin(q3\beta)$	$\rho_2 + (\rho_4 - \rho_2)(3q-1)$	$\rho_4 - \rho_4(3q-2)$
$z(q)$	$z_3 - a_{\mathrm{n}2} \cos(q3\beta)$	$z_2 + (z_4 - z_2)(3q-1)$	z_4
$\hat{\boldsymbol{n}}(q)$	$\sin(q3\beta)\hat{\boldsymbol{\rho}} - \cos(q3\beta)\hat{\boldsymbol{z}}$	$\dfrac{(z_4 - z_2)\hat{\boldsymbol{\rho}} - (\rho_4 - \rho_2)\hat{\boldsymbol{z}}}{\sqrt{(z_4 - z_2)^2 + (\rho_4 - \rho_2)^2}}$	$\hat{\boldsymbol{z}}$
$\mathrm{d}\ell/\,\mathrm{d}q$	$a_{\mathrm{n}2} 3\beta$	$3\sqrt{(z_4 - z_2)^2 + (\rho_4 - \rho_2)^2}$	$3\lvert\rho_4\rvert$
$\cos\theta(q)$	$\cos(3q\beta)$	$\dfrac{3q(\rho_4 - \rho_2)}{\sqrt{(z_4 - z_2)^2 + (\rho_4 - \rho_2)^2}}$	-1

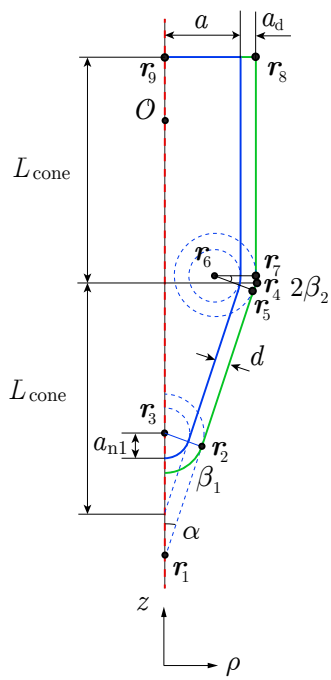

Figure 25: A rounded cone-cylinder scatterer with total height $2L + 2a$ and width a, coated with an absorber with thickness d.

Table 7: Key points of interest for parametrization of a rounded cone-cylinder scatterer coated with an absorber.

	$\boldsymbol{r}_1$	$\boldsymbol{r}_2$	$\boldsymbol{r}_3$	$\boldsymbol{r}_4$	$\boldsymbol{r}_5$	$\boldsymbol{r}_6$	$\boldsymbol{r}_7$	$\boldsymbol{r}_8$	$\boldsymbol{r}_9$
ρ_i	ρ_1	ρ_2	ρ_3	$a+d$	$\rho_6 + a_{\mathrm{n}2}\cos(\alpha)$	$\rho_4 - a_{\mathrm{n}2}$	ρ_4	ρ_4	0
z_i	z_1	z_2	z_3	$L/2$ $-d\tan(\alpha/2)$	$z_6 - a_{\mathrm{n}2}\sin(\alpha)$	$z_4 + x$	z_6	$L/2$ $+L_{\mathrm{cone}}$	z_8

Table 8: Parametrization of the scatterer in Figure 25.

	Spherical nose	Cone segment
q	$0 \le q < 1/5$	$1/5 \le q < 2/5$
$\rho(q)$	$a_{\mathrm{n}2}\sin(5q\beta_1)$	$\rho_2 + (\rho_5 - \rho_2)(5q-1)$
$z(q)$	$z_3 - a_{\mathrm{n}2}\cos(5q\beta_1)$	$z_2 + (z_5 - z_2)(5q-1)$
$\hat{\boldsymbol{n}}(q)$	$\sin(5q\beta_1)\hat{\boldsymbol{\rho}} - \cos(5q\beta_1)\hat{\boldsymbol{z}}$	$\dfrac{(z_5-z_2)\hat{\boldsymbol{\rho}} - (\rho_5-\rho_2)\hat{\boldsymbol{z}}}{\sqrt{(z_5-z_2)^2+(\rho_5-\rho_2)^2}}$
$\mathrm{d}\ell/\,\mathrm{d}q$	$a_{\mathrm{n}2}5\beta_1$	$5\sqrt{(z_5-z_2)^2+(\rho_5-\rho_2)^2}$
$\cos\theta(q)$	$\cos(5q\beta_1)$	$\dfrac{5q(\rho_5-\rho_2)}{\sqrt{(z_5-z_2)^2+(\rho_5-\rho_2)^2}}$

	Rounded edge	Straight cylinder
q	$2/5 \le q < 3/5$	$3/5 \le q < 4/5$
$\rho(q)$	$\rho_6 + a_{\mathrm{n}2}\cos((5q-3)2\beta_2)$	ρ_7
$z(q)$	$z_6 + a_{\mathrm{n}2}\sin((5q-3)2\beta_2)$	$z_7 + (z_8 - z_7)(5q-3)$
$\hat{\boldsymbol{n}}(q)$	$\cos((5q-3)2\beta_2)\hat{\boldsymbol{\rho}}$ $+\sin((5q-3)2\beta_2)\hat{\boldsymbol{z}}$	$\hat{\boldsymbol{\rho}}$
$\mathrm{d}\ell/\,\mathrm{d}q$	$a_{\mathrm{n}2}10\beta_2$	$5(z_8 - z_7)$
$\cos\theta(q)$	$-\sin((5q-3)2\beta_2)$	0

	Flat top	
q	$4/5 \le q \le 1$	
$\rho(q)$	$\rho_8 - \rho_8(5q-4)$	
$z(q)$	z_8	
$\hat{\boldsymbol{n}}(q)$	$\hat{\boldsymbol{z}}$	
$\mathrm{d}\ell/\,\mathrm{d}q$	$5\rho_8$	
$\cos\theta(q)$	-1	

Appendix C Full wave benchmark simulations and mesh convergence

A capped cylinder with the parameters $a = 4\lambda_0/3$, $L_{\text{tot}} = 16\lambda_0/3$, $w = 8\lambda_0/3$ has been simulated both in FEKO and in Comsol Multiphysics for validation of simulation results from the 2D axially symmetric solver in Comsol Multiphysics, which is used for most full wave simulations in this work. The structure was simulated both with and without a Salisbury absorber, using 10 steps per wavelength mesh setting, and the results in Figure 26 show good agreement between the softwares. In the right plot in Figure 26 a mesh convergence study is presented, where a PEC capped cylinder of the same size as in the left plot has been simulated using different mesh settings. It can be seen that when 10 steps per wavelength (at the shortest wavelength of the simulation λ_2) mesh setting is used, the agreement is good in comparison to much finer mesh settings.

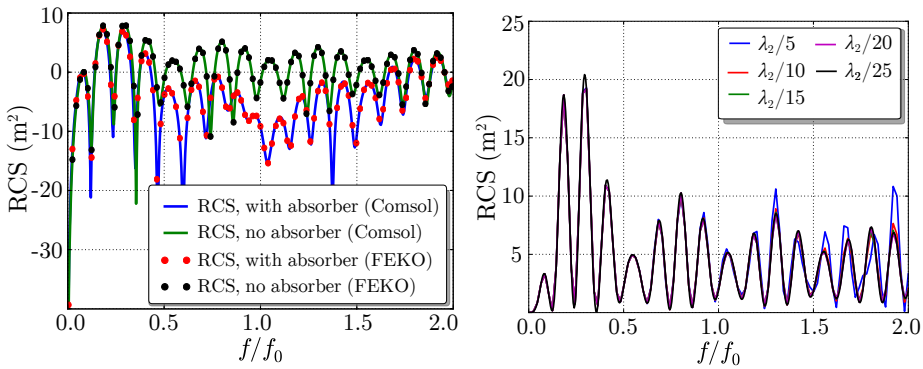

Figure 26: In the left plot the monostatic RCS of a capped cylinder simulated both in FEKO and in Comsol Multiphysics, with and without a Salisbury screen absorber, are presented. In the right figure a PEC capped cylinder scatterer has been simulated in Comsol Multiphysics using different mesh settings.

References

[1] S. A. Akhmanov and S. Y. Nikitin. *Physical Optics*. Clarendon Press, 1997.

[2] C. A. Balanis. *Antenna Theory*. John Wiley & Sons, Hoboken, NJ, third edition, 2005.

[3] A. Bondeson, T. Rylander, and P. Ingelström. *Computational Electromagnetics*. Springer-Verlag, Berlin, 2005.

[4] M. Born and E. Wolf. *Principles of optics: electromagnetic theory of propagation, interference and diffraction of light*. Elsevier, 2013.

[5] R. Coifman, V. Rokhlin, and S. Wandzura. The fast multipole method for the wave equation: A pedestrian prescription. *IEEE Antennas Propag. Mag.*, **35**(3), pp. 7–12, 1993.

[6] D. B. Davidson. *Computational Electromagnetics for RF and Microwave Engineering*. Cambridge University Press, 2005.

[7] O. Ergul and L. Gurel. *The multilevel fast multipole algorithm (MLFMA) for solving large-scale computational electromagnetics problems*. John Wiley & Sons, 2014.

[8] A. Ericsson, J. Lundgren, and D. Sjöberg. Experimental characterization of circular polarization selective structures using linearly single-polarized antennas. *IEEE Trans. Antennas Propag.*, **65**(8), pp. 4239–4249, 2017.

[9] A. Ericsson and D. Sjöberg. Design and analysis of a multilayer meander line circular polarization selective structure. *IEEE Trans. Antennas Propag.*, **65**(8), pp. 4089–4101, 2017.

[10] A. Ericsson, D. Sjöberg, C. Larsson, and T. Martin. Scattering from a multilayered sphere - applications to electromagnetic absorbers on double curved surfaces. Technical Report LUTEDX/(TEAT-7249)/1–32/(2017), Lund University, Department of Electrical and Information Technology, P.O. Box 118, S-221 00 Lund, Sweden, 2017.

[11] A. Ericsson, D. Sjöberg, C. Larsson, and T. Martin. Scattering for doubly curved functional surfaces and corresponding planar designs. In *Antennas and Propagation (EuCAP), 2016 10th European Conference on*, pp. 1–2. IEEE, 2016.

[12] M. Ferrando-Bataller, F. V. Bondìa, and A. Valero-Nogueira. Fast physical optics for smooth surfaces. In *Proceedings of the Fourth European Conference on Antennas and Propagation*, pp. 1–3, April 2010.

[13] P. R. Foster. The region of application in GTD/UTD. In *1996 Third International Conference on Computation in Electromagnetics (Conf. Publ. No. 420)*, pp. 382–386, Apr 1996.

[14] E. Garcia, C. Delgado, L. Lozano, I. Gonzalez-Diego, and M. F. Catedra. An efficient hybrid-scheme combining the characteristic basis function method and the multilevel fast multipole algorithm for solving bistatic rcs and radiation problems. *Progress In Electromagnetics Research B*, **34**, pp. 327–343, 2011.

[15] W. C. Gibson. *The method of moments in electromagnetics*, volume 1. Chapman & Hall/CRC London, UK, 2008.

[16] J. M. Jin. *Theory and Computation of Electromagnetic Fields*. Wiley, 2011.

[17] E. Jones, T. Oliphant, P. Peterson, et al. SciPy: Open source scientific tools for Python, 2001. Available at: http://www.scipy.org/, accessed 2017-06-07.

[18] J. B. Keller. Geometrical theory of diffraction. *J. Opt. Soc. Am.*, **52**(2), pp. 116–130, Feb 1962.

[19] E. F. Knott, J. F. Shaeffer, and M. T. Tuley. *Radar Cross Section*. SciTech Publishing Inc., 5601 N. Hawthorne Way, Raleigh, NC 27613, 2004.

[20] R. Maaskant, R. Mittra, and A. Tijhuis. Fast analysis of large antenna arrays using the characteristic basis function method and the adaptive cross approximation algorithm. *IEEE Trans. Antennas Propag.*, **56**(11), pp. 3440–3451, Nov 2008.

[21] R. Mittra and K. Du. Characteristic basis function method for iteration-free solution of large method of moments problems. *Progress In Electromagnetics Research B*, **6**, pp. 307–336, 2008.

[22] K. Mitzner. Incremental length diffraction coefficients. Technical report, DTIC Document, 1974.

[23] X.-M. Pan, L. Cai, and X.-Q. Sheng. An efficient high order multilevel fast multipole algorithm for electromagnetic scattering analysis. *Progress In Electromagnetics Research*, **126**, pp. 85–100, 2012.

[24] G. T. Ruck, D. E. Barrick, W. D. Stuart, and C. K. Krichbaum. *Radar Cross-Section Handbook*, volume 1 and 2. Plenum Press, New York, 1970.

[25] T. Shijo, L. Rodriguez, and M. Ando. The modified surface-normal vectors in the physical optics. *IEEE Trans. Antennas Propag.*, **56**(12), pp. 3714–3722, Dec 2008.

[26] D. Sjöberg and A. Ericsson. Computation of radar cross section using the physical optics approximation. Technical Report LUTEDX/(TEAT-7255)/1–16/(2017), Lund University, Department of Electrical and Information Technology, P.O. Box 118, S-221 00 Lund, Sweden, 2017.

[27] D. G. Smith. *Field Guide to Physical Optics*. SPIE Press, 2013.

[28] O. N. Stavroudis. *The Mathematics of Geometrical and Physical Optics: the k-function and its Ramifications*. John Wiley & Sons, 2006.

[29] P. Y. Ufimtsev. Method of edge waves in the physical theory of diffraction. Technical report, DTIC Document, 1971.

[30] P. Y. Ufimtsev. *Fundamentals of the physical theory of diffraction*. John Wiley & Sons, 2007.

[31] Y. Z. Umul. Modified theory of physical optics. *Opt. Express*, **12**(20), pp. 4959–4972, Oct 2004.

[32] J. G. van Bladel. *Electromagnetic Fields*. IEEE Press, Piscataway, NJ, second edition edition, 2007.

Compressive Sensing Techniques for mm-Wave Non-Destructive Testing of Composite Panels

Jakob Helander, Andreas Ericsson, Mats Gustafsson,
Torleif Martin, Daniel Sjöberg and Christer Larsson

Paper IX

Published as: J. Helander, A. Ericsson, M. Gustafsson, T. Martin, D. Sjöberg and C. Larsson, "Compressive Sensing Techniques for mm-Wave Non-Destructive Testing of Composite Panels," *IEEE Transactions on Antennas and Propagation*, Vol. PP, No. 99, pp. 1–9, 2017.

Abstract

This paper presents imaging results from measurements of an industrially manufactured composite test panel, utilizing two introduced algorithms for data post-processing. The system employs a planar near-field scanning setup for characterizing defects in composite panels in the 50–67 GHz band, and can be considered as a complementary diagnostic tool for non-destructive testing purposes. The introduced algorithms are based on the reconstruction of the illuminating source at the transmitter, enabling a separation of the sampled signal with respect to the location of its potential sources; the scatterers within the device under test or the transmitter. For the second algorithm, a L_1-minimization problem formulation is introduced that enables compressive sensing techniques to be adapted for image retrieval. The algorithms are benchmarked against a more conventional imaging technique, based on the Fourier Transform, and it is seen that the complete imaging system provides increased dynamic range, improved resolution and reduced measurement time by removal of a reference measurement. Moreover, the system provides stable image quality over a range of frequencies.

1 Introduction

Non-destructive testing (NDT) is the science and practice of evaluating various properties of a device under test (DUT) without compromising its utility and usefulness [33]. Applications where NDT is used are for example welding inspection and structural evaluation of composite materials [2, 33]. Composite structures, manufactured with low permittivity and low loss materials such as honeycomb or foam, are increasingly utilized in *e.g.* aircraft structural components and radomes [1], and in order to conduct NDT on such structures, the method of choice must be capable of detecting defects related to low conductivity and inhomogeneity.

In recent years, millimeter wave (mm-wave) (30 – 300 GHz) imaging has attracted much attention as an electromagnetic testing technique for NDT applications [1, 2, 4, 22, 41]. High resolution imaging is possible at these frequencies due to the inherent short wavelengths. Other advantageous properties of mm-wave imaging systems are: low power consumption, compact size, low weight, and that they can easily be integrated into existing industrial scanning platforms [22]. Millimeter-wave NDT is particularly well-suited for inspection of composite structures since it has been proven useful for detection of material inhomogenities, disbonds, delaminations and inclusions in low loss dielectrics [8,41]; all potential defects in composite structures. For example, in [21] it was shown that subsurface voids in insulating foam were detectable in a wide range of the mm-wave spectrum.

A near-field mm-wave imaging system can either operate in reflection, such as in security applications [2,12], or in transmission as in radome diagnostics [28] and near-field antenna measurements [40]. The spatial sampling of the scattered

signals can be acquired either through mechanical scanning [40] or electronic scanning by utilizing antenna arrays [2]. Much time can be saved if an electronic scan can be performed, but at mm-wave frequencies it is non-trivial to develop cost-effective imaging arrays of high complexity. This complexity can be reduced by performing a one-dimensional (1D) raster scan using a 1D imaging array, which provides a good compromise between complexity and scan time [10]. Depending on the application, either a single frequency or a broadband electromagnetic signal is used to illuminate the object. In this work, the focus is on transmission based near-field scanning systems. These systems traditionally utilize either planar, cylindrical or spherical scanning [13, 17, 40].

Once the signals have been acquired over a given spatial area, the aim is to reconstruct the unknown sources on a given surface. This is an inverse problem which has traditionally been solved using reconstruction in the Fourier domain, commonly referred to in literature as time reversal, digital beam forming (DBF), aperture synthesis, back propagation, back projection or migration technique [34, 35].

Alternatively, compressive sensing (CS) based processing techniques could be used for image retrieval if the inverse problem could be modelled as an underdetermined linear system [5,6,19]. The strategy is to formulate the relation between the data and unknowns as a linear mapping, modelled by a rectangular matrix, and where the unknown vector has only a few non-zero entries with respect to a defined basis. Since the industrial manufacturing standard is good, existing defects in composite structures would be few and CS processing techniques would be adaptable to the problem at hand. Furthermore, the theory behind CS states that, if adapted to a sparse problem, the sought after solution can be recovered using far fewer samples than what is classically required by the Nyquist theorem [23], allowing for a potentially reduced measurement time as the number of required data samples decreases.

The characteristics of CS have resulted in a fast development in a variety of applications related to electromagnetics [23] such as: array synthesis [26], antenna diagnostics [24], direction-of-arrival estimation [7], ground penetrating radar [15], and inverse scattering [27, 31, 32]. The state-of-the-art within CS techniques for microwave imaging includes a variety of formulations to target specific problems and improve performance; wavelet basis functions for CS and total-variation CS can be adapted to solve problems with non-sparse scatterers (with respect to a pixel basis) [3, 14, 25]. Additional examples are the contrast field based CS [29] applicable to weak scatterers and multi-task Bayesian CS [30].

As spatial resolution, the achievable dynamic range and overall measurement time for acquiring data is generally considered the main measures of performance of an imaging system [2], mm-wave imaging using CS offers a promising foundation for further development of electromagnetic testing techniques for NDT applications.

In this paper, we introduce a mm-wave imaging technique based on CS that aims at: (1) reducing the required measurement time by removal of a reference measurement, and (2) improving the dynamic range compared to the conventional

imaging technique based on time reversal of the measured fields. A 50 – 67 GHz imaging system is constructed using a planar near-field scanning setup, and is then applied to industrially manufactured composite test panels. The technique could be seen as a complement to currently used diagnostic tools used in industry such as ultrasonic testing.

The technique is developed in two steps, where first a source separation algorithm is introduced that separates the components of the scattered signal related to the defects in the DUT from the total received signal by subtracting the illuminating field. This implies that no reference measurement is needed. After the illuminating field has been subtracted, a weak scattered field from a few sparse defects is acquired. This linear inverse problem is then formulated in a CS sense in order to improve the dynamic range.

2 Algorithm descriptions

For clarity, the notation used in the rest of this pap er is summarized here: boldface uppercase and boldface lowercase are used for matrix- and vector notation, respectively.

2.1 Measured signal

The measured signal is sampled at a distance z from the illuminating antenna over a finite rectangular aperture. The sampling is performed over a uniform rectangular grid, and the measured signal for each fixed frequency in the corresponding grid point can be represented as the sampled signal s (a complex number at each spatial grid point)

$$\begin{aligned} &s(x_i, y_j, z) = s(x_1 + (i-1)\Delta, y_1 + (j-1)\Delta, z), \\ &i = 1, 2, \ldots, N_\mathrm{x}, \\ &j = 1, 2, \ldots, N_\mathrm{y}. \end{aligned} \tag{2.1}$$

Here, Δ is the sample increment in the x- and y-direction, and (x_1, y_1) is the grid point in the lower left corner of the grid. The aggregated samples of the signal (or field) in the measurement plane for each fixed frequency is represented as a $N_\mathrm{m} \times 1$ column vector, where $N_\mathrm{m} = N_\mathrm{x} N_\mathrm{y}$.

2.2 Time reversal technique

For a measured signal $s(x, y, z_2)$ sampled continuously at a fixed distance $z = z_2$, the time reversal technique exploits the Fourier transform and its inverse in order to translate the signal between different xy-planes [35]. The signal's spatial spectrum at $z = z_2$ is

$$S(k_\mathrm{x}, k_\mathrm{y}, z_2) = \int_{-\infty}^{\infty} \int_{-\infty}^{\infty} s(x, y, z_2) \mathrm{e}^{\mathrm{j}(k_\mathrm{x} x + k_\mathrm{y} y)} \mathrm{d}x \, \mathrm{d}y, \tag{2.2}$$

where k_x and k_y are the x- and y-component of the wavenumber, respectively. In the spectral domain, the signal can be translated to a xy-plane closer to the source using a simple exponential, i.e., the signal's spectrum at $z = z_1$ is

$$S(k_\mathrm{x}, k_\mathrm{y}, z_1) = \mathrm{e}^{\mathrm{j}k_\mathrm{z}d} S(k_\mathrm{x}, k_\mathrm{y}, z_2). \tag{2.3}$$

Here, $k_\mathrm{z} = \sqrt{k^2 - k_\mathrm{x}^2 - k_\mathrm{y}^2}$, $d = z_1 - z_2 < 0$ and $k = 2\pi f/c$ with f being the frequency and c being the speed of light in air. Applying the inverse Fourier transform yields the signal in the spatial domain $s(x, y, z_1)$. For discrete signals, the usage of the discrete versions of the Fourier transform and its inverse allows for the time reversal technique to be efficiently implemented using fast Fourier transform (FFT) algorithms. Aliasing can be avoided by choosing the sample increment as $\Delta \leq \lambda/2$ in accordance to the Nyquist criterion. In the setup considered in this paper, the choice of Δ can be relaxed as discussed further in Section 3.

In order to retrieve the vector field components from the measured signal, it is necessary to compensate for the probe that samples the signal. The probe correction, explained in detail in [20, 40], is based on the a priori knowledge of the receiving characteristic of the probe. Using an open-ended waveguide, the far-field in the spectral domain can be modelled using formulas in [39]. The procedure can be used in order to extract either a scalar field or a vector field where the vector field extraction requires two independent measurements of the same signal. These are commonly chosen as the co-polarized and cross-polarized measurements. If the field is normalized with that obtained from a reference measurement, the time reversal technique can be applied for image retrieval of a DUT containing defects.

2.3 Source separation algorithm

A general model of the imaging setup with appropriate field vectors and operators defined is seen in Figure 1. As depicted in the figure, for a single frequency the field extracted from the corresponding discrete samples in the measurement plane is assembled into the $N_\mathrm{m} \times 1$ vector $\mathbf{b}_\mathrm{m}$. The n_m:th entry of $\mathbf{b}_\mathrm{m}$ corresponds to the field value in the spatial grid point (x_i, y_j) with $n_\mathrm{m} = (j-1)N_\mathrm{x} + i$ in relation to the introduced indices in (2.1). In order to expand the field in an arbitrary plane, all surfaces of interest are discretized into rectangular mesh cells with rooftop functions acting as local basis functions. The operator $\mathbf{A}_{ij}$, constructed analogously to conventional method of moments [9], thus maps the currents in plane j to the field in plane i.

The scattered field from the defects is assumed to be orders of magnitude smaller in amplitude compared to the total field in the measurement plane in the sense that critical defects (*e.g.*, delaminations and debonding) have only a minor impact on the electromagnetic properties of the DUT. The measured field $\mathbf{b}_\mathrm{m}$ can then be decomposed into the illuminating field $\mathbf{b}_2$ from the antenna and the

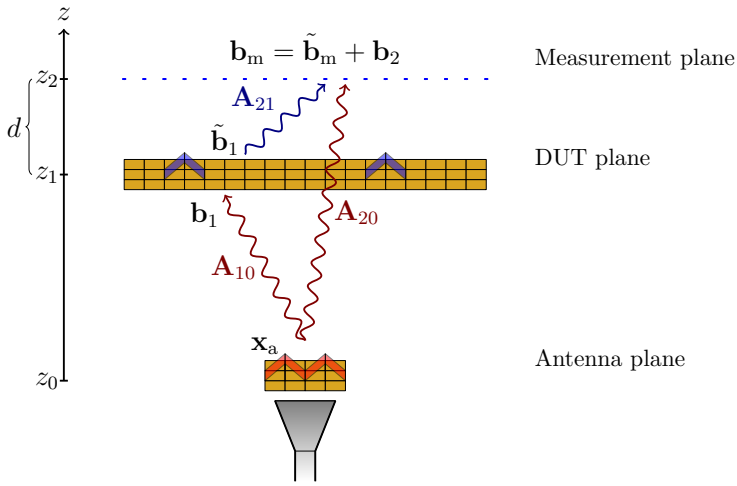

Figure 1: Discretized model of the imaging setup with operators and field vectors as depicted.

slab of the DUT, and the scattered field $\tilde{\mathbf{b}}_m$ arising only from the interior defects

$$\mathbf{b}_m = \tilde{\mathbf{b}}_m + \mathbf{b}_2. \tag{2.4}$$

Using (2.4), $\tilde{\mathbf{b}}_m$ can be extracted if $\mathbf{b}_2$ can be estimated appropriately. This is done by finding the currents on the antenna aperture represented by the $N_a \times 1$ vector $\mathbf{x}_a$, using the operator $\mathbf{A}_{20}$ (size $N_m \times N_a$). A singular value decomposition (SVD) is applied to $\mathbf{A}_{20}$

$$\mathbf{A}_{20} = \mathbf{U}\boldsymbol{\Sigma}\mathbf{V}^H. \tag{2.5}$$

Here, $\mathbf{U}$ and $\mathbf{V}$ are unitary matrices, and $\boldsymbol{\Sigma}$ is a diagonal matrix containing the non-zero positive singular values of $\mathbf{A}_{20}$. The normalized singular values are truncated according to a prescribed threshold τ, selected by means of the L-curve criterion [18]. The pseudo inverse is then constructed as [11]

$$\mathbf{A}_{20}^{\dagger} = \mathbf{V}\boldsymbol{\Sigma}^{\dagger}\mathbf{U}^H. \tag{2.6}$$

Here, $\boldsymbol{\Sigma}^{\dagger}$ is a diagonal matrix, with all entries corresponding to singular values whose normalized value is below τ set to zero. The remaining entries contain the reciprocal of the corresponding singular value. Applying $\mathbf{A}_{20}^{\dagger}$ to the measured field $\mathbf{b}_m$ yields

$$\mathbf{x}_a = \mathbf{A}_{20}^{\dagger}\mathbf{b}_m, \tag{2.7}$$

and the field contribution from the antenna, $\mathbf{b}_2$, is found as

$$\mathbf{b}_2 = \mathbf{A}_{20}\mathbf{x}_a. \tag{2.8}$$

After finding $\mathbf{b}_2$, the analysis is restricted to the scattered field $\tilde{\mathbf{b}}_m$, where the source separation algorithm utilizes the time reversal technique to retrieve the

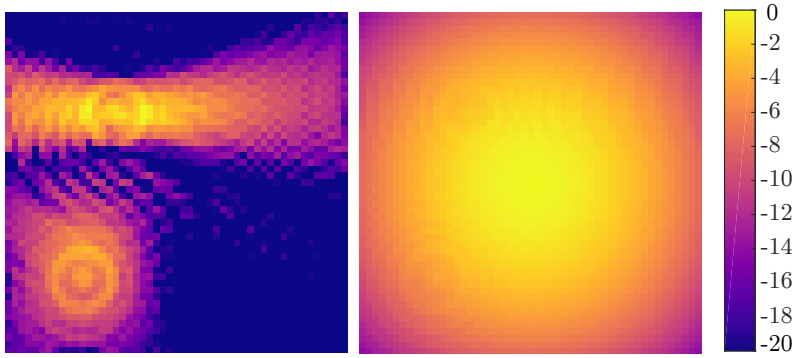

Figure 2: Extracted scattered field $\tilde{\mathbf{b}}_\mathrm{m}$ (left) from a total field $\mathbf{b}_\mathrm{m}$ in the measurement plane (right) from an example simulation using the theory presented in Section 2.3. The figures depict independently normalized absolute values of the fields in dB-scale. The relative power difference between total and scattered field is $\simeq 30\,\mathrm{dB}$.

final image in the DUT plane. The CS algorithm introduced in Section 2.4 is instead based on the formulation of the L_1-minimization optimization problem. The partitioning of the field as a result of the source separation is illustrated in Figure 2.

2.4 Compressive sensing algorithm

The CS algorithm utilizes the SPGL1 Matlab solver based on the general basis pursuit denoise (BPDN) L_1-minimization problem [37,38]. For a single frequency, the target image can be acquired from the scattered field $\tilde{\mathbf{b}}_\mathrm{m}$, by finding the corresponding scattered field $\tilde{\mathbf{b}}_1$ in the DUT plane. The initial optimization problem is then formulated as

$$\begin{aligned} &\text{minimize} && ||\tilde{\mathbf{b}}_1||_1 \\ &\text{subject to} && ||\mathbf{A}_{21}\tilde{\mathbf{b}}_1 - \tilde{\mathbf{b}}_\mathrm{m}||_2 \leq \sigma. \end{aligned} \tag{2.9}$$

The choice of the user-defined threshold σ is discussed in the final part of this section. In order to reconstruct properties of the defects rather than the scattered field $\tilde{\mathbf{b}}_1$, we introduce the scattering amplitudes $\mathbf{s}$ as

$$\tilde{\mathbf{b}}_1 = \mathbf{B}_1\mathbf{s}, \tag{2.10}$$

with

$$\mathbf{B}_1 = \mathrm{diag}(\mathbf{b}_1) = \begin{bmatrix} b_{1,1} & 0 & \dots & 0 \\ 0 & b_{1,2} & \dots & 0 \\ \vdots & \vdots & \ddots & \vdots \\ 0 & 0 & \dots & b_{1,N_1} \end{bmatrix}$$

representing the incident field on the panel at $z = z_1$ from the antenna, see Figure 1. N_1 spatial grid points are assumed in the DUT plane. Using $\mathbf{x}_\mathrm{a}$ and the operator $\mathbf{A}_{10}$ (size $N_1 \times N_\mathrm{a}$), and, $\mathbf{b}_1$ can be found through

$$\mathbf{b}_1 = \mathbf{A}_{10}\mathbf{x}_\mathrm{a}. \tag{2.11}$$

The scattering amplitudes $\mathbf{s}$ comprise N_1 unknowns, induced by the scatterers in the DUT plane. In a pixel basis, only few non-zero elements would be needed to represent the defects if their physical size is on a wavelength scale. This would correspond to defects no larger than a few centimeters when considering the 60 GHz band; a reasonable scenario since industrial manufacturing processes rarely results in large-size fabrication errors. The optimization problem then reads

$$\begin{aligned} &\text{minimize} && ||\mathbf{s}||_1 \\ &\text{subject to} && ||\mathbf{A}_{21}\mathbf{B}_1\mathbf{s} - \tilde{\mathbf{b}}_\mathrm{m}||_2 \leq \sigma. \end{aligned} \tag{2.12}$$

The incident field, expressed in $\mathbf{B}_1$, is not uniformly distributed over the DUT plane which results in a non-uniform weighting of the scattering amplitudes in this formulation. To re-compensate for this effect the final formulation is obtained as

$$\begin{aligned} &\text{minimize} && ||\mathbf{s}||_1 \\ &\text{subject to} && ||\mathbf{B}_{2,\mathrm{inv}}\mathbf{A}_{21}\mathbf{B}_1\mathbf{s} - \mathbf{B}_{2,\mathrm{inv}}\tilde{\mathbf{b}}_\mathrm{m}||_2 \leq \sigma, \end{aligned} \tag{2.13}$$

where $\mathbf{B}_{2,\mathrm{inv}}$ represents the magnitude of the inverse of the incident field in the measurement plane

$$\mathbf{B}_{2,\mathrm{inv}} = \begin{bmatrix} |b_{2,1}|^{-1} & 0 & \dots & 0 \\ 0 & |b_{2,2}|^{-1} & \dots & 0 \\ \vdots & \vdots & \ddots & \vdots \\ 0 & 0 & \dots & |b_{2,N_\mathrm{m}}|^{-1} \end{bmatrix}.$$

2.4.1 Choice of the threshold σ

For a known field $\tilde{\mathbf{b}}_\mathrm{m}$, an estimate of the scattering amplitudes $\hat{\mathbf{s}}$ is retrieved by time reversing $\tilde{\mathbf{b}}_\mathrm{m}$ using the adjoint operator $\mathbf{A}_{21}^*$

$$\mathbf{B}_1\hat{\mathbf{s}} = \mathbf{A}_{21}^*\tilde{\mathbf{b}}_\mathrm{m}. \tag{2.14}$$

By applying $\mathbf{A}_{21}$ to $\mathbf{B}_1\hat{\mathbf{s}}$, the estimated scattered field in the measurement plane $\hat{\mathbf{b}}_\mathrm{m}$ is found as

$$\hat{\mathbf{b}}_\mathrm{m} = \mathbf{A}_{21}\mathbf{B}_1\hat{\mathbf{s}} = \mathbf{A}_{21}\mathbf{A}_{21}^*\tilde{\mathbf{b}}_\mathrm{m}. \tag{2.15}$$

Finally, the threshold is chosen as

$$\sigma = ||\tilde{\mathbf{b}}_\mathrm{m} - \hat{\mathbf{b}}_\mathrm{m}||_2 = ||(1 - \mathbf{A}_{21}\mathbf{A}_{21}^*)\tilde{\mathbf{b}}_\mathrm{m}||_2. \tag{2.16}$$

This choice of σ is stable, and the performance of the algorithm would not be compromised by small fractional changes to this value.

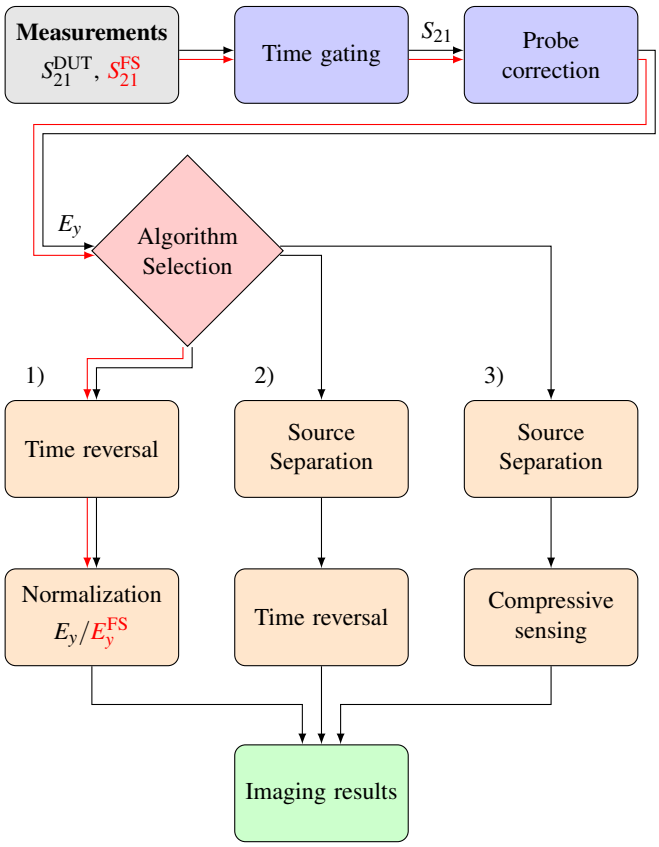

Figure 3: Block diagram depicting the post processing steps used in this work. The top row corresponds to processing that were carried out for all measurement data. The three parallel schemes at the bottom correspond to 1) the time reversal technique, 2) the source separation algorithm and 3) the CS algorithm.

2.4.2 Comment on implementation

Given that the measurement and DUT plane are discretized identically, it follows that $\mathbf{A}_{21}$ is a block Toeplitz matrix. Due to the large number of grid points necessary for a reasonable resolution, it is not desirable to compute the complete matrix operator. Rather, $\mathbf{A}_{21}$ can be extended to a circulant matrix due to its Toeplitz characteristic, and the general linear operations $\mathbf{A}_{21}\mathbf{x}$ and $\mathbf{A}_{21}^{*}\mathbf{b}$ can instead be evaluated efficiently in a matrix free way using an FFT algorithm [11, 16].

3 Performance

The three implemented algorithms are:

1. The time reversal technique, as described in Section 2.2. This technique employs time reversal of the field $\mathbf{b}_\mathrm{m}$ in the measurement plane with DUT present and a free space reference. The final image is obtained after normalization with the free space field back-propagated to the DUT plane.

2. The source separation algorithm. This algorithm utilizes source separation to estimate the scattered field $\tilde{\mathbf{b}}_\mathrm{m}$ in the measurement plane (Section 2.3), and thereafter employs time reversal of $\tilde{\mathbf{b}}_\mathrm{m}$ (Section 2.2) in order to retrieve the final image.

3. The CS algorithm. This algorithm utilizes source separation to estimate the scattered field $\tilde{\mathbf{b}}_\mathrm{m}$ in the measurement plane (Section 2.3), and thereafter employs the general BPDN L_1-minimization optimization problem formulation in (2.13), in order to retrieve the final image (Section 2.4).

A block diagram describing the algorithms can be seen in Figure 3. As depicted, the top row of blocks represents measurement post-processing procedures and thus only apply to measured data (Section 3.2). When executing the time reversal routine in algorithm 1) or 2), interpolation of the data can be employed using zero padding of the signal's spatial spectrum. For all results presented in this section, sampling is carried out in the measurement plane at $z_2 = 530\,\mathrm{mm}$, with $\Delta = 5\,\mathrm{mm}$ and $N_\mathrm{m} = 51^2 = 2\,601$, resulting in a total finite square aperture of $250 \times 250\,\mathrm{mm}^2$. The DUT plane is at $z_1 = 470\,\mathrm{mm}$ with $N_1 = 203^2 = 41\,209$ of spatial grid points. The distance between the measurement plane and the DUT plane is $d = 60\,\mathrm{mm}$. The antenna aperture plane is at $z_0 = 0\,\mathrm{mm}$.

Note that in the frequency band of interest 50 – 67 GHz, the sample increment is $\Delta \approx \lambda$ and thereby the Nyquist criterion is violated. However, no aliasing is introduced that affects the final image due to the fact that the geometrical setup limits the possible incident plane waves under consideration, or equivalently restricts the $(k_\mathrm{x}, k_\mathrm{y})$-spectrum. Consequently, any aliasing that occurs falls outside of the wavenumber region of interest.

3.1 Synthetic data

The above described algorithms are employed on synthetic data, extracted from simulations using FEKO. This discards any deterministic measurement errors that might appear when measured data is considered, and consequently provides a proof of concept of the algorithms themselves.

The E_y-component (co-polarization) in the aperture of a standard gain horn antenna at 60 GHz is used as the illuminating source, and three rectangular resistive sheets with $R = 100\,\Omega$ represent the DUT. The setup can be seen in

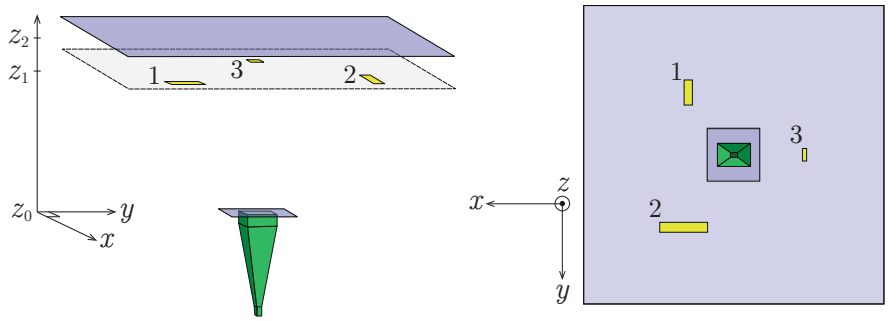

(a) Side view. (b) Top view.

Figure 4: Simulation setup in FEKO for synthetic data generation. Measures not to scale. Highlighted regions in (a) denote the measurement-, DUT- and antenna plane respectively in descending order.

Figure 4. With labelling according to Figure 4b, the dimensions of the resistive sheets are $1.5 \times 10\,\mathrm{mm}^2$, $5 \times 2.5\,\mathrm{mm}^2$ and $1 \times 1\,\mathrm{mm}^2$.

Retrieved images using the time reversal technique, source separation algorithm and the CS algorithm can be seen in Figure 5. As seen, for the depicted color range ($[-60,\ 0]\,\mathrm{dB}$), the CS algorithm provides the best dynamic range as only scattering amplitudes related to the physical dimension of the resistive sheets have non-zero entries, *i.e.*, the sparse solution to the problem is found. The time reversal technique gives little information whereas the source separation algorithm manages to detect the defects, with noticeable low power noise present. Due to the large difference in dynamic range for the different algorithms, the images from the time reversal technique and source separation algorithm are shown in Figure 6 for customized color ranges. It is seen that the source separation algorithm provides a dynamic range of around $\simeq 20\,\mathrm{dB}$. As Figures 5 and 6 (a) depict the time reversed field normalized with a free space measurement ($|E_\mathrm{y}|/|E_\mathrm{y}^\mathrm{FS}|$), the shadowing effect from the resistive sheets is clearly seen as the amplitude around the defects is lower than the surrounding medium. However, both the source separation algorithm and CS algorithm act on the scattered field using (2.4), and consequently the images in Figure 5 (b), (c) and Figure 6 (b) show the resistive sheets as the maximum amplitude in the DUT plane. Truncation effects, *i.e.* sidelobes, arising from the finite aperture of the measurement plane can be seen for both the time reversal technique and source separation algorithm, most clearly seen in Figure 5 (b) as the vertical- and horizontal lines springing from the resistive sheets. The sidelobes can be suppressed by applying an appropriate windowing function, reducing the effect of the finite aperture of the measurement plane, with the cost of degraded resolution. However, these sidelobes do not appear for the CS algorithm, due to the usage of operators for transforming between xy-planes. Moreover, the CS algorithm manages to resolve the $1 \times 1\,\mathrm{mm}^2$ ($0.2\lambda \times 0.2\lambda$) defect, whereas this defect is not detected by neither the time reversal technique nor the source separation algorithm.

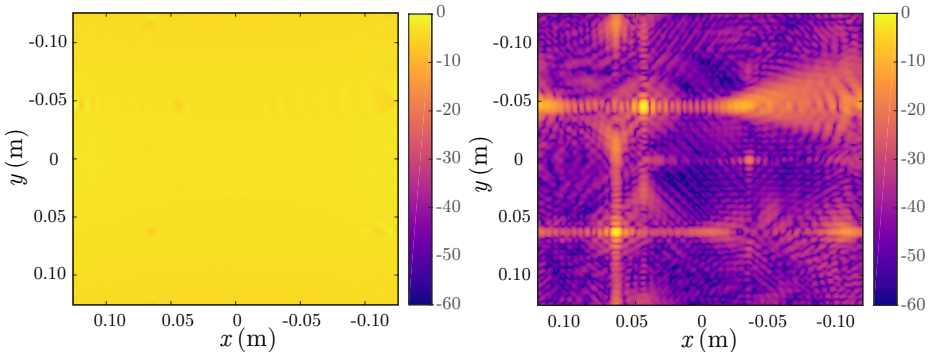

(a) Time reversal technique.

(b) Source separation algorithm.

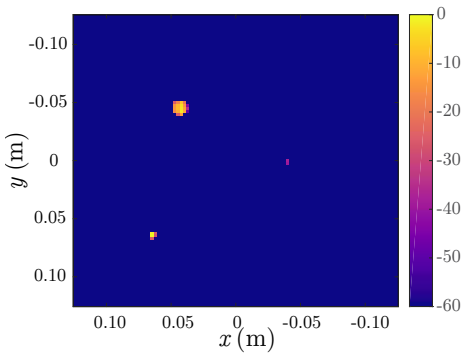

(c) CS algorithm.

Figure 5: Retrieved images at 60 GHz for the synthetic data using the three different algorithms. (a) depicts $|\mathrm{E}_y|/|\mathrm{E}_y^{\mathrm{FS}}|$, were $\mathrm{E}_y^{\mathrm{FS}}$ denotes the free space reference measurement, (b) depicts $|\mathrm{E}_y|$, and (c) depicts the absolute value of the scattering amplitudes $\mathbf{s}$. All figures are in normalized dB-scale ($20\log_{10}(|u|/\max(|u|))$, where u is the parameter being plotted) with color range $[-60,\, 0]$ dB.

3.2 Measurements

Measurements were carried out in the microwave laboratory at Lund University, Sweden. The illuminating source was chosen as a 50 – 67 GHz standard gain horn antenna, and an open-ended waveguide was used as the scanning probe. A single planar scan was conducted, with both horn and probe being y-polarized. The transmitted signal was measured using an Agilent E8361A network analyzer, and a low noise amplifier (LNA) was added on the receiver side. The transmit power was -7 dBm, the intermediate frequency (IF) bandwidth was set to 300 Hz and a linearly spaced frequency sampling with 201 points across the whole operational band of the horn antenna was used.

In order to acquire the necessary data as input for the algorithms, post-

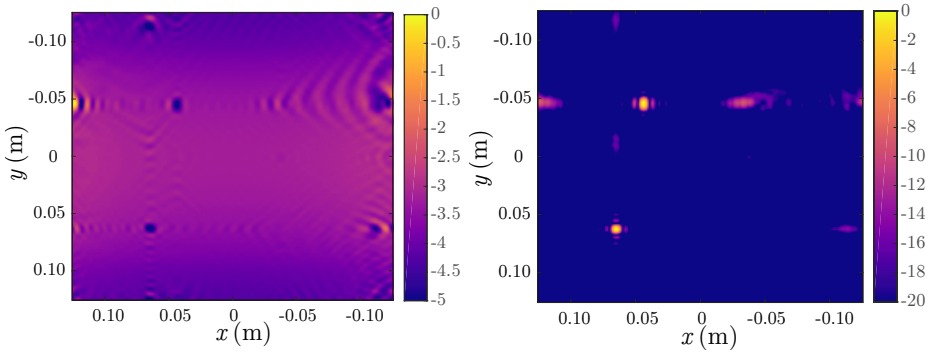

(a) Time reversal technique. (b) Source separation algorithm.

Figure 6: Retrieved images at 60 GHz for the synthetic data using the time reversal technique and source separation algorithm with customized color range. (a) depicts $|\mathrm{E}_y|/|\mathrm{E}_y^{\mathrm{FS}}|$ were $|\mathrm{E}_y^{\mathrm{FS}}|$ denotes the free space reference measurement, and (b) depicts $|\mathrm{E}_y|$. Both figures are in normalized dB-scale ($20\log_{10}(|u|/\max(|u|))$, where u is the parameter being plotted) with color range: (a) $[-5,\, 0]$ dB, and (b) $[-20,\, 0]$ dB.

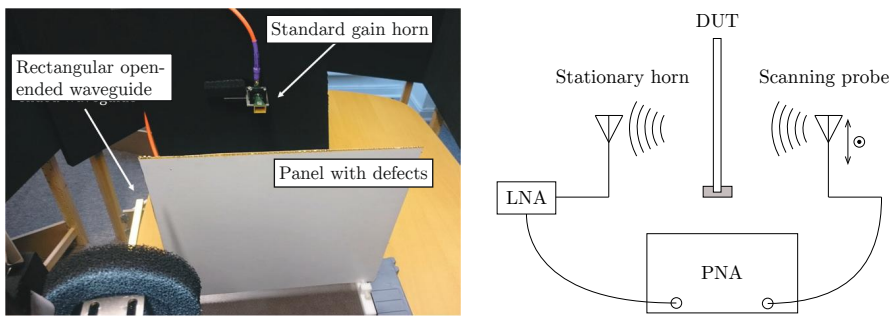

Figure 7: Photo (a), and block schematic (b) of the measurement setup. Receiving antenna is a 50 – 67 GHz standard gain horn antenna, and the transmitting scanning probe is a rectangular open-ended waveguide. Surrounding absorbers are seen in black (a).

processing routines were employed on the measured S_{21}, as seen in the top row of blocks in Figure 3. First, multipath scattering components of the signal are suppressed by applying an appropriate window function in the time domain, here chosen as a Hanning window. An interesting remark is that even with a free space path loss of $\simeq 68\,\mathrm{dB/m}$ at 60 GHz, and additional losses due to reflection and surrounding absorbers, the data filtering resulted in a considerable improvement of the purity of the S_{21} over the measurement aperture. Secondly, probe correction is applied in order to extract the field components from the S_{21} as described in Section 2.2. Using one planar scan, only a single scalar component may be extracted, here chosen as the co-polarized component of the electric field, *i.e.*, E_y according to the alignment of the horn and the probe. It should be noted that the probe correction is not limited to a specific field or component [20]. Rather, there exists a flexibility in which field and which component to extract. As mentioned in Section 2.2, an additional planar scan with the probe rotated 90° would allow for the extraction of the complete vector fields, with the cost of doubling the total measurement time.

The measurement setup is shown in Figure 7. The DUT is an industrially manufactured composite test panel provided by Saab Aerostructures with dimension $300 \times 300 \times 3\,\mathrm{mm}^3$. The panel consists of a 2 mm thick low permittivity over-expanded Nomex honeycomb core sandwiched between two 0.5 mm sheets of TenCate EX-1515, a cyanate ester quartz fabric prepreg [36]. The panel was assembled using TenCate EX-1516, an adhesive developed for bonding solid, honeycomb or foam core structures used in aircraft and space applications [36], and covered with a fluoropolymer film. The defects, inserted into the Nomex honeycomb core, were selected in order to investigate the detection limits of the imaging methods for metallic and dielectric objects with different shapes and sizes. A picture of the inner layers of the panel before assembly is seen in Figure 10. Defects in the right column are metallic while the remaining defects consist of the same adhesive used for assembling the panel. The largest dimension of all defects are between $2 - 20\,\mathrm{mm}$, *i.e.* ranging in size from sub-wavelength to a few wavelengths of the illuminating signal. With the geometrical settings presented earlier, one planar scan took 4 h to conduct, *i.e.*, the total measurement time for retrieving the necessary data for the different algorithms is 8 h, 4 h and 4 h for the time reversal technique, the source separation algorithm and the CS algorithm, respectively.

Retrieved images at $f = 60\,\mathrm{GHz}$ using the time reversal technique, the source separation algorithm and the CS algorithm can be seen in Figure 8. Note the customized color scale for every image, motivated by the large difference in dynamic range achieved by the different algorithms. The image quality obtained in the synthetic case is maintained for the measured data. As for the synthetic case, the CS algorithm provides the best dynamic range. The source separation algorithm and CS algorithm provide stable images regardless of the choice of frequency, demonstrated by the similarity of the equivalent images at $f = 61\,\mathrm{GHz}$ shown in Figures 9 (b) and (c). Errors arising from the measurement setup can be seen to affect the image quality of Figures 8 and 9 (a) to a larger extent, perhaps

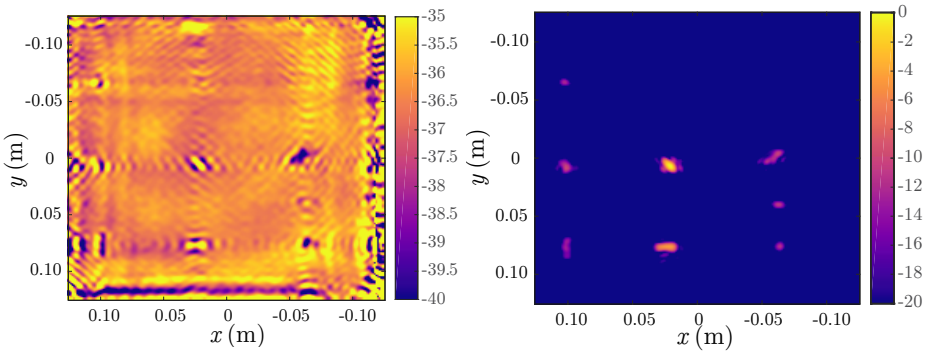

(a) Time reversal technique.

(b) Source separation algorithm.

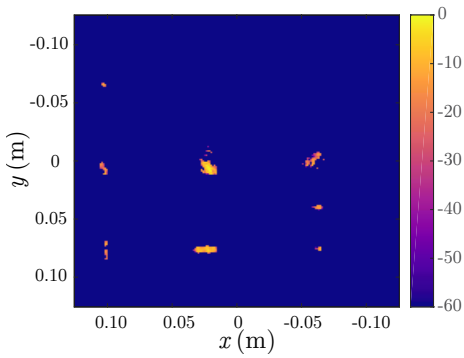

(c) CS algorithm.

Figure 8: Retrieved images at 60 GHz for the measured data using the three different algorithms. (a) depicts $|\mathrm{E}_y|/|\mathrm{E}_y^{\mathrm{FS}}|$, were $\mathrm{E}_y^{\mathrm{FS}}$ denotes the free space reference measurement, (b) depicts $|\mathrm{E}_y|$, and (c) depicts the absolute value of the scattering amplitudes $\mathbf{s}$. All figures are in normalized dB-scale ($20\log_{10}(|u|/\max(|u|))$, where u is the parameter being plotted) with color range: (a) $[-40, -35]$ dB, (b) $[-20, 0]$ dB and (c) $[-60, 0]$ dB.

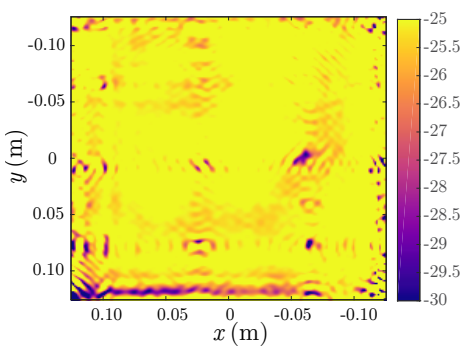

(a) Time reversal technique.

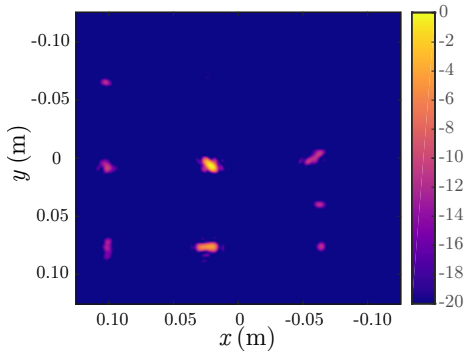

(b) Source separation algorithm.

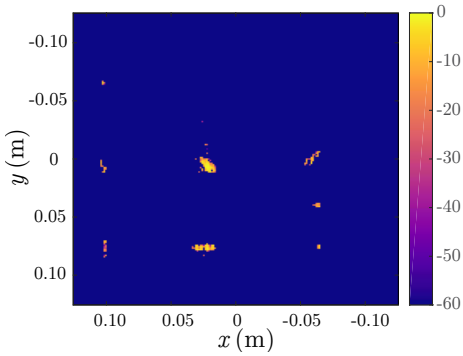

(c) CS algorithm.

Figure 9: Retrieved images at 61 GHz for the measured data using the three different algorithms. (a) depicts $|\mathrm{E}_y|/|\mathrm{E}_y^{\mathrm{FS}}|$, were $\mathrm{E}_y^{\mathrm{FS}}$ denotes the free space reference measurement, (b) depicts $|\mathrm{E}_y|$, and (c) depicts the absolute value of the scattering amplitudes $\mathbf{s}$. All figures are in normalized dB-scale ($20\log_{10}(|u|/\max(|u|))$, where u is the parameter being plotted) with color range: (a) $[-30, -25]$ dB, (b) $[-20, 0]$ dB and (c) $[-60, 0]$ dB.

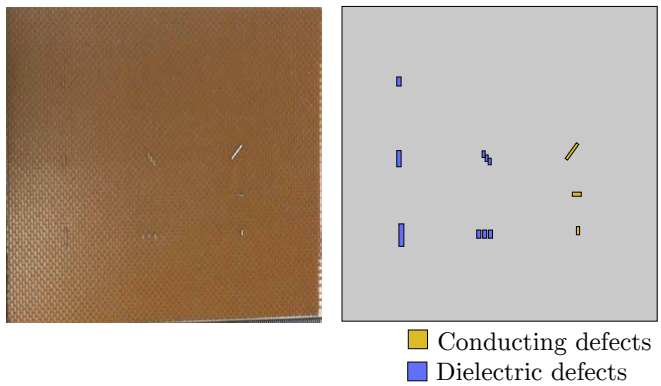

Figure 10: Photo (left) and schematic (right) of the panel under test as seen from the probe. The size of the panel is $300 \times 300 \times 3\,\mathrm{mm}^3$.

explained by the exploitation of data from two independent measurements (one with DUT present and one free space reference). Whereas the dynamic range is maintained, the color scale is different for the different frequencies in (a) in order to provide the best image. The effect of the weighting compensation introduced by the operator $\mathbf{B}_{2,\mathrm{inv}}$ can also be seen in Figures 8 and 9 (c), as the scattering amplitudes for all defects are of the same magnitude unlike as in (a) and (b).

4 Conclusion

A complete imaging system using a planar near-field scanning setup operating in the 50 – 67 GHz band has been presented. Its potential as a complementary tool for industrial NDT diagnostic purposes has been validated through measurements on an industrially manufactured composite test panel using two introduced post-processing algorithms. The source separation algorithm can be regarded as a stepping-stone in the development of the more efficient CS algorithm, yet both algorithms provide noticeable enhancements compared to the more conventional time reversal technique. These enhancements include reduction of measurement time by removal of a reference measurement, increased dynamic range, and stable image quality over a range of frequencies. All three are critical measures of system performance.

It should be noted that sparsity is a relative concept in CS, and a scatterer can be sparse in some basis but not sparse with respect to another one. The pixel basis used in this work is convenient due to the small physical size of the defects under consideration.

Further development of the CS algorithm is ongoing, mainly for reduction of measurement time while maintaining image quality. The single frequency problem formulation provided in (2.13) allows for a straightforward extension to the multiple frequency scenario, in which data from several fixed frequencies can

be utilized in order to solve for the scattering amplitudes. Potentially, this would allow for a reduction in spatial samples without compromising image quality. This implementation is currently in progress.

Acknowledgement

The authors would like to thank Mikael Petersson at Saab Aerostructures for manufacturing the test panel. The authors would also like to thank Carl Gustafson and Iman Vakili for assisting with the measurements.

References

[1] M. A. Abou-Khousa, A. Ryley, S. Kharkovsky, R. Zoughi, D. Daniels, N. Kreitinger, G. Steffes, D. O. Thompson, and D. E. Chimenti. Comparison of X-ray, millimeter wave, shearography and through-transmission ultrasonic methods for inspection of honeycomb composites. In *AIP Conference Proceedings*, volume 894, pp. 999–1006. AIP, 2007.

[2] S. S. Ahmed, A. Schiessl, F. Gumbmann, M. Tiebout, S. Methfessel, and L.-P. Schmidt. Advanced microwave imaging. *IEEE Microw. Mag.*, **13**(6), pp. 26–43, 2012.

[3] N. Anselmi, M. Salucci, G. Oliveri, and A. Massa. Wavelet-based compressive imaging of sparse targets. *IEEE Trans. Antennas Propag.*, **63**(11), pp. 4889–4900, 2015.

[4] J. Blitz. *Electrical and Magnetic Methods of Non-Destructive Testing*, volume 3. Springer Science & Business Media, 2012.

[5] E. Candes and J. Romberg. Sparsity and incoherence in compressive sampling. *Inverse problems*, **23**(3), pp. 969, 2007.

[6] E. J. Candès and M. B. Wakin. An introduction to compressive sampling. *IEEE Signal Process. Mag.*, **25**(2), pp. 21–30, 2008.

[7] M. Carlin, P. Rocca, G. Oliveri, F. Viani, and A. Massa. Directions-of-arrival estimation through bayesian compressive sensing strategies. *IEEE Trans. Antennas Propag.*, **61**(7), pp. 3828–3838, July 2013.

[8] J. T. Case, S. Kharkovsky, R. Zoughi, G. Steffes, F. L. Hepburn, D. O. Thompson, and D. E. Chimenti. Millimeter wave holographical inspection of honeycomb composites. In *AIP Conference Proceedings*, volume 975, pp. 970–975. AIP, 2008.

[9] W. C. Chew, M. S. Tong, and B. Hu. *Integral equation methods for electromagnetic and elastic waves*, volume 12. Morgan & Claypool, 2008.

[10] M. T. Ghasr, S. Kharkovsky, R. Bohnert, B. Hirst, and R. Zoughi. 30 GHz linear high-resolution and rapid millimeter wave imaging system for NDE. *IEEE Trans. Antennas Propag.*, **61**(9), pp. 4733–4740, 2013.

[11] G. H. Golub and C. F. van Loan. *Matrix Computations*. The Johns Hopkins University Press, Baltimore, MD, 1983.

[12] B. Gonzalez-Valdes, Y. Alvarez, S. Mantzavinos, C. M. Rappaport, F. Las-Heras, and J. Á. Martínez-Lorenzo. Improving security screening: A comparison of multistatic radar configurations for human body imaging. *IEEE Antennas Propag. Mag.*, **58**(4), pp. 35–47, 2016.

[13] S. Gregson, J. McCormick, and C. Parini. *Principles of planar near-field antenna measurements*, volume 53. IET, 2007.

[14] L. Guo and A. M. Abbosh. Microwave imaging of nonsparse domains using born iterative method with wavelet transform and block sparse bayesian learning. *IEEE Trans. Antennas Propag.*, **63**(11), pp. 4877–4888, Nov 2015.

[15] A. C. Gurbuz, J. H. McClellan, and W. R. Scott. A compressive sensing data acquisition and imaging method for stepped frequency GPRS. *IEEE Trans. Signal Process.*, **57**(7), pp. 2640–2650, 2009.

[16] M. Gustafsson, M. Sebesta, B. Bengtsson, S.-G. Pettersson, P. Egelberg, and T. Lenart. High resolution digital transmission microscopy—a Fourier holography approach. *Optics and Lasers in Engineering*, **41**(3), pp. 553–563, 2004.

[17] J. E. Hansen, editor. *Spherical Near-Field Antenna Measurements*. Number 26 in IEE electromagnetic waves series. Peter Peregrinus Ltd., Stevenage, UK, 1988.

[18] P. C. Hansen. *Discrete inverse problems: insight and algorithms*, volume 7. Society for Industrial & Applied Mathematics, 2010.

[19] S. Ji, Y. Xue, and L. Carin. Bayesian compressive sensing. *IEEE Trans. Signal Process.*, **56**(6), pp. 2346–2356, 2008.

[20] D. Kerns. Correction of near-field antenna measurements made with an arbitrary but known measuring antenna. *Electron. Lett.*, **6**(11), pp. 346–347, 1970.

[21] S. Kharkovsky, J. T. Case, M. A. Abou-Khousa, R. Zoughi, and F. L. Hepburn. Millimeter-wave detection of localized anomalies in the space shuttle external fuel tank insulating foam. *IEEE Trans. Instrum. Meas.*, **55**(4), pp. 1250–1257, 2006.

[22] S. Kharkovsky and R. Zoughi. Microwave and millimeter wave nondestructive testing and evaluation - overview and recent advances. *IEEE Instrum. Meas. Mag.*, **10**(2), pp. 26–38, 2007.

[23] A. Massa, P. Rocca, and G. Oliveri. Compressive sensing in electromagnetics-a review. *IEEE Antennas Propag. Mag.*, **57**(1), pp. 224–238, 2015.

[24] M. D. Migliore. A compressed sensing approach for array diagnosis from a small set of near-field measurements. *IEEE Trans. Antennas Propag.*, **59**(6), pp. 2127–2133, June 2011.

[25] G. Oliveri, N. Anselmi, and A. Massa. Compressive sensing imaging of non-sparse 2d scatterers by a total-variation approach within the born approximation. *IEEE Trans. Antennas Propag.*, **62**(10), pp. 5157–5170, Oct 2014.

[26] G. Oliveri and A. Massa. Bayesian compressive sampling for pattern synthesis with maximally sparse non-uniform linear arrays. *IEEE Trans. Antennas Propag.*, **59**(2), pp. 467–481, Feb 2011.

[27] L. Pan, X. Chen, and S. P. Yeo. A compressive-sensing-based phaseless imaging method for point-like dielectric objects. *IEEE Trans. Antennas Propag.*, **60**(11), pp. 5472–5475, Nov 2012.

[28] K. Persson, M. Gustafsson, G. Kristensson, and B. Widenberg. Radome diagnostics — source reconstruction of phase objects with an equivalent currents approach. *IEEE Trans. Antennas Propag.*, **62**(4), 2014.

[29] L. Poli, G. Oliveri, and A. Massa. Microwave imaging within the first-order born approximation by means of the contrast-field bayesian compressive sensing. *IEEE Trans. Antennas Propag.*, **60**(6), pp. 2865–2879, June 2012.

[30] L. Poli, G. Oliveri, F. Viani, and A. Massa. Mt-bcs-based microwave imaging approach through minimum-norm current expansion. *IEEE Trans. Antennas Propag.*, **61**(9), pp. 4722–4732, Sept 2013.

[31] L. Poli, G. Oliveri, P. P. Ding, T. Moriyama, and A. Massa. Multifrequency Bayesian compressive sensing methods for microwave imaging. *JOSA A*, **31**(11), pp. 2415–2428, 2014.

[32] L. C. Potter, E. Ertin, J. T. Parker, and M. Cetin. Sparsity and compressed sensing in radar imaging. *Proc. IEEE*, **98**(6), pp. 1006–1020, 2010.

[33] P. J. Shull. *Nondestructive Evaluation: Theory, Techniques, and Applications*. New York: Marcel Dekker, 2002.

[34] M. Soumekh. *Fourier Array Imaging*. Prentice-Hall, Inc., 1994.

[35] R. H. Stolt. Migration by fourier transform. *Geophysics*, **43**(1), pp. 23–48, 1978.

[36] Tencate film adhesives. Available at: http://www.tencate.com, accessed 2017-05-20.

[37] E. van den Berg and M. P. Friedlander. SPGL1: A solver for large-scale sparse reconstruction, 2007. Available at: http://www.cs.ubc.ca/labs/scl/spgl1, accessed 2017-06-10.

[38] E. van den Berg and M. P. Friedlander. Probing the Pareto frontier for basis pursuit solutions. *SIAM Journal on Scientific Computing*, **31**(2), pp. 890–912, 2008.

[39] A. D. Yaghjian. Approximate formulas for the far field and gain of open-ended rectangular waveguide. *IEEE Trans. Antennas Propag.*, **32**(4), pp. 378–384, april 1984.

[40] A. D. Yaghjian. An overview of near-field antenna measurements. *IEEE Trans. Antennas Propag.*, **34**(1), pp. 30–45, January 1986.

[41] R. Zoughi. *Microwave Non-Destructive Testing and Evaluation Principles*, volume 4. Springer Science & Business Media, 2000.